SMALL-SCALE CONVECTION AND THE EVOLUTION OF THE LITHOSPHERE

by

Walter Roger Buck

B.S., The College of William and Mary
(1978)

SUBMITTED TO THE DEPARTMENT OF
EARTH, ATMOSPHERIC, AND PLANETARY SCIENCES
IN PARTIAL FULFILLMENT
OF THE REQUIREMENTS
FOR THE DEGREE OF

DOCTOR OF PHILOSOPHY

at the

MASSACHUSETTS INSTITUTE OF TECHNOLOGY

October 1984

Signature of Author_____
Department of Earth and Planetary Sciences
October, 1984

Certified by_____
M. Nafi Toksöz
Thesis Supervisor

Accepted by_____
Theodore R. Madden
Chairman, Department Committee

SMALL-SCALE CONVECTION AND THE EVOLUTION OF THE LITHOSPHERE

by

W. Roger Buck

Submitted to

the Department of Earth, Atmospheric and Planetary Sciences on October 18,1984 in partial fulfillment of the requirements of the Degree of Doctor of Philosophy in Geophysics

ABSTRACT

In this thesis we calculate the effect of small-scale convection on the thickness and temperature structure of the lithosphere for three cases where geophysical and geological data may allow us to see these effects. The problems are: (1) the cooling of the oceanic lithosphere; (2) the cooling of a passive rift temperature structure; and (3) the rate of thinning of lithosphere which has been thickened in a continental convergence zone. In all these cases the convection is driven by the temperature gradients at the base of the lithosphere and the key to the interaction between the lithosphere and the flow in the asthenosphere is the viscosity relation we assume. It is very likely that the viscosity of the mantle depends on temperature and we take that to be the case. Viscosity which also depends on pressure and stress is also considered in these calculations. We study all these problems using finite difference numerical methods and, where possible, we derive general relations between the model parameters and predicted data.

For the problem of the cooling of the oceanic lithosphere we find that a linear relation is predicted between the subsidence of the ocean floor and $(\text{time})^{1/2}$, even after small-scale convection has begun. The slope of this plot depends on the viscosity structure of the convecting region, and its magnitude is less than the corresponding subsidence for purely conductive cooling. Small-scale convection can begin to affect the subsidence age relation after only a few million years of lithospheric cooling. Convection which begins under lithosphere of this age can produce vertical deformations of

the surface of the sea floor, which should produce a detectible gravity signal. Previous workers have shown that small-scale convection beneath the moving oceanic plates should have the orientation of two-dimensional rolls with axes aligned parallel to the direction of plate motion. In that case the gravity signals produced by the convection should be aligned in the direction of plate motion and so may account for signals with this orientation which have been observed over several areas of the oceans in Seasat altimeter data. We suggest that the short wavelength (<300 km) topography produced by the convection is "frozen in" by the elastic lithosphere as the plate cools. For convection to be sufficiently vigorous under the young lithosphere to produce the topographic and gravity signals, before the elastic lithosphere is so thick as to damp out these signals, requires minimum asthenospheric viscosities less than 10^{18} Pa-s. Such values are consistent with estimates of average mantle viscosity if a pressure dependence of viscosity is included. Another body of data which may reflect the effects of small-scale convection under the oceanic plates concerns the offset of the geoid height across fracture zones. This data reflects the difference in lithospheric thickness across fracture zones. The convective models considered here can account for the trend and most of the magnitude of the data. Conductive thermal models cannot. Including lateral flow across the fracture zone may account for the data variations not matched here.

We are able to use theoretical relationships between the heat flux out of a convecting region and the viscosity parameters which describe the rheology of that region to study the problem of the cooling of the oceanic lithosphere. This allows us not only to elucidate the features of our models which are important to the physics of the cooling of the lithosphere, but also allows us to define general reltionships between the predicted subsidence, geoid height and heat flow, and the model parameters. We use the mathematical formulation of the Stefan problem to describe the temperatures in the lithosphere with time given the variations predicted for the heat transport across the convecting region. We find that one parameter (λ) describes the changes in the temperatures and thickness of the model lithosphere caused by small-scale convection, which is driven by cooling from above. This parameter can be related directly to the average viscosity of the convecting asthenosphere and to the temperature and pressure dependence of the viscosity. The parameter λ varies nearly linearly with the log of the average viscosity of the convecting region. For a change in the average viscosity of a factor of ten, λ changes by about 20%. Several geophysically interesting model predictions can be related to the parameter λ. The predicted subsidence varies linearly with λ and the

isostatic geoid height varies approximately with λ^2 while, the surface heat flux goes like $1/\lambda$. Subsidence variations for different areas of the oceans can be related to the differences in the asthenospheric viscosities and presumably temperatures (through the temperature dependence of viscosity) using the derived relationships. The asthenospheric temperatures can be estimated using seismic methods, and then compared to the estimates based on subsidence data using this model.

To deal with the problem of calulating the flow induced by the large horizontal temperature gradients under a rift we developed a simple finite difference method for approximating a curved, no-slip boundary called the "repeated corner approach". It is valid because the viscosities decrease rapidly going away from a boundary in this problem, so the flow rates near the boundary are much less than further away.

It is shown that the effects of convection induced by a passive rift temperature structure can explain data on the uplift of the flanks of rifts and details of the subsidence history of rifted continental margins. Uplift of the flanks of about 1 km is shown to be consistent with the lateral transfer of heat beneath a rift, caused by a combination of conduction and convection. The amount of uplift depends on the viscosities assumed, but they must be low to match observed uplifts (a minimum of about 10^{18} Pa-s is required for 1 km of uplift). The stress dependence of viscosity also contributes to the uplift of the flanks. Also, we find that the narrower the rift, the greater the uplift.

Finally, we test the hypothesis that small-scale convection under lithosphere, which has been thickened in a convergence zone, can thin "normal" lithosphere in only a few tens of millions of years. This is required to explain the high surface heat flux in convergence zones if the lithosphere is thickened along with the crust. If the visosity depends on temperature through laboratory estimated parameters, we find that the rate of thinning of the lithosphere is not significantly increased by the instability of the thickened boundary layer at the base of the lithosphere. In Tibet, the crust was thickened within the past 40 m.y., but the surface heat fluxes are presently higher than normal. This leads us to suggest that the mantle lithosphere was not thickened along with the crust in that region, but was subducted in a manner similar to that observed for oceanic lithosphere.

Thesis Advisor: M. Nafi Toksöz

Title: Professor of Geophysics

ACKNOWLEDGEMENTS

Nothing in this thesis could have been done without the help and advice of others. Though I have sometimes stubbornly ignored the advice of elders, I appreciate their efforts immensely. Nafi Toksöz, my advisor, has helped me through it all. He has shown an uncanny sense of when I needed a pat on the back or a warning and when I could be left to my own devices. I have essentially had a second advisor in Marc Parmentier, during the period of doing this thesis. He was patient with me when I was learning the basics of doing numerical fluid dynamics. Every few months, when we got together at Brown or at M.I.T., he was willing to listen to every interpretation of the results of such calculations and to suggest other possibilities. Sean Solomon has been another great source of advice on everything from the moon to how to write a title with punch. The other members of this department have contributed to my growth here by example and through their teaching.

The richness of the experience I have had since coming here has been largely a result of the association with the other graduate students. This association has taken many forms, from late night discussions of the meaning of life with Lynn Hall or politics with Dan Davis to chasing aftershocks across the frozen wastes of New Brunswick with the likes of Paul Huang and Carl Godkin. Steve Taylor, Mike Fehler and Arthur Cheng took me under their wings when I first got here and showed me the ropes. Room 521 has been a great office with a healthy

exchange of ideas and opinions happening all the time. Thanks to Gerardo Suarez, Rob Comer, Mark Willis, Jim Muller, Dan Davis and lately to Paul Okubo, Mark Murray, Greg Beroza, Bob Grimm, Kiyoshi Yomogida for making it that way. Bob Nowack, Sharon Feldstein, Guy Consolmagno, Eric Bergman, Joao Rosa, Tianqing Cao and Kaye Shedlock have helped to make the 5th floor the social and academic garden spot of the department. I don't know how my housemates -Scott Phillips, Steve Bratt and Mark Murray -have managed with my rantings about geophysics when we should have been watching Nightline.

Thanks to Carol Blackway, Steve Gildea and Al Tyalor who helped me with computer problems and to all those ERL VAX users who suffered so when I was running big calculations.

I often think that I have learned more about basketball, softball and bicycling since I came to M.I.T. than I have about geophysics. Thanks to Dan Davis and Cliff Thurber for dragging me over to play basketball when I committed more fouls than I scored points. Since those early days Scott Phillips, Steve Roecker, Dave Olgaard and recently Bobby Rivera have provided great companionship when we played pick-up games together. A lot of people suffered when they tried to rebound against me (sorry, Steve). Thanks also to the Boston Celtics for providing such an entertaining example of how to come from behind. Spring has meant Rocksliders softball around here. I especially want to thank the guys on the team who never gave up believing I could be a power hitter, even though I didn't hit a a home run until the last game of my contract in Boston. Thanks to Bob King, Irwin Shapiro and the rest of the Nine

Planets softball team for making the last summer I worked on my thesis bearable. Thanks to Paul Okubo for helping me to understand the finer points of biking and to Lind Gee for organizing some great bike trips.

Former teachers got me going in the direction which led here and inspired me along the way. In high school Mrs. Ramar stood out. I would not have gone into physics had it not been for Professors like Dr. Siegel, Dr. Kane and Dr. Welch at Willian and Mary. Geology was brought to life for me there by Dr. Benham, Dr. Bick, Dr. Clement, Dr. Goodwin and Dr. Johnson.

Thanks to Jan Nattier-Barbaro for typing this manuscript and to Sharon Quayle, Lynn Hall, Luce Fleitout, Beth Robinson, Kiyoshi Yomogida and Mark Murray for help in proofing parts of the manuscript. Nafi Toksöz, Marc Parmentier, Barry Parsons, Leigh Royden and Tim Grove gave me suggestions which improved the text. The figures of gravity data for the oceans were kindly provided by Jeff Weissel.

Thanks to my mother and father who encouraged me to be inquisitive and to follow up on my interests. They have always supported me in every way they could.

Special thanks to Bobby Rivera who constantly reminded me that there was a lot happening in Cambridge which had nothing to do with the schools there. He also helped with the figures.

Sharon Quayle managed to encourage me through all the work of this thesis, even when the worst of it came when she was starting in medical school.

Financial support for this work has come from an Exxon Teaching Fellowship.

TABLE OF CONTENTS

"The terrible fluidity of self-revelation".

-Henry James,"The Ambassadors."

CHAPTER 1

INTRODUCTION

Convection in the earth has long been associated with plate tectonics, but only in about the last ten years has much attention been paid to the possibility of a scale of mantle convection smaller than the horizontal dimensions of the lithospheric plates. It is this "small-scale" convection, and particularly the effect of such convection on the thermal state and thickness of the lithosphere, which is the subject of this work. The subduction of material at oceanic trenches and the upwelling at mid-ocean ridges requires some form of large-scale mantle convection, but the form of that convection is hotly debated. The existence of small-scale convection in the earth is not so clearly required by one kind of data. However, there is a growing body of data which is most easily explained as a result of small-scale convection. This study focuses on small-scale convection which is associated with the temperature gradients at the base of the lithosphere. Since there are several ways to measure the effects of variations in the thickness of the lithosphere, we may be able to verify the predictions of the calculations presented here.

Three specific problems of geologic interest which involve the interaction of small-scale convection and the lithosphere will be discussed. In all the problems we consider viscosity to be a function of temperature and other parameters. It is the difference in temperature and therefore viscosity which defines the lithosphere in all these problems. The lithosphere considered here is the thermal lithosphere and is defined in terms of the mode of heat transfer in the mantle. The lithosphere is the area where the dominant mode of heat transfer is conductive, while in the asthenosphere advection is the dominant mode. The first problem we consider is that of the cooling of the lithosphere including the effect of small-scale convection directly below the lithosphere. Since the data on the cooling of the oceanic lithosphere offer the best opportunity of verifying the effects of small-scale convection we will discuss the relation between geophysical data for the oceans and our calculated estimates of those effects. The next topic of consideration is convection induced by the strong lateral temperature variations which result from rifting of the lithosphere. The third geophysical problem is the role of small-scale convection in thinning the lithosphere which has been thickened in a continental convergence zone.

In studying these three problems we employ numerical methods which are discussed in the Appendix. Our first goal is to find out whether small-scale convection can account for data in each of these cases and be consistent with other geophysical data which constrains the range of physical parameters, most

importantly the rheology of the mantle. However, we do not intend simply to construct numerical models which fit the data, we try to understand and elucidate the parameters which control the physics of these problems. Therefore, we vary the parameters which affect our numerical models and where possible derive general relationships between these parameters and the predicted geophysical observables.

In Chapter 2 the problem of the cooling of the oceanic lithosphere is described and numerical experiments on the effect of small-scale convection on that process are described. The data considered are (1) ocean floor subsidence rates, (2) satellite-derived small-wavelength (< 500 km) gravity anomalies, and (3) the offset of geoid anomalies across fracture zones. Our numerical calculations differ from previous work in that we consider not only fixed cells but the growth of convection cells as the system evolves, and a wider range of viscosity parameters than others have considered. In the interest of understanding a simple problem well, we focus on the early evolution of the lithosphere and neglect heat sources which will only have a great effect later in the cooling history of the lithosphere.

The problem considered in Chapter 3 is the same as that of Chapter 2, but it is treated using analytic and not numerical methods. General relationships are derived between the physical parameters which described cooling and convection and predicted geophysical observables. To do this we use the relationship between the heat flux transported by a convecting region and the parameters which define that region which were

derived for simple constant viscosity systems. To describe the temperatures and thickness of the model lithosphere we use the mathematics of the Stefan problem. Using the general relations derived here we can predict the effect of different viscosity parameters on the model predictions without doing costly and difficult numerical calculations.

In Chapter 4 we treat the problem of lithospheric rifting. Simple conductive thermal models do not explain data on the subsidence of rifted areas and do not explain the large uplift observed for their flanks. The horizontal temperature variations produced by rifting will cause convective flow which will affect the cooling of that rift temperature structure. We consider numerical models of this process for the simplest form of rifting: passive rifting. The term "passive" refers to the role of the asthenosphere. Thus in our models no special heat flux or viscosity is assumed for the asthenosphere. We start our calculations with a temperature structure assumed to be derived from the tensional stretching of the lithosphere and compare the simple conductive cooling of that temperature structure and its cooling modified by convection.

It has been suggested that the thickening of the lithosphere might accompany the thickening of the crust in those regions, and further that small-scale convection can rapidly thin the lithosphere back to its original thickness. In Chapter 5, "The Mechanisms of Lithospheric Deformation in Convergence Zones," we first review the geologic and geophysical data on one major convergence zone (Tibet). These

data require that the lithospheric heat flow and therefore the thickness of the mantle lithosphere must be close to normal according to simple conductive thermal models of the crust. We then describe numerical experiments which are similar in formulation to those described in Chapter 2, except that the initial horizontally averaged temperature profile is that resulting from the thickening of a "normal" lithospheric temperature profile by a factor of 2. The purpose of these calculations is to see if small-scale convection which is induced by the instability of the thickened thermal boundary layer at the base of the lithosphere can thin the lithosphere to 1/2 of its thickened value in less than 40 m.y., as is required by the data for Tibet. A variety of viscosity parameters is considered in these calculations. We also derive a simple equation for the time required to thin doubly thickened lithosphere to its original thickness if the original thickness is in equilibrium with the average mantle heat flux. Finally, we consider the possibility that the mantle lithosphere in a convergence zone is not thickened along with the crust, but is subducted as the crust is scraped off.

In the Appendix we discuss the numerical methods used here and the reasons for not using other methods. Also the parameters defined in the following chapters are tabulated for quick reference.

"Castrol GTX showed no significant breakdown in viscosity even after 5,000 miles."

-From the can.

CHAPTER 2

SMALL-SCALE CONVECTION AND THE COOLING OF THE OCEANIC LITHOSPHERE

2.1 Introduction

Convection beneath the oceanic plates on a scale smaller than the horizontal dimensions of the lithospheric plates has been suggested to explain several geophysical observables. This provides one possible explanation for the deviation of seafloor subsidence with age from that predicted by simple conductive cooling of the oceanic lithosphere (Parsons and McKenzie, 1978). More recently, in their analysis of Seasat altimeter data, Haxby and Weissel (1983) have noted linear gravity anomalies which trend in the direction of plate motion. They have suggested that these features may be the result of small-scale convection. Based on theoretical considerations Richter (1973) predicted that small-scale convection should take the form of two-dimensional rolls with axes oriented in the direction of plate motion, thus providing an explanation for the form of the observed gravity anomalies. In this chapter we describe numerical calculations aimed at understanding small-scale flow which may occur under the

oceanic plates. The purpose of this work is to investigate whether models which are consistent with subsidence-age data for the oceans and other geophysical data can produce the observed gravity features.

In this chapter first we describe previous work on small-scale convection, next discuss the formulation of approximate models of convection and describe how we calculate several geophysical observables predicted by the models. A range of models is considered based on laboratory measurements of physical properties of mantle minerals and estimates of mantle viscosity. The predictions of the models are compared with data for subsidence of the ocean floor and gravity and geoid data for the oceans.

A number of investigations have been carried out on the effect of shearing flow on the form of thermal convective instabilities, including experimental work by Graham (1933) and theoretical stability studies by Ingersoll (1966) and Gage and Reid (1968). Richter (1973) showed that finite amplitude convective motions could be reoriented by shearing flow for an infinite Prandtl number fluid, and suggested that large scale mantle flow associated with plate motions could control the form of small-scale flow beneath a plate. This was corroborated by laboratory experiments performed by Richter and Parsons (1975) and Curlet (1975). Theoretical work has been carried out on the stability of the top thermal boundary layer of the large scale mantle flow (Parsons and McKenzie, 1978; Jaupart, 1981; Yuen et al., 1981; and Yuen and Fleitout, 1984). Parsons and McKenzie (1978) treated a mantle of uniform

viscosity below a fixed boundary and found that a thermal boundary layer could go unstable after 70 m.y. of cooling if its viscosity were $\sim 10^{22}$ Pa-s. Yuen et al. (1981) considered a viscosity structure resulting only from temperature dependent viscosity. For viscosities which depend only on temperature and which are consistent with post-glacial rebound estimates of whole mantle viscosity, they conclude that no instabilities develop in a cooling boundary layer for a time equal to the age of the oldest oceanic plates (200 m.y.). Jaupart and Parsons (1983) studied the linear stability problem for a depth dependent viscosity structure and concluded that for the base of the oceanic lithosphere to go unstable after 70 m.y. of conductive cooling required average viscosities there on the order of 10^{21} Pa-s. They also noted that the ratio of the maximum to the minimum viscosity in the convecting region was at most about a factor of 10. Yuen and Fleitout (1984) concluded that viscosity which depends on pressure as well as temperature is required to allow boundary layer average viscosities to be low enough for small-scale convection to occur under the ocean plates (i.e. a low viscosity zone) and still match other constraints on mantle viscosity. Our finite amplitude calculations, reported by Buck (1983), led to the same conclusion. Two previous studies which have considered the time evolution of convection are similar in formulation to the present work (Houseman and McKenzie, 1982; and Fleitout and Yuen, 1984). Both studies are concerned with the possibility that small-scale convection can explain a decrease in the rate of ocean subsidence which is indicated by the data to occur

after about 70 m.y. age of the lithosphere.

There are several important differences between these studies and the present work. The formulation of Houseman and McKenzie does not allow for the motion of the boundary between the lithosphere and the convecting region below and we do allow for this. This is necessary in their model because they treat the convecting region to be constant viscosity and the lithosphere to be rigid. Thus their model the boundary layers could not go unstable until cooling had penetrated past this boundary. In our formulation the boundary layers can go unstable and convection can begin at a time which is only determined by the viscosity parameters we choose. In our problem the lithosphere and the convecting region are allowed to interact and the thickness of the lithosphere changes with time. We consider the viscosity to be temperature and pressure dependent as do Fleitout and Yuen (1984). In that study the wavelength and depth of penetration of the flow are proscribed, unlike the present study. Also in our study we consider a wide range of viscosity parameters and we try to constrain the acceptible range of viscosties in terms of geophysical data.

2.2 Model Description

2.2.1 Simplifying Approximations

Small-scale convection in the form of rolls with axes parallel to the direction of plate motion is illustrated in Figure 2.1. As in previous studies (Houseman and McKenzie, 1982 and Fleitout and Yuen, 1984), we simplify the three dimensional problem to consider only two-dimensional flow in a vertical

plane parallel to a ridge crest. In doing this we ignore the effect of vertical gradients in horizontal velocity perpendicular to the ridge crest and both the thermal and mechanical coupling between vertical planes parallel to the ridge. These approximations reduce the problem to one of time dependent two-dimensional convection. The plane of the calculation is considered to move with the plate, so model time is proportional to distance from the ridge crest. The thermal effect of neglecting the third dimension of flow should not be great when the vertical gradients in the velocities parallel to the plate motion are small.

The depth of penetration of the small-scale cells into the mantle depends in part on the structure of the large-scale flow which is uncertain. Here, we consider no penetration deeper than 400 km since we are mainly concerned with the effects of small-scale convection soon after it has begun, when the cells are of small vertical extent. For depths that are much greater than this the interaction of the large and small-scale flow will almost certainly be more complicated than we assume here. Also the gravity anomalies described by Haxby and Weissel (1983) generally have wavelengths less than 400 km. The depth of penetration of convection cells should be of the same order the wavelength of the gravity anomalies they produced, as will be seen in the model results. In chapter 3 a parameterization of the convective contribution to cooling and its scaling with the size of the convecting region are discussed.

Vertical velocity gradients must exist in association with

plate motion. For our model results to apply to the cooling of the oceanic lithosphere those gradients must be small. This assumption does not violate the conclusions of Richter and McKenzie(1978) who noted the lack of correlation of plate velocity and subsidence with size of the plate. They argued that these observations require that there be a low viscosity region where vertical velocity gradients produced by the plate motion can exist without producing large horizontal pressure gradients. Their model requires either a thin region of very low viscosity or a thicker one of higher viscosity. We assume the latter case applies for viscosities used in our calculations, causing the region of velocity gradients to be of fairly broad depth extent. Seismic data analysed by Montager and Jobert (1983) supports this assumption. They studied the shear wave velocity structure of the upper mantle under the Pacific using Rayleigh waves and found that velocities down to at least 300 km increase steadily with increasing age of the overlying plate. Small-scale convection extending to these depths would produce this effect only if material at depth were being transported at close to the plate velocity.

2.2.2 Equations

Given the assumptions just discussed our problem reduces to studying thermal convection in a box of variable viscosity fluid driven by cooling from above. A schematic of this box is is given in Figure 2.2. We define a region of calculation (or box) to be of width (W_b) and depth (D_b). In that region we solve the two-dimensional Navier-Stokes equations for mass,

momentum and energy conservation (Batchelor, 1967). They are modified for the problem of flow in the earth's mantle by dropping inertial terms and terms that depend on material compressibility (Turcotte et al., 1972). The values of the physical parameters which were used to non-dimensionalize the equations is given in table 1. The governing equations were solved using a finite difference scheme with centered differences for the diffusion terms and upwind differences for the advection terms. Forward time stepping was used for the time derivatives. We used variable spacing of grid points using a difference scheme developed by Parmentier (1975). This allowed higher resolution in the regions of the largest gradients of viscosity and flow, without an excessive number of points overall. In the region of highest resolution the grid spacing is uniform, so formal second-order accuracy in the centered difference approximations is preserved (Roache, 1978). The grid positions are shown in Figures 2.3 and 2.4 as tick marks around the boxes.

Resolution of the solutions on the grids used here was established in two ways. First, the numerical experiments were done on successively refined grids until the same results were achieved on two different grids. Second, the heat flux out of the grid was compared to the average rate of change of temperature of the box to ensure conservation of energy.

2.2.3 Viscosity Relation

We consider olivine to be the dominant mineral in the upper mantle (Ringwood,1975) and adopt a relation for the

dynamic viscosity (μ) from (Weertman and Weertman, 1975) given by:

$$\mu(T,P) = A \exp\left((E + PV^*)/RT\right) \qquad (2.1)$$

where E is the activation energy; V* is the effective activation volume which is defined below; A is a constant varied to adjust the average visosity, and R is the Universal gas constant. The value of the activation energy, which controls the temperature dependence of the viscosity is estimated from data from three different kinds of laboratory measurements. Goetze (1978) summarizes measurements of creep in olivine giving 520 ± 20 KJ/mol as the range of values for E. Measurement of the oxygen self-diffusion rate for fosterite by Reddy et al. (1980) gives E = 372 ± 13 KJ/mol. Finally, based on analysis of the dislocation recovery during static annealing Kohlstedt et al. (1980) find that E = 300 ± 20 KJ/mol. We define the effective activation volume (V*) as the activation volume minus a value which corresponds to the negative viscosity gradient resulting from an adiabatic temperature gradient. An adiabatic gradient of .3°K/km was assumed. Sammis et al. (1981) show that estimates of the activation volume based on experimental and theoretical methods give about the same range for olivine of 10-20 x 10^{-5} m^3/mol. The activation volume, V*, which controls the pressure dependence of the viscosity, is critical to reconciling different estimates of mantle viscosity based on geophysical observations.

An average mantle value for viscosity of about 10^{21} Pa-s is

required by post glacial rebound rates (Cathles, 1975; Peltier and Andrews, 1976). Several geophysical observations require much lower viscosities at shallower depths in the mantle under the oceanic lithosphere and under tectonically active regions of the continents. Passey (1983) has analysed the rebound of dried lakes in Utah and infers shallow mantle viscosities lower than 10^{19} Pa-s. Richter and McKenzie (1978) and Weins and Stein (1984) require asthenospheric viscosities beneath the oceans in the range of 10^{18} -10^{19} Pa-s based on the distribution of stresses in the oceanic plates. Viscosity must increase with pressure and therefore depth to reconcile low viscosities at shallow depths and high viscosities for the average mantle. Figures 2.3 and 2.4 show viscosity calculated with equation (2.1) plotted versus depth for the viscosity parameters given in table 2.2.

2.2.4 Boundary and Initial Conditions

At the top of a cooling variable viscosity fluid, temperatures are low and temperature gradients are high. Therefore, viscosity, given by equation 2.1, in the top of the box can be so large that flow is negligible in that region compared to deeper in the box. In this lid heat transfer takes place exclusively by conduction. The lid is analogous to the thermal lithosphere. Below this region convection is active and is the dominant mechanism of heat transport. Since we are considering the transient cooling of a fluid and not a steady-state condition, both the lid thickness and the vigor of the convection in the interior will change with time through

the calculations. It is the interaction of the cooling lid with the convecting region below which is of interest. The convection is driven by the temperature gradients at the base of the lid and in turn the rate of thickening of the lid (or lithosphere) is affected by the convection. The study of Houseman and McKenzie (1982) also considered a conducting region overlying a convecting region. But the boundary between the conductive and convective regions was kept fixed at one depth in the model so the interaction could not be studied.

The boundary conditions for the flow on all sides of the region of calculation are taken to be shear stress-free. However, it is computationally more efficient to place a no-slip (fixed) boundary at the depth in the lid where viscosity is three orders of magnitude above the minimum viscosity in the flow region. Because viscosities are so high in the cold lid, there is effectively no flow there. Calculations with the boundary placed higher in the lithosphere, where the viscosity is higher, give the same results, but require more computer time. The boundary conditions on the temperature are fixed (corresponding to 273°K) at the top and insulating on the sides and bottom. In the study of Fleitout and Yuen (1984) the boundary conditions are the same as used here except that a constant tempoerature is prescribed at the bottom of the box. This condition is also used in some of the cases considered by Houseman and McKenzie (1982), but they also use an insulating bottom boundary for cases where heat sources are distributed throughout the

convecting region. These conditions were used because both of these studies are concerned with the approach of the lithospheric thickness to a value which is in equilibrium with background mantle heat flux. We are mainly concerned with the early evolution of the oceanic lithosphere, when the effect of heat sources in the mantle on the rate of cooling of the lithosphere should be small.

Two types of initial conditions on the temperature are used. For both, the initial horizontally uniform temperature profile is that resulting from 5 m.y. of conductive cooling of an initial box temperature (T_m) of 1573°K. Convection may begin earlier than this for some of the viscosity structures we examine, but temperature and viscosity gradients are so large for smaller initial cooling times that they are difficult to resolve even on relatively fine grids. Some of the results of these calculations should apply at earlier times than 5 m.y. Two types of initial temperature perturbations are superimposed on the horizontally uniform temperature profile to induce convective motion. In the first, a random pertubation of less than 1°K was introduced at each grid point. In the second, a periodic temperature perturbation with a wavelength equal to twice the width of the box and with a 1°K amplitude is used to induce the growth of only one convective wavelength.

2.2.5 Description of Models Considered

A list of the model parameters which are common to all the calculations is given in table 2.1. The parameters varied from one calculation to another are the average viscosity (through

parameter A), the activation energy (E), the effective activation volume (V*), the width (W_b) and depth (D_b) of the box. They are listed in table 2.2. A random initial temperature perturbation was used in only one of the models. This is case 15 which is carried out in the widest box of any of the calculations. This model is designed to examine changes in the depth of penetration and wavelength of the convection cells through the course of a calculation. In the other model calculations only one convection cell is induced by the periodic temperature perturbation. These smaller simpler cases are used to study the effect of varying a wide variety of parameters since both the size of a large box and the variability of the flow caused by the random initial conditions require large amounts of computer time. Another reason to consider fixed width convection cells is to examine the effects of different convective wavelengths.

Non-Newtonian viscosity calculations have been carried out, but are not included in the detailed discussions here. Using nearly the same parameters for stress dependence of viscosity as were used in Fleitout and Yuen (1984) we found that this had no effect on our calculations. In their formulation there is effective cut-off in deviatoric stress of 10 bars, below which the viscosity is Newtonian. The deviatoric stresses in our calculations are generally less than this cut-off because the wavelengths of our calculations is small compared to theirs.

2.3 Calculation of Model Geophysical Observables

Subsidence due to cooling of the lithosphere is estimated in two ways. The first is based on the average temperature in the lithosphere. To do this we define three regions: a conductive lid, a flow boundary layer and a convecting region (see Figure 2.2). The depth to the top of the convecting region is defined as the level where there is a maximum in the horizontally averaged advective heat flux (Q_c) which is defined as:

$$Q_c(z) = \frac{1}{W_b} \int_0^{W_b} w(x,z)T(x,z)\, dx \qquad (2.2)$$

where w is the vertical component of the velocity. The convecting region is considered to be all the area below this depth. The average temperature of the region is defined as T_{cr}. The base of the conductive lid (Z_L) is defined as the depth where the horizontally averaged temperature equals .9 T_{cr}. We can then define a useful measure of the temperatures in the conductive lid as :

$$T_L = \frac{1}{W_b \cdot Z_L} \int_0^{Z_L} \int_0^{W_b} \frac{T(z)}{.9\ T_{cr}}\, dxdz \qquad (2.3)$$

Figure 2.5 shows values of T_L for a number of the model cases. The subsidence calculated using T_L is given by:

$$S(t) = \left(\frac{\alpha \rho_m}{\rho_m - \rho_w} \right) \left(T_m - T_L \cdot T_{cr}\right) Z_L \qquad (2.4)$$

implying that the conductive lid is in isostatic equlibrium. The values of the depth $Z_L(t)$ are plotted as a function of $t^{1/2}$ in Figures 2.6 and 2.7 for two of the numerical models. These

plots show that the convection has changed the slope of the curves but that during most of the calculation they are linear on such a plot. This suggests that the dependence of Z_L on time can be written as:

$$Z_L(t) = 2 \lambda (\kappa t)^{1/2} \quad . \qquad (2.5)$$

Where κ is the thermal diffusivity. This relation is similar to the standard description of the increase in the depth to a given isotherm for the case of purely conductive cooling with λ given by $erf^{-1}(.9)$ (Carslaw and Jeager, 1959). For the cases here the value of λ will depend on the vigor of convection beneath the lid. The relation between λ and the viscosity and other model parameters are given in chapter 3. The parameter λ can be related to the geophysical observables as discussed below.

The second way to estimate the subsidence is to calculate the change in the average temperature of the upper part of the box to a depth of compensation (Z_C). Here Z_C is taken to be 150 km. The material above Z_C is asssumed to be in isostatic equilibrium. This is the same method used by Jarvis and Peltier (1982) for calculation of subsidence associated with large scale mantle flow and by Houseman and McKenzie (1982) and Fleitout and Yuen (1984). An average temperature from the top of the box to the depth (Z_C) is defined as (T_C) and can be used to calculate subsidence using equation (2.4) by replacing $T_L \cdot T_{cr}$ with (T_C) and replacing Z_L with Z_C. The subsidence calculated using either method is nearly the same because the

temperature change with time below the boundary layer is small compared to that in the conductive lid. The physical parameters used in equation (2.4) are given in table 2.1. Since the thermal expansion coefficient is temperature dependent, the appropriate temperature range for the temperature change should be used. For this problem the average temperature drop in the conductive lid is about 600°K, so the appropriate temperature for calculating the average value of α is about 1573°C - 600/2. = 1273°K. For olivine α_v(T=1273°K) is about 4.0×10^{-5} °K (Skinner, 1966). Over the pressure range in the lithosphere the effect of pressure on the thermal expansion coefficient should be small. Figures 2.6(a) and 2.7(b) shows the non-dimensional subsidence calculated using equation 2.4 and part (b) of those figures show plots which are proportional the non-dimensional subsidence using (Z_C) equal to 150 km.

In the calculation of subsidence a depth of compensation (Z_C) where isostacy is attained, is assumed. If the depth is varied by about ±50 km from the value of 150 km used here, the results do not change drastically. However, if the depth of compensation is taken to be near the bottom of the box then the subsidence relative to that for purely conductive cooling is quite different. Whereas the subsidence at a given time calculated for the models using a shallow depth of compensation is less than that for the conductive case, it would be greater than the conductive value if the depth of compensation were taken to be much deeper. The justification for a shallow depth

of compensation is related to the viscosity structure we have assumed. Horizontal pressure gradients in the direction perpendicular to the plane of the calculations, which are not explicitely calculated here, should arise due to temperature variations in that direction. Flow will be driven by these pressure gradients and this flow may affect subsidence. The definition of the depth of compensation is the level where horizontal pressure gradients cannot be maintained by the strength of the materials. The level we have chosen for the depth of compensation is the depth where the viscosity is low over the duration of the numerical calculations. This amounts to assuming that the flow at this level will not produce any long wavelength topography. This kind of behavior is seen in calculations of convection in fluids with depth dependent viscosity. Such studies (McKenzie, 1977; Parsons and Daly, 1983; Richards and Hager, 1984) show that the topography due to convection in fluids with lower viscosities near the top of convection cells than deeper down is much smaller than for constant viscosity fluids.

The isostatic geoid anomaly (Haxby and Turcotte, 1978) is given by :

$$H(t) = \frac{-2\pi G}{g} \left\{ \frac{(\rho_m - \rho_w)(S(t))^2}{2} + \alpha \rho_m \int_0^{Z_L} (T_m - T_h(z))\, z\, dz \right\} \qquad (2.6)$$

where $T_h(z)$ is the horizontally averaged temperature at a depth (z). This expression is valid only if the density variation producing the anomaly is isostatically compensated and if its

vertical extent is small compared to horizontal distances over which density variations occur. Thus, it should be valid as long as variations in temperature and therefore density, below Z_L are small. This is the case for the offset of the geoid across fracture zones.

The gravity anomaly at the top of the box is another observable to calculate from our model results. There are three components which contribute to an anomaly. One is due to temperature and therefore density variations in the box. A second is due to the deformation of the top surface of the box as a result of convective stresses. Thirdly, hydrostatic pressure variations due to horizontal temperature differences within the conductive lid also contributes to the stresses and deformation of the top boundary of the box. The first component of the anomaly is calculated by numerically integrating the following expression for the vertical component of gravity (G_T) due to distributed two-dimensional density anomalies:

$$G_T(x') = \frac{2G\rho_m\alpha\Delta T}{5W_b} \int_0^D \int_{-2W_b}^{+3W_b} \left(T_h(z) - T(x,z)\right) \frac{z}{(x-x')^2+z^2} dxdz \qquad (2.7)$$

where G = gravitational constant, and the other values have been defined before. The temperature structure in the box is assumed to be periodic with wavelength $2W_b$. The range of integration is over 2.5 wavelengths to get rid of any edge effects.

To determine the component of the gravity anomaly due to

the flow we must calculate the normal stress (σ_{zz}) on the flow boundary of the conductive lid. Following McKenzie (1977), and Parmentier and Turcotte (1978), the normal stress at any boundary point is given by:

$$\sigma_{zz}(x) = \frac{\nu\kappa}{D_b^2} (-P(x) + \tau_{zz}(x)) \qquad (2.8)$$

where ν is the kinematic viscosity (μ/ρ_m) and τ_{zz} and P are the non-dimensional deviatoric stress and pressure, respectively.

$$\tau_{zz}(x) = 2\eta \frac{\partial \omega}{\partial z} \quad . \qquad (2.9)$$

where (ω) is the vorticity and ($\eta = \nu/\nu_o$) is the non-dimensional viscosity. The pressure is obtained by integrating the horizontal pressure gradient on the boundary

$$P(x) = \int_0^x \frac{\partial P}{\partial x} dx = - \int_0^x \eta \frac{\partial \omega}{\partial z} dx \; . \qquad (2.10)$$

The stress at the surface of the box must include the effect of temperature variations in the conductive lid (σ_T), given by

$$\sigma_T(x) = \rho_m \alpha_v g \int_0^{Z_L} (T_h(z) - T(x,z)) \, dz \; . \qquad (2.11)$$

Assuming free vertical motion in the lid, that the stress is transmitted to the surface, the total normal stress at the surface (σ_{ns}) is:

$$\sigma_{ns} = \sigma_{zz}(x) + \sigma_T(x) \qquad (2.12)$$

The stress at the surface is adjusted such that the average is zero. The gravitational effect of these stresses in our model is determined by the resulting elevation (E(x)) of the surface. To determine this we must assume a flexural rigidity (D) of the elastic lithosphere. If we assume D to be zero resulting in a point-wise isostatic response, hydrostatic stresses due to elevation of the surface must match the normal stress at each point giving:

$$E(x) = \frac{\sigma ns(x)}{(\rho_m - \rho_w)} g \qquad (2.13)$$

where g is the acceleration of gravity. But, if D is non-zero the elevation will be reduced by an amount which depends on the wavenumber (k)of each Fourrier component of the stress distribution. For a given stress harmonic the observed elevation (E_f) is:

$$E_f(x) = \frac{E(x)}{\left(1 + D \frac{k^4}{\rho_m g}\right)} \qquad (2.14)$$

(McKenzie and Bowin,1976). The flexural rigidity is proportional to the cube of the thickness of the the elastic lithosphere. For an elastic layer thickness of 10 km, and using values for elastic parameters from Watts and Steckler (1980), the flexural rigidity (D) = 10^{23} kg-m^2/s^2. For this flexural rigidity, a stress distribution with wavelengths less than 200 km produces almost no surface elevation.

The gravity anomaly at a point due to this elevation anomaly is calculated assuming that the extra mass due to the

surface elevation can be considered an infinite sheet. This is a good approximation for features with a wavelength greater than several tens of km, which is true of all the variations discussed here. Then the gravity anomaly caused by elevation is given by

$$G_E(x) = 2\pi\ G(\rho_m-\rho_\omega)E_F(x) = G_\sigma + G_L \qquad (2.15)$$

where G_σ is the part of the signal due to the stresses produced by flow and G_L is the component due the the variation of the lithospheric temperatures.

Finally, the average heat flux out of the top of the box ($Q_s(t)$) is given by the product of the average temperature gradient at z=0. and the conductivity (K).

$$Q_s(t) = K\ \frac{1}{W_b}\int_o^{W_b} \left.\frac{dT}{dz}\right|_{(x,o)} dx \qquad (2.16)$$

where dT/dz is estimated using the centered finite difference form given in the appendix.

2.4 Results

2.4.1 Large Box Calculations

The results of a calculation within a box representing a 400 x 400 km region of the mantle are illustrated in Figure 2.3. The figure shows several quantities which describe the flow at four times. The temperature contours give an idea of the rate of movement of material as cold blobs are sinking and hot plumes rising because advective heat transfer dominates the conductive transfer in the region where isotherms are distorted from horizontal. The streamlines show the number of convection cells at a given time and the depth of penetration of the flow. The cells are seen to grow larger during the early part of the calculation. The initial wavelength of the flow is controlled by the thickness of the thermal boundary layer which first becomes unstable. Jaupart (1981) points out that the fastest growing wavelength of the instability for a boundary layer in which viscosity decreases exponentially with depth should be between π and 2π times the boundary layer thickness. The boundary layer defined here is the region where both the advective and conductive heat flux vary rapidly with depth. This region is located between the conductive lid and the convecting region (see Figures 2.2, 2.3 and 2.4). After 2 m.y. of the calculation the wavelength of the flow in Figure 2.3 is about 60 km. This is consistent with an initial boundary layer thickness of about 10 km. In just another 2 m.y. the wavelength of the flow increases to nearly 120 km. The growth of the cells is rapid early in the calculation then later slows

and finally stops when the box is filled. The slowing of the growth of the cells depends on the pressure dependence of the viscosity since this causes the viscosity to increase with depth. In a model where viscosity did not depend on pressure the cells filled the box more rapidly than for any of the other cases.

The plots of the advective heat flux shown for different times in Figure 2.3, exhibit some interesting features. For a model time of 2 m.y. the convection is just starting to develop and very little heat is being transported by the flow. At the next two times, 4 and 5 m.y. into the calculation, the plots of advective heat flux have an extra local maxima due to a large amount of cold material from the original unstable boundary layer moving down. The profiles of the advected heat flux for the rest of the calculation look more like that for case 20 shown in Figure 2.4. There the largest advective heat flux occurs at the base of the boundary layer, and it decreases montonically with depth.

The horizontally averaged temperature profiles in Figure 2.3 show large gradients in the conductive lid but are relatively uniform below the boundary layer. The difference between the horizontally averaged temperature at a given depth and the temperature which would result from purely conductive cooling for the same amount of time is also shown. In the convecting region the temperatures are lower than they would be in the absence of convection, while in the conductive lid the temperatures are higher than they would be for purely

conductive cooling.

The average temperature in the lid (T_L), given by equation 3, is shown in Figure 2.5. For case 15, T_L decreases from the value for purely conductive cooling faster than the other cases where only one convective wavelength is present in the box. The small cells, present early in the run for case 15, are more efficient in getting heat out of the convecting region than are the longer wavelength cells. The local heat flux across the boundary layer at a given horizontal distance (x_c) from the center of upwelling between two cells should vary approximately as $x_c^{-1/2}$. Therefore the smaller the cell the higher the horizontally averaged value of the heat flux across the boundary layer. The higher the heat flux into the convecting region the faster the average lid temperature decreases. The small dip in the curve of T_L centered on 40 m.y. is due to the uncooled material at the bottom of the box moving up en masse and is a result of the unrealistic boundary condition at the bottom of the box on the stress (ie. free stress). During most of the calculation the value of T_L is remarkably constant.

The depth of the base of the conductive lid (Z_L defined by equation 2.5) is plotted versus $t^{-1/2}$ in Figure 2.6. The plots are nearly linear during time intervals when T_L is constant, but the slopes differ from the conductive solution. This means that the subsidence ($S(t)$) which is proportional to the product of T_L and Z_L will also be linear with $t^{-1/2}$. The non-dimensional subsidence is shown for case 15 in Figure 2.6, and the plot is indeed nearly linear with $t^{-1/2}$. The slope of

this line is proportional to the parameter λ which is estimated from the plot of Z_L, also in Figure 2.6, and listed in table 2.2. Theory described in chapter 3 predicts that S(t) should depend on $\lambda \alpha T_m (\kappa t)^{1/2}$.

The isostatic geoid anomaly (H(t)) for case 15 as a function of time, calculated using equation 2.6 is shown in Figure 2.8 along with plots for several other model cases. The slope of these curves is proportional to $\lambda^2 \alpha T_m \kappa$ as shown in chapter 3. The slope is more appropriate for comparing with the data for the oceanic lithosphere. In Figure 2.9 the derivative of the geoid height anomaly is shown as it varies with time. Data from Cazenave (1984) on the offset of the geoid height across fracture zones, where there is a change in the age of the lithosphere across the zone and is also shown on Figure 2.9 . The model results have a similar trend to this data, but the full magnitude of the slope change is not predicted by case 15.

The total gravity anomaly associated with the small-scale convective rolls is shown in Figure 2.3, assuming no flexural damping of the signal. The amplitude of the anomalies increases with time, especially after the cells cease to grow very rapidly. This is true because the effect of temperature variations in the lid lag the change in cell size. Clearly, time is required for the lateral differences in advective heat flux to be conducted into the lid. The components which make up the total model gravity anomaly (G_σ, G_L and G_T) are shown in Figure 10 for one time in calculation of case 15. Clearly, most of the total anomaly arises due to the combination of

stresses at the base of the lithosphere (G_σ) and pressure variations through the lithosphere (G_L), both of which will be reduced in magnitude due to flexural damping of the elastic lithosphere. In Figure 2.11 the magnitude of the maximum difference in peak to trough amplitude for the three components of the gravity signal are shown as a function of time for several of the cases including case 15. Just as for the isostatic geoid anomaly the gravity anomaly changes most rapidly soon after the calculation is begun. Again, this is due to the efficiency of the small cells in transporting material and heat. The component of the signal due to the flow induced stresses (G_σ) grows very quickly at first, but later maintains a nearly constant value. The component resulting from lithospheric temperature variations (G_L) grows more slowly, but continues to grow through most of the calculation. This is partly due to the increasing wavelength of the flow with time, which leads to a larger contrast in the heat flux locally flowing from the convection cell into the conductive lid. It also increases with time after the cell width has become constant, because, as the lid thickens, the temperature variations resulting from the horizontal variation in heat flux extend over a greater depth. The magnitude of the signal arising from density contrasts throughout the box (G_T) follows the same trend as G_L. The amplitude of G_T is much smaller than that of G_L and is opposite in sign from G_σ and G_L. The trend of G_T parallels G_L because most of that signal originates within the conductive lid.

A contour plot of the total model gravity signal, the sum of G_T, G_σ and G_L, is shown in Figure 2.12 for case 15. Distance is scaled with time through an assumed plate velocity of 4 cm/yr. Some of the profiles used to construct this figure are shown in Figure 2.3. No flexural damping was included. As was seen before, the wavelengths of the signal increase with time and the amplitude also increases somewhat. Over the range of times shown the effects of the finite size of the box in constraining cell size is not large.

2.4.2 Small Box Calculations

Numerical calculations with the same boundary conditions as for the large box calculation (case 15), but with a periodic initial temperature perturbation were carried out for a number of cases which are listed in Table 2.2. The parameters varied in this set of calculations are the average viscosity (through parameter A in equation 2.1), the activation energy (E), the effective activation volume (V*) and the width (W_b) and depth (D_b) of the box. The number of grid points for calculations with the same physical parameters is also varied. This was done to asses the accuracy of the numerical results. To illustrate the one cell calculations the same quantities which were shown in Figure 2.3 for the large box calculation are shown in Figure 2.4 for case 20, which has the same viscosity parameters as case 15. Only one time is illustrated. The single convection cell starts out penetrating only part way through the depth of the box and goes through the stage of cell

growth noted for the large box calculation. Here there is no increase in the width of the cell, only its depth extent increases. One of these small box cases, case 17, did not go through the stage of slow downward penetration of the cell. For that case there was no pressure dependence of viscosity and so no viscosity increase with depth.

In two of the cases (17 and 19) the initial single cell of flow broke down into two cells. Case 19 has the same viscosity parameters as case 20, but the width of the convecting region is twice as great (see Table 2.2). Case 17 was for the same width box as case 20. The reason for this cell breakdown is that the initially preferred wavelength of the flow was much smaller than the box width.

Several general relations between the geophysical observables calculated for this set of models should be pointed out. One of the most obvious is that the rate of change of the temperature structure of the conductive lid is inversely proportional to the average viscosity in the boundary layer and also depends on the activation energy E. The convective heat flux controls the variation of the average lid temperature (T_L) with time plotted in Figure 2.5. This figure shows that case 14, which has an average viscosity five times that of case 20, is much slower to change from the conductive value of T_L. This same slow growth is clearly seen in the rate of decrease in dH/dt shown in Figure 2.9 and in the slow increase in the amplitudes of the gravity components in Figure 2.11. For case 18, which has nearly the same initial viscosity for the region

below the boundary layer, but a lower activation energy E, growth is faster than for case 14. The decreased temperature dependence for case 18 results in a larger temperature difference across the boundary layer. As noted before, the size of the convection cells also affects the rate of heat transfer from the convecting to the conducting regions. Case 22, which has a box half the width of case 20, but with all other parameters the same, showed a much faster change in T_L in the early part of the run. For cases 22 and 20, the average advective heat flux for the smaller width box was greater by a factor of about $(2)^{1/2}$ when the viscosities were the same in the boundary layer region.

The heat flux at the surface ($Q_s(t)$) is slow to respond to changes in the heat flux from below because this heat must be conducted through the lid. Eventually, a difference in $Q_s(t)$ from the conductive cooling values will result from the convective enhancement of heat transfer below the lid. Figure 2.13 shows a plot of $Q_s(t)$ versus time for case 20 and that this model can match data for average heat flow with sea floor age from Sclater et al. (1980). We can also show how model results which are more constant in time depend on the model parameters. These comments apply to the time period when T_L is nearly constant. First, the average viscosity is inversely proportional to the deviation of T_L from the the conductive value (see Figure 2.5). This results from the fact that the rate of advective heat transfer is controlled by the average viscosity in the convecting region. The lower the viscosity,

the higher the heat flux. Since the subsidence (S(t)) is nearly linearly dependent on (λ) and the isostatic geoid height (H(t)) scales with λ^2, it is necessary to consider only the effect of variations in the model parameters on λ. The effect on the geophysical parameters follows, except for the gravity anomalies.

Case 14, with the highest value of viscosity (table 2.2) of all the cases has the highest value of λ. It follows that this case also has the highest value for T_L, the highest rate of subsidence and the largest average value of dH/dt. Decreasing the temperature dependence of viscosity, by lowering the activation energy (E) in case 18, decreases the value of λ. The average viscosity in the isothermal region is nearly the same at the start of the calculation for both case 14 and 18; but with E = 290 KJ/mol the change in the viscosity with temperature is half as great as for the other cases which had E = 410 KJ/mol. As the convecting region cools the viscosity and therefore the advective heat transfer does not decrease as rapidly as for case 14 .

Lowering the pressure dependence of viscosity by reducing the effective activation volume (V*) has much the same effect as lowering the temperature dependence of the viscosity. As the depth to the base of the boundary layer increases with time of cooling, the viscosity there will be increasing because pressure is proportional to depth. The viscosity in the boundary layer controls the advective heat flux. Thus for case 17 where the effective activation volume (V*) is zero the heat

flux decreases at a slower rate than it would if (V*) were larger.

The effect of a smaller wavelength for the convection is demonstrated by case 22. The width of the box is half that for case 20, but other parameters are the same. The heat flux at early times is much higher than for case 20, but later in the calculation it becomes lower than for the wider box. Model 22 departs somewhat from the simple behavior of constant (λ) and T_L in the later part of the run.

Reducing the depth extent of the convective cooling increases the value of (λ) as shown by case 23 for which the depth of the box is 3/4 of that for the other cases. The cause for this is simply that the rate of change of temperature in the smaller convecting region is greater for a given advective heat flux. As with case 22 the long term cooling departs from constancy of T_L.

The average lid temperature (T_L) and the slope of the plot of the lid thickness versus $t^{1/2}$ remains constant for most of the calculations after about 30 m.y. of model time. This is a consequence of the negative feedback of the convecting system (ie. the higher the advective heat flux the quicker the convecting region cools and so the viscosity goes up and the heat flux then goes down). Thus any system with strongly temperature dependent viscosity should behave in this regular fashion.

The model parameters control the time variation of the conponents of the gravity signal produced by convection in a

way that does not scale simply with the parameter (λ). The components (G_σ, G_L, and G_T) are shown for several of the runs in Figure 2.11. One result from these calculations is that the component due to flow stresses (G_σ) is fairly constant in amplitude after an early period of change. The early rate of change of this signal is greater for the cases with lower viscosity in the convecting region. The magnitude of the constant level of (G_σ) does not vary much with average viscosity in the boundary layer region, but it does inrease with increasing wavelength of the flow and with smaller values of the activation energy (E). The component of the gravity anomaly which depends on the stresses produced by temperature variations in the conductive lid (G_L) increases continuously with time for all the cases. The magnitude of the rate of increase is greater for the longer wavelength cases. Finally, the part of the gravity signal arising from density differences throughout the lid and convecting region (G_T) tends to parallel (G_L), but is lower in amplitude and opposite in sign at most points from (G_L).

2.5 Discussion

2.5.1 Gravity Anomalies

We will first discuss the implications of the model gravity anomalies, then make general remarks about the other model geophysical observables. The amplitudes and wavelengths of the signals shown in Figure 10 for case 15 are in the range observed by Haxby and Weissel (1984) in their analysis of gravity features derived from SEASAT altimetry data for the Central East Pacific. They observed anomalies with a wavelength of 150-250 km and a peak-to-trough amplitude of 8-20 x $10^{-5}(m/s^2)$ over ocean floor of greater than 6 m.y. age. The highs and lows of these features make linear trends in the direction of plate motion. The amplitude of the total gravity anomalies for all the small box calculations were also in this range for at least part of the time duration of the calculations. Two important features of the model gravity anomalies do not match the data. The first is that the increase in the wavelength of the anomalies with age observed by Haxby and Weissel is less than that predicted by the results of case 15 (see Figure 2.12). Secondly, when flexural damping of the components of the gravity signal, G_σ and G_L, due to the elastic lithosphere is included in the calculation of the model signals, their amplitude for short wavelengths (<250 km) become less than the observed signals. Figure 2.14 illustrates how strongly elastic lithosphere will damp signals as a function of their wavelength through a plot of the flexural filter ($F(k)= E_f(x)/E(x)$ as defined by equation 2.14. We convolve this

filter with the model anomaly components G_σ and G_L to approximate the effect of the elastic lithosphere. The result of doing this for different assumed values of the lithospheric thickness at different times for case 15 is shown in Figure 2.15. Using the variation of the elastic lithospheric thickness with age for the oceans estimated by Watts et al. (1980), signals with wavelengths less than 250 km will be damped by more than 90% for lithospheric ages greater than 15 m.y. Only when the small-scale convective wavelengths are greater than 400 to 500 km will the effect of the elastic lithosphere in damping the signals of G_σ and G_T become small for all lithospheric ages. There is some indication in the data of coherent signals around 500 km wavelength which also trend in the direction of plate motion (Haxby and Weissel, 1984). Figure 2.16 shows example gravity anomalies from Haxby and Weissel, 1984 and Figure 2.17 gives the location of those lines of data. Clearly, the amplitude of these anomalies are in the range observed in our calculations.

The elastic lithosphere acts to support topography in the same way that it suppresses the topographic expression of convective stresses. This may explain how small-scale convection can result in the observed pattern of short wavelength gravity anomalies. Topographic variations produced by convection when the elastic lithosphere is thin can be "frozen" into the lithosphere as the thickness and therefore the flexural rigidity of the lithosphere increases with age. This topography and the associated gravity anomalies should not

change greatly even as the convective pattern beneath the lithosphere changes. These gravity anomalies would have a linear trend in the direction of plate motion as on the observations. If so, the stresses due to convection must be well developed before the flexural rigidity of the lithosphere is large enough to suppress their topographic expression. From the model results we estimate that this requires that the asthenopheric viscosities be less than about 10^{18} Pa-s under young oceanic lithosphere. This seems like a very small value, but when the increase in viscosity with depth is taken into account, values become more like the ones estimated from other measurements discussed before. Even with an activation volume at the low end of the experimentally determined range of the for olivine (Sammis et al., 1981), 10 cm^3/mol, the viscosity reaches the estimated average mantle value of 10^{21} Pa-s at between 300 and 400 km depth.

2.5.2 Isostatic Geoid Anomalies

The calculated plots of the derivative of the model isostatic geoid height with time (shown in Figure 2.9) reproduce the early trend in the data on the offset of the geoid height across fracture zones. To match the magnitude of the change in dH(t)/dt seen in the data of Cazenave (1984) requires a lower viscosity than in any of the models considered here. Since the value of dH(t)/dt should scale with $\lambda^2 \kappa \alpha T_m$, it is possible to find a combination of these parameters which match both the average rate of subsidence and the rate of change of the isostatic geoid height. Another possibility is

that the low observed values of dH(t)/dt may be related to convection induced by differences in lithospheric thickness across fracture zones. This may cause faster homogenization of the asthenospheric temperatures and lithospheric thicknesses in the vicinity of the fracture zone. The calculations described in chapter 4 illustrate some features of this problem.

2.5.3

Subsidence and Lateral Heterogeneity of Mantle Temperatures

The comparison of the model results to data on the subsidence of the ocean basins is also interesting. For small-scale convection to be associated with the gravity and geoid features just discussed, it must develop in the first few million years after the lithosphere starts to cool. This means the onset of small-scale convection cannot produce the change in slope of the subsidence-age relation at about 70 m.y. as suggested by Parsons amd McKenzie (1978) and Houseman and McKenzie (1982). A number of alternative explanations for this feature of the subsidence data have been given (Forsyth, 1975; Schubert et al. 1976, Heestand and Crough, 1981; Jarvis and Peltier, 1982; Fleitout and Yuen, 1984), all involving a heat flux from the mantle brought to the base of the lithosphere by either convection or conduction.

Our main interest is the early evolution of the oceanic lithosphere where the effect of a heat flux from deeper in the mantle should be negligible. We have shown that the rate of subsidence should depend on $\lambda\alpha T_m(\kappa t)^{1/2}$ for cooling of the

mantle in the absence of heat sources. The average subsidence of the North Atlantic and the North Pacific ocean basins as estimated by Parsons and Sclater (1977) can be fit by a model with viscosities low enough to produce the gravity signals discussed above. Here we assume the thermal expansion (α) to be 3.8×10^{5} $^{\circ}K^{-1}$ This illustrated in Figure 2.18 which shows the subsidence-$t^{-1/2}$ plot for one of the models along with data on the variation of the subsidence rate for several oceanic plates or parts of those plates compiled by Hayes (1983) can be explained by the effects of small scale convection. The cause of these variations, in our view, is the difference in asthenospheric temperatures (T_m) under different lithospheric plates. A value of (T_m) which is 7% higher than a reference value will produce a change viscosity there of a factor of ten assuming an activation energy of 410 KJ/mol. Based on the cases described here and on the parameterization derived in chapter 3, we estimate that this change in viscosity will result in a decrease in the cooling parameter (λ) of about 18%. Thus, the overall effect is to decrease the rate of subsidence by around 12%. For conductive half-space cooling, with no small-scale convection, the rate would increase by 7% because of the effect of the higher temperature.

One way to estimate the variation in temperatures in the mantle is to consider differences in shear wave velocitites. Models of upper mantle shear wave velocities, based on surface waves, have been published by a number of workers (Woodhouse and Dziewonski, 1984; Nakanishi and Anderson, 1982). If the

cause of the shear velocity differences is taken to be differences in temperature, the magnitude of the required temperature variations can be estimated using a value of the derivative of the shear velocity of 3.4×10^{-4} km/s-°K estimated from data on Simmons and Wang (1971). We have compared the estimate of the relative temperature differences in the mantle in one area where variations in subsidence rates are large. The approximately 25% difference in subsidence rate between the African and South American sides of the South Atlantic in the latitude range from 35 to 45° South noted by Hayes (1983) would require at least a 200°K difference in temperature for our model. The shear wave model of Woodhouse and Dziewonski (1984) requires about this temperature difference and so requires that the area of inferred hotter mantle underlie the lithospheric plate which is subsiding more slowly.

The surface heat flux ($Q_s(t)$) should vary like $(T_m/\lambda)(Kc_p/t)^{1/2}$ as described in chapter 3. Uncertainties in our knowledge of the conductivity (K) and the specific heat (c_p) (Schatz and Simmons, 1972; Goranson ,1942) are sufficiently large that average oceanic heat flow values can be matched by a variety of models from purely conductive cases to models with vigorous small-scale convection. It is the lateral variations in heat flux which may allow us to put some constraints on the vigour of small-scale convection under different areas of the oceanic plates.

2.6 Conclusions

These calculations have shown that small-scale convection can produce the magnitude of gravity anomaly for short wavelengths observed for at least one area of the oceanic lithosphere and also be consistent with seafloor subsidence data. The linearity of a plot of subsidence versus $t^{1/2}$ seen in the data is also reproduced by model results, but the slope of such a plot depends on the vigour of the small-scale convection. The data on oceanic heat flow can also be fit with a model which includes convection on a small-scale. Data on the offset of the geoid height across fracture zones is more nearly matched by our results than a model that includes only conductive cooling. We feel that inclusion of the effect of differences in lithospheric thickness across fracture zones on small-scale convection may explain the geoid data more completely.

The model proposed here to explain small wavelength gravity anomalies over the oceans requires that small-scale convection begin in the first few m.y. after formation of the lithosphere at a mid-ocean ridge. The viscosities below such lithosphere must have a minima around 10^{18} Pa-s for this to occur. We suggest that topographic variations were produced when the elastic lithosphere was so thin that it could be easily deformed by the stresses associated with small-scale convection. This topography, which gives rise to the observed gravity anomalies, are supported by the strength of the elastic lithosphere as it cools and thickens, or "frozen in".

Lateral variations in the temperature of the asthenosphere should affect the vigour of convection and affect the rate of subsidence, the surface heat flow, the geoid height across fracture zones and the amplitude of the gravity anomalies associated with small-scale convection. This relation will hold if the viscosity of the mantle is strongly dependent on temperature. We have shown that there are indications that estimates of asthenospheric temperatures based on seismic date are consistent with this model and the variations of rates of seafloor subsidence. More work should be done on correlating seismic estimates of mantle temperatures and the variations in the other parameters just mentioned.

TABLE 2.1

Symbol	Name	Value	Units
κ	diffusivity	10^{-6}	m^2/s
L	length scale	$4.0x10^5$	meters
ΔT	temperature scale	1300	°K
α	thermal expansion coefficient	$3.0x10^5$	1/°K
μ	viscosity	$1.0x10^{21}$	Pa-s
g	acceleration of gravity	9.8	m/s^2
ρ_m	mantle density	3500	kg/m^3
ρ_w	water density	1000	kg/m^3
K	conductivity	3.2	J/m-s-°K
c_p	specific heat	900	J/kg-°K

Table 2.1 Parameters used for non-dimensionalizing the governing equations which are given in the appendix and calculating the model results.

TABLE 2.2

Run #	μ_{ref} $[10^{18}$ Pa-s$]$	E $[\frac{kcal}{mole}]$	V^* $[\frac{cm^3}{mole}]$	W_b [km]	Z_b [km]	λ
12	1.0	110	7.5	120	400	.80
14	5.0	110	7.5	120	400	.93
15	1.0	110	7.5	400	400	.87
17		102	0	120	400	.74
18	5.0	80	7.5	120	400	.78
19	1.0	110	7.5	240	400	.79
20	1.0	110	7.5	120	400	.81
21		102	0	120	400	—
22	1.0	110	7.5	60	400	.80
23	1.0	110	7.5	120	300	.84

Table 2.2 The parameters which define the numerical cases are listed here. The reference viscosity (μ_{ref}) is the value of viscosity at the start of a calculation at 150 km depth in the model box and it defines the value of A in equation 2.1. The other parameters are described in the text.

Figure Captions

Figure 1. This schematic of the oceanic mantle shows the orientation expected for small-scale convection beneath the oceanic lithosphere. The end view which shows cross-sections of the small-scale rolls is the plane in which the calculations are done.

Figure 2. The set-up and boundary conditions for the numerical experiments described in this paper are shown. The conductive lid is the area where the advective heat flux is negligible compared to the conductive heat flux. The boundary layer is defined in the text as are the boundary conditions.

Figure 3. The results of one numerical calculation of small-scale convection are shown for a box which represents a 400 x 400 km region of the mantle for the times of cooling 2,4,5 and 10 m.y. after the convection calculation was begun and these snapshots are labled (a),(b),(c) and (d), respectively. Of course, an initial temperature profile from 5 m.y. of conductive cooling was used. The positions of the 10^4 grid points used are indicated by the tick marks on the contour plots. A random temperature perturbation was given to each point at the start of the calculation. The dominant wavelength of flow has increased from a value of about 80 km after 2 m.y. to 200 km after 10 m.y. The temperature contours identify 1473, 1523 and

1553°K, in order from the top, and the streamfunction contours are evenly spaced between maximum and minimum values which are given in the figures. The shaded regions above the top contour of temperature indicates the region of the conductive lid or lithosphere. Parameter A in equation 2.1 is set to give a viscosity of 10^{18} Pa-s at 150 km and 1573 °K. The horizontally averaged temperature and the difference between that and the temperatures for purely conductive cooling of a half-space for the same time of cooling are shown plotted against depth next to the temperature contour plots. The horizontal average of the viscosity and the vertically advected heat flux are shown next to the streamfunction. Above the temperature contours is shown the model gravity anomaly which includes the effect of temperature variations and the effect of vertical deformations produced by the flow, given by equations 2.8 to 2.15. No flexural damping of the gravity signals is included.

Figure 4. The same quantities which were displayed in figure 2.3 are shown for case 20 at a time 56 m.y. into the calculation. Note that several of the scales have been changed. The temperature contours are set at 1433, 1458, 1483 and 1508 °K in order from top to bottom. The minimum of the streamfunction is -4.44×10^{-5} m^2/s and the maximum is 0.

Figure 2.5. Values of the average lid temperature (T_L) defined by equation 2.3 are plotted against time for the cases indicated. Table 1 gives the parameters used in each case. Figure 5(a) gives these plots for cases 12, 14, 15, 17 and 18 while 5(b) is for 15, 19, 20 and 22. The cases displayed in 5(b) all have the same viscosity parameters, but different box widths (W) and case 15 had different initial conditions than the others. A value of non-dimensionalized temperature of .60 corresponds to the conductive solution and a value of .50 indicates a linear temperature profile. Note that for times greater than 50 m.y. the values of T_L are nearly constant in time. This is the period of "transient equilibrium" described in the text.

Figure 2.6. The values of six parameters calculated for model 15 are shown plotted versus $t^{1/2}$. Plot (a) shows the negative non-dimensional subsidence ($=S(t)*(\rho_m - \rho_w)/\alpha\rho_m$) given by equation 2.4. The average temperature in the lid is T_L, the depth to the bottom of the lid is z_L and T_m is the initial temperature in the box. Graph (b) gives the negative of the average non-dimensional temperature drop in the top 150 km of the box (T_c-T_m) which is can be used to calculate another estimate of subsidence as escribed in the text. Plot (c) gives z_L and plot (d) shows the variation of log(D) where D is the average value in the box of the second invariant of the strain rate tensor ($\dot{e}^2$). In graph (e) the ratio of the

integral of the average heat flux out the box with time (IHF) and the average temperature drop within the box (TD) are shown. The deviation of this plot from a horizontal line indicates the degree of non-conservation of energy on the numerical grid due to incomplete convergence of the vorticity and stream function equations. The change in this quantity is only about 0.2% after the first few time steps. Finally, the log of the dissipation weighted viscosity ($\log(\mu)$) is shown in plot (f).

Figure 2.7. The same quantities as were plotted in figure 2.6 are shown for test 20. The time variation of these quantities are smmother than for case 15 because there was a more gradual increase in the cell size in the narrower box used for this model case.

Figure 2.8. This shows the variation of the isostatic geoid height (H) given by equation 2.6 relative to a zero value at the ridge crest versus time for several of the cases and for purely conductive cooling.

Figure 2.9. Shown are the values of the slope of the plots in Figure 2.8 (dH/dt) versus time. The slope change can be related to data on the offset of the geoid height across fracture zones, and data from Cazenave (1984) is plotted on the figure.

Figure 2.10. The components of the model gravity signal described in the text are shown for at time 15 m.y. into the model 15 calculation. The conponent due to deviatoric stress and pressure variations at the base of the conductive lid is G_σ, that due to pressure variations in the lid is G_L and G_T is the signal due to density variations throughout the box. No flexureal damping of G_σ and G_L was done here.

Figure 2.11. The maximum peak-to-trough amplitude of the three components of the gravity signal, which are defined in the text, are shown as they vary with time for four of the cases considered. G_σ and G_L are generally of the same sign at a give point while G_T is opposite in sign. The test cases are labeled on each plot (a) to (d).

Figure 2.12. This is a contour map of the total model gravity for case 15 for a range of model times from 4 to 25 m.y. Time is related to distance by assuming a plate velocity of 4×10^{-2} m/yr. The contour interval is 2×10^{-5} m/s^2 (mgals). flexural damping of the signals was included when calculating gravity. Note that the wavelength increaces rapidly with time along with a moderate increase in the amplitude of gravity.

Figure 2.13. The variation of the model surface heat flux ($Q_s(t)$) described in the text is plotted against time for case 20. The thermal conductivity (K) is assumed to be 3.3×10^5 ergs/cm^3-s-°K (Schatz and Simmons, 1972). Also shown is data for the average depth of the ocean basins and one standard deviation from the compilation of Sclater et al. (1980).

Figure 2.14. The flexural filter F(k) defined in the text is plotted against the wavenumber (k) and the wavelength (γ) for three values of the thickness of the elastic lithsphere (h). The physical parameters assumed for the elastic lithosphere are given in the text. This plot shows that the signals G_σ and G_L for wavelengths below a certain value will be largely damped out. This wavelength cut-off depends strongly on the thickness of the elastic lithosphere.

Figure 2.15. These plots show the effect on the total model gravity signal ($G_\sigma + G_L + G_T$) of flexural damping due to elastic lithospheres of different thicknesses for several times in the calculation of case 15. Plots (a), (b), (c) and (d) correspond to times 5, 10, 15 and 25 m.y. into the model clculations. The thickness of the elastic lithosphere (h) used to calculate the filter F(k) is given at the top of each plot.

Figure 2.16. This is a comparison of Seasat-derived gravity anomalies and shipboard gravity and bathymetry data for the same area from Haxby and Weissel (1984). It shows that there is good correspondence between the filtered shipboard data and the Seasat signals. Also the wavelength and amplitude range of these anomalies is similar to that seen in the model reults presented here. The position of the shipboard data is given in Figure 2.17.

Figure 2.17. Location of the data for the shipboard gravity data shown in Figure 2.16.

Figure 2.18. The water loaded thermal subsidence for test 20, calculated using equation using T_c asdescribed in the text is shown versus $(t)^{1/2}$ along with the conductive case. A value of the thermal expansion coefficient (α) of 3.8×10^{-5} $^{\circ}K^{-1}$ was used to calculate the subsidence. Also shown are data for depth of the North Pacific from Sclater et al. (1972). The top line labeled AF is the best fitting straight line through data on the depth and age of the ocean floor of the African plate side of the South Atlantic at about 45° S latitude and the line marked SA is for the South American side of the mid-ocean ridge at about the same latitude, both from Hayes (1983). This shows the large variation in subsidence rates for different oceanic plates.

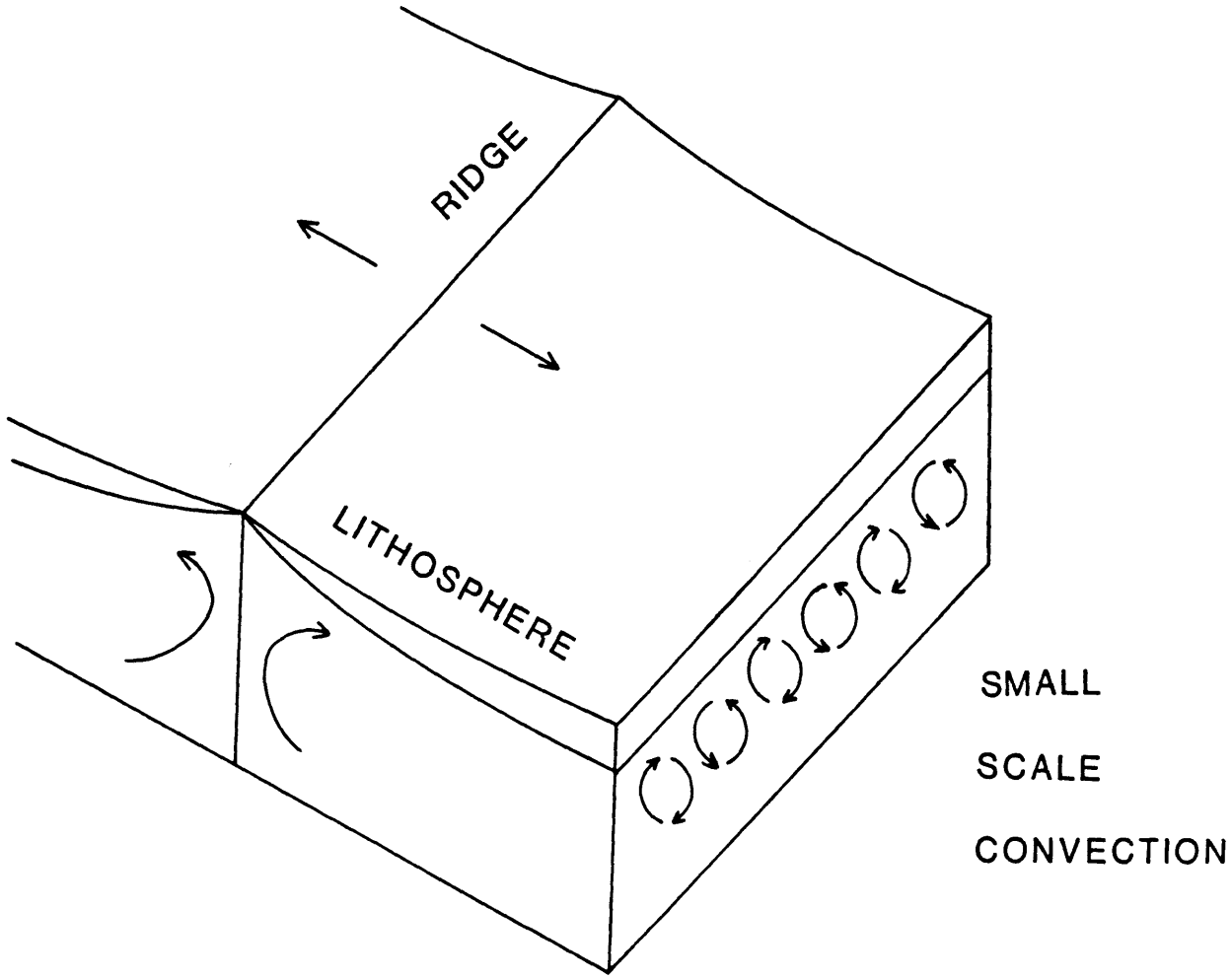

Figure 2.1

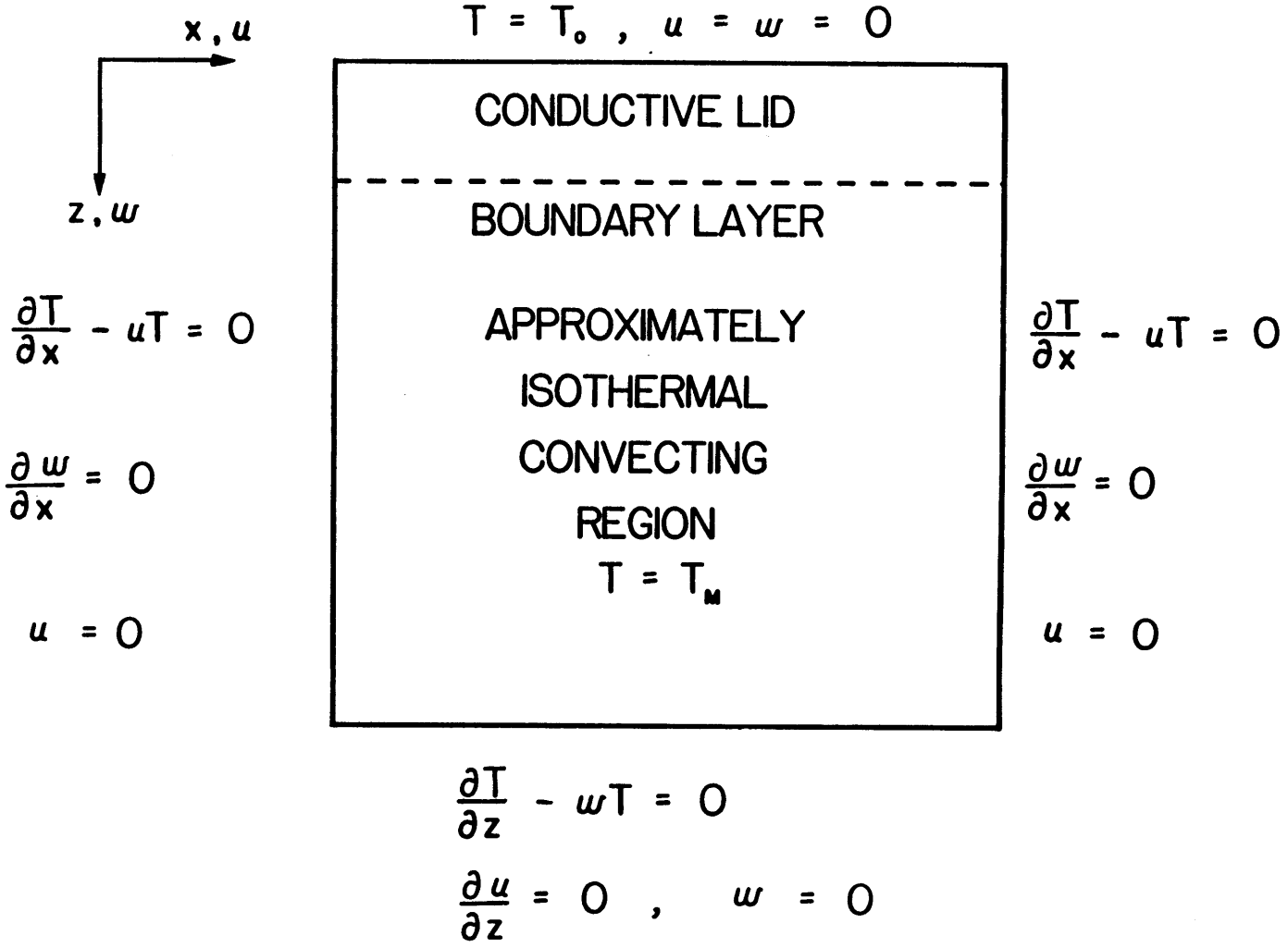
x , u
z , w
T = T₀ , u = w = 0
CONDUCTIVE LID
BOUNDARY LAYER
APPROXIMATELY
ISOTHERMAL
CONVECTING
REGION
T = T_M
∂T/∂x - uT = 0
∂w/∂x = 0
u = 0
∂T/∂x - uT = 0
∂w/∂x = 0
u = 0
∂T/∂z - wT = 0
∂u/∂z = 0 , w = 0

Figure 2.2

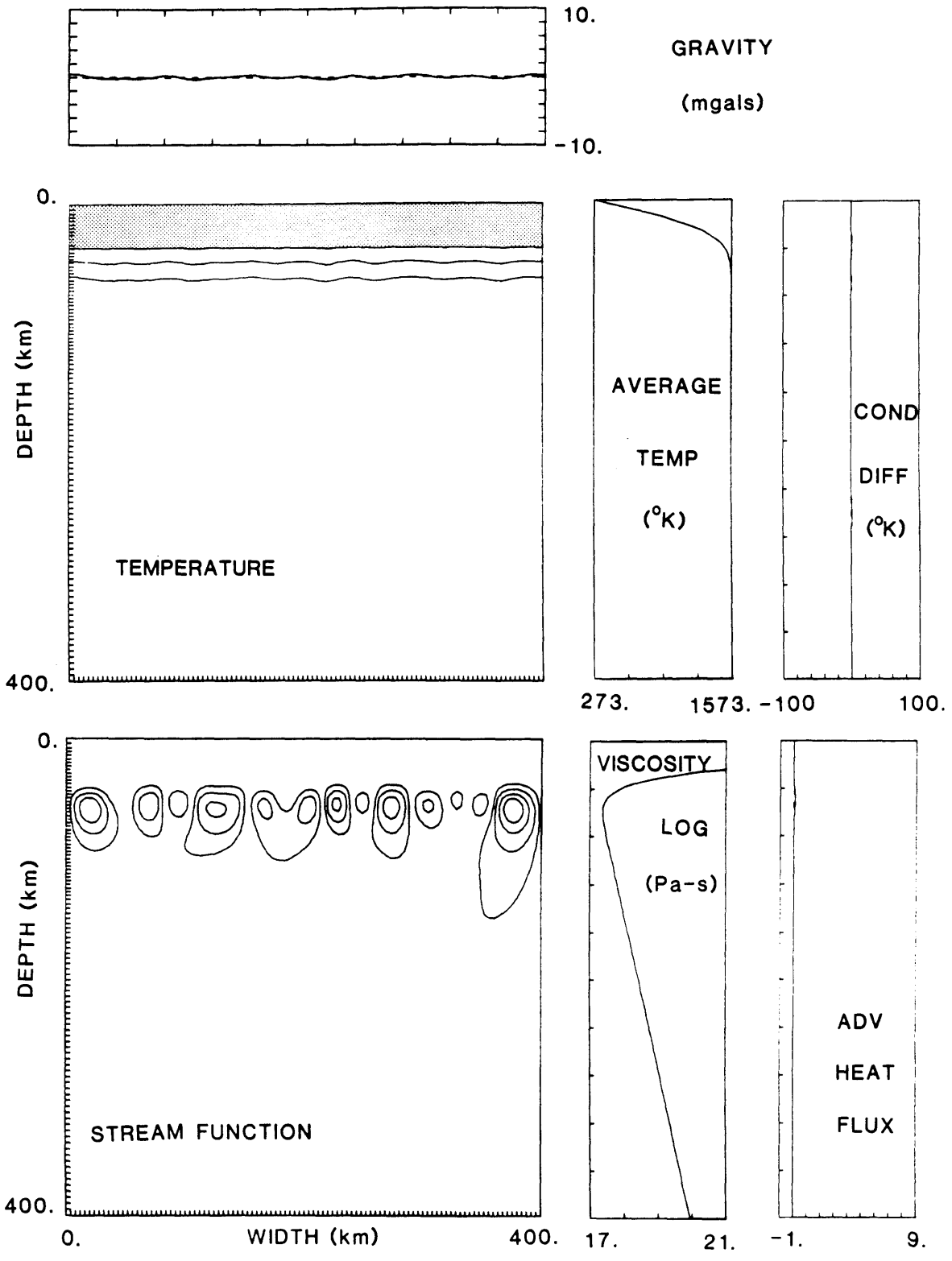
10.
GRAVITY
(mgals)
-10.
0.
DEPTH (km)
TEMPERATURE
400.
AVERAGE
TEMP
(°K)
273.
1573.
COND
DIFF
(°K)
-100
100.
0.
DEPTH (km)
STREAM FUNCTION
400.
VISCOSITY
LOG
(Pa-s)
17.
21.
ADV
HEAT
FLUX
-1.
9.
0.
WIDTH (km)
400.

Figure 2.3(a)

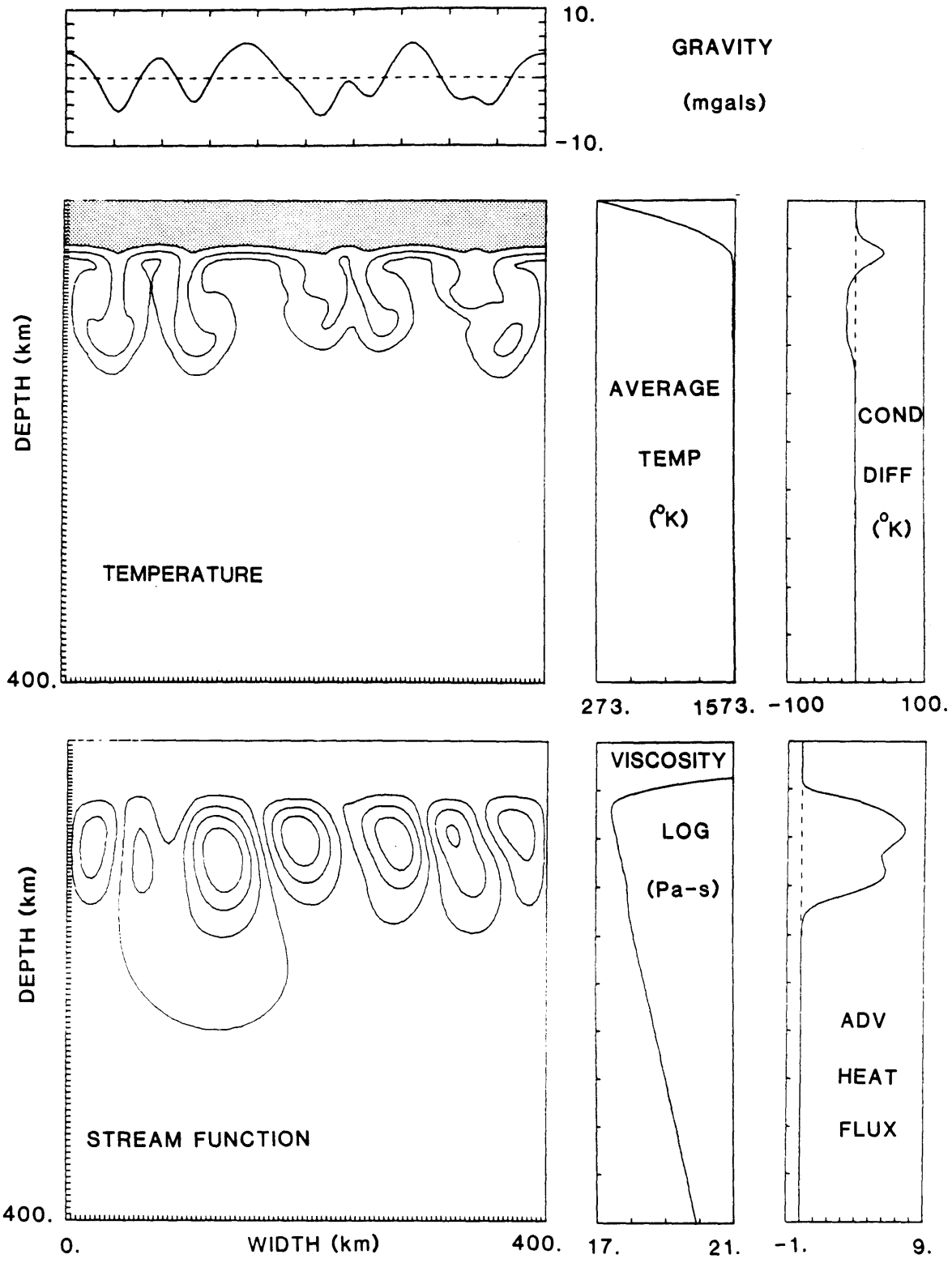
10.
GRAVITY
(mgals)
-10.
DEPTH (km)
TEMPERATURE
400.
AVERAGE
TEMP
(°K)
273.
1573.
COND
DIFF
(°K)
-100
100.
VISCOSITY
LOG
(Pa-s)
17.
21.
ADV
HEAT
FLUX
-1.
9.
DEPTH (km)
STREAM FUNCTION
400.
0.
WIDTH (km)
400.

Figure 2.3(b)

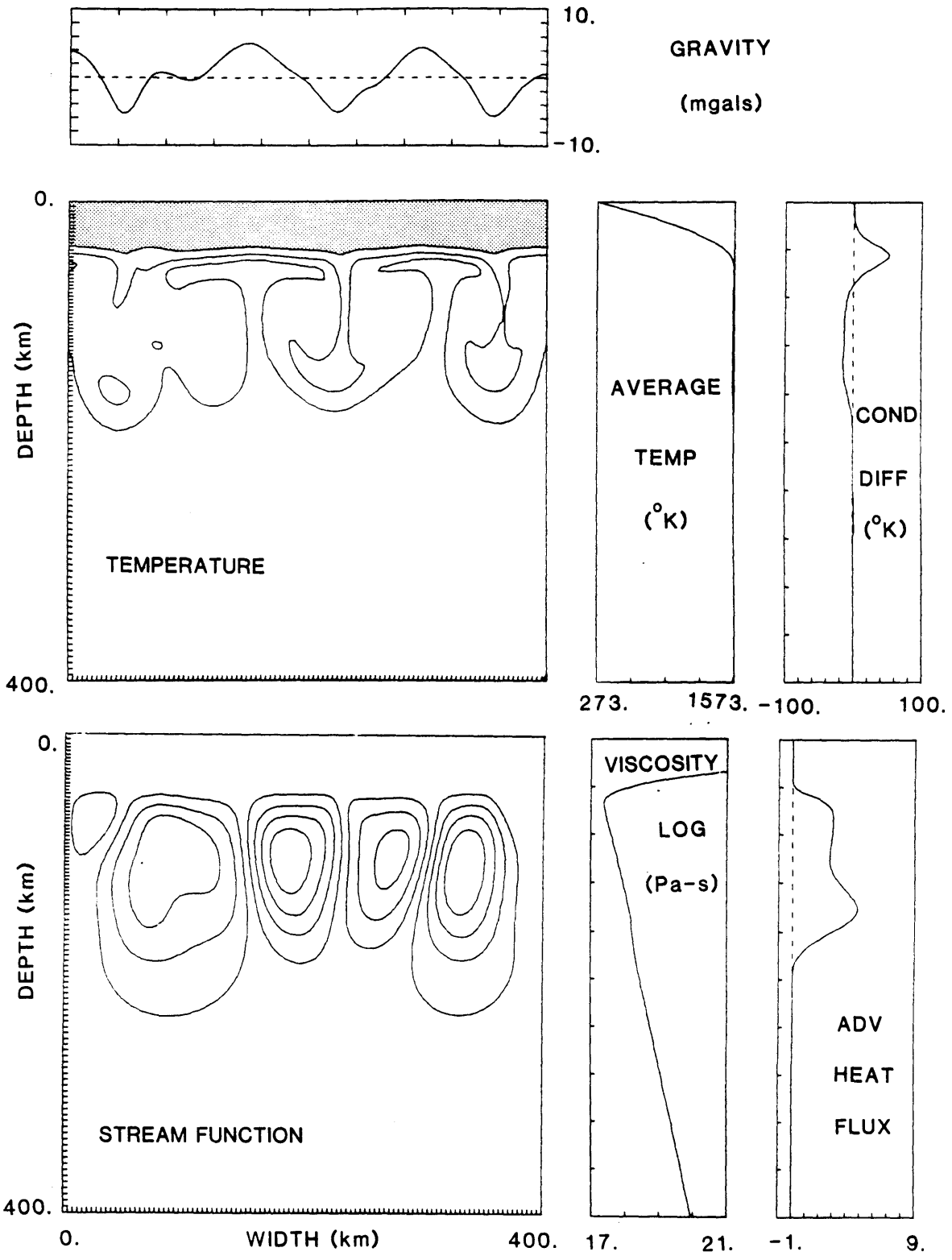
10.
GRAVITY
(mgals)
-10.
0.
DEPTH (km)
TEMPERATURE
400.
AVERAGE
TEMP
(°K)
273.
1573.
COND
DIFF
(°K)
-100.
100.
0.
DEPTH (km)
STREAM FUNCTION
400.
0.
WIDTH (km)
400.
VISCOSITY
LOG
(Pa-s)
17.
21.
ADV
HEAT
FLUX
-1.
9.

Figure 2.3(c)

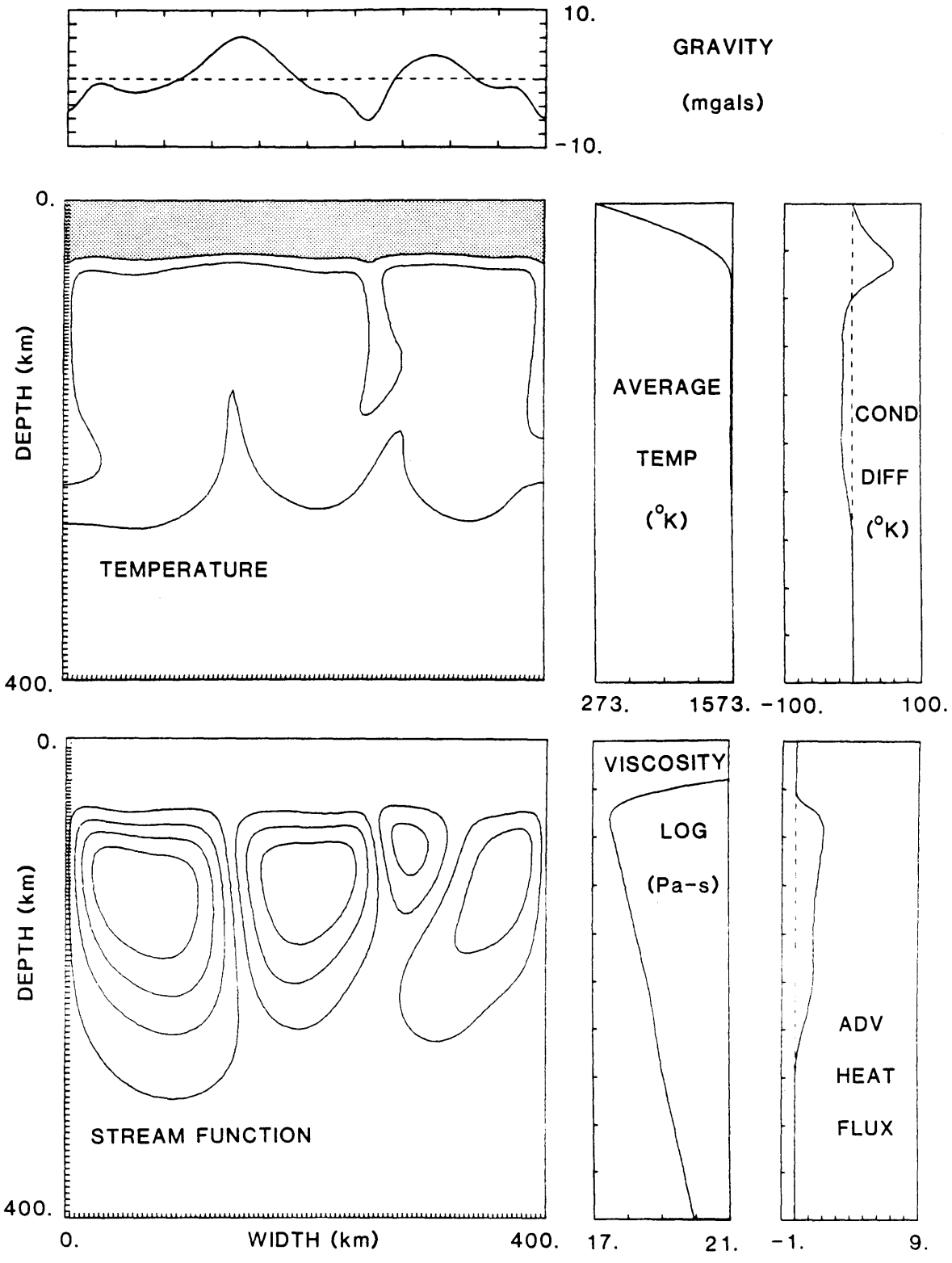
10.
GRAVITY
(mgals)
-10.
0.
DEPTH (km)
TEMPERATURE
400.
AVERAGE
TEMP
(°K)
273.
1573.
COND
DIFF
(°K)
-100.
100.
0.
DEPTH (km)
STREAM FUNCTION
400.
VISCOSITY
LOG
(Pa-s)
17.
21.
ADV
HEAT
FLUX
-1.
9.
0.
WIDTH (km)
400.

Figure 2.3(d)

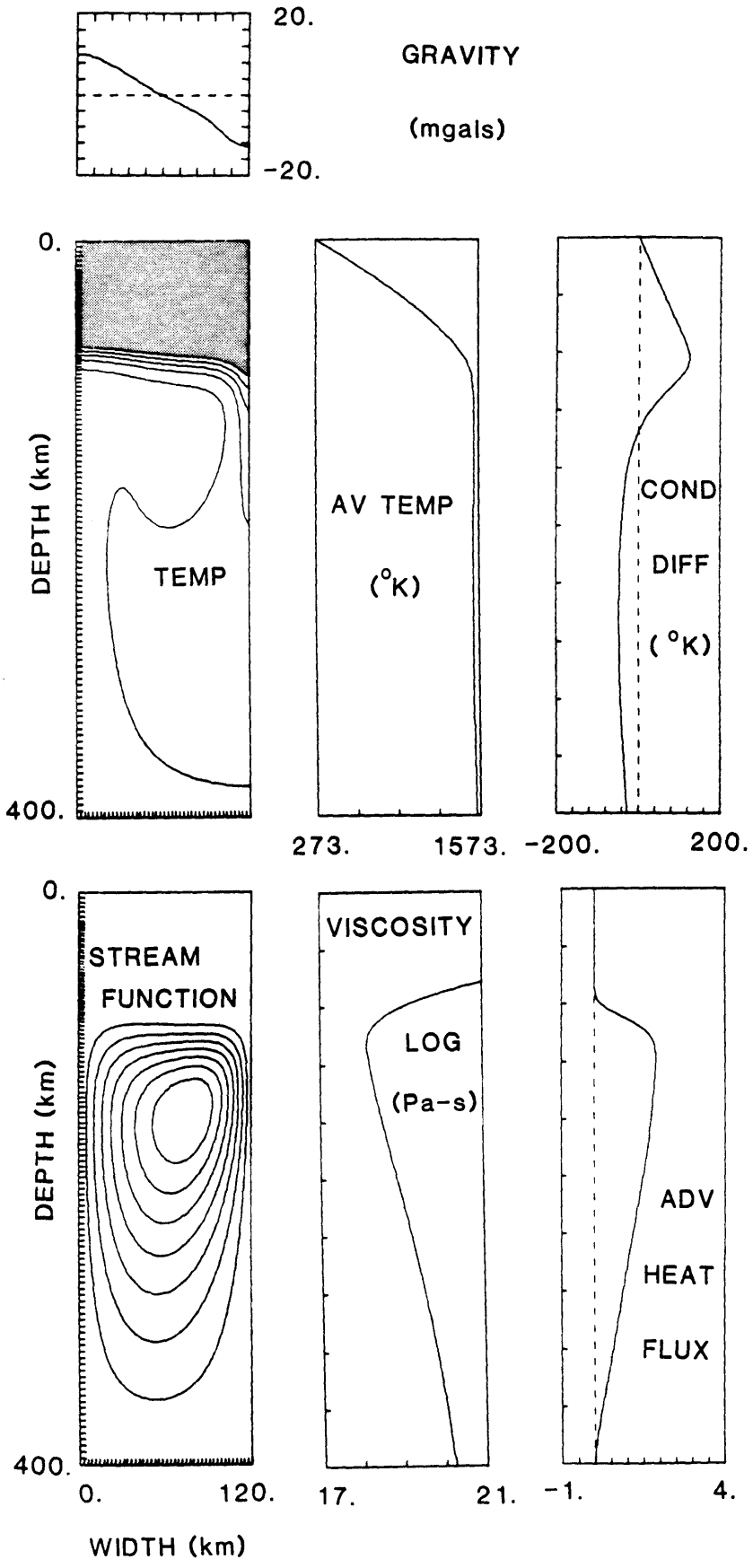
20.
GRAVITY
(mgals)
-20.
0.
DEPTH (km)
TEMP
400.
AV TEMP
(°K)
273.
1573.
COND
DIFF
(°K)
-200.
200.
0.
STREAM
FUNCTION
DEPTH (km)
400.
0.
120.
WIDTH (km)
VISCOSITY
LOG
(Pa-s)
17.
21.
ADV
HEAT
FLUX
-1.
4.

Figure 2.4

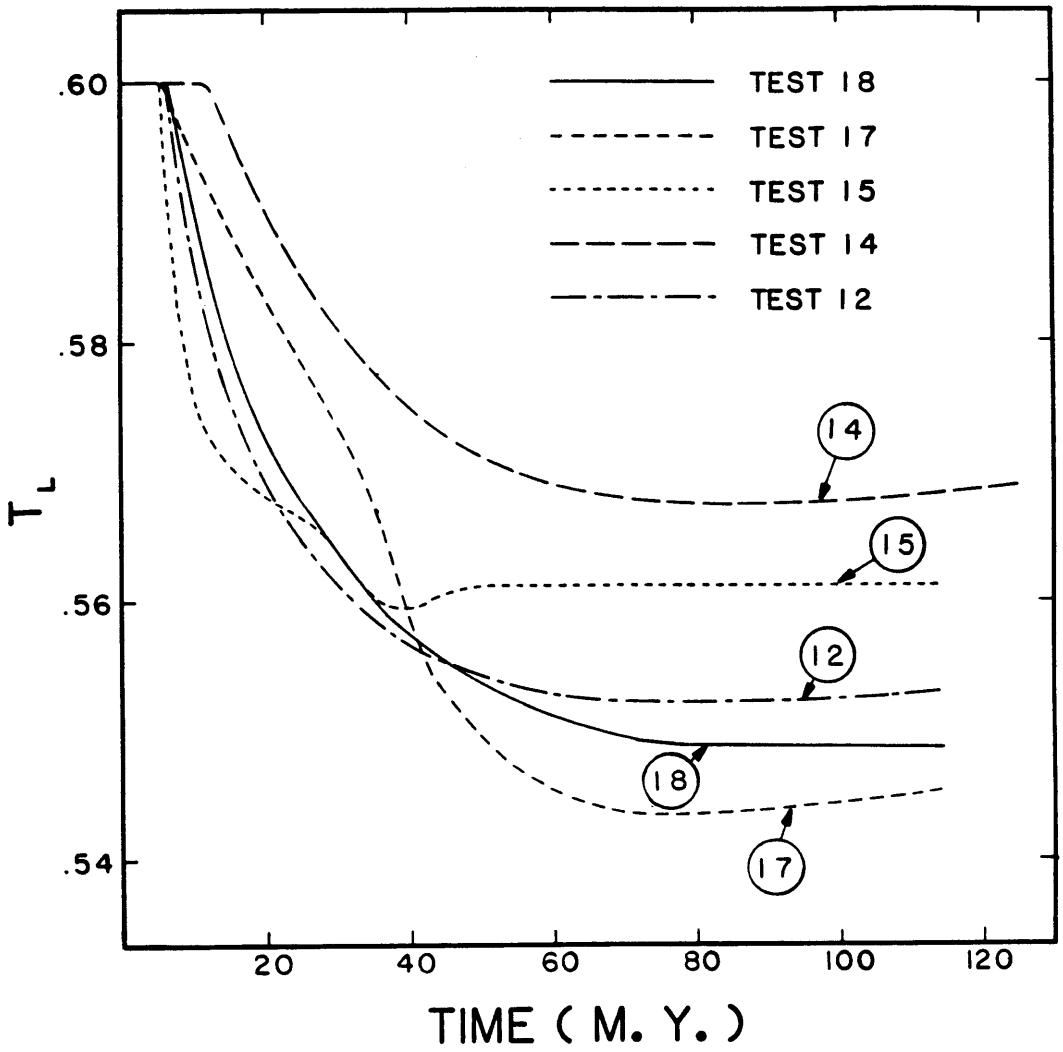
TEST 18
TEST 17
TEST 15
TEST 14
TEST 12
.60
.58
.56
.54
T_J
14
15
12
18
17
20
40
60
80
100
120
TIME (M. Y.)

Figure 2.5(a)

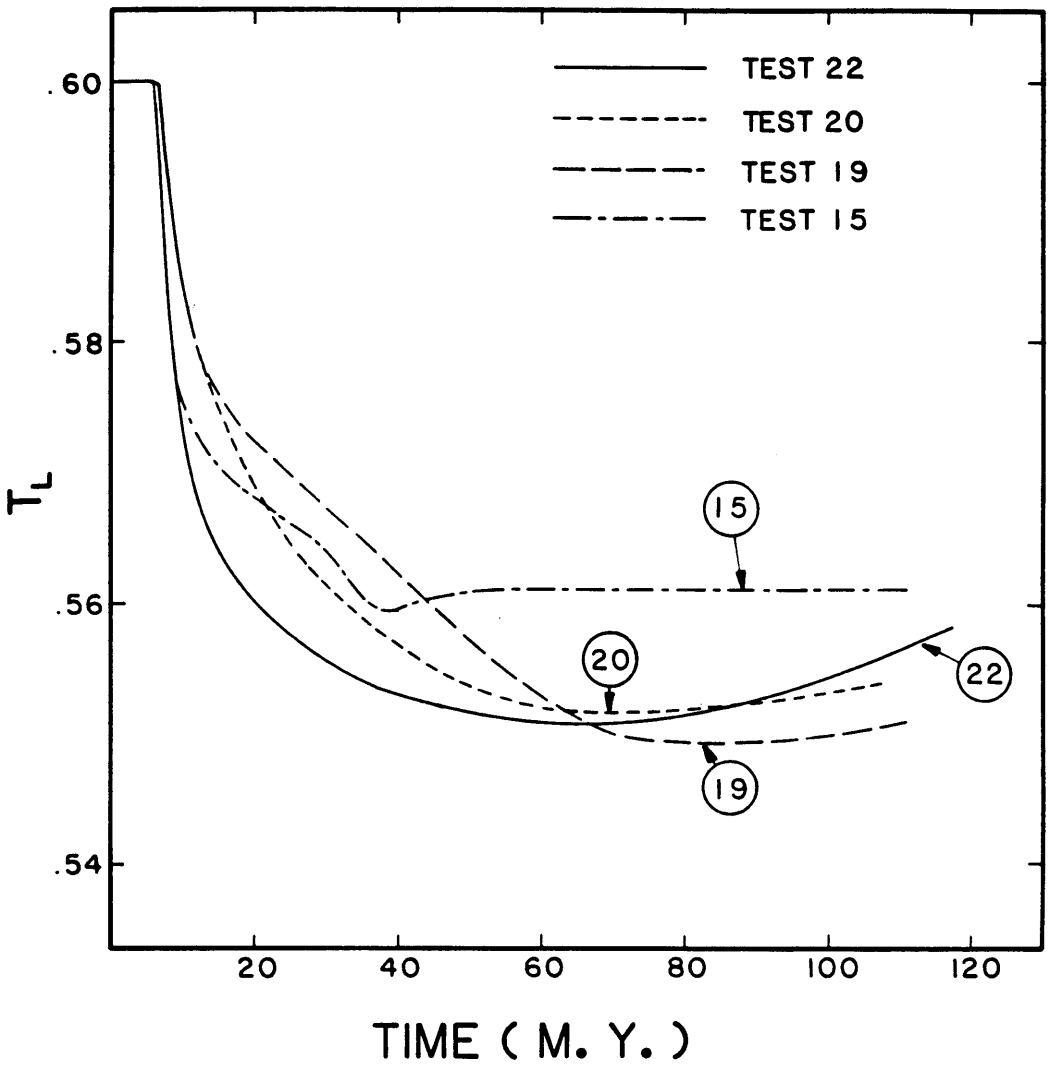
TEST 22
TEST 20
TEST 19
TEST 15
.60
.58
.56
.54
T_L
15
20
22
19
20
40
60
80
100
120
TIME (M. Y.)

Figure 2.5(b)

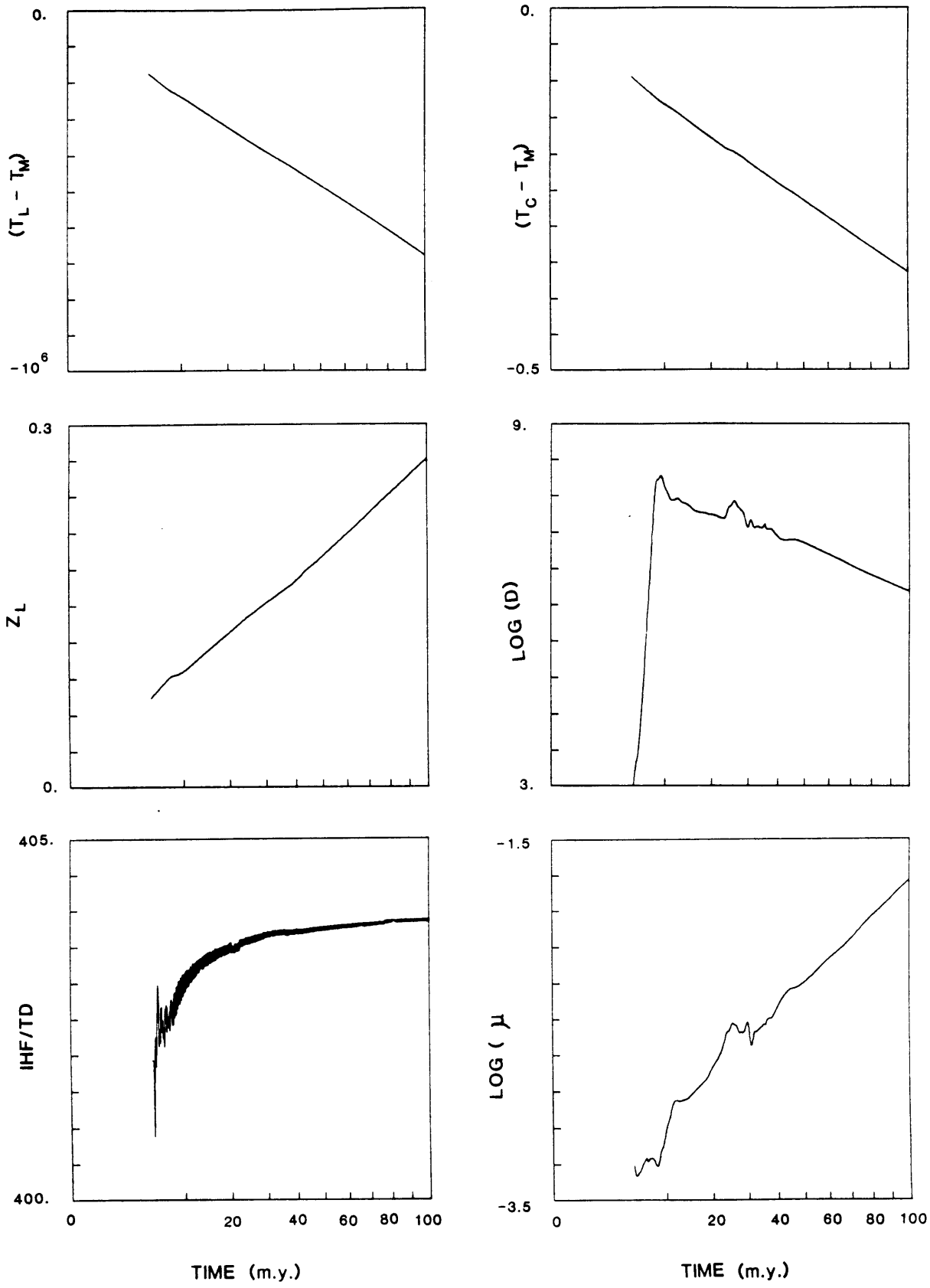
TEST 15
0.
$(T_L - T_M)$
-10^6
0.
$(T_C - T_M)$
-0.5
0.3
Z_L
0.
9.
LOG (D)
3.
405.
IHF/TD
400.
-1.5
LOG (μ
-3.5
0
20
40
60
80
100
TIME (m.y.)
0
20
40
60
80
100
TIME (m.y.)

Figure 2.6

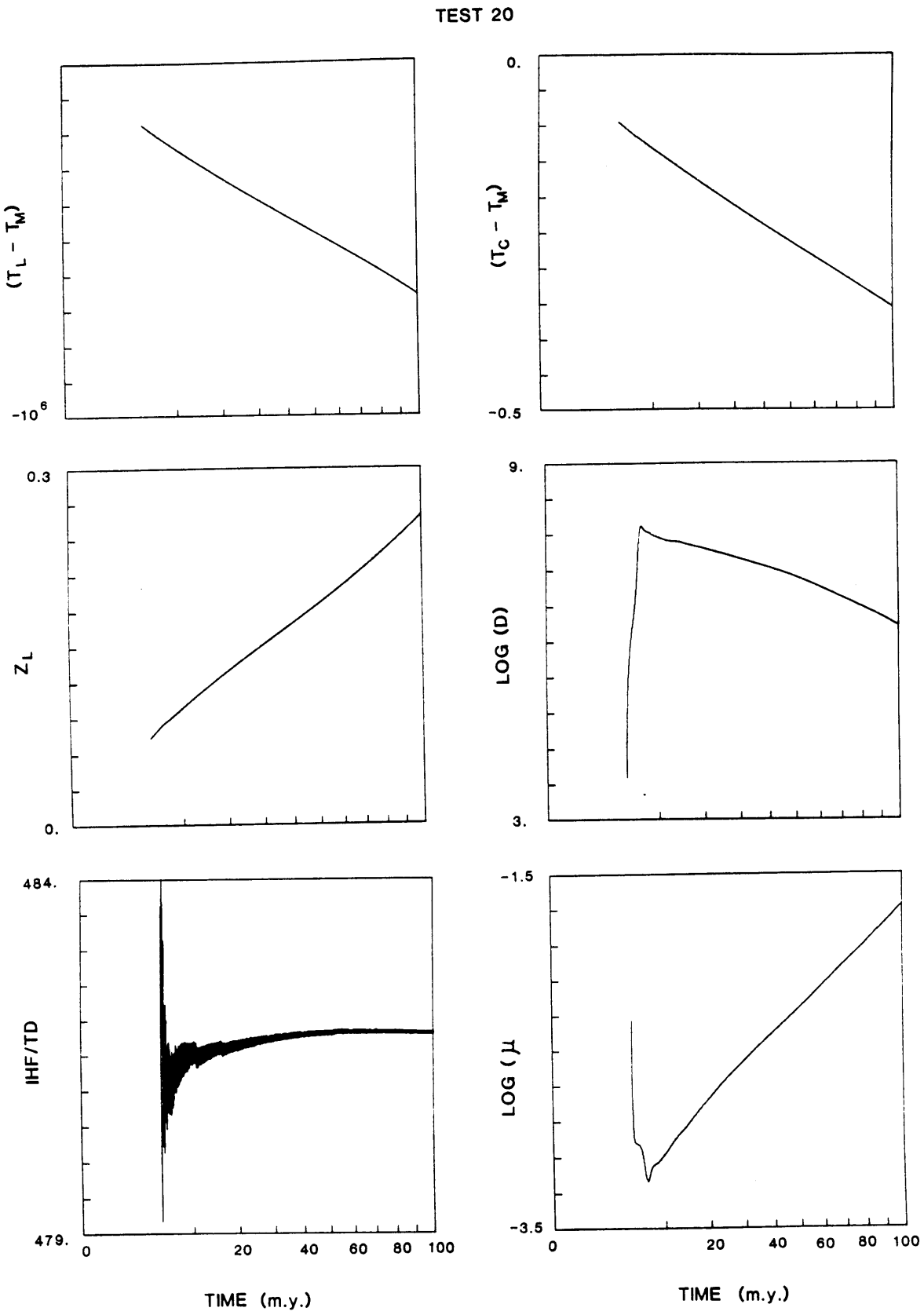
TEST 20
$(T_L - T_M)$
-10^6
$(T_C - T_M)$
0.
-0.5
Z_L
0.3
0.
LOG (D)
9.
3.
IHF/TD
484.
479.
LOG (μ
-1.5
-3.5
0
20
40
60
80
100
TIME (m.y.)
TIME (m.y.)

Figure 2.7

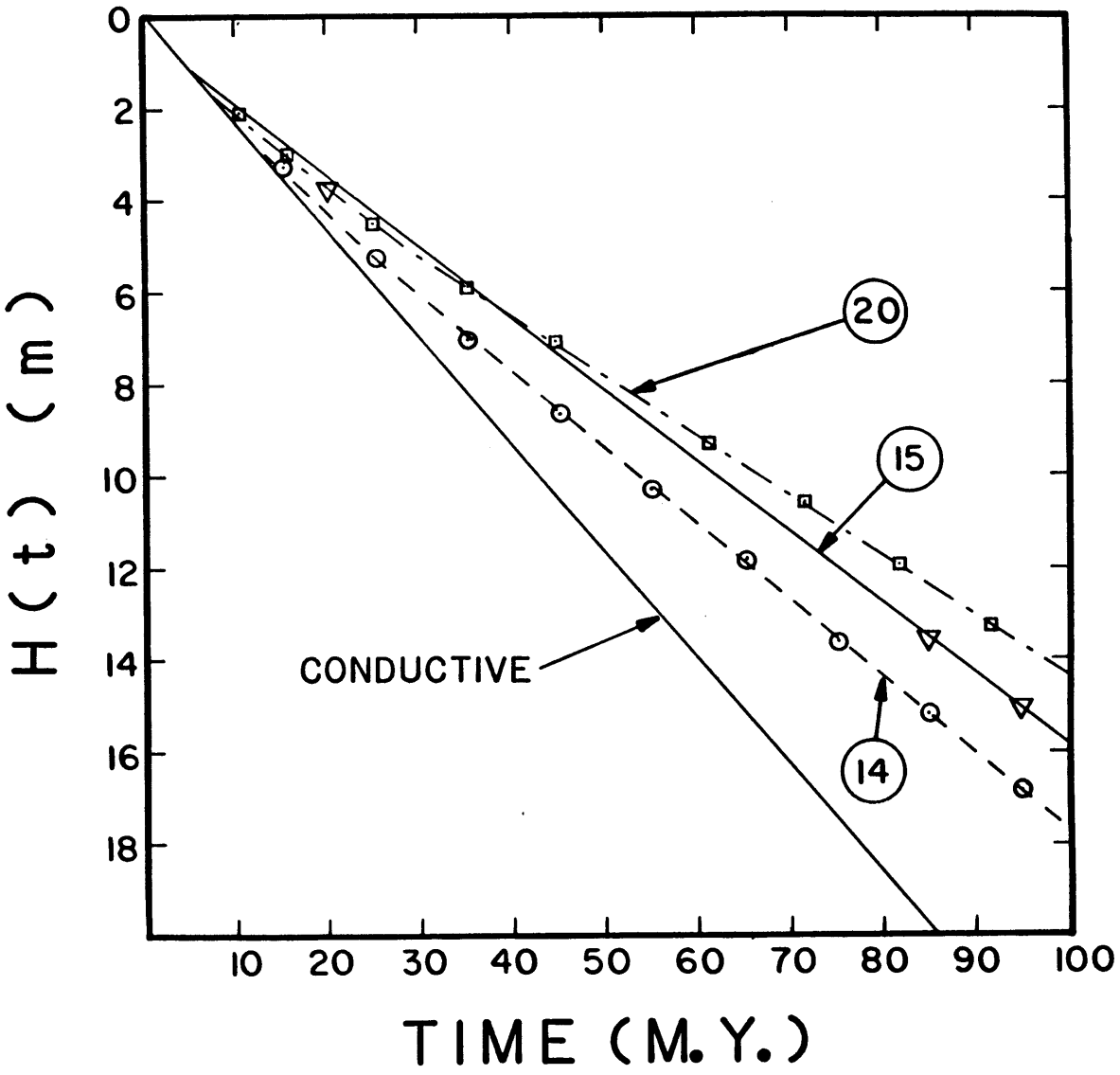
H(t) (m)
0
2
4
6
8
10
12
14
16
18
10
20
30
40
50
60
70
80
90
100
TIME (M.Y.)
20
15
14
CONDUCTIVE

Figure 2.8

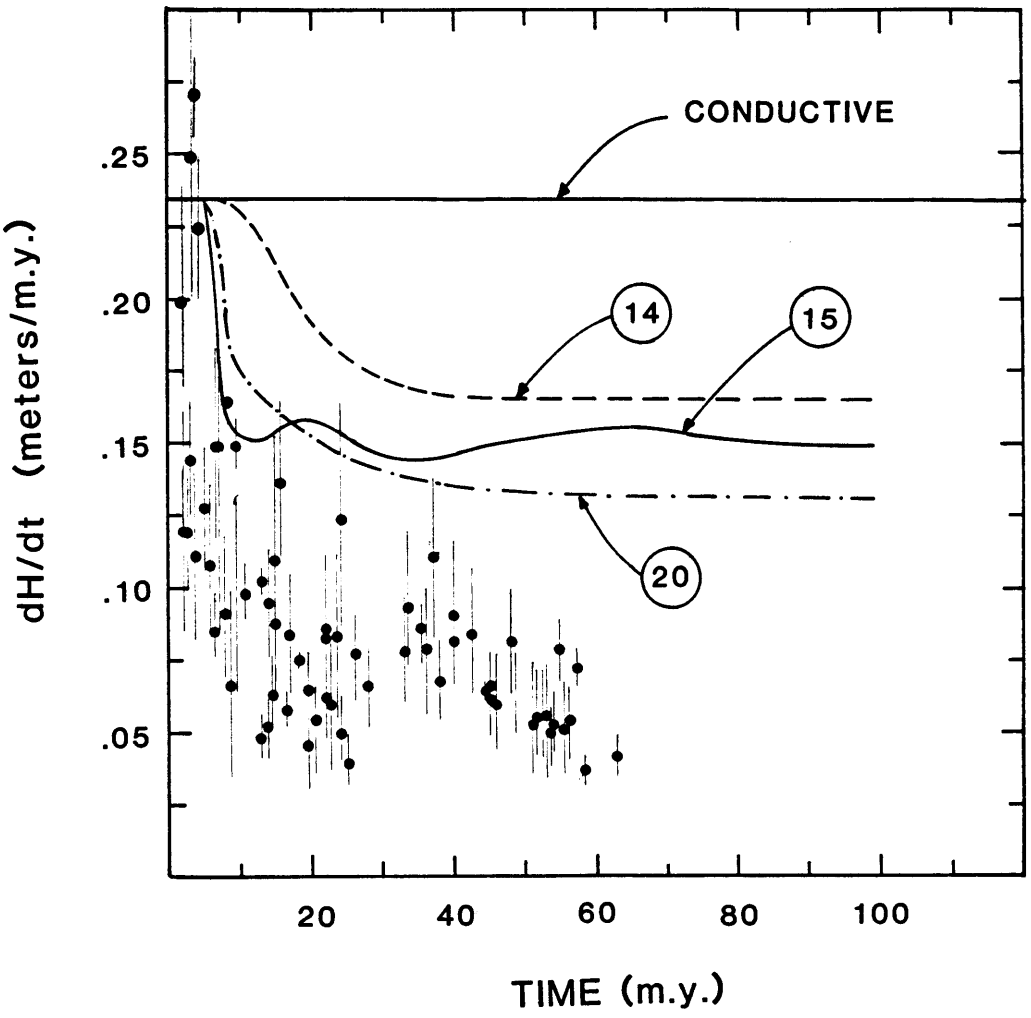
CONDUCTIVE
14
15
20
.25
.20
.15
.10
.05
dH/dt (meters/m.y.)
20
40
60
80
100
TIME (m.y.)

Figure 2.9

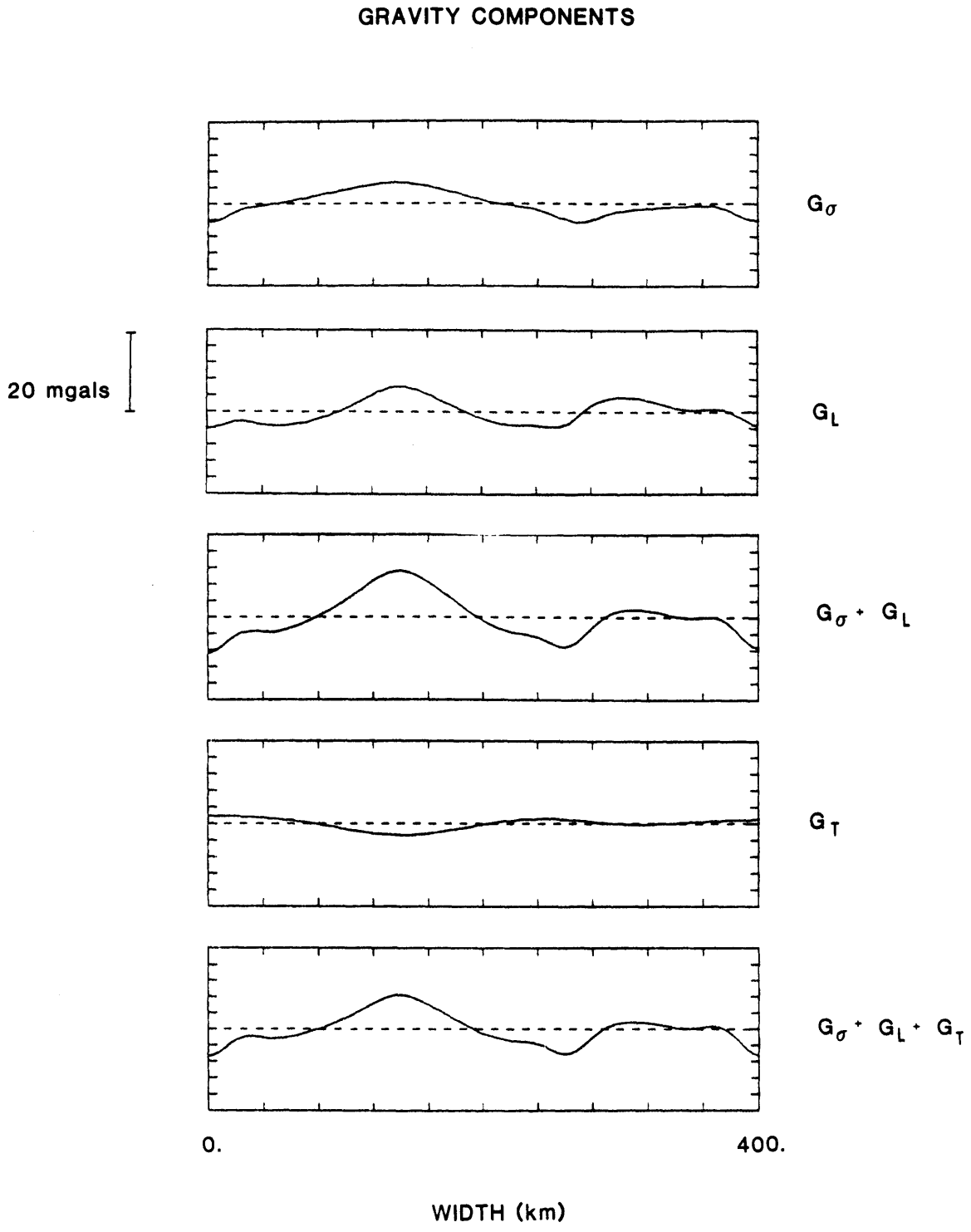
GRAVITY COMPONENTS
20 mgals
G_σ
G_L
$G_\sigma + G_L$
G_T
$G_\sigma + G_L + G_T$
0.
400.
WIDTH (km)

Figure 2.10

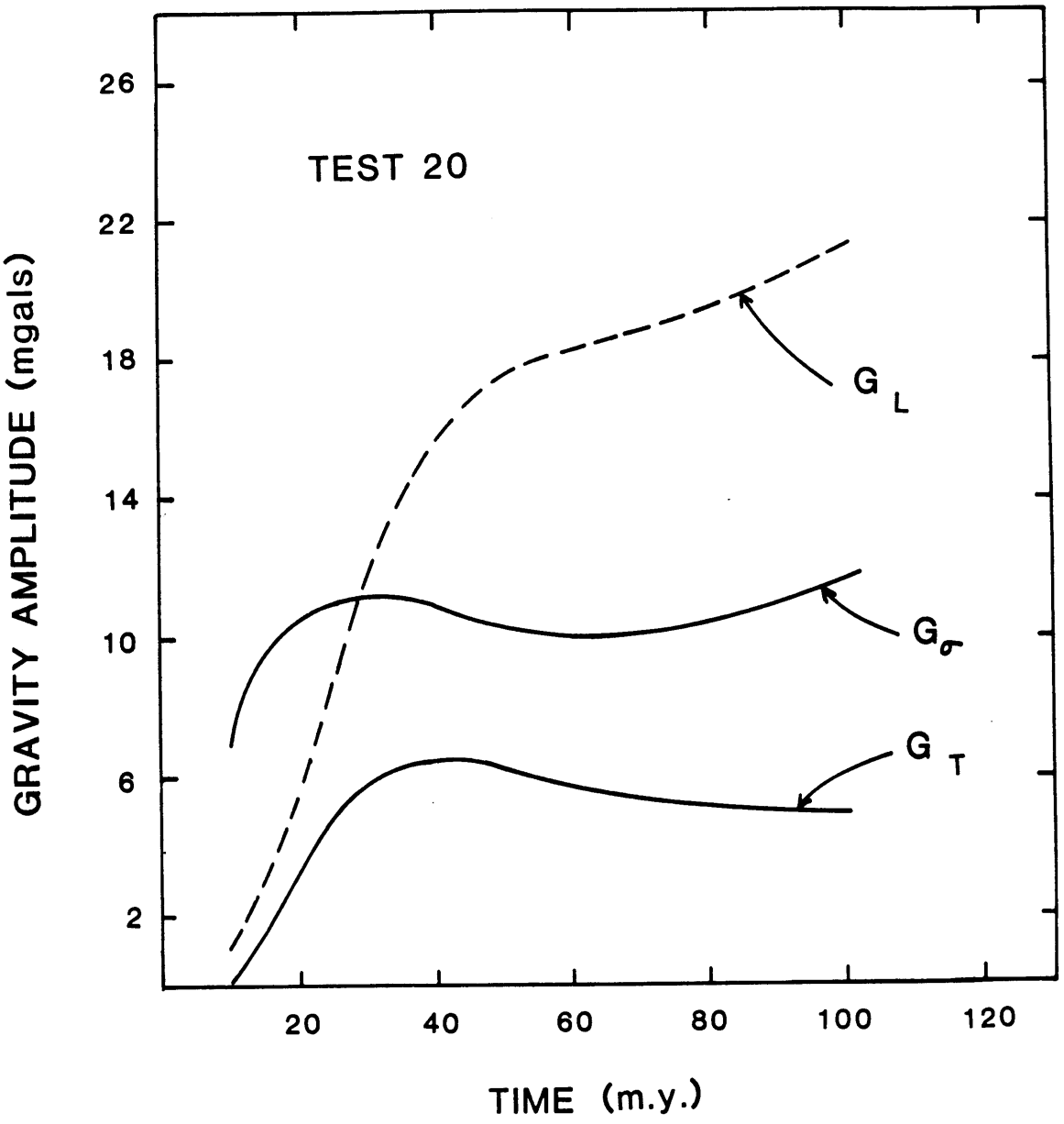
TEST 20
GRAVITY AMPLITUDE (mgals)
26
22
18
14
10
6
2
20
40
60
80
100
120
TIME (m.y.)
G L
G σ
G T

Figure 2.11(a)

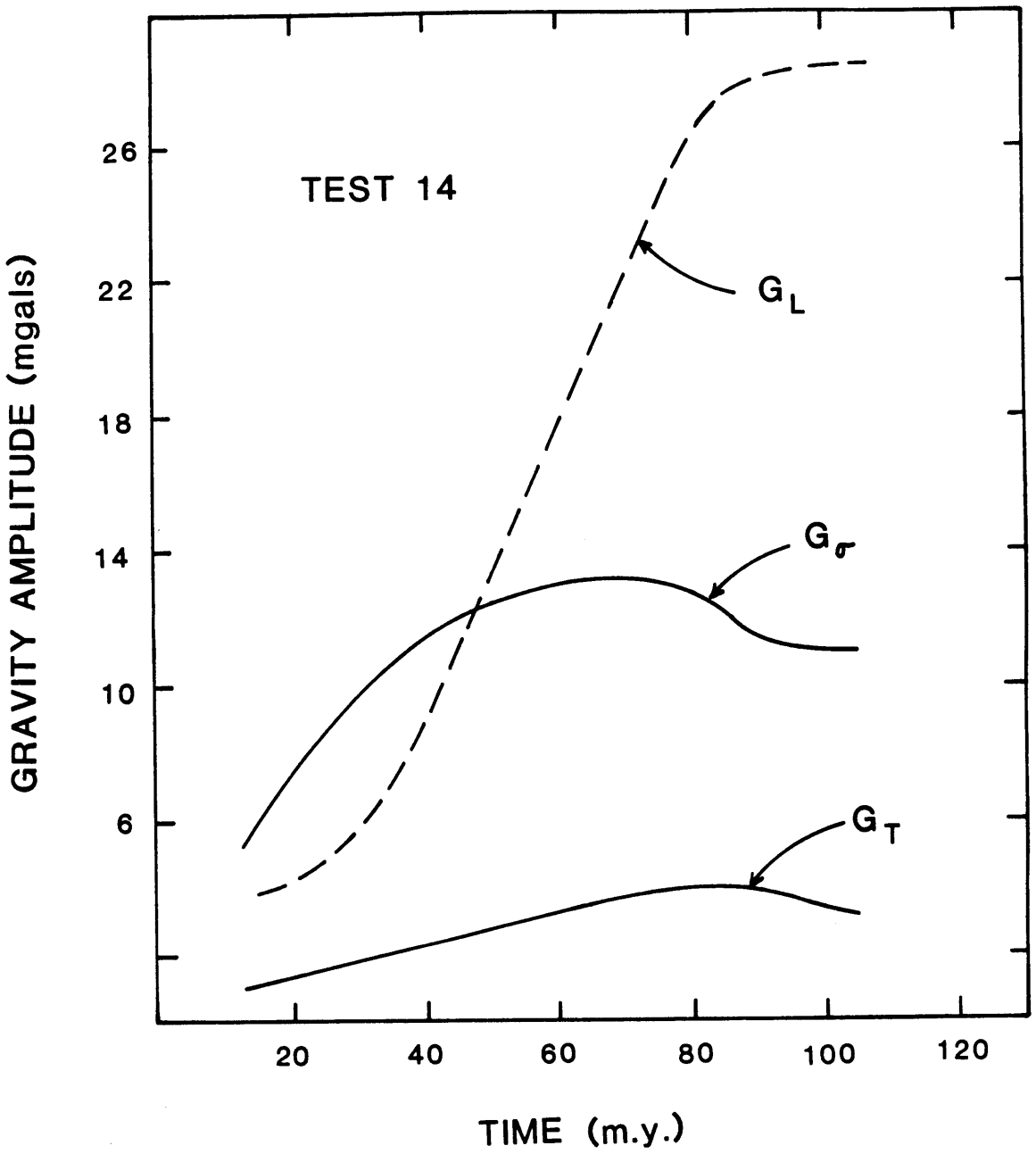
TEST 14
GRAVITY AMPLITUDE (mgals)
26
22
18
14
10
6
20
40
60
80
100
120
TIME (m.y.)
G_L
G_σ
G_T

Figure 2.11(b)

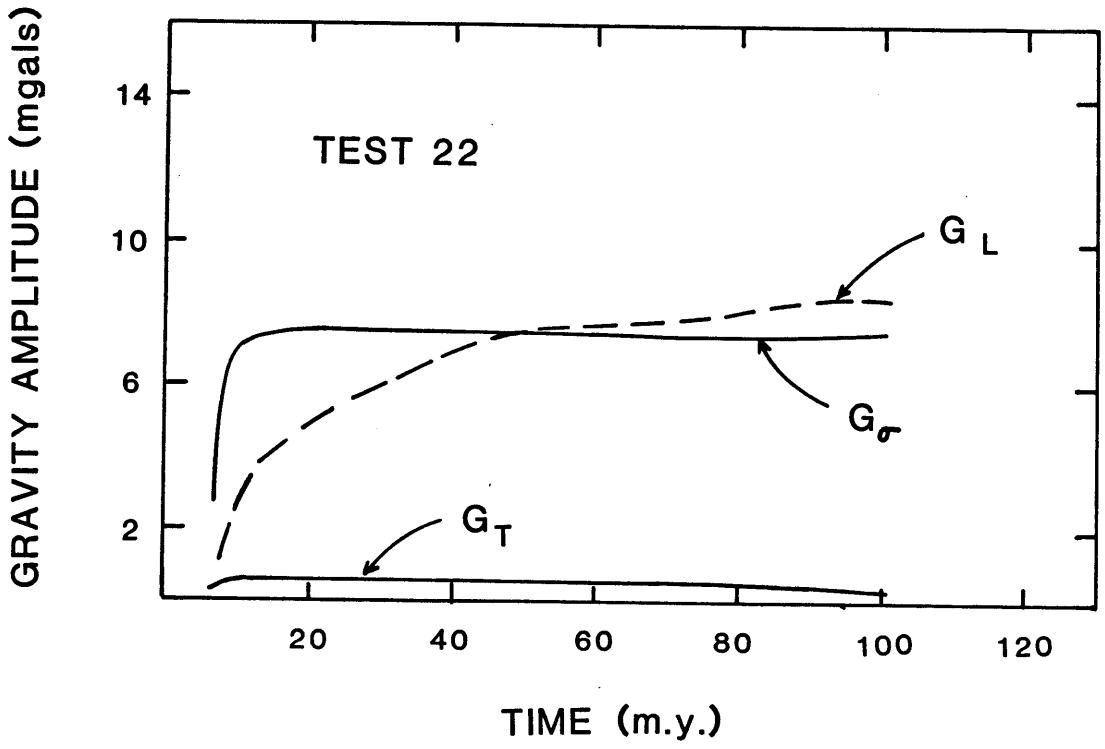
GRAVITY AMPLITUDE (mgals)
14
10
6
2
TEST 22
G L
Gσ
GT
20
40
60
80
100
120
TIME (m.y.)

Figure 2.11(c)

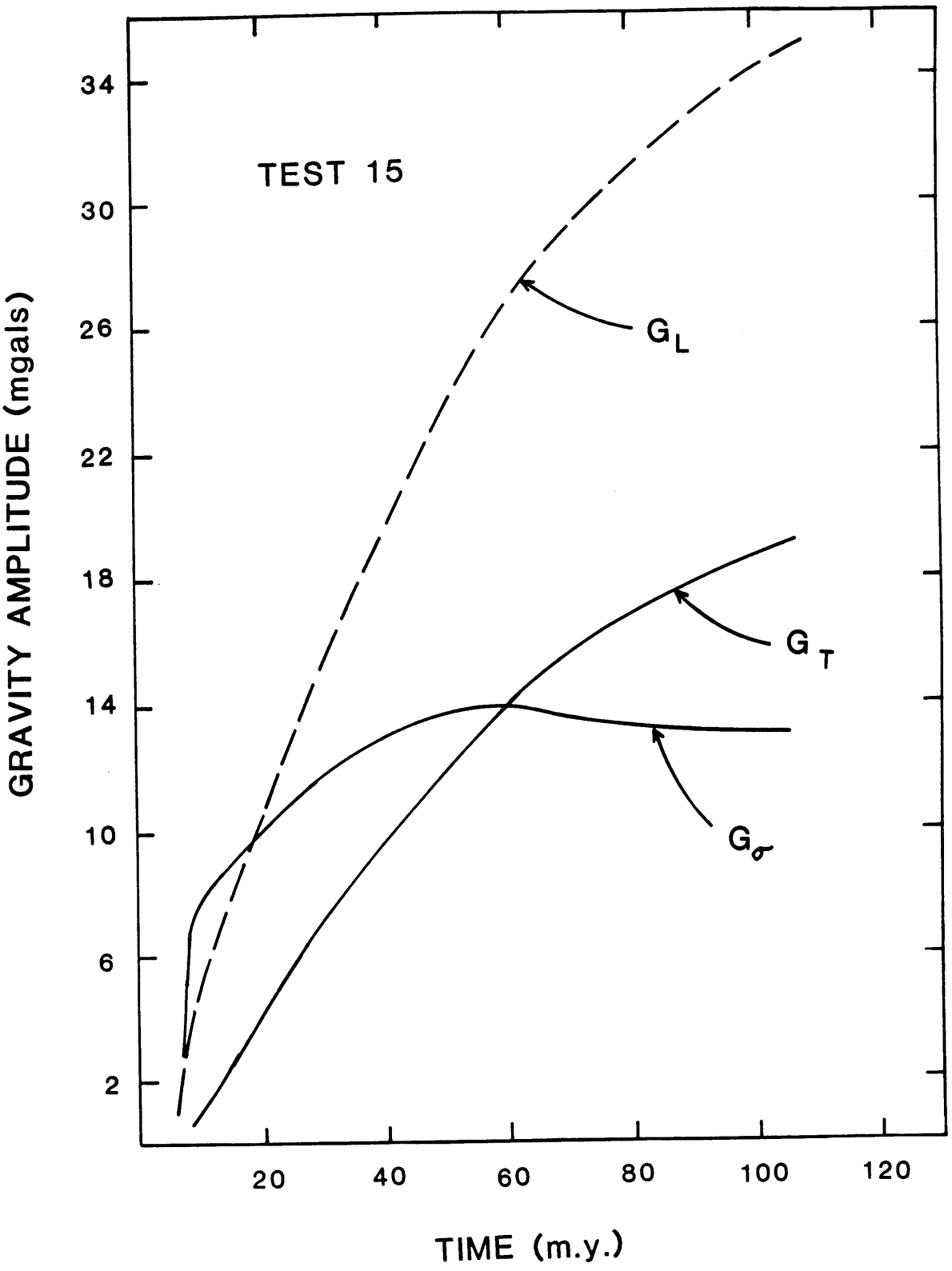
TEST 15
GRAVITY AMPLITUDE (mgals)
TIME (m.y.)
34
30
26
22
18
14
10
6
2
20
40
60
80
100
120
G_L
G_T
G_σ

Figure 2.11(d)

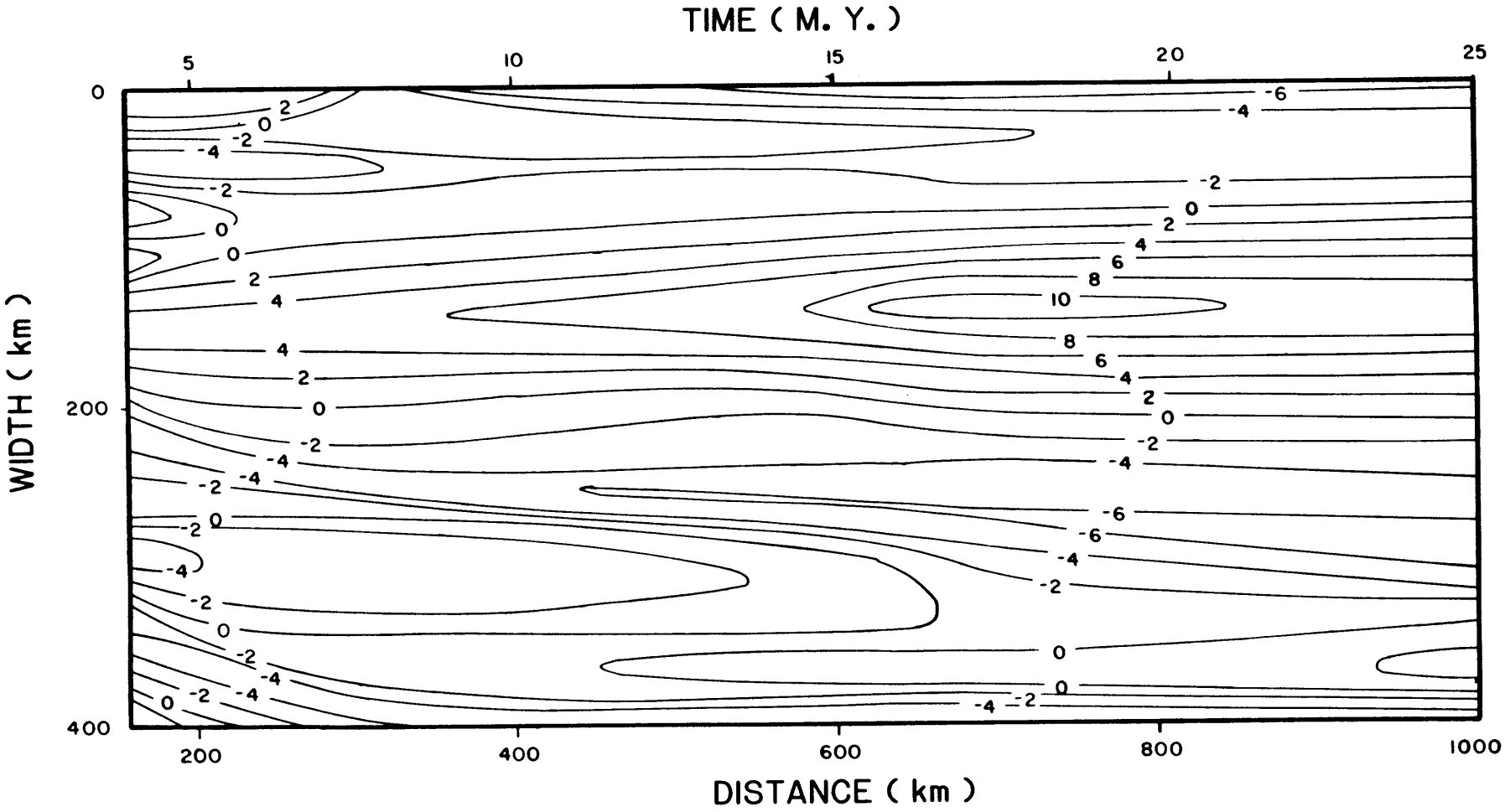
TIME (M. Y.)
5
10
15
20
25
0
200
400
WIDTH (km)
200
400
600
800
1000
DISTANCE (km)

Figure 2.12

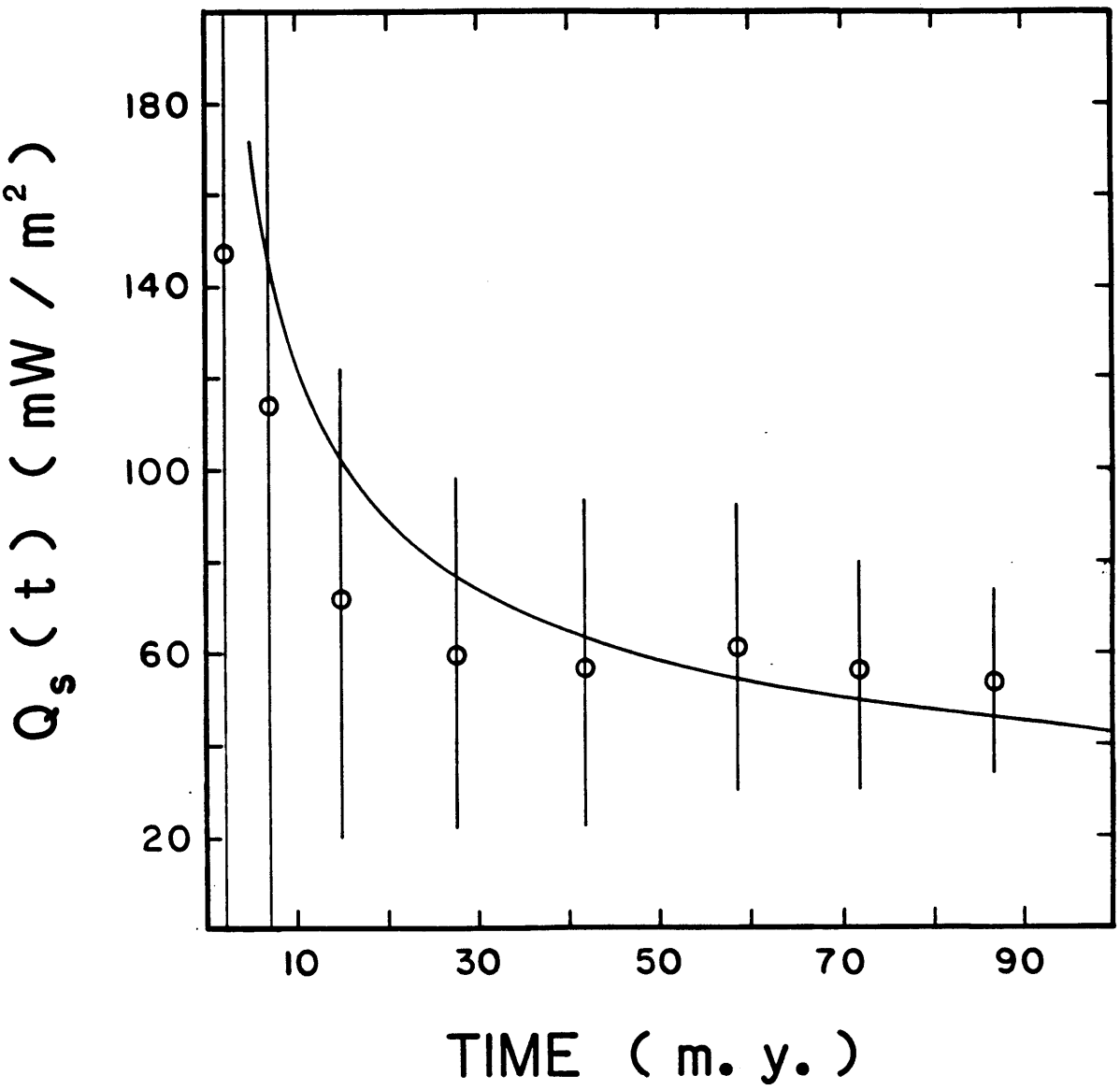

Figure 2.13

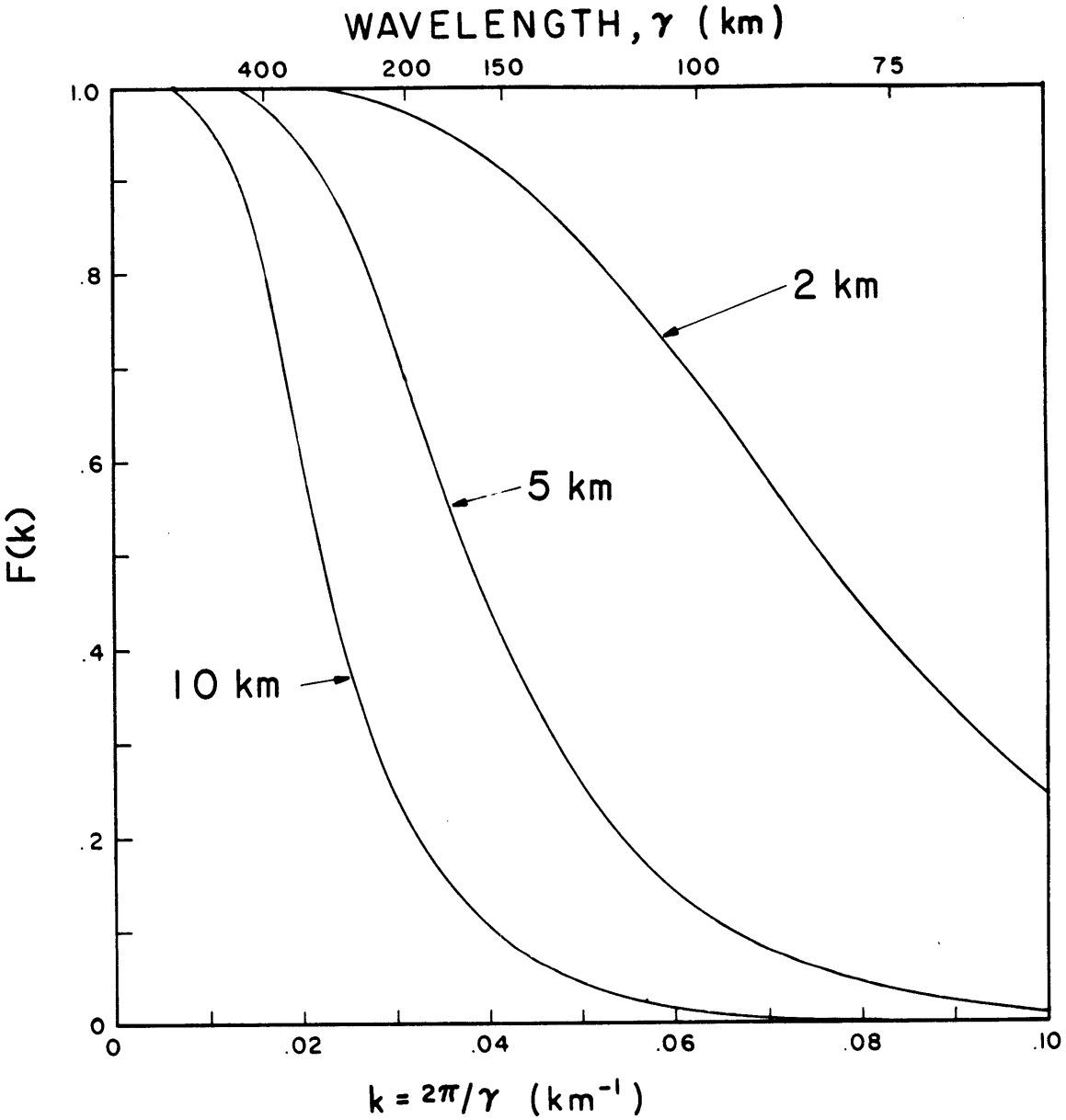
WAVELENGTH, γ (km)
400
200
150
100
75
1.0
.8
.6
.4
.2
0
F(k)
2 km
5 km
10 km
0
.02
.04
.06
.08
.10
k = 2π/γ (km⁻¹)

Figure 2.14

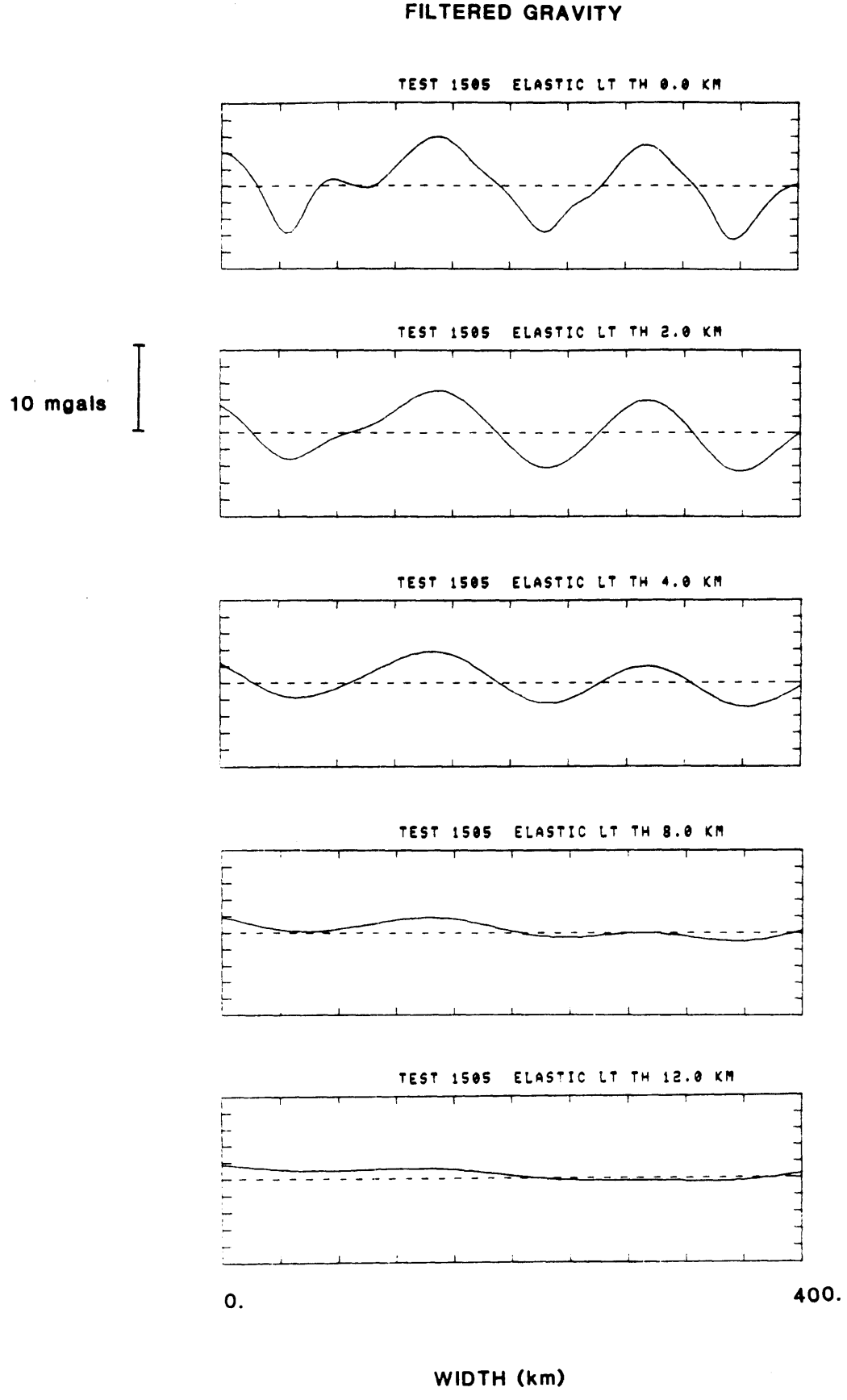
FILTERED GRAVITY
TEST 1505 ELASTIC LT TH 0.0 KM
TEST 1505 ELASTIC LT TH 2.0 KM
10 mgals
TEST 1505 ELASTIC LT TH 4.0 KM
TEST 1505 ELASTIC LT TH 8.0 KM
TEST 1505 ELASTIC LT TH 12.0 KM
0.
400.
WIDTH (km)

Figure 2.15(a)

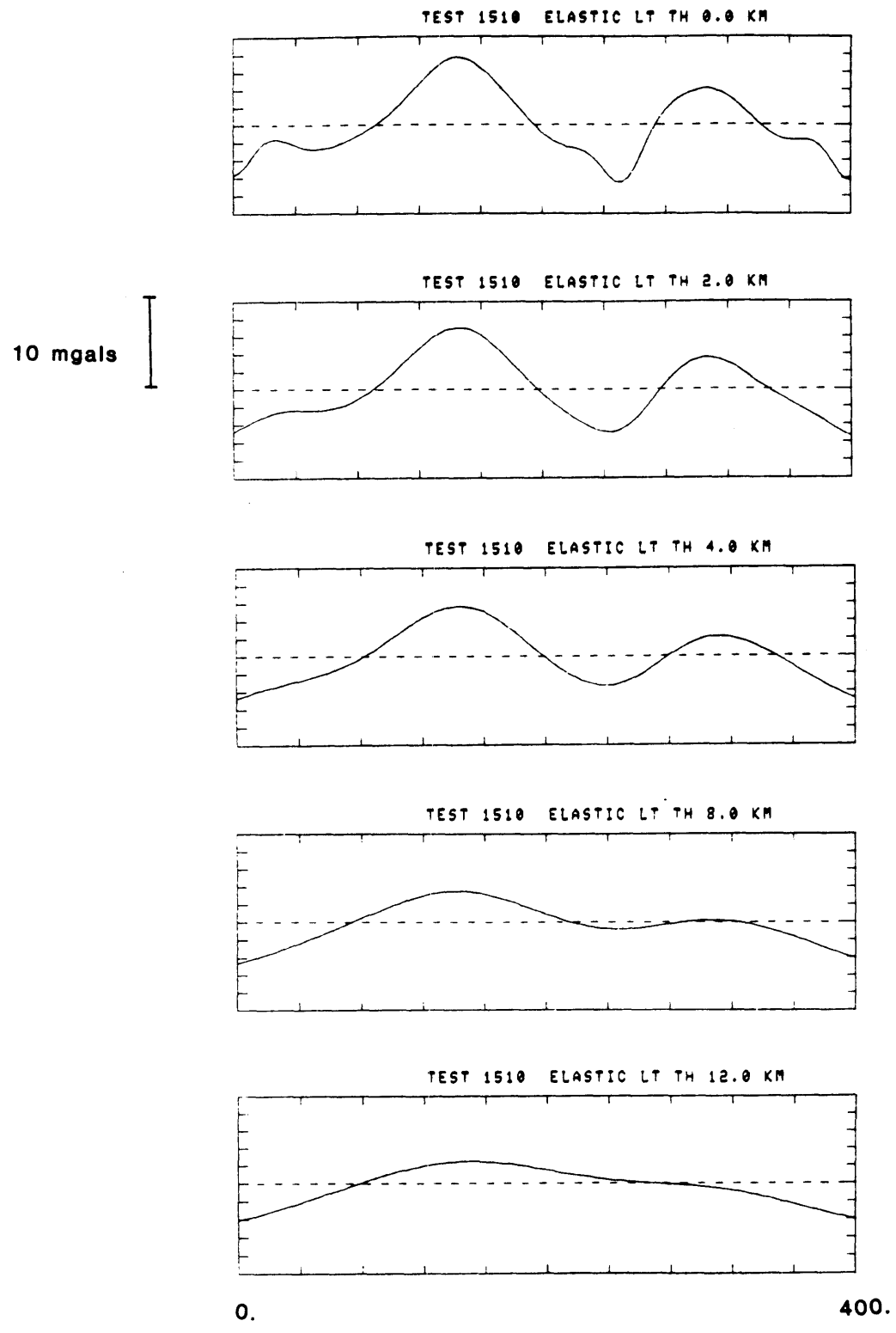
FILTERED GRAVITY
TEST 1510 ELASTIC LT TH 0.0 KM
TEST 1510 ELASTIC LT TH 2.0 KM
10 mgals
TEST 1510 ELASTIC LT TH 4.0 KM
TEST 1510 ELASTIC LT TH 8.0 KM
TEST 1510 ELASTIC LT TH 12.0 KM
0.
400.
WIDTH (km)

Figure 2.15(b)

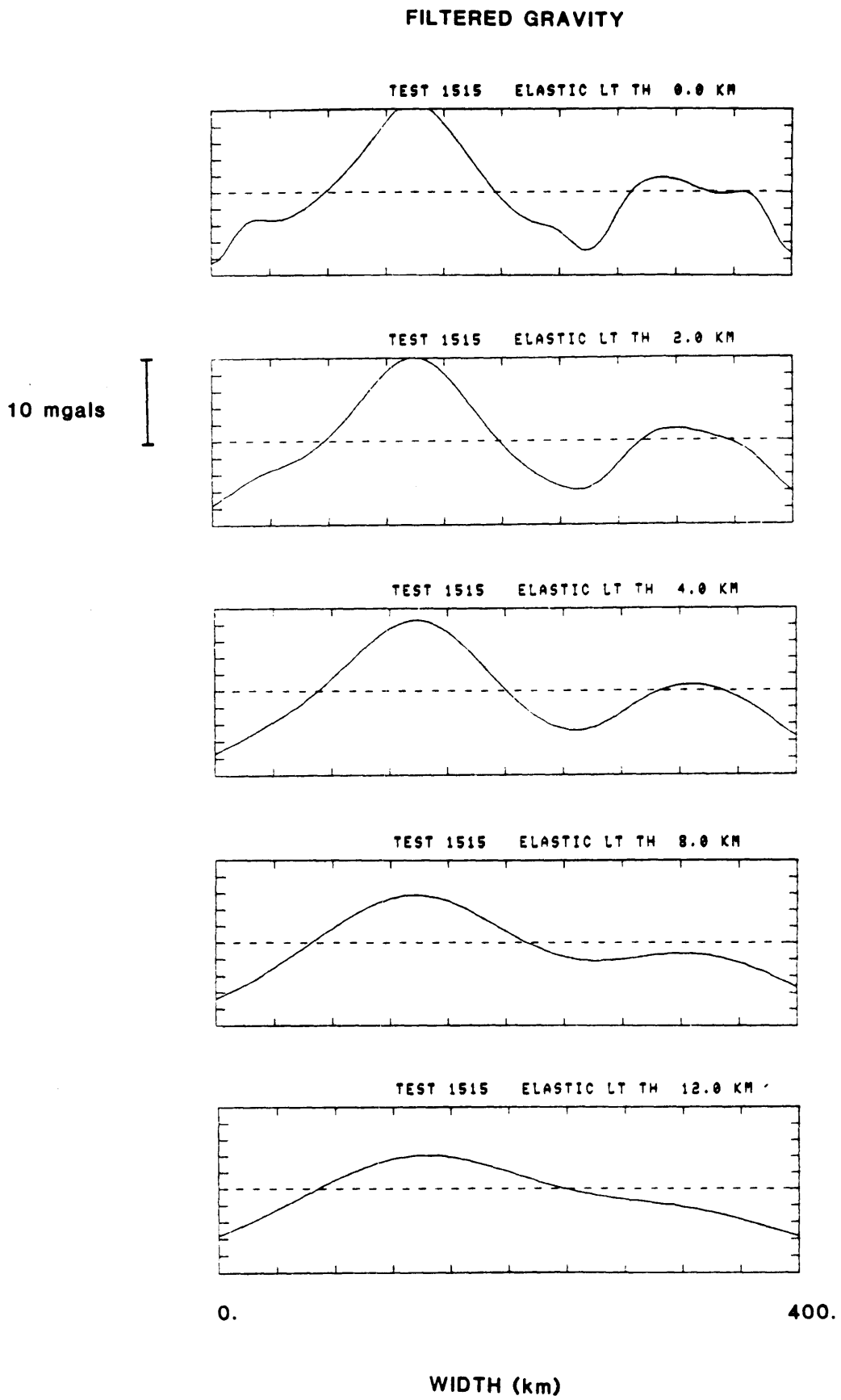
FILTERED GRAVITY
TEST 1515 ELASTIC LT TH 0.0 KM
TEST 1515 ELASTIC LT TH 2.0 KM
10 mgals
TEST 1515 ELASTIC LT TH 4.0 KM
TEST 1515 ELASTIC LT TH 8.0 KM
TEST 1515 ELASTIC LT TH 12.0 KM
0.
400.
WIDTH (km)

Figure 2.15(c)

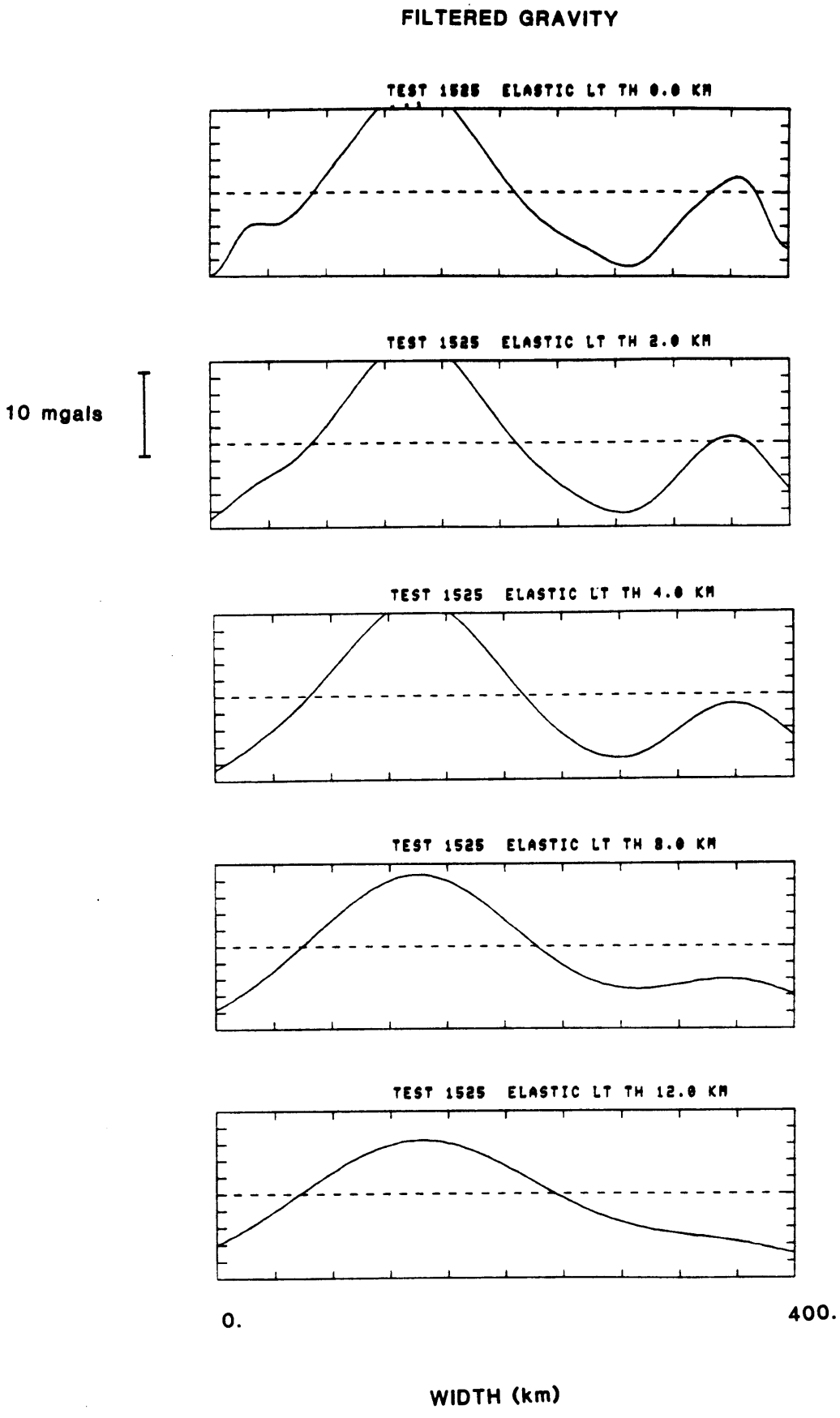
FILTERED GRAVITY
TEST 1525 ELASTIC LT TH 0.0 KM
TEST 1525 ELASTIC LT TH 2.0 KM
10 mgals
TEST 1525 ELASTIC LT TH 4.0 KM
TEST 1525 ELASTIC LT TH 8.0 KM
TEST 1525 ELASTIC LT TH 12.0 KM
0.
400.
WIDTH (km)

Figure 2.15(d)

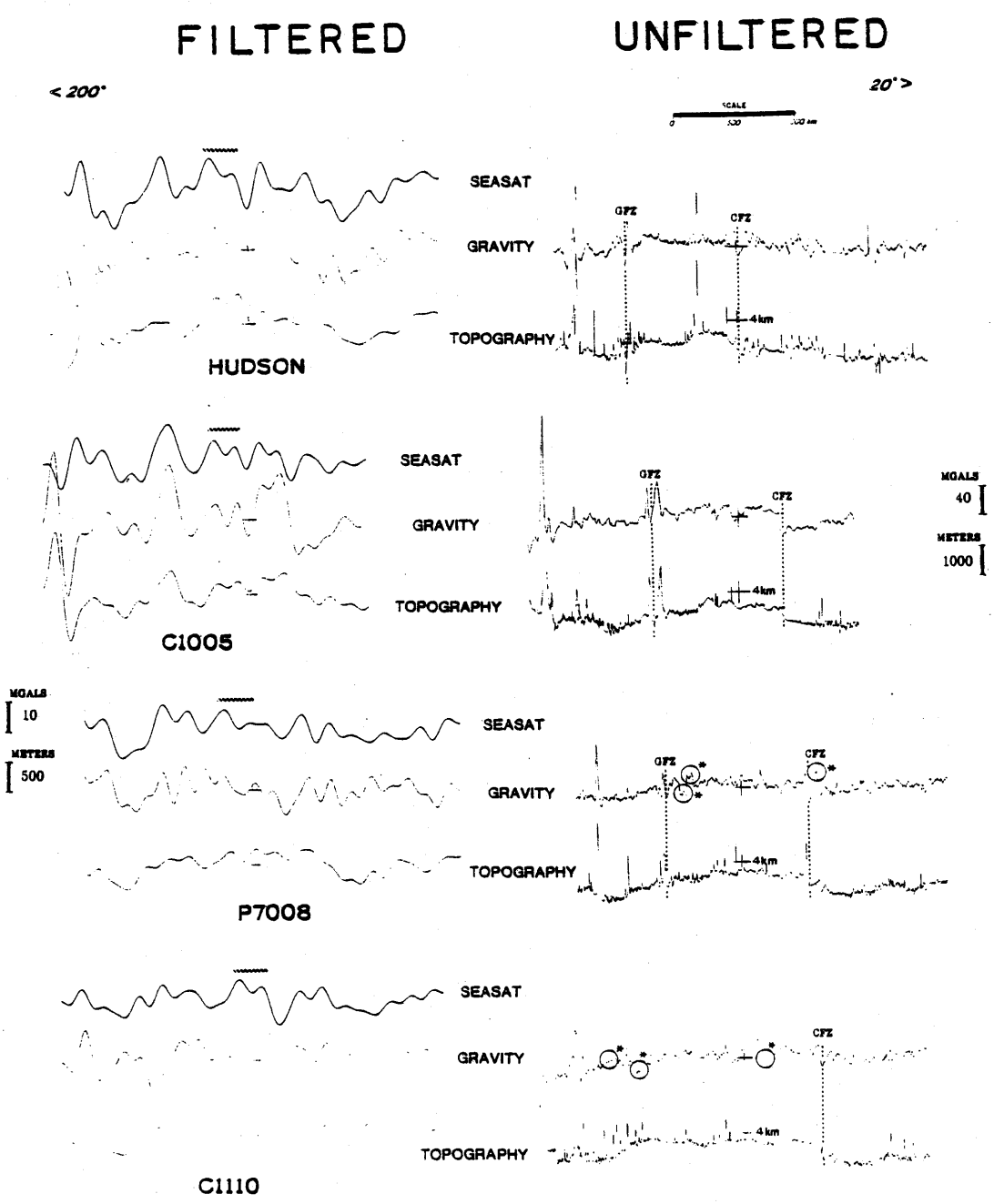
FILTERED
UNFILTERED
< 200°
20° >
SCALE
0
500
SEASAT
GRAVITY
TOPOGRAPHY
GFZ
CFZ
4km
HUDSON
C1005
MGALS
40
METERS
1000
MGALS
10
METERS
500
P7008
C1110

Figure 2.16

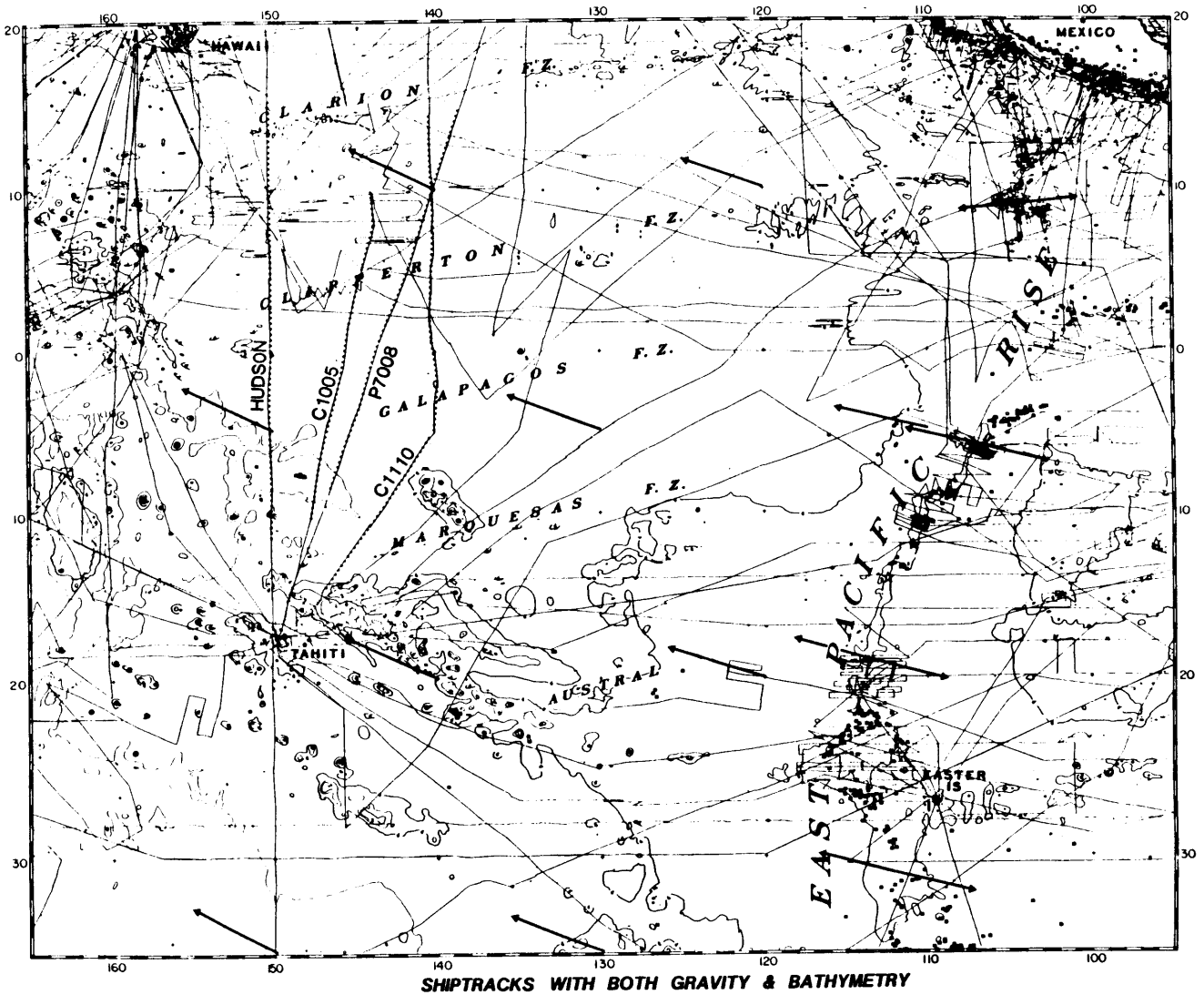

SHIPTRACKS WITH BOTH GRAVITY & BATHYMETRY

Figure 2.17

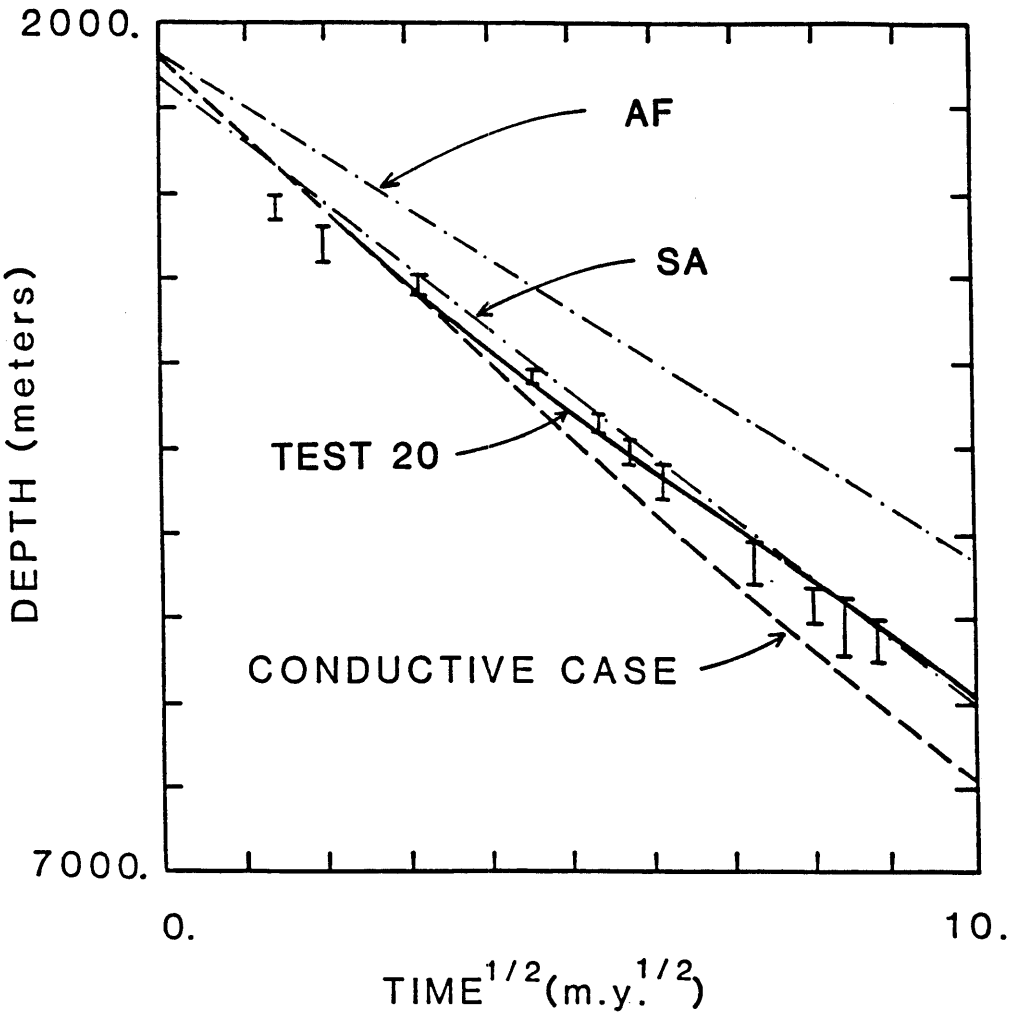
2000.
7000.
0.
10.
DEPTH (meters)
TIME$^{1/2}$(m.y.$^{1/2}$)
AF
SA
TEST 20
CONDUCTIVE CASE

Figure 2.18

"C'est brutal, mais ça marche!"

-René Panhard (commenting on the car gearbox he'd invented).

CHAPTER 3

PARAMETERIZATION OF THE COOLING OF A VARIABLE VISCOSITY FLUID WITH APPLICATION TO THE LITHOSPHERE

3.1 Introduction

We now give a mathematical description of the behavior seen in numerical experiments on the cooling of variable viscosity fluids from above. The aim of this work is to derive general relationships between the physical properties which control the strength of convection in a variable viscosity fluid and the rate of cooling of the conductive lid which forms when the viscosity is strongly temperature dependent. Next, the cooling rate for the conductive lid will be related to the geophysical observables for the oceanic lithosphere which depend on the thickness and temperature structure of the lithosphere. The rate of subsidence, the heat flux, the offset of geoid height at fracture zones, and small wavelength gravity and topographic signals should vary with the viscosity and temperature of the asthenosphere. The uncertainty in estimates of the viscosity and the pressure and temperature dependence of viscosity as well as other physical parameters makes it imperative to understand the relationship between these values and the rate of cooling of

the lithosphere. The predictions of the equations derived here will be compared to the results of two-dimensional numerical calculations which are described in chapter 2.

For this discussion results of the numerical calculations which led us to consider the mathematical approach used here are briefly explained. The next section demonstrates why the cooling of the conductive lid overlying a convecting variable viscosity fluid should behave in a simple manner in time. First, it is shown that convective heat varies in a simple way with a suitably defined Rayleigh number (Ra) for a variable viscosity fluid as is predicted by boundary-layer theory. Next, theory is developed which predicts that the heat flux variation should have the same functional dependence on time as for a similarity solution describing a moving boundary in a cooling problem. The dependence of the heat flux variation on the parameters which determine the viscosity is shown as well as the dependence of the parameter λ on these quantities. Finally, the relationships between λ and the predicted geophysical observables of water loaded subsidence of the lithosphere and local geoid anomaly is derived for the similarity problem.

3.2 Numerical Calculation Results

The rate of cooling of a fluid with viscosity which depends on temperature and pressure will be affected by the vigor of the convection in that fluid. When a box of temperature dependent fluid is cooled from above a region may develop at the top of that box where viscosities are so high as to preclude any significant convective flow there. It is the temperatures

within such a conductive lid and the rate of growth of the lid which has been studied using numerical methods which are described in detail in chapter 2. The same terminology and variables are used in this chapter as were used there. The set-up for these calculations is shown in Figure 2.2. For boxes of various widths and depths the two-dimensional Navier-Stokes equations of energy, mass and momentum conservation in a variable viscosity, infinite Prandtl number fluid are studied using numerical methods. The viscosity is taken to depend on temperature and pressure through equation 2.1. The activation energy (E) is the parameter which controls the temperature dependence of viscosity and the effective activation volume (V*) controls the pressure dependence. In the numerical cases these two parameters were varied as well as the average value of the viscosity which is defined by a reference viscosity (μ_{ref}) described in chapter 2. Table 3.1 gives results of the numerical models which will be compared with the theory developed in this chapter.

For our system to behave like a similarity solution over some period of time the average temperature in the conductive lid should be constant over that time interval. The average temperature of the conductive lid at a given time ($T_L(t)$) is defined by equation 2.3 as the average temperature down to the depth $z_L(t)$ where the horizontally averaged temperature is equal to 90% of the average temperature in the convecting region (T_{cr}). T_{cr} is calculated by averaging the temperature below the bottom of the thermal boundary layer which is discussed in the next section. Figure 2.5 shows the variation of T_L with time

for several of the computer runs which have been done. In all cases there is a decrease in T_L from an initial value, which corresponds to the value for purely conductive cooling, to a lower and nearly constant value which depends on the case considered. It is the constancy of the value in time for the numerical calculations which leads to the consideration of a similarity solution which also exhibits this behavior of having a constant value of the average temperature in a conductively cooling region.

3.3 Parameterization of variable viscosity cooling

Knowing that the temperature structure of the conductive lid overlying a convecting region behaves in a fairly simple manner we will try to understand why this should occur. Then a parameterization of the rate of cooling and thickening of the lid will be developed.

3.3.1 Rayleigh-Nusselt Relations for Variable Viscosity Flow

Two standard parameters are calculated through time for the convecting regions. They are the Rayleigh number (Ra) and the Nusselt number (Nu). The physically meaningful definition of the Rayleigh number for this problem is:

$$Ra = \frac{\rho \; g \; \alpha \; \Delta T \; \ell^3}{\kappa \; \bar{\mu}} \qquad (3.1)$$

where ρ (density), g (acceleration of gravity) and α (thermal expansion) are the same for all calculations. Table 2.1 gives the values of these constants. Because this problem is transient and viscosities vary across the convecting region the

values of ΔT (temperature drop), ℓ (length scale) and $\bar{\mu}$ (average viscosity) must be defined in a self-consistent and physically reasonable way. These values change with time in the calculations.

The temperature difference across the convecting region is ΔT. To calculate it we must define the point which separates the convecting and conducting regions. This is done in terms of the horizontal average of the vertical advective heat flux $(Q_c(z))$:

$$Q_c(z) = \frac{1}{W_b} \int_0^{W_b} w(x,z)\, T(x,z)\, dx \qquad (3.2)$$

In the boundary layer at the top of the convecting regions this function varies approximately linearly with depth. Figure 3.1 shows $Q_c(z)$ at one time for case 20 and the relation to the temperatures in the conductive lid and convecting region. In the figures we show the nondimensional advective heat flux which can be dimensionalized using the factor $k\Delta T/L$, where k is conductivity and ΔT and L are defined in chapter 2. For these cases the value of this factor is 10.4 mW/m^2. A straight line is fit through two points of this curve at .2 Q_{cmax} and .8 Q_{max} as illustrated in Figure 3.2. The depth at which the value of this linear function is zero is considered to be the top of the boundary layer (z_t). The bottom of the boundary layer (z_b) is defined as the point where this line intersects Q_{cmax} (also in Figure 3.2). To define the temperature difference for the convecting region (ΔT) the horizontally averaged temperature $(T_h(z))$ is used. The difference between the top and bottom of the boundary layer is $\Delta T = T_h(z_b) - T_h(z_t)$. To define a length

scale we also use the vertical advective heat flux. Since we want the length over which the flow is vigorous we define it as:

$$\ell = \int_0^z \frac{Q_c(z)\, dz}{Q_{cmax}} \tag{3.3}$$

The viscosity to be used in the calculation of the Rayleigh number is an average weighted by the second invariant of the strain rate tension ($\dot{e}$), which was suggested by Parmentier (1978). This is expressed as:

$$\bar{\mu} = \frac{\iint_A \mu(x,z)\, \dot{e}^2(x,z)\, dx\, dz}{\iint_A \dot{e}^2(x,z)\, dx\, dz} \tag{3.4}$$

Finally, the Nusselt number is defined as the maximum horizontally averaged vertical heat flux (Q_{cmax}) divided by the steady state conductive heat flux over the convecting region.

$$Nu = \frac{Q'_{cmax} \cdot \ell}{K\, \Delta T} \tag{3.5}$$

where the prime denotes the dimensional advective heat flux. This is a slight variation on the normal definition of the Nusselt number, which is defined for a steady state condition as the ratio of the total heat flux in the presence of convection to the heat flux across the same region when there is only conductive transport of heat (McKenzie et al.,1974). The convection here is quasi steady state, that is the heat flux is changing slowly with time, but at a given time the convection is in equilibrium with the heat flux it is transporting. This wiil be shown below. The use of the maximum convective heat flux (Q_{cmax}), instead of the total heat flux, in the definition of the Nusselt number is justified because at the level where the convective heat flux is a maximum the conductive heat transport

is negligible. Values of Q_{cmax} and the Rayleigh number defined by equation 3.1 given in Tables 3.2 to 3.11 for different times into the calculation for the models discussed in chapter 2. In all these cases there is a decrease in Q_{cmax} and Ra with time except at a time about 20 m.y. into case 15 when the entire bottom portion of the contents of the box moved upward.

Theory predicts that for steady state convection the relation between Ra and Nu should be given by

$$Nu = a\ R_a{}^b \qquad (3.6)$$

where b is a constant between 1/5 and 1/3 (Roberts, 1979) for convective flow with between fixed boundaries. Figure 3.3 shows the relation between log(Nu) and log(Ra) for several cases. For a range of Rayleigh numbers for each case considered there is a linear relation between these quantities. The slope of this plot is about 0.30 (= b in equation 3.6). The points which do not lie on this line are all for times early in the calculation, when the average lid temperature (T_L) was varying. For all these points the Nusselt number is lower than it would be if it fell on the linear trend. This suggests that in this period the lid temperature structure is changing in response to the changing input of heat from the convecting region. Something about the system is causing the variation of the convective heat flux to vary with time in a way which does not allow an equilibrium temperature structure to be established early in most of the calculations. At any rate we will concentrate on the region where T_L is constant, which shall be referred to as the interval of "transient equilibrium" of the lid with the

convecting region.

The heat flux out of the convecting region affects the rate of cooling of the lid and the value of T_L. The Nusselt number describes that heat flux and we will investigate how it varies with time during cooling. Since the Nusselt number depends on the Rayleigh number (via equation 3.6) it is necessary to find the parameter which is causing the variation of the Rayleigh number with time. The area where the viscosity is minimum is the area where the strain rate is greatest and therefore $\dot{e}$ is highest as illustrated in Figure 3.4. Therefore, the average viscosity ($\bar{\mu}$) is weighted most heavily toward the minimum viscosity. The minimum viscosity occurs at the base of the thermal boundary layer where $z = z_b$ because this is the shallowest depth at which the temperature of the convecting region, which is nearly isothermal, is found. The viscosities deeper than this are higher if the effective pressure dependence of viscosity (V* in equation 2.1) is greater than zero. When V* = 0 the convecting region is nearly isoviscous, except in the narrow boundary layer. Figure 3.5 shows a plot of the ratio of the average viscosity ($\bar{\mu}$) defined by equation (3.4) versus the viscosity at the base of the boundary layer ($\mu(z_b)$) for two numerical cooling calculations through time. In case 20 V* = 7.5 cm^3/mole and in case 17 V* = 0. In both cases $\bar{\mu}$ was linearly related to $\mu(z_b)$, but the ratio of the relation is different. The ratio was nearly 1.0 for case 17 (no pressure dependence on viscosity) and about 5.0 for V* = 7.5 cm^3/mole in case 20. The values of these two quantities and their ratio is also given in Tables 3.2 to 3.11 for all the numerical models

and the ratio is always nearly constant for a given model. Thus throughout a calculation the effective average viscosity ($\bar{\mu}$) can be related to $\mu(z_b)$ as:

$$\bar{\mu} = c_1 \mu(z_b) \tag{3.7}$$

where c_1 is a constant that is greater than one and depends on V*. Three factors affect the value of the minimum viscosity ($\mu(z_b)$). One is the average viscosity determined by A in equation (2.1). The other two factors are more interesting because they change with time. One is the average temperature of the convecting region (T_{cr}) which affects viscosity in proportion to the magnitude of the activation energy (E) in equation (2.1). The other is the depth to the bottom of the thermal boundary layer (z_b), since pressure (P) in equation (2.1) depends on depth. The effect of variations in the average temperature (T_{cr}) and in the depth (z_b) on the Nusselt number will be considered. Further, it will be shown that both effects are consistent with the Nusselt number being proportional to $t^{-1/2}$ over a significant range of time.

3.3.2 Cooling of a Fluid with Temperature Dependent Viscosity

If only the temperature dependence of the viscosity is considered, then equation (2.1) reduces to:

$$\mu(T) = A \exp\left(\frac{E'}{RT}\right) \tag{3.8}$$

where

$$E' = E + P_o V$$

where P_o is a reference value of pressure.

Combining (3.8) with equations (3.6) and (3.7) gives a

relation between the Nusselt number and temperature:

$$Nu^{(T)} = A_1 \exp\left(-\frac{bE'}{RT}\right) \tag{3.9}$$

where

$$A_1 = a\left(\frac{\alpha\rho g\Delta T\ell^3}{\kappa c_1 A}\right)^b$$

To approximate the dependence of Nu on temperature T can be expanded around T_o in terms of T to give:

$$Nu^{(T)} = A_1\left[\exp\left(\frac{-2bE'}{RT_o}\right)\right]\left[\exp\left(\frac{bE'T}{RT_o^2}\right)\right] \tag{3.10}$$

The second exponential in equation (3.10) can be expanded around a reference temperature of the convecting region (T_o) to give:

$$Nu^{(T)} = Nu(T_o)\left[1 + (T-T_o)\frac{bE'}{RT_o^2}\right] \tag{3.11}$$

where

$$Nu(T_o) = A_1 \exp\left[\frac{-bE'}{RT_o}\right]$$

This suggests that the heat flux out of the convecting region varies approximately linearly with temperature. To illustrate how good this approximation is, Figure 3.6 shows the variation of Nu with T for equation (3.11) compared to equation (3.9). Figure 3.7 shows that this relation is also linear for the numerical calculations. The temperature of the convecting region (T_{cr}) is simply related to the heat flux out of the region or Nu by:

$$\frac{\partial T_{cr}}{\partial t} = -c_2\, Nu \tag{3.12}$$

where $c_2 = k\Delta T/(\ell\rho C_p\Delta Z)$. The depth extent of the convecting region is defined as ΔZ . It is not the same as (ℓ) defined by

equation (3.3), but extends to the bottom of the box. Differentiating (3.11) with $T = T_{cr}$ and combining with (3.12) gives:

$$\frac{\partial Nu(t)}{\partial t} = - c_2 c_3 Nu(t) \qquad (3.13)$$

where $$c_3 = \left(\frac{bE'}{RT_o^2}\right) Nu(T_o) \ .$$

Integrating equation (3.13), assuming $t = 0$ when $Nu^{(T)} = Nu(T_o)$, gives:

$$Nu^{(t)} = Nu(T_o) \exp(-c_2 c_3 t) \qquad (3.14)$$

Expanding t around t_o in terms of $t^{-1/2}$ gives:

$$Nu^{(t)} = Nu(T_o) \left[\exp(-3c_2 c_3 t_o)\right]\left[\exp(2c_2 c_3 t_o^{3/2} t^{1/2})\right] \qquad (3.15)$$

Then by expanding the exponential term which depends on $t^{-1/2}$ around $t_o^{-1/2}$ gives:

$$Nu^{(t)} = Nu(t_o) \left[1 + (t^{-1/2} - t_o^{-1/2}) t_o^{3/2} 2c_2 c_3\right] \qquad (3.16)$$

where

$$Nu(t_o) = Nu(T_o) e^{-c_2 c_3 t_o} \ .$$

To show that equation (3.16) is a good approximation to equation (3.14) for the range of parameters considered here values of $Nu^{(t)}/Nu(t_o)$ were calculated using both formulas. Using $b = 0.3$ $E' = 4.18 \times 10^5$ J/mole, $\rho c_p = 3 \times 10^{-6}$ J/m^3°K, $Nu(T_o) = 20$, $\Delta Z = 300$ km, $\ell = 150$ km, $\Delta T = 100$ °K, $k = 3.2$ J/m-s-°K and $T_o = 1550$°K it is found that the average error due to the approximation was less than 2% over a period of 50 m.y. centered on $t_o = 50$ m.y (see Figure 3.8). The heat flux into the lithosphere at t_o with these parameters is about 1 HFU or 41 ergs/cm^2-s. Also, by choosing $t_o = 50$ m.y., the value of

$2c_2c_3t_o$ is 1 so that the constant terms in equation (3.16) drop out. Therefore, for a cooling convecting fluid with temperature dependent viscosity given by equation (2.1) the Nusselt number can be shown to vary with $t^{-1/2}$.

3.3.3 Effect of Pressure Dependence of Viscosity

A similar analysis can be applied to the variation of the Nusselt number with the depth to the isothermal convecting region. The analysis is somewhat different because it will be assumed that z_b varies as $t^{1/2}$, which is the case for the numerical results, and then it will be shown that this causes the Nusselt number to vary as $t^{-1/2}$.

Holding temperature constant so that viscosity at ($z=z_b$) only varies with z_b equation (2.1) can be rewritten:

$$\mu(z_b) = A_2 \exp\left(\frac{z_b V'}{R T_{cr}}\right) \qquad (3.17)$$

where $V' = V^*\rho g$ and $A_2 = A\exp(E/RT_{cr})$. Since the Nusselt number (Nu) depends on the average viscosity through equations (3.1), (3.6) and (3.7) it will depend on Z_b as:

$$Nu = a(Ra_o\mu_o)^b \left[A_2c_1 \exp\left(\frac{z_bV'}{R T_{cr}}\right)\right]^{-b} \qquad (3.18)$$

where Ra_o is the Rayleigh number defined with μ_o replacing $\bar{\mu}$ in equation (3.1). The boundary layer thickness changes little during the numerical calculations compared to z_L and it is small compared to z_L so z_b can be nearly equal to z_L. The dependence of z_L on time is assumed to be proportional to $2\lambda(\kappa t)^{1/2}$. Thus (3.18) can be changed to give Nusselt number as a function of time:

$$Nu(t) = Nu(t=0)\, e^{-c_4t^{1/2}} \qquad (3.19)$$

with:

$$c_4 \equiv \frac{2bV^*\rho g\lambda(\kappa)^{1/2}}{R\ T_o}$$

because we have replaced z_b with $2\lambda(\kappa t)^{1/2}$. Expanding $t^{1/2}$ around t_o in terms of $t^{-1/2}$ gives:

$$Nu(t) = Nu(t=0)[\exp(-2c_4 t_o^{1/2})][\exp(c_4 t_o t^{-1/2})]. \quad (3.20)$$

Again expanding the second exponential in (3.20) around t_o gives:

$$Nu(t) = Nu(t_o)[1 + (t^{-1/2} - t_o^{-1/2})c_4 t_o] \quad (3.21)$$

where

$$Nu(t_o) = Nu(t=0)e^{-c_4 t_0^{1/2}} .$$

As with the variation of Nusselt number with T_{cr} the variations due to changes in z_b are linear with $t^{-1/2}$.

3.3.4 Similarity solution for lid temperatures

It will now be shown that when the Nusselt number varies linearly with $t^{-1/2}$, as it does for this problem, then the cooling of the conductive lid can be described by a similarity solution. The treatment of this solution follows Carslaw and Jaeger (1959) and the problem is similar to a moving boundary problem where there is a change of phase which was first treated by Stefan (1891). The heat flux at a depth $z_p(t)$, the base of the lid, is taken to be the maximum convective heat flux:

$$K \left.\frac{\partial T}{\partial z}\right|_{z_p} = Q'_{cmax} \quad (3.22)$$

where K is the thermal conductivity. The position of the phase boundary (z_p) is assumed to move with time at a rate given by:

$$z_p = 2\,\lambda\,(\kappa t)^{1/2} \qquad (3.23)$$

where κ is the thermal diffusivity and λ is a constant which depends on the Nusselt number of the system at a given time. λ_c is the value of the constant which gives the rate of thickening of the lid for the purely conductive case - with no convection. The temperatures in the lid must satisfy the conductive heat transport equation. Such a solution is:

$$T(z,t) = B\ \mathrm{erf}(z/2(\kappa t)^{1/2})) \qquad (3.24)$$

Since at depth z_p the temperature is Tp the constant B is given by:

$$B = Tp/\mathrm{erf}(\lambda) \qquad (3.25)$$

Recall that the temperature at the base of the lid (Tp) is given by $T_{cr} - \Delta T$, where T_{cr} is the average temperature of the convecting region and ΔT is the temperature drop across the boundary layer. T_{cr} is nearly equal to the temperature at the base of the boundary layer ($T(z_b)$) so Tp is approximately equal to the temperature at the top of the boundary layer ($T(z_t)$). Since T_{cr} varied slowly in the numerical cases considered here and ΔT was nearly constant, we take Tp to be constant for this problem. For the conductive case B equals T_{cr} and the value of λ which describes the motion of point z_p can be calculated using equation (2.25).

Combining equations 3.22 to 3.25 we find that the convective heat flux indeed must vary linearly with $t^{-1/2}$ for equation 3.23 to hold. This gives:

$$Q'_{cmax} = \left[\frac{K\ T_p}{(\pi\kappa)^{1/2}} \frac{e^{-\lambda^2}}{\mathrm{erf}\lambda} \right] t^{-1/2} \qquad (3.26)$$

Using the relationship between the Rayleigh number and the Nusselt number (equation 3.6) we can relate the average viscosity (μ) to the parameter λ. This is:

$$\frac{\mu}{\mu_o} = Ra_o \left[\frac{\ell \, T_p \, e^{-\lambda^2}}{a\Delta T(\pi\kappa t)^{1/2} \, \mathrm{erf}\lambda} \right]^{-1/b} \qquad (3.27)$$

where Ra_o is the Rayleigh number give by equation (3.1) with μ_o replacing $\bar{\mu}$. Figure 3.9 shows how changes in the average viscosity will affect λ. The parameter λ is approximately linearly related to the log of the average viscosity.

Next, we can show that for this problem the average temperature of the lid is constant in time and depends on λ. The lid similarity temperature (T_s) is defined as the average temperature down to the change of phase ($z = z_p$). It is gotten by integrating down to z_p

$$T_s = \frac{1}{z_p(t)} \int_0^{z_p(t)} \left(\frac{Tp}{\mathrm{erf}\ \lambda}\right) \mathrm{erf} \frac{z}{2(\kappa t)^{1/2}} dz \qquad (3.28)$$

Equation (3.28) can be evaluated to give:

$$Ts = Tp \left[1 - \frac{(1 - e^{-\lambda^2})}{\lambda \ \mathrm{erf}\ \lambda \ (\pi)^{1/2}}\right] \qquad (3.29)$$

Thus T_s is a function only of λ and T_p and does not vary with time. This quantity is analogous to the average lid temperature (T_L) which was shown to be nearly constant for the numerical calculations already described. In Figure 3.10 T_s defined by equation (3.29) is plotted against λ. This shows that T_s is a nearly linear function of λ.

3.3.5 Comparisons between Theory and Numerical Results

The combined effect of variations in T_{cr} and z_b is simple to get since it is proper to multiply equations (3.16) and (3.21) to give:

$$\frac{Nu(t)}{Nu(t_o)} = [1+(t^{-1/2}-t_o^{-1/2})2c_2c_3t_o^{3/2}][1+(t^{-1/2}-t_o^{-1/2})c_4t_o]$$

$$\cong 1 + (t^{-1/2}-t_o^{-1/2})(2c_2c_3t_o^{3/2}+c_4t_o) \qquad (3.30)$$

with

$$Nu(t_o) = Nu(t=0)\ e^{-(c_2c_3t_0+c_4t_0^{1/2})} .$$

By choosing t_o such that

$$t_o = \left(\frac{-c_4 + \sqrt{c_4^2-8c_2c_3}}{4\ c2\ c3}\right)^2 \qquad (3.31)$$

the terms in equation (3.30) which do not depend on $t^{-1/2}$ drop out. It is interesting to note that for Q_{cmax} assumed to be 2 HFU at t_o = 36.7 m.y. the term $2c_2c_3t_o^{3/2}$ is just over twice c_4t_o for for V' = 7.5. In that case the change of T_{cr} is twice as important as that of Z_b in determining the dependence of Nu on time. Figure 3.11 shows plots of Qcmax versus $t^{-1/2}$ for several of the runs and it is clear that the trend is linear in the region of "transient equilibrium". Also the plots show that a line can be fit to the points which have slopes which are equal to the product of Qcmax(t) x $t^{-1/2}$. This is required for equation (3.26) to hold.

To compare the predictions of this theory against the results of the numerical calculations we must calculate the parameters c_2, c_3 and c_4 and be able to relate some combination of them to some features of the model results. One way to do this is to combine equations (3.15) and (3.20) and assume that the ratio of the Nusselt number (Nu) to Qcmax is constant through a given numerical

calculation. This gives us:

$$\frac{Qcmax(t)}{Qcmax(t=0)} = \exp\left(\frac{-c_4 t_o^{1/2}}{2}\right) \exp\left[-\left(c_2 c_3 + \frac{c_4 t_o^{-1/2}}{2}\right)t\right] \quad (3.32)$$

where t_o is the time around which we make the expansions. On a plot of ln(Qcmax) versus time the slope should be given by $-(c_2 c_3 + c_4/2t_o^{1/2})$ and the y-intercept will be $\ln(Qcmax(t=0)) - c_4/2t_o^{1/2}$. Over the range of the "transient equilibrium" there is a range of times we could choose for t_o, but this affects the slope of the $\ln(Q_{cmax})$ plot for equation (3.35) by only about 10%. Figure 3.12 shows that the plots of ln(Qcmax) versus time is indeed linear over a large range of time. Table 3.1 gives the values of the slopes from these plots along with the predicted values of the slope based on the calculated values of c_2, c_3 and c_4. In the estimation of these parameters no effort was made to adjust for the differences in the depth extent of the efficient cooling by convection (ΔZ) , which would affect the value of c_2, nor was the value of t_o allowed to vary from case to case. Still for only runs 17 and 23 were the predicted slopes more than 10% different than the measured values. For case 17 this error could be due in part to the difficulty in calculating Qcmax since the flow broke into two cells for that run. In test 23 either the length scale for cooling (ΔZ) is smaller than estimated or the Rayleigh number is so low near the end of the run that the log linear Rayleigh-Nusselt relation was no longer valid.

To determine λ in terms of the coefficients of viscosity -A, E and V*, equation (3.30) can be combined with equation (3.27) to give:

$$Q'_{cmax}(t_o)\ (2c_2 c_3 to^{3/2} + c_4 t_o) = \frac{k\ T_p\ e^{-\lambda^2}}{(\pi\kappa)^{1/2}\ erf\lambda} \quad (3.33)$$

with t_o given by equation (3.31). This relation shows that λ does not depend on time for our theoretical development, but only on the physical parameters of the system. It is more difficult to use this relation to compare predictions to the numerical results, because of the large number of terms, than it is using equation (3.32). However, in the numerical calculations the variation of λ with A, E and V* agrees well with the predictions of equation (3.33). The value of λ for these calculations is estimated by calculating T_L using equation (2.3) and relating it to λ through equation (3.29) (assuming $T_L = T_s$). The effect on λ of the change in the average viscosity is large compared to the effect of the parameters which depend on the temperature and pressure dependence of viscosity. Therefore, the most useful relation is the one between λ and μ which is implied by equation (3.33) but also given by equation (3.27).

We did not explicitly consider a parameterization of the effects of non-Newtonian viscosity. This was omitted for two reasons. First, stress dependence added to temperature dependence should affect the long term evolution of the convecting system in a relatively simple way. As shown by our studies of stress dependent viscosity and also shown by the more extensive study of this subject by Christensen (1983) the effect is to increase the thickness and temperature drop (ΔT) across the boundary layer. This effect will change the parameter (λ) by increasing the Rayleigh number given by equation (3.1). This effect will scale like a change in the average viscosity (μ). If the size of the increase in ΔT is known then equation (3.33) and Figure 3.9 can be used to estimate the effect on λ. The second reason for

neglecting stress dependent rheology is that the stresses depend on the wavelength and Rayleigh number of the convective flow. For the small wavelengths and moderate Rayleigh numbers used in our model calculation the effect of stress should not be large if it is appropriate to use a cut-off stress below which the rheology in stress independent as is done in Fleitout and Yuen (1984).

3.4 Dependence of Observables on the Stefan Parameter (λ)

In the preceding sections a mathematical description of the temperatures in a cooling lid over a variable viscosity convecting region was developed. The dependence of the only parameter needed to describe the system (λ) on average viscosity (which depends on parameter A), the temperature dependence of viscosity (E) and the pressure dependence of viscosity (V*) was shown. Now, the variation of the geophysical observables of lithospheric subsidence, local isostatic geoid height variations, and heat flow will be discussed in terms of their variation with λ.

A word should be said about the assumptions used to relate the simple one dimensional mathematical model presented here to the case of the three-dimensional mantle of the Earth. As has been shown the one-dimensional model matches the horizontally averaged temperature of the two-dimensional numerical calculations quite well. Thus, this theory should be good when there is no other convection than that driven by cooling from above. Even if that flow is three-dimensional in nature this should be true since the same kind of Rayleigh number-Nusselt

number relations (equation 3.6) should hold for a simple three-dimensional flow driven by cooling from above. There are special problems in applying these results to the cooling of the oceanic lithosphere. The main problem is that there is a large scale of flow associated with the motion of the lithospheric plates. This flow should be perpendicular to the flow calculated in the numerical runs considered here. Therefore, these results are applicable to the cooling of the oceanic lithosphere only to the extent that there are no vertical gradients of velocity in the direction of the large scale flow (i.e., out of the page in Figure 2.2). The depth range for which this is a good assumption depends on the form of the large scale flow.

To the extent that the subsidence of the lithosphere is a result of its cooling and not of the cooling of the asthenosphere there is a relationship between λ and subsidence. The cooling of the asthenosphere, or the changes in T_{cr}, should not affect the subsidence because the viscosities in the asthenosphere are so low that significant horizontal gradients of pressure cannot be maintained there. With this assumption in mind the subsidence with time (s(t)) is given by:

$$s(t) = \int_0^{zp} \left[T_m - \left(\frac{T_p}{\text{erf}\lambda}\right) \text{erf}\left(\frac{z}{2(\kappa t)^{1/2}}\right)\right] dz \qquad (3.34)$$

which reduces to

$$s(t) = \frac{2\lambda(\kappa t)^{1/2}\alpha\rho_m}{(\rho_m-\rho_w)} \left\{T_m - Tp\left[\frac{(1-e^{-\lambda^2}}{\lambda(\pi)^{1/2}\text{erf}\lambda}\right]\right\} \qquad (3.35)$$

where ρ_m and ρ_w are the densities of mantle and water, respectively To first order s(t) varies linearly with λ. Figure (3.13) is a plot of non-dimensional subsidence versus λ for equation (3.35). The plot is nearly linear with a slope of about 0.7. Thus a decrease in λ of 10% should cause a decrease in subsidence at a given time by 7%. Therefore we can approximate the dependence of subsidence on physical parameters as $\lambda \alpha T_m(\kappa t)^{1/2}$.

For estimation of "local" isostatic geoid height anomalies $(H(t))$ as a function of time and of λ it will also be assumed that only temperature variations in the conductive lid affect this value. The anomaly is termed local because the primary interest is in offset of geoid height across oceanic fracture zones. These are short wavelength features where the above assumption should be valid. Following the definition of the isostatic geoid height in Haxby ahd Turcotte (1978) the relationship between λ, T_p and H(t) can be written as:

$$H(t) = -\frac{2\pi G}{g}\left\{\int_{-s(t)}^{0} z\,(\rho_m-\rho_w)\,dz + \int_{0}^{2\lambda(\kappa t)^{1/2}} \rho_m \alpha z\left[T_m-\left(\frac{T_p}{\mathrm{erf}\lambda}\right)\mathrm{erf}\left(\frac{z}{2(\kappa t)^{1/2}}\right)\right]dz\right\} \quad (3.36)$$

The integrals can be evaluated to give:

$$H(t) = \frac{-2\pi G}{g}\,(2\lambda^2\alpha\rho m\kappa t)\left\{\frac{\alpha\rho_m}{(\rho_m-\rho_w)}\left[Tm + \frac{T_p(1-e^{-\lambda^2})}{\lambda(\pi)^{1/2}\mathrm{erf}\lambda} - T_p\right]^2 + Tm + T_p\left[\frac{1}{2\lambda^2} - 1 - \frac{e^{-\lambda^2}}{\lambda(\pi)^{1/2}\mathrm{erf}\lambda}\right]\right\} \quad (3.37)$$

The local isostatic geoid height is seen to vary nearly linearly with λ^2 and linearly with time (t). Figure 3.14 is a plot of H(t) given by equation (3.37) versus λ^2. For a change in λ^2 of 20% the change in $\Delta N(t)$ is about 16% for the range of values of λ seen in the numerical calculations. Thus, H(t) is approximately proportional to $\lambda^2 \alpha T_m \kappa t$.

The relationship between the heat flux at the surface of the lithosphere ($Q_s(t)$) and the physical parameters of the cooling system is easy to derive for the time period when the equations of the Stefan problem apply. Differentiating equation (3.24) and setting z = 0. gives:

$$Q_s(t) = T_m \left(\frac{\mathrm{erf}(\lambda_c)}{\mathrm{erf}(\lambda)} \right) \left(\frac{K \rho c_p}{\pi t} \right)^{1/2} \qquad (3.38)$$

where λ_c is the value of λ for the purely conductive case and we have used the fact that $T_m = T_p/\mathrm{erf}(\lambda_c)$. Since erf($\lambda$) is nearly linearly related to λ for the range of variations in the Stefan parameter considered here we may state that $Q_s(t)$ is approximately proportional to $(T_m/\lambda)(K \rho c_p/t)^{1/2}$.

3.5 Conclusions

In this chapter we have given derivations which give some theoretical understanding to the process of the cooling of a variable viscosity fluid. Such a cooling process, where the lower viscosity portions of the fluid is driven to convect by the cooling from above, may occur in the Earth. The cooling fluid is seperated into two regions which behave differently: the conductive lid where heat is transported completely by conduction and a convecting region where the dominant mode of heat transfer

is by convection. The two regions are coupled because there must be a balance between the heat flux out of the convecting region and that which is conductively transported at the base of the lid. The rate of convective transport of heat controls the rate of thickening of the lid as the system cools. Because the rate of reduction in the convective heat transfer with time behaves in a simple way, the conductive lid thickness and its temperature structure can behave in a simple regular fashion in time. When this occurs we say that there is a "transient equilibrium" between the lid and the convecting region

A simple mathmatical description was given for the regular features seen in numerical experiments on cooling fluids with different viscosity parameters including the terms in a viscosity relation which control the temperature and pressure dependence of viscosity. Several approximations were used to show that simple equations can be used to describe the lid temperatures with time for this problem. Only one parameter was needed to describe the cooling of the lid and it was explicitly shown how to relate the viscosity and other parameters of the convecting system to that parameter (λ). The predictions of the theory developed here were shown to be in good agreement with the numerical results. Finally, the relationship between several geophysical observables which depend on the thermal structure of the lithosphere and the parameter (λ) is derived. In chapter 2 the data on subsidence of the oceans and the offset of geoid anomalies at fracture zones is discussed in relation to the possible values of (λ).

The parameterization derived here allows one to estimate the effect of changes in model parameters on the geophysically

relavent results of the models without doing costly computer models. The results of this chapter can be used to relate the values of one parameter (λ) to estimates of viscosity or of viscosity variations between different areas. This is then used to describe the change in lithospheric subsidence, isostatic geoid anomalies and heat flow produced by small-scale convection.

Case #	E [kcal/mole]	V* [cm³/mole]	ΔZ [km]	λ/λ_c	λ	Q_{cmax} t_o=64	c_2c_3/Q_{cmax} [my^{-1}]	$.5c_4\sqrt{64}$ [x 10^3 my$^{-1/2}$]	dlnQc/dt graph x 10^3	dlnQc/dt theory x 10^3	dlnQc/dt percent difference
12	110	7.5	300	.69	.80	1.85	2.46×10^{-3}	3.12×10^{-3}	-7.90	-7.67	-2.9
14	110	7.5	300	.80	.93	1.12	2.46	3.63	-6.62	-6.39	-3.5
15	110	7.5	300	.75	.87	1.35	2.46	3.44	-6.10	-6.76	+10.8
17	102	0	300	.64	.74	2.11	2.28	0	-6.99	-4.81	-31.2
18	80	7.5	300	.67	.78	1.95	1.93	3.04	-6.21	-6.80	+9.6
19	110	7.5	300	.68	.79						
20	110	7.5	300	.70	.81	1.85	2.46	3.16	-8.48	-7.71	-9.1
21	102	0	300								
22	110	7.5	300	.69	.80	1.95	2.46	3.12			
23	110	7.5	200	.72	.84	1.25	3.68	3.28	-12.1	-7.88	-34.3

Table 3.1 The first four columns give the model case numbers and the parameters which define them. Next, the ratio of the parameter λ defined by equation 3.23 for the model case and the same parameter for the conductive case which is 1.16 for the way we define it. Q_{cmax} is the value of the maximum horizontally averaged heat flux at 64 m.y. model time. The values of c_2, c_3 and c_4 are defined in the text and are calculated useing the model parameters given in the table. The combinations of these parameters are those that go into equation 3.32 and are used to get the predicted value of dln(Qc)/dt. The graphical value of dln(Qc)/dt is gotten from figure 3.12.

Table 3.2

TEST 12

TIME (m.y.)	Q_{cmax}	Ra	ℓ (km)	Δz_b (km)	ΔT_b (°K)	T_L (°K)	$\mu(z_b)$ (Pa-s)	$\overline{\mu}$ (Pa-s)	$\frac{\overline{\mu}}{\mu(z_b)}$
10.0	2.32	3.30×10^5	169.3	19.1	88.2	675.0	0.314×10^{18}	0.129×10^{19}	4.12
25.9	2.20	2.38×10^5	191.5	20.9	106.1	657.1	0.593×10^{18}	0.313×10^{19}	5.29
35.9	2.17	1.71×10^5	190.9	23.5	109.5	651.6	0.782×10^{18}	0.445×10^{19}	5.69
63.8	1.74	4.91×10^4	170.8	24.5	98.0	644.7	0.183×10^{19}	0.995×10^{19}	5.44
83.8	1.48	2.37×10^4	160.5	28.0	99.7	646.0	0.324×10^{19}	0.174×10^{20}	5.36
103.9	1.27	1.20×10^4	154.6	29.4	91.5	647.5	0.547×10^{19}	0.281×10^{20}	5.15

Table 3.2 -3.11 Calculated values of model parameters defined in the text at given times after the start of the numerical runs (TIME in m.y.). The maximum horizontally averagerd advective heat flux is Q_{cmax}; the Rayleigh number is Ra; the convective length scale is ℓ; the thickness of the boundary layer is (Δz_b); the temperature difference acros the boundary layer is ΔT_b; the average temperature in the condictive lid is T_L; the horizontally averaged viscosity at the base of the boundary layer is $\mu(z_b)$; the effective average viscosity is ($\overline{\mu}$).

Table 3.3

TEST 14

TIME (m.y.)	Q_{cmax}	Ra	ℓ (km)	Δz_b (km)	ΔT_b (°K)	T_L (°K)	$\mu(z_b)$ (Pa-s)	$\bar{\mu}$ (Pa-s)	$\frac{\bar{\mu}}{\mu(z_b)}$
15.0	1.24	0.619×10^{4}	73.6	28.4	77.8	694.6	0.206×10^{19}	0.500×10^{19}	2.42
25.0	1.16	0.154×10^{5}	129.7	23.4	71.1	684.3	0.266×10^{19}	0.101×10^{20}	3.78
35.0	1.25	0.126×10^{5}	139.0	22.3	71.2	675.5	0.369×10^{19}	0.151×10^{20}	4.10
45.0	1.24	0.124×10^{5}	147.8	26.3	84.1	669.0	0.504×10^{19}	0.218×10^{20}	4.33
55.0	1.16	0.106×10^{5}	152.1	29.4	88.8	665.6	0.668×10^{19}	0.295×10^{20}	4.42
65.0	1.10	0.828×10^{4}	153.0	30.5	88.3	663.7	0.869×10^{19}	0.382×10^{20}	4.39
75.1	1.04	0.664×10^{4}	152.2	33.1	89.5	662.8	0.112×10^{20}	0.476×10^{20}	4.26
85.0	0.98	0.516×10^{4}	151.2	33.7	86.4	662.5	0.141×10^{20}	0.579×10^{20}	4.11
95.1	0.90	0.403×10^{4}	149.0	34.4	84.6	662.8	0.177×10^{20}	0.694×10^{20}	3.92
105.0	0.84	0.311×10^{4}	145.7	35.1	82.4	662.5	0.220×10^{20}	0.819×10^{20}	3.72

Table 3.4

TEST 15

TIME (m.y.)	Q_{cmax}	Ra	ℓ (km)	Δz_b (km)	ΔT_b (°K)	T_L (°K)	$\mu(z_b)$ (Pa-s)	$\bar{\mu}$ (Pa-s)	$\frac{\bar{\mu}}{\mu(z_b)}$
2.0	0.07	0.584×10^{3}	17.0	10.0	62.7	701.9	0.310×10^{18}	0.523×10^{18}	1.68
4.0	7.43	0.576×10^{5}	69.3	24.1	101.7	679.5	0.298×10^{18}	0.586×10^{18}	1.97
5.0	4.84	0.793×10^{6}	85.7	149.9	993.7	671.8	0.160×10^{19}	0.788×10^{18}	0.49
10.0	2.05	0.185×10^{6}	135.7	16.7	89.2	668.6	0.323×10^{18}	0.121×10^{19}	3.74
15.0	2.24	0.277×10^{6}	169.3	21.1	98.4	665.5	0.415×10^{18}	0.172×10^{19}	4.15
17.0	2.00	0.482×10^{6}	208.2	23.6	109.8	665.1	0.452×10^{18}	0.206×10^{19}	4.55
20.0	6.08	0.726×10^{6}	166.4	157.9	465.3	664.7	0.375×10^{19}	0.295×10^{19}	0.79
23.0	2.90	0.334×10^{6}	206.0	32.3	100.5	661.5	0.494×10^{18}	0.263×10^{19}	5.32
25.1	1.94	0.170×10^{6}	177.7	18.1	90.2	660.4	0.569×10^{18}	0.297×10^{19}	5.23
30.1	2.85	0.883×10^{5}	143.2	23.5	89.0	655.8	0.667×10^{18}	0.296×10^{19}	4.44
35.1	1.49	0.209×10^{6}	201.3	18.1	97.2	652.9	0.999×10^{18}	0.378×10^{19}	3.79
40.1	2.02	0.228×10^{6}	200.1	33.8	133.6	655.8	0.936×10^{18}	0.469×10^{19}	5.01
5.01	1.56	0.154×10^{6}	186.6	36.0	141.7	656.1	0.123×10^{19}	0.598×10^{19}	4.87
60.1	1.30	0.100×10^{6}	183.9	31.1	125.7	656.4	0.168×10^{19}	0.778×10^{19}	4.63
70.1	1.27	0.653×10^{5}	173.7	35.9	128.4	656.9	0.216×10^{19}	0.103×10^{20}	4.78
80.1	1.20	0.484×10^{5}	173.4	35.6	122.6	656.8	0.272×10^{19}	0.132×10^{20}	4.86
90.1	1.16	0.316×10^{5}	166.7	36.7	114.9	656.2	0.338×10^{19}	0.168×10^{20}	4.98
100.1	1.11	0.235×10^{5}	166.4	37.0	107.4	655.9	0.413×10^{19}	0.211×10^{20}	5.10

Table 3.5

TEST 17

TIME (m.y.)	Q_{cmax}	Ra	ℓ (km)	Δz_b (km)	ΔT_b (°K)	T_L (°K)	$\mu(z_b)$ (Pa-s)	$\bar{\mu}$ (Pa-s)	$\frac{\bar{\mu}}{\mu(z_b)}$
15.0	1.36	0.890×10^{6}	199.2	22.2	74.0	682.5	0.671×10^{18}	0.657×10^{18}	0.98
25.0	1.38	0.152×10^{7}	191.7	37.5	158.0	672.4	0.716×10^{18}	0.734×10^{18}	1.02
35.0	2.13	0.304×10^{6}	149.9	17.4	82.2	652.4	0.104×10^{19}	0.910×10^{18}	0.87
45.1	2.22	0.423×10^{6}	190.1	14.2	64.9	644.1	0.136×10^{19}	0.105×10^{19}	0.77
55.0	2.13	0.318×10^{6}	177.4	15.6	71.6	638.5	0.168×10^{19}	0.126×10^{19}	0.75
65.1	2.05	0.338×10^{6}	178.8	19.8	89.2	635.9	0.196×10^{19}	0.151×10^{19}	0.77
75.1	1.90	0.284×10^{6}	175.8	21.9	93.4	635.1	0.229×10^{19}	0.178×10^{19}	0.78
85.1	1.76	0.218×10^{6}	171.7	23.2	90.7	635.7	0.265×10^{19}	0.210×10^{19}	0.79
95.1	1.63	0.176×10^{6}	169.9	24.0	88.1	637.3	0.305×10^{19}	0.245×10^{19}	0.80

Table 3.6

TEST 18

TIME (m.y.)	Q_{cmax}	Ra	ℓ (km)	Δz_b (km)	ΔT_b (°K)	T_L (°K)	$\mu(z_b)$ (Pa-s)	$\bar{\mu}$ (Pa-s)	$\frac{\bar{\mu}}{\mu(z_b)}$
10.0	1.90	0.438×10^{5}	128.7	22.7	100.0	678.5	0.133×10^{19}	0.486×10^{19}	3.65
20.0	2.25	0.326×10^{5}	138.8	21.8	110.3	666.5	0.197×10^{19}	0.906×10^{19}	4.60
30.0	2.11	0.302×10^{5}	152.8	22.7	116.9	656.7	0.269×10^{19}	0.138×10^{20}	5.12
40.0	2.10	0.233×10^{5}	155.0	24.4	119.2	652.4	0.361×10^{19}	0.190×10^{20}	5.27
50.1	2.02	0.174×10^{5}	158.1	25.0	114.9	649.0	0.480×10^{19}	0.260×10^{20}	5.42
60.1	1.93	0.134×10^{5}	159.7	25.8	112.7	646.1	0.632×10^{19}	0.342×10^{20}	5.42
70.1	1.82	0.112×10^{5}	160.5	28.1	118.8	644.5	0.816×10^{19}	0.349×10^{20}	5.37
80.1	1.72	0.890×10^{4}	159.6	29.7	119.8	644.3	0.104×10^{20}	0.547×10^{20}	5.25
90.1	1.60	0.690×10^{4}	157.3	31.0	118.7	644.7	0.133×10^{20}	0.669×10^{20}	5.05
100.1	1.48	0.527×10^{4}	153.6	32.2	117.1	645.8	0.168×10^{20}	0.804×10^{20}	4.80

Table 3.7

TEST 19

TIME (m.y.)	Q_{cmax}	Ra	ℓ (km)	Δz_b (km)	ΔT_b (°K)	T_L (°K)	$\mu(z_b)$ (Pa-s)	$\bar{\mu}$ (Pa-s)	$\frac{\bar{\mu}}{\mu(z_b)}$
5.0	3.18	0.462×10^{6}	164.2	35.6	112.2	683.4	0.332×10^{18}	0.107×10^{19}	3.23
10.0	1.71	0.339×10^{6}	171.1	19.0	91.2	673.6	0.331×10^{18}	0.135×10^{19}	4.07
20.0	1.94	0.217×10^{6}	173.6	19.3	77.1	667.3	0.468×10^{18}	0.186×10^{19}	3.97
30.0	1.84	0.140×10^{6}	163.7	20.5	81.1	661.6	0.644×10^{18}	0.253×10^{19}	3.93
40.0	1.94	0.848×10^{5}	158.0	18.9	77.0	655.6	0.880×10^{18}	0.358×10^{19}	4.07
50.1	1.90	0.799×10^{5}	162.1	24.1	97.7	649.8	0.122×10^{19}	0.521×10^{19}	4.26
70.1	1.76	0.592×10^{5}	175.9	29.8	120.0	644.0	0.230×10^{19}	0.110×10^{20}	4.80
80.1	1.66	0.430×10^{5}	177.7	30.5	114.3	643.7	0.299×10^{19}	0.149×10^{20}	4.99
90.1	1.55	0.300×10^{5}	174.8	30.7	107.2	643.8	0.378×10^{19}	0.191×10^{20}	5.04
100.1	1.41	0.199×10^{5}	167.1	31.0	101.6	644.6	0.475×10^{19}	0.238×10^{20}	5.01

Table 3.8

TEST 20

TIME (m.y.)	Q_{cmax}	Ra	ℓ (km)	Δz_b (km)	ΔT_b (°K)	T_L (°K)	$\mu(z_b)$ (Pa-s)	$\bar{\mu}$ (Pa-s)	$\frac{\bar{\mu}}{\mu(z_b)}$
7.1	7.33	0.513×10^{5}	59.0	53.8	144.9	697.4	0.402×10^{18}	0.580×10^{18}	1.44
10.1	2.04	0.252×10^{6}	142.4	16.5	73.0	683.0	0.238×10^{18}	0.834×10^{18}	3.51
14.2	2.24	0.323×10^{6}	163.6	17.9	85.8	674.7	0.293×10^{18}	0.116×10^{19}	3.97
15.1	2.21	0.329×10^{6}	166.4	18.1	88.8	672.5	0.305×10^{18}	0.124×10^{19}	4.08
25.1	2.34	0.270×10^{6}	179.5	20.4	105.3	660.6	0.461×10^{18}	0.226×10^{19}	4.89
35.1	2.24	0.219×10^{6}	189.7	21.8	110.4	653.8	0.651×10^{18}	0.344×10^{19}	5.28
45.1	2.14	0.151×10^{6}	189.4	22.8	107.2	649.4	0.867×10^{18}	0.481×10^{19}	5.55
61.5	1.88	0.701×10^{5}	179.0	22.7	97.2	645.9	0.143×10^{19}	0.795×10^{19}	5.57
71.5	1.71	0.459×10^{5}	170.6	24.2	96.4	645.8	0.189×10^{19}	0.104×10^{20}	5.52
81.5	1.57	0.308×10^{5}	163.8	25.5	94.2	645.9	0.247×10^{19}	0.134×10^{20}	5.43
91.5	1.45	0.222×10^{5}	158.7	27.3	95.2	646.7	0.322×10^{19}	0.171×10^{20}	5.32
101.5	1.33	0.150×10^{5}	153.7	27.4	89.6	647.5	0.421×10^{19}	0.217×10^{20}	5.15

Table 3.9

TEST 21

TIME (m.y.)	Q_{cmax}	Ra	ℓ (km)	Δz_b (km)	ΔT_b (°K)	T_L (°K)	$\mu(z_b)$ (Pa-s)	$\bar{\mu}$ (Pa-s)	$\frac{\bar{\mu}}{\mu(z_b)}$
6.0	0.21	0.206×10^{8}	263.9	158.2	675.0	585.0	0.551×10^{18}	0.603×10^{18}	1.09
11.8	1.18	0.551×10^{6}	169.8	20.7	69.3	692.6	0.605×10^{18}	0.616×10^{18}	1.02
16.4	1.31	0.119×10^{7}	226.7	19.9	67.2	686.3	0.648×10^{18}	0.655×10^{18}	1.01
17.8	1.46	0.119×10^{7}	224.0	22.9	70.2	684.6	0.647×10^{18}	0.661×10^{18}	1.02
31.2	5.45	0.526×10^{5}	77.2	37.6	105.2	668.6	0.821×10^{18}	0.921×10^{18}	1.12
41.3	2.73	0.525×10^{7}	172.7	238.0	917.7	587.2	0.842×10^{18}	0.900×10^{18}	1.07

Table 3.10

TEST 22

TIME (m.y.)	Q_{cmax}	Ra	ℓ (km)	Δz_b (km)	ΔT_b (°K)	T_L (°K)	$\mu(z_b)$ (Pa-s)	$\bar{\mu}$ (Pa-s)	$\frac{\bar{\mu}}{\mu(z_b)}$
20.0	2.77	0.125×10^{6}	133.4	14.5	82.7	656.1	0.444×10^{18}	0.157×10^{19}	3.54
30.0	2.57	0.913×10^{5}	141.6	15.6	83.8	650.1	0.717×10^{18}	0.260×10^{19}	3.63
40.0	2.31	0.683×10^{5}	148.2	16.3	82.1	647.0	0.110×10^{19}	0.391×10^{19}	3.55
50.0	2.15	0.469×10^{5}	147.0	17.6	81.6	645.8	0.157×10^{19}	0.553×10^{19}	3.52
60.0	2.00	0.317×10^{5}	144.4	18.3	79.2	645.0	0.223×10^{19}	0.754×10^{19}	3.38
70.0	1.83	0.235×10^{5}	141.1	20.4	84.2	644.1	0.316×10^{19}	0.101×10^{20}	3.19
80.0	1.64	0.171×10^{5}	137.2	22.7	86.8	644.8	0.437×10^{19}	0.131×10^{20}	3.00
90.0	1.45	0.119×10^{5}	132.6	24.1	84.9	646.4	0.599×10^{19}	0.166×10^{20}	2.77
100.0	1.26	0.812×10^{4}	127.4	25.3	81.2	648.7	0.816×10^{19}	0.207×10^{20}	2.53
110.0	1.08	0.559×10^{4}	121.9	26.4	78.1	651.3	0.110×10^{20}	0.253×10^{20}	2.30
120.0	0.91	0.390×10^{4}	116.9	27.7	75.5	654.3	0.147×10^{20}	0.306×10^{20}	2.08

Table 3.11

TEST 23

TIME (m.y.)	Q_{cmax}	Ra	ℓ (km)	Δz_b (km)	ΔT_b (°K)	T_L (°K)	$\mu(z_b)$ (Pa-s)	$\bar{\mu}$ (Pa-s)	$\frac{\bar{\mu}}{\mu(z_b)}$
15.0	1.77	0.188×10^{6}	143.0	15.7	76.0	669.1	0.322×10^{18}	0.118×10^{19}	3.66
34.6	1.47	0.620×10^{5}	129.1	17.8	86.0	654.8	0.816×10^{18}	0.299×10^{19}	3.66
44.7	1.38	0.377×10^{5}	127.4	18.4	79.4	652.5	0.118×10^{18}	0.435×10^{19}	3.67
54.7	1.33	0.211×10^{5}	125.1	16.2	68.2	649.7	0.180×10^{19}	0.633×10^{19}	3.51
64.7	1.20	0.163×10^{5}	122.2	20.6	81.9	647.5	0.261×10^{19}	0.917×10^{19}	3.52
74.7	1.06	0.106×10^{5}	116.9	23.2	85.0	647.6	0.376×10^{19}	0.128×10^{20}	3.41
84.7	0.93	0.708×10^{4}	111.8	26.3	87.9	648.8	0.525×10^{19}	0.174×10^{20}	3.31
94.7	0.83	0.471×10^{4}	107.7	27.6	86.6	651.0	0.736×10^{19}	0.230×10^{20}	3.12
104.7	0.73	0.297×10^{4}	103.6	27.7	79.1	652.8	0.102×10^{20}	0.297×10^{20}	2.91
114.7	0.64	0.204×10^{4}	100.0	28.6	77.1	654.7	0.139×10^{20}	0.377×10^{20}	2.72
124.7	0.56	0.145×10^{4}	96.5	31.1	77.1	657.6	0.187×10^{20}	0.471×10^{20}	2.51

FIGURE CAPTIONS

Figure 3.1 An example of the variation of the convective heat flux, (Q_c) defined by equation (3.2), as it varies with depth is shown for a time 20 m.y. into the calculation for Test 20 along with the horizontally averaged temperature and the difference betwen that temperature (T_h) and the temperature profile resulting from purely conductive cooling (T_d).

Figure 3.2 This is an illustration of the method of estimation of the boundary layer thickness (Δz) and the position of the top (z_t) and bottom (z_b) of the boundary layer form the variation of the convective heat flux (Q_c). Since the Q_c is nearly a linear function of depth in the range where it chances most rapidly a straight line can be fit through that region. The two points which are somewhat arbritrarily chosen to define that line are the points where Q_c equals 20% and 80% of Q_{cmax}. Varying those arbitrary values does not greatly alter the resulting estimate of the boundary layer position, but a consistent way of doing the estimate must be chosen. The depth at which this line has a value of zero for Q_c is defined as z_t and where it equals Q_{cmax} is the bottom (z_b).

Figure 3.3 A plot of log(Nu) versus log(Ra) where the nusselt number (Nu) is given by equation 3.5 and the Rayleigh number (Ra) is given by equation 3.1 and other definitions in the text is shown for several cases. The values of Ra

and Nu are listed for all cases in tables 2-11. All of the cases can be fit with straight lines with slopes, which equals b in equation 3.6, between about 0.2 and 0.3. The offset of the points for Test 18 relative to the other cases indicate that Nu and Ra may not be perfectly defined for all different possible viscosity parameters, but given the large variation in parameters used in the calculations the correspondence of the results is remarkable.

Figure 3.4 Plots of the log of the horizontal averages of the viscosity (μ_h) and the second invariant of the strain rate tensor ($\dot{e}^2{}_h$) are shown against depth. Two cases are illustrated. For case 20, where V* = 7.5 cm^3/mole, the minimum in viscosity is at the same depth as the maximum in the strain rate. But, for case 17, where V* = 0.0, both the viscosity and the strain rate were nearly constant with depth.

Figure 3.5 The time variation of the ratio of the average viscosity, ($\bar{\mu}$) as defined by equation 3.4 and the horizontally averaged viscosity at the base of the boundary layer ($\mu(z_b)$) is shown for the two cases illustrated in figure 3.8. Over the time of the calculations the ratio is nearly constant.

Figure 3.6 The solid line is a plot of Nu/A_1 versus temperature (T) given by equation 3.20. Here E' = 100 kcal/mole, b = 0.25 and To = 1523 °K. There is a change in T of 100 °K for this plot. The dashed line is the best

fitting straight line approximation to this relation over the same range and is given by equation (3.22).

Figure 3.7 The variation of Nu with changing temperature of the convecting region (T_{cr}) is shown for two of the numerical cases considered here by plotting Nu against (T_{cr}-T_o). The trends are clearly linear.

Figure 3.8 This shows the dependence of $Nu(t)/Nu(t_o)$ for equation 3.14 and the linear approximation to that relation given by equation 3.16 on $(t)^{-1/2}$. The two plots were made to coincide at time (t = 50 m.y.), which correspondes to $(t)^{-1/2}$ = 0.141. The time range for the plots is 50 m.y.

Figure 3.9. The variation of ($\lambda/\lambda c$) is plotted versus $(\mu/\mu_o)' = \frac{\mu}{\mu_o}\ \frac{1}{Ra_o}\ \left[\frac{\ell\ T_p}{a\Delta T(\pi\kappa t)^{1/2}}\right]^{1/b}$ for equation 3.22. A decrease in μ/μ_o by a factor of 10 leads to decrease in λ/λ_c of about 0.15 in the center range of the values plotted.

Figure 3.10 The variation of T_s, the average lid temperature for the similarity solution given by equation (3.27), versus the parameter (λ) is shown. The relationship is nearly linear.

Figure 3.11 For two cases the variations of the Q_{cmax} is plotted versus $(\text{time})^{-1/2}$. The relation is linear in the same time interval when T_L is relatively constant

(see Figure 2.5). Test 20 has an average viscosity which is a factor of 5 lower than case 14.

Figure 3.12 The natural log of Qcmax is shown plotted against time for several of the numerical calculations of chapter 2. Table 3.1 gives values of the slope of the plots which can be related to the model parameters by equation 3.32. Part (a) shows this plot for cases 12,15,19,22 and 23 while (b) shows cases 14,17,18 and 20.

Figure 3.13 The plots show subsidence variation with $(\lambda/\lambda c)$ for two values of λ_c. S'(t) is defined as $S(t)(\rho_m-\rho_w)/2(\kappa t)^{1/2}\alpha\rho_m$, where S(t) is given by equation 3.35.

Figure 3.14 The variation of the local isostatic geoid anomaly with $(\lambda/\lambda_c)^2$ is shown. H'(t) is defined as $H(t)g/2\pi G\alpha\rho_m\kappa t$ where H(t) is given by equation 3.37.

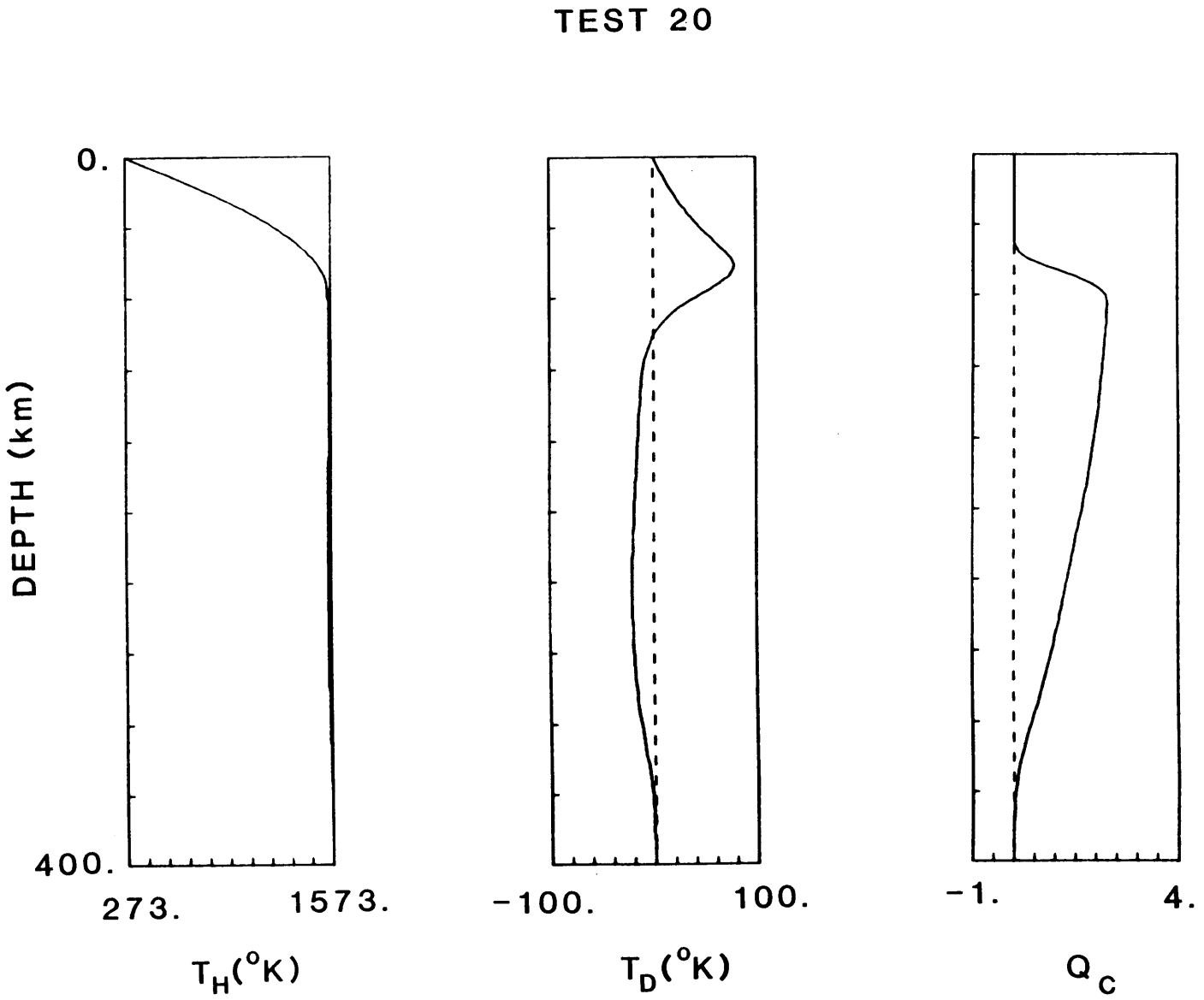

Figure 3.1

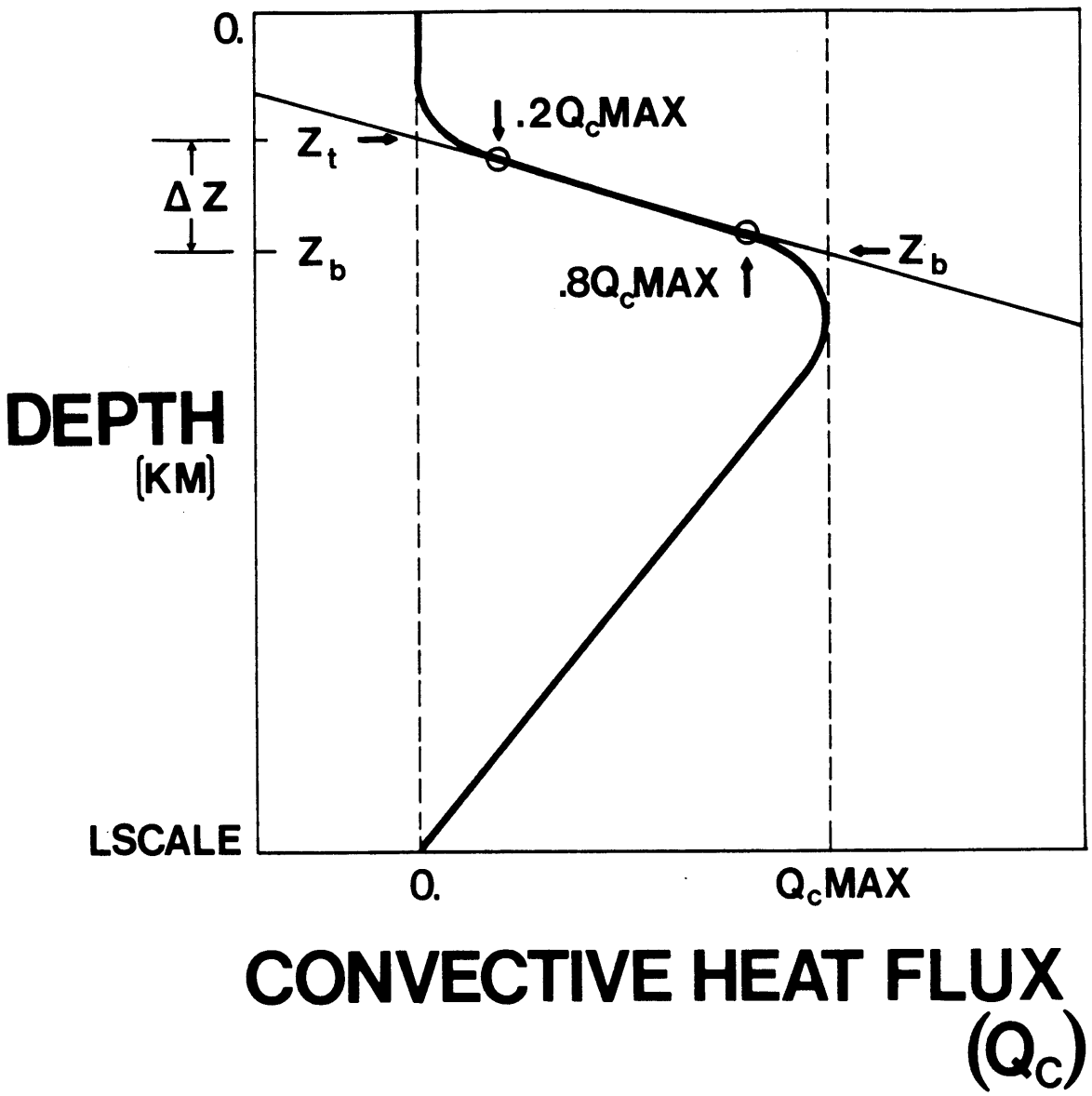
0.
.2Q$_c$MAX
Z$_t$
ΔZ
Z$_b$
.8Q$_c$MAX
Z$_b$
DEPTH
(KM)
LSCALE
0.
Q$_c$MAX
CONVECTIVE HEAT FLUX
(Q$_C$)

Figure 3.2

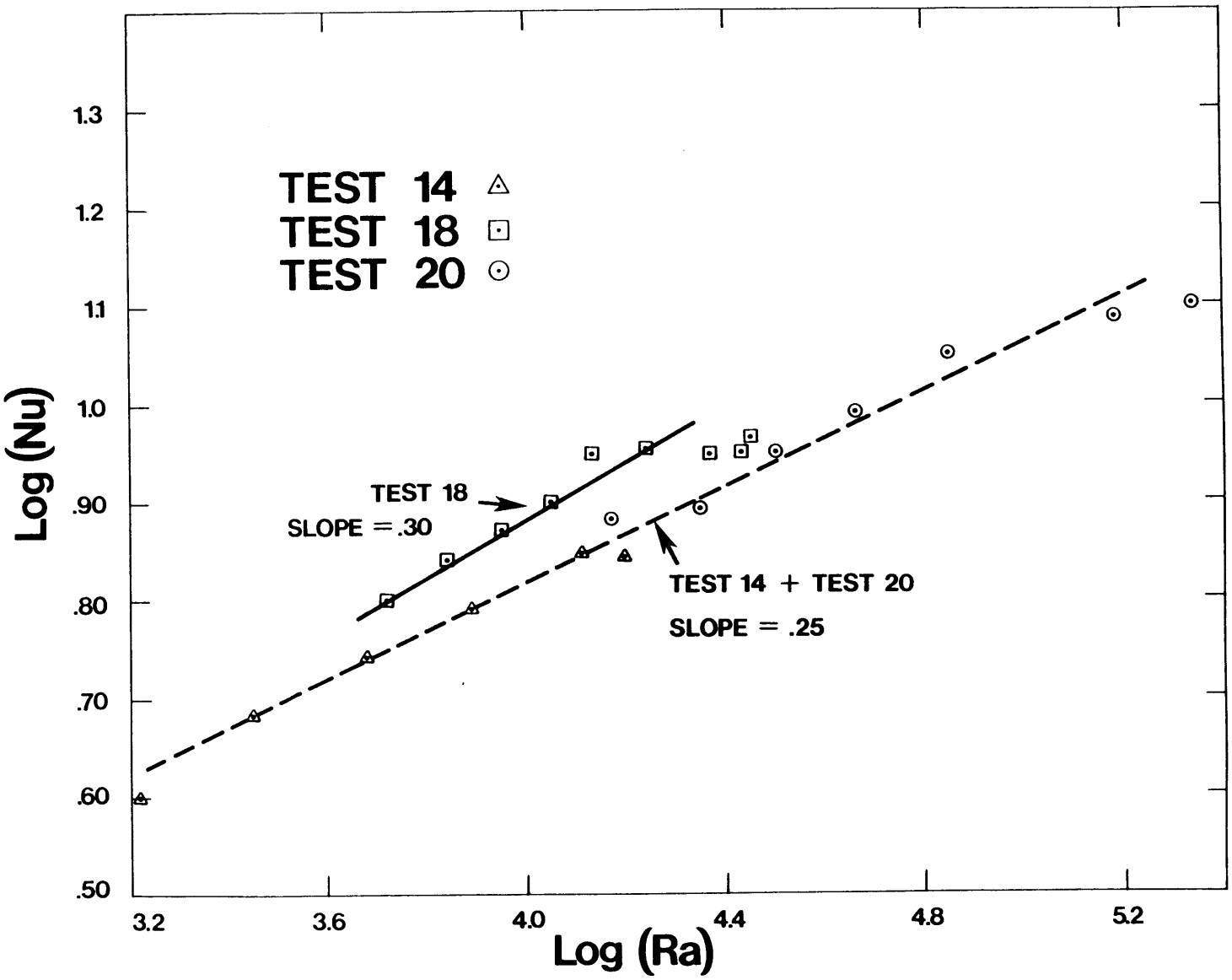
TEST 14
TEST 18
TEST 20
TEST 18
SLOPE = .30
TEST 14 + TEST 20
SLOPE = .25
Log (Nu)
Log (Ra)
1.3
1.2
1.1
1.0
.90
.80
.70
.60
.50
3.2
3.6
4.0
4.4
4.8
5.2

Figure 3.3

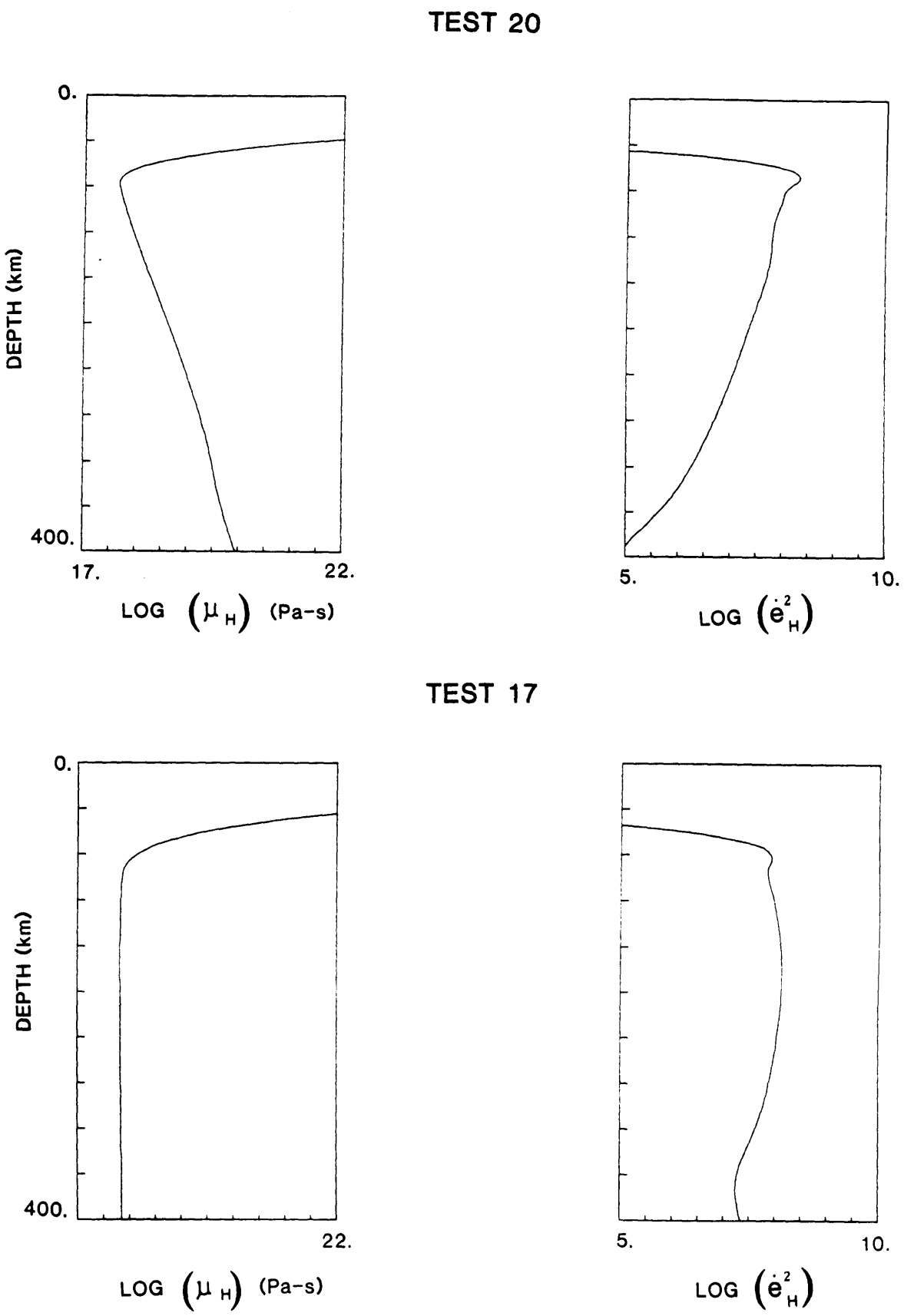
TEST 20
0.
400.
DEPTH (km)
17.
22.
LOG (μ_H) (Pa-s)
5.
10.
LOG $(\dot{e}^2_H)$
TEST 17
0.
400.
DEPTH (km)
22.
LOG (μ_H) (Pa-s)
5.
10.
LOG $(\dot{e}^2_H)$

Figure 3.4

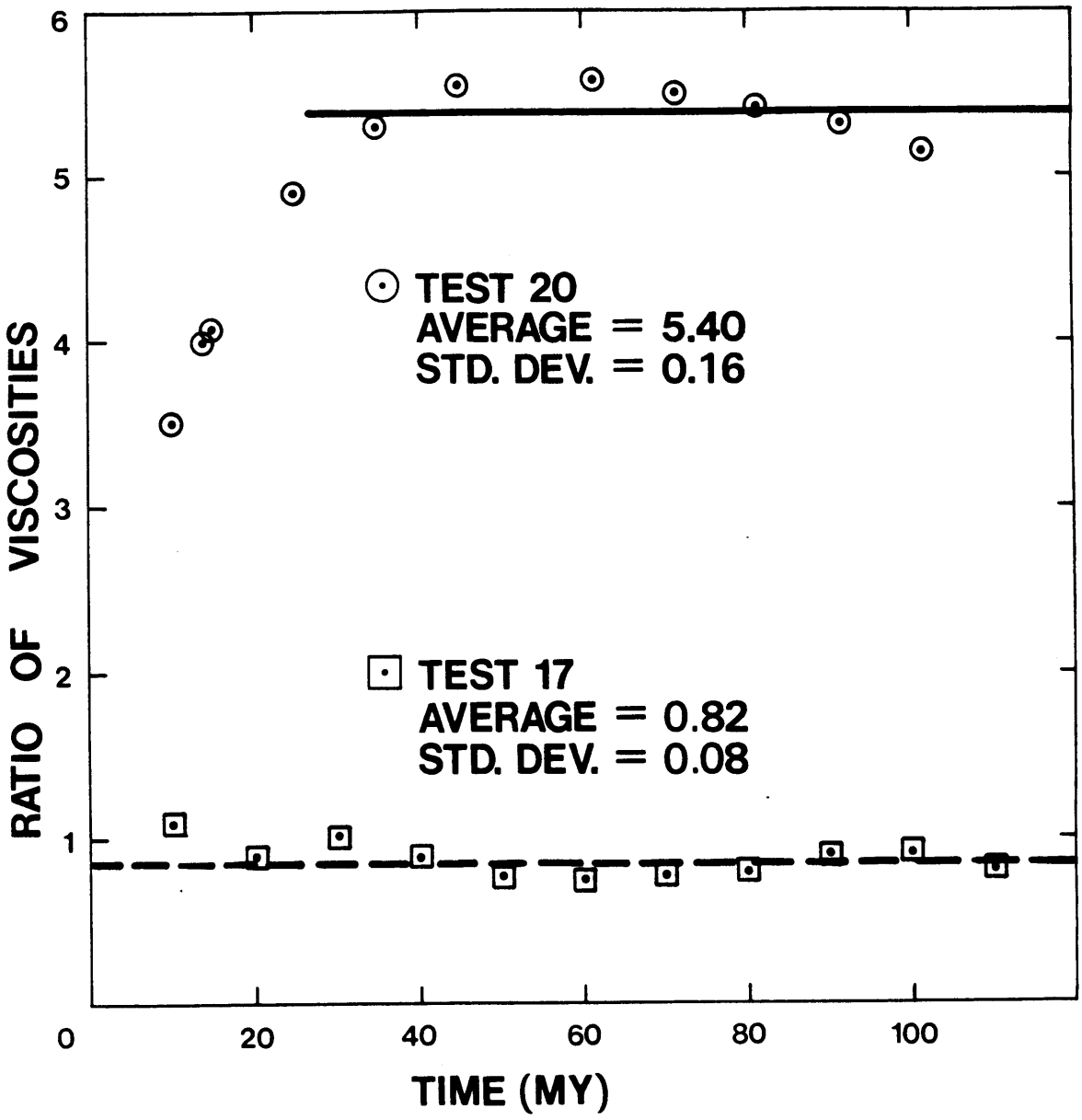
RATIO OF VISCOSITIES
TIME (MY)
TEST 20
AVERAGE = 5.40
STD. DEV. = 0.16
TEST 17
AVERAGE = 0.82
STD. DEV. = 0.08
0
1
2
3
4
5
6
20
40
60
80
100

Figure 3.5

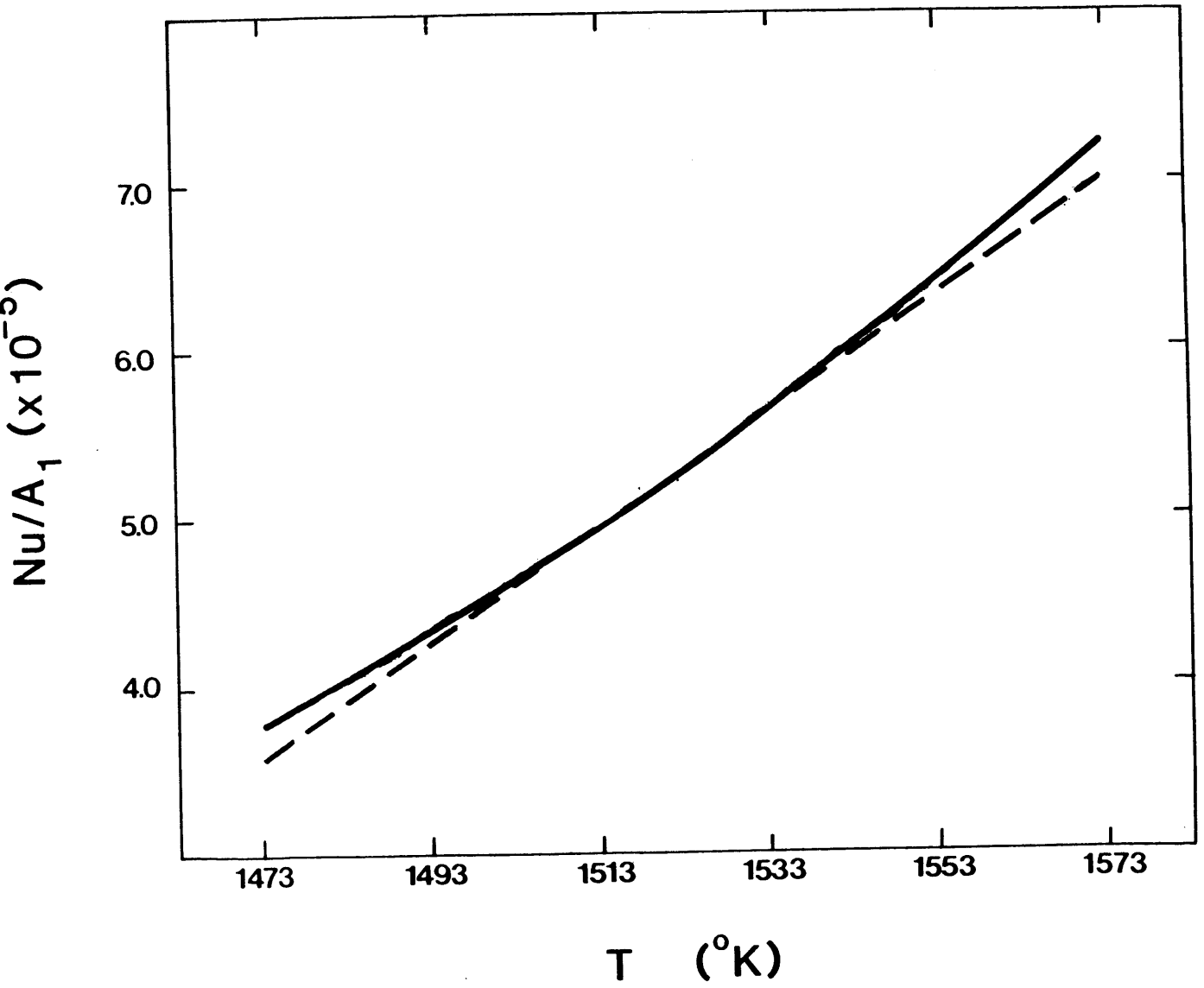

Figure 3.6

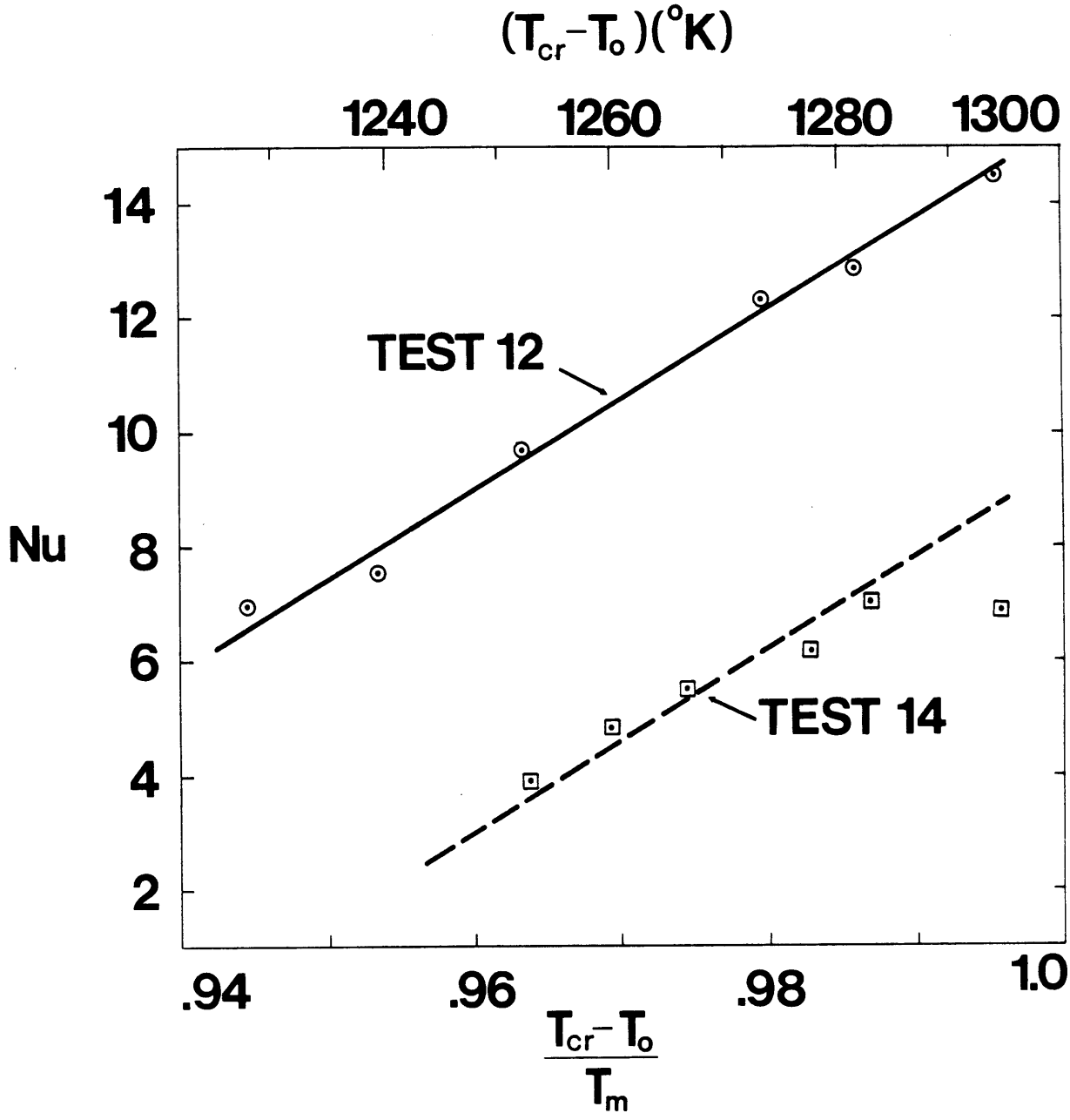
$(T_{cr}-T_o)(^oK)$
1240
1260
1280
1300
14
12
10
8
6
4
2
Nu
TEST 12
TEST 14
.94
.96
.98
1.0
$\frac{T_{cr}-T_o}{T_m}$

Figure 3.7

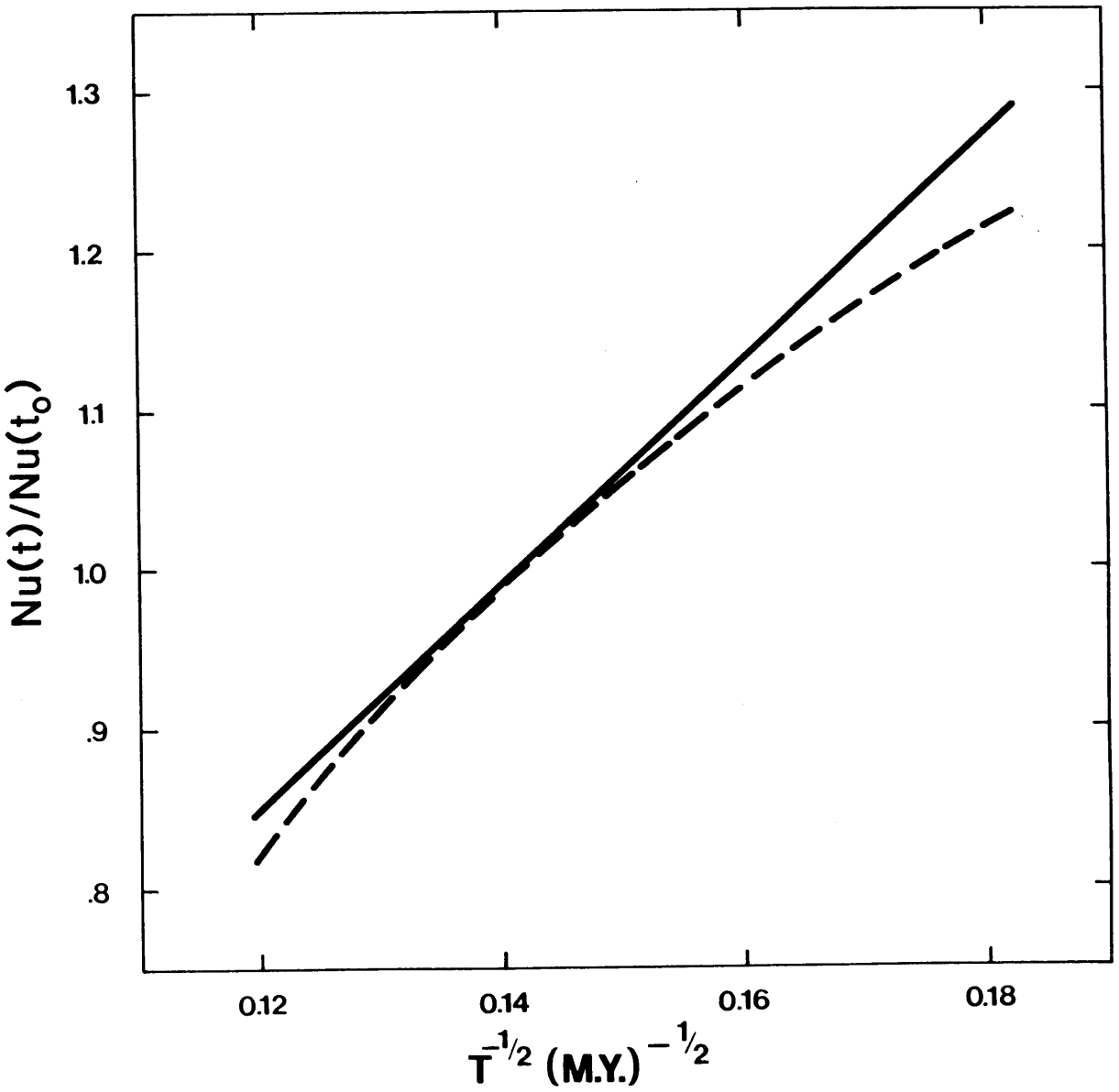

Figure 3.8

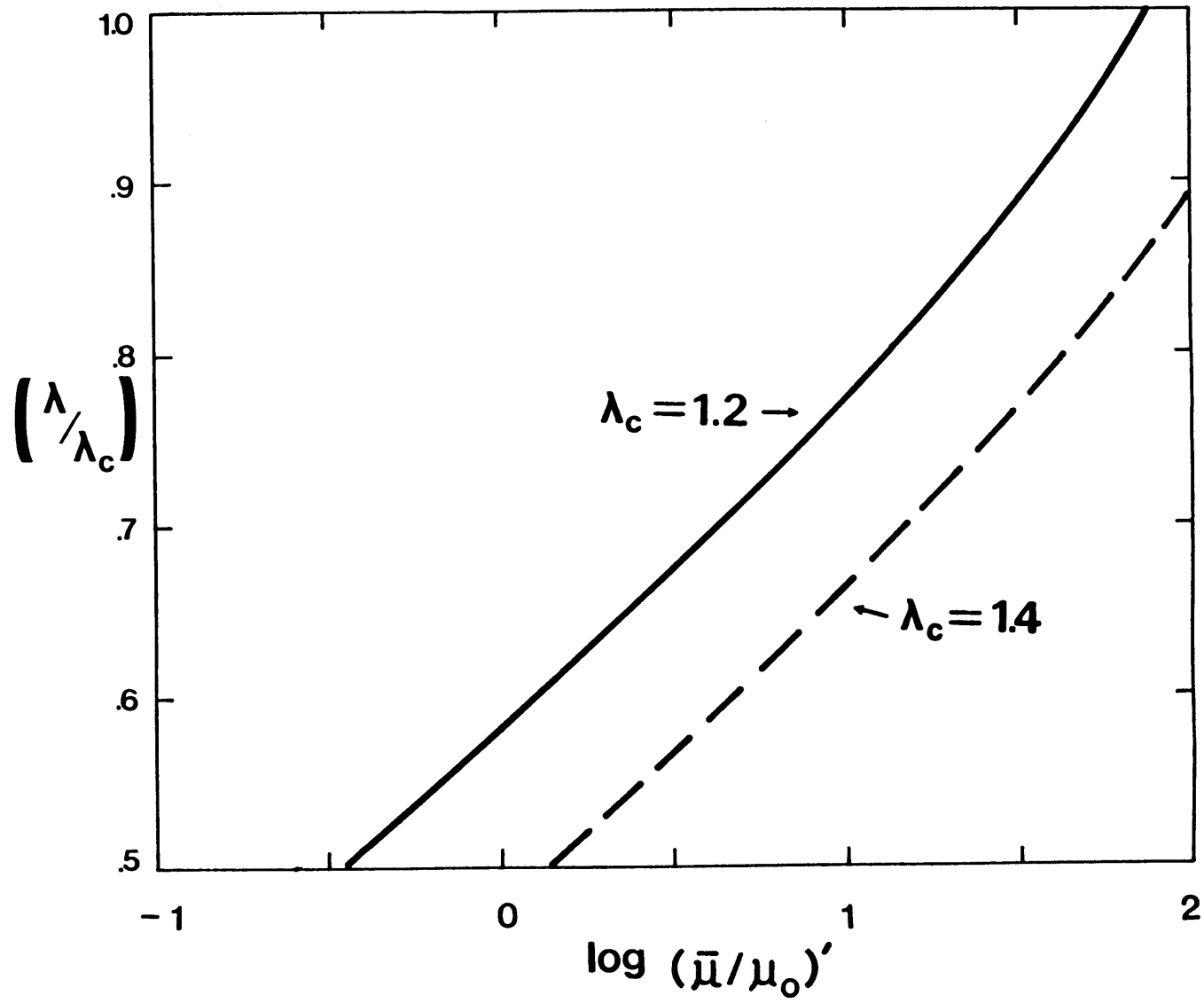
1.0
.9
.8
.7
.6
.5
(λ/λ_c)
$\lambda_c = 1.2$
$\lambda_c = 1.4$
-1
0
1
2
log $(\bar{\mu}/\mu_o)'$

Figure 3.9

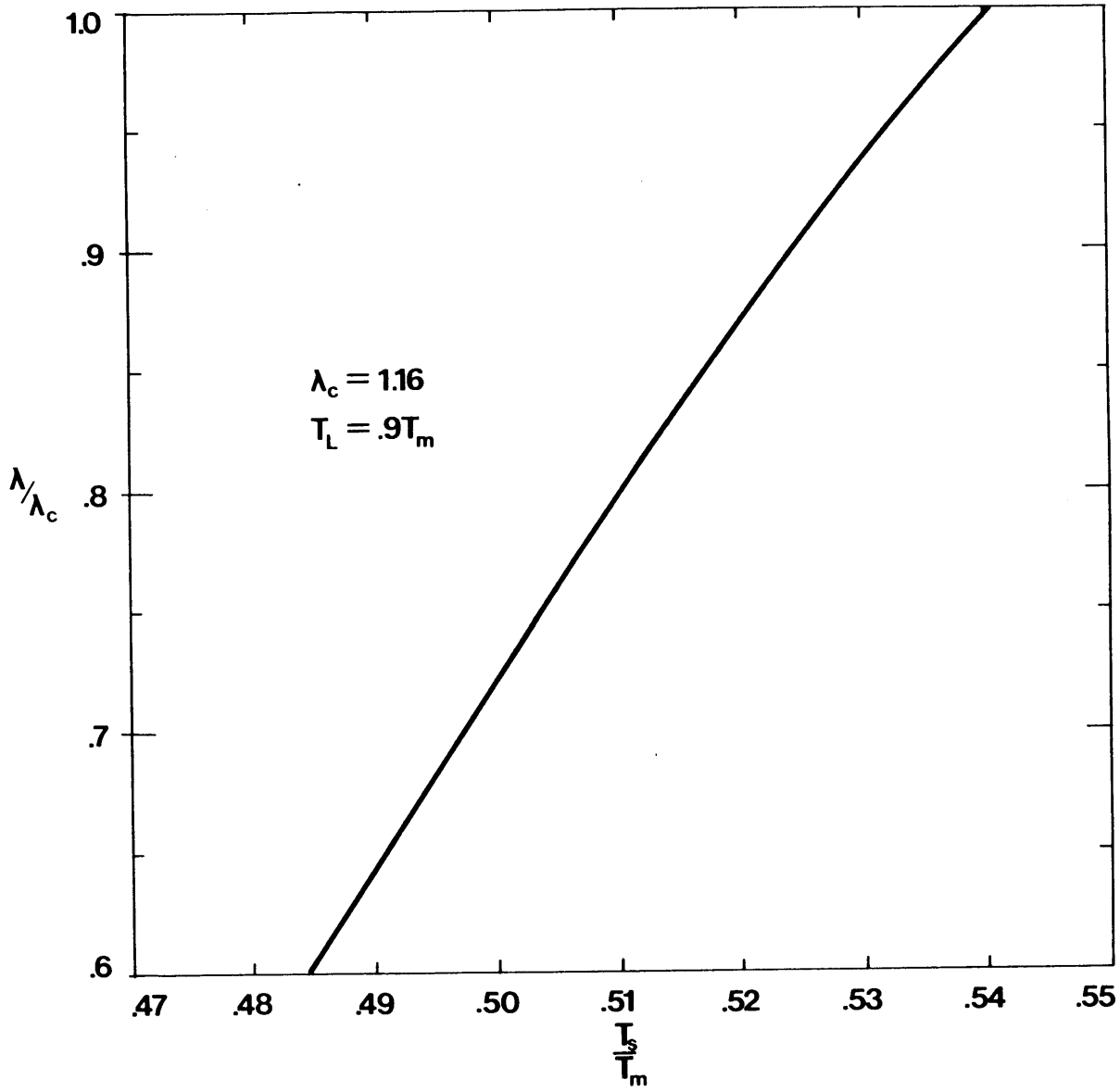
1.0
.9
.8
.7
.6
λ/λ_c
$\lambda_c = 1.16$
$T_L = .9T_m$
.47
.48
.49
.50
.51
.52
.53
.54
.55
$\frac{T_s}{T_m}$

Figure 3.10

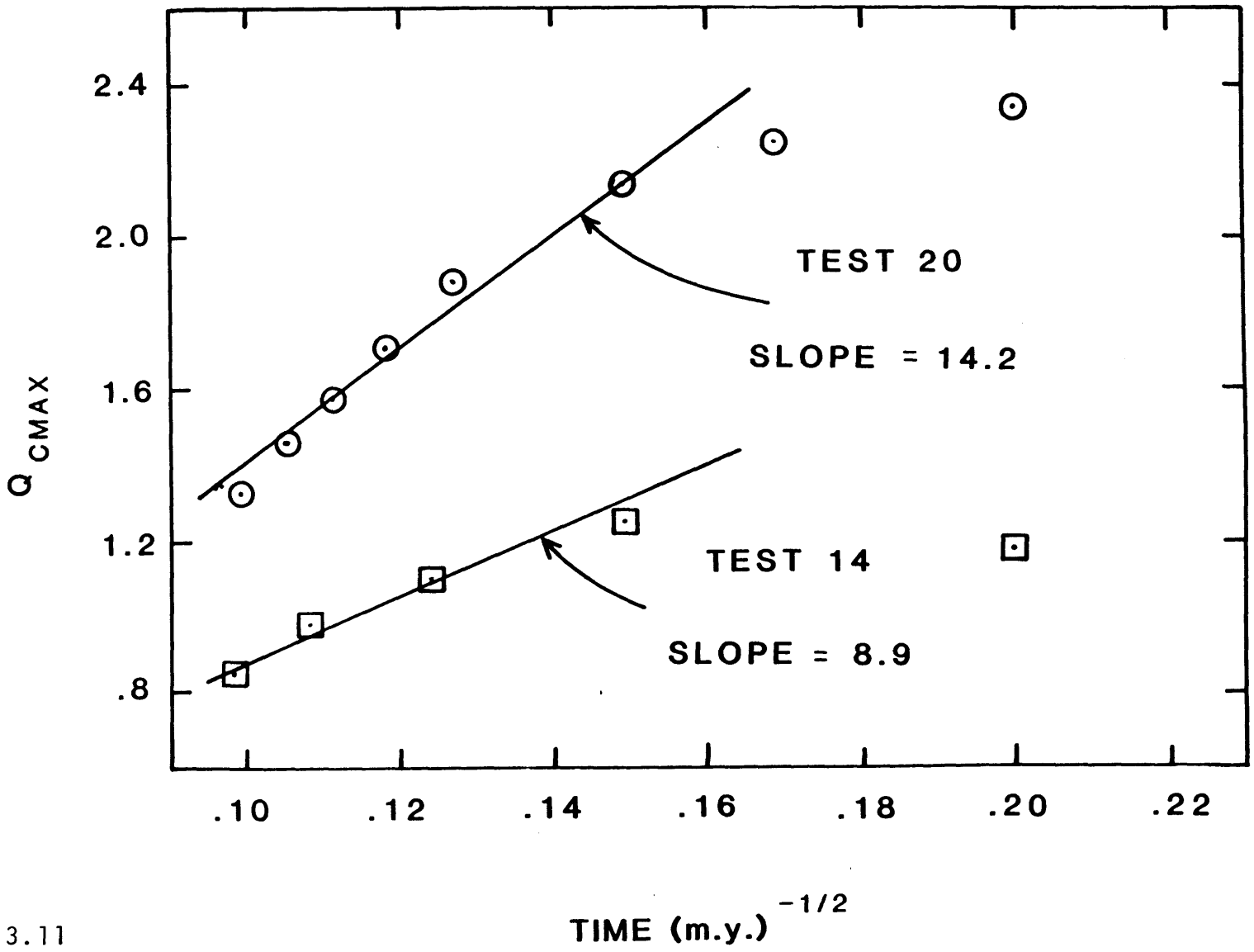
2.4
2.0
1.6
1.2
.8
Q_{CMAX}
TEST 20
SLOPE = 14.2
TEST 14
SLOPE = 8.9
.10
.12
.14
.16
.18
.20
.22
TIME (m.y.)$^{-1/2}$

Figure 3.11

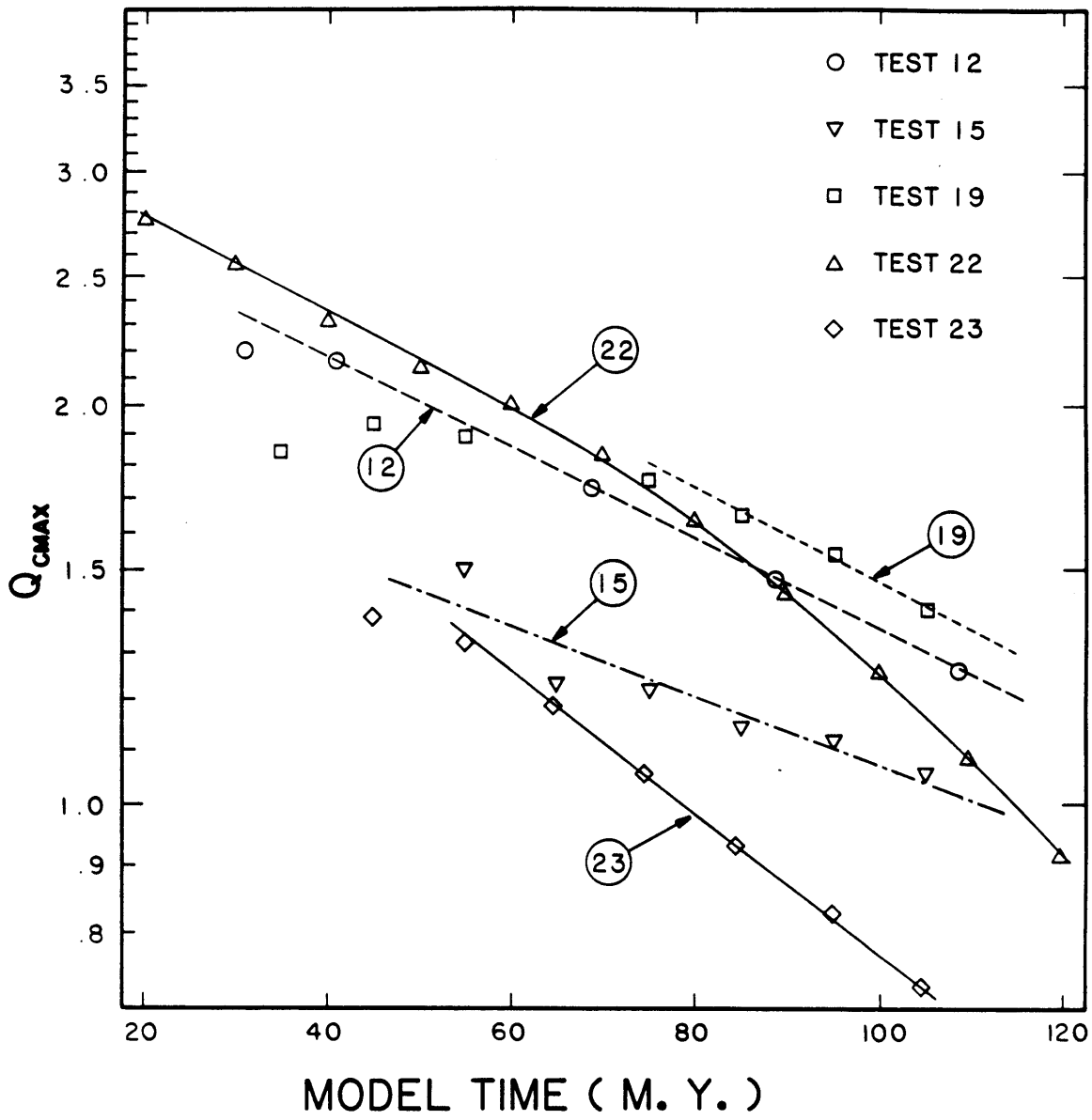
TEST 12
TEST 15
TEST 19
TEST 22
TEST 23
22
12
19
15
23
3.5
3.0
2.5
2.0
1.5
1.0
.9
.8
Q_{CMAX}
20
40
60
80
100
120
MODEL TIME (M. Y.)

Figure 3.12 (a)

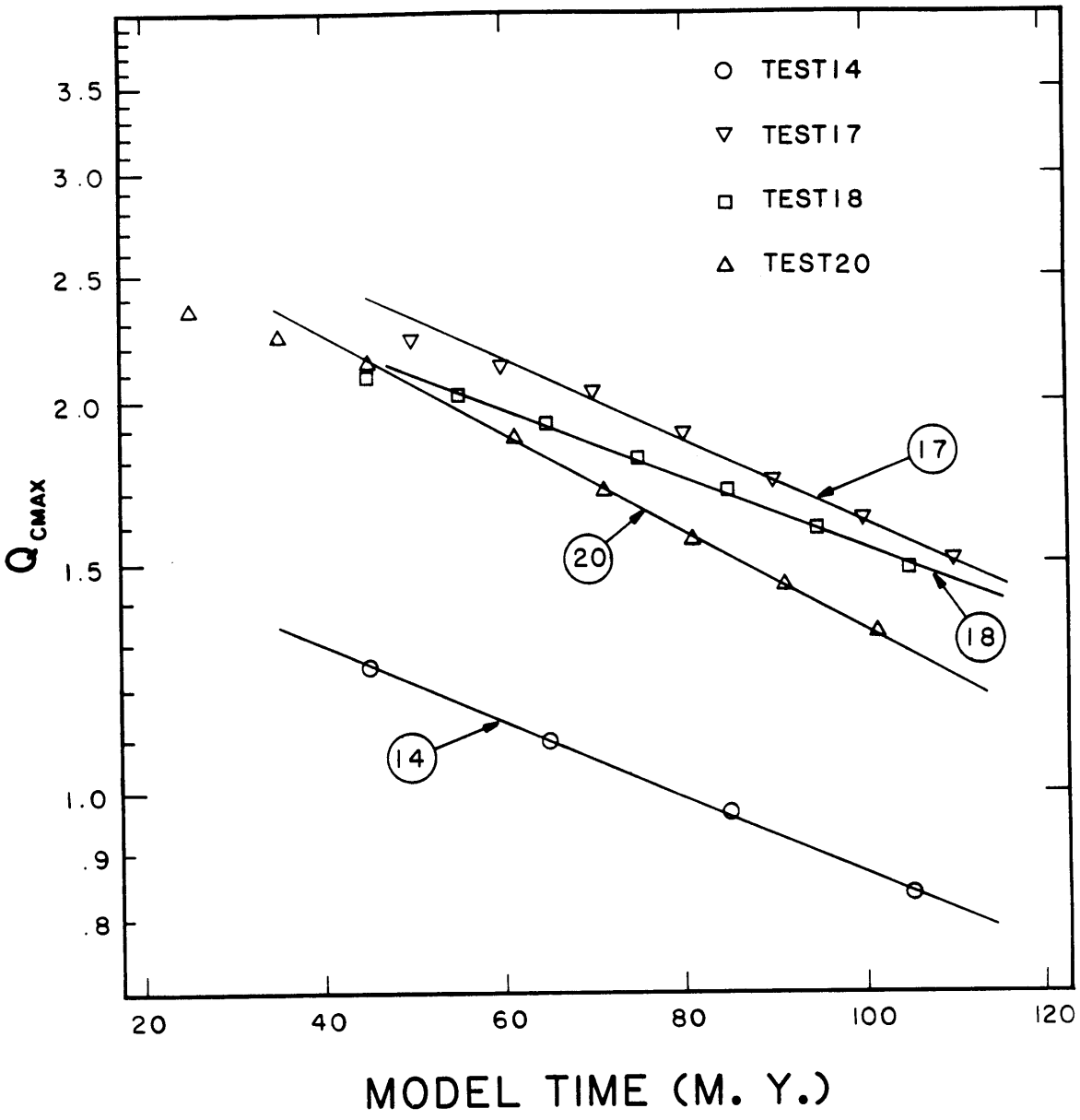
TEST14
TEST17
TEST18
TEST20
17
20
18
14
Q_{CMAX}
3.5
3.0
2.5
2.0
1.5
1.0
.9
.8
20
40
60
80
100
120
MODEL TIME (M. Y.)

Figure 3.12(b)

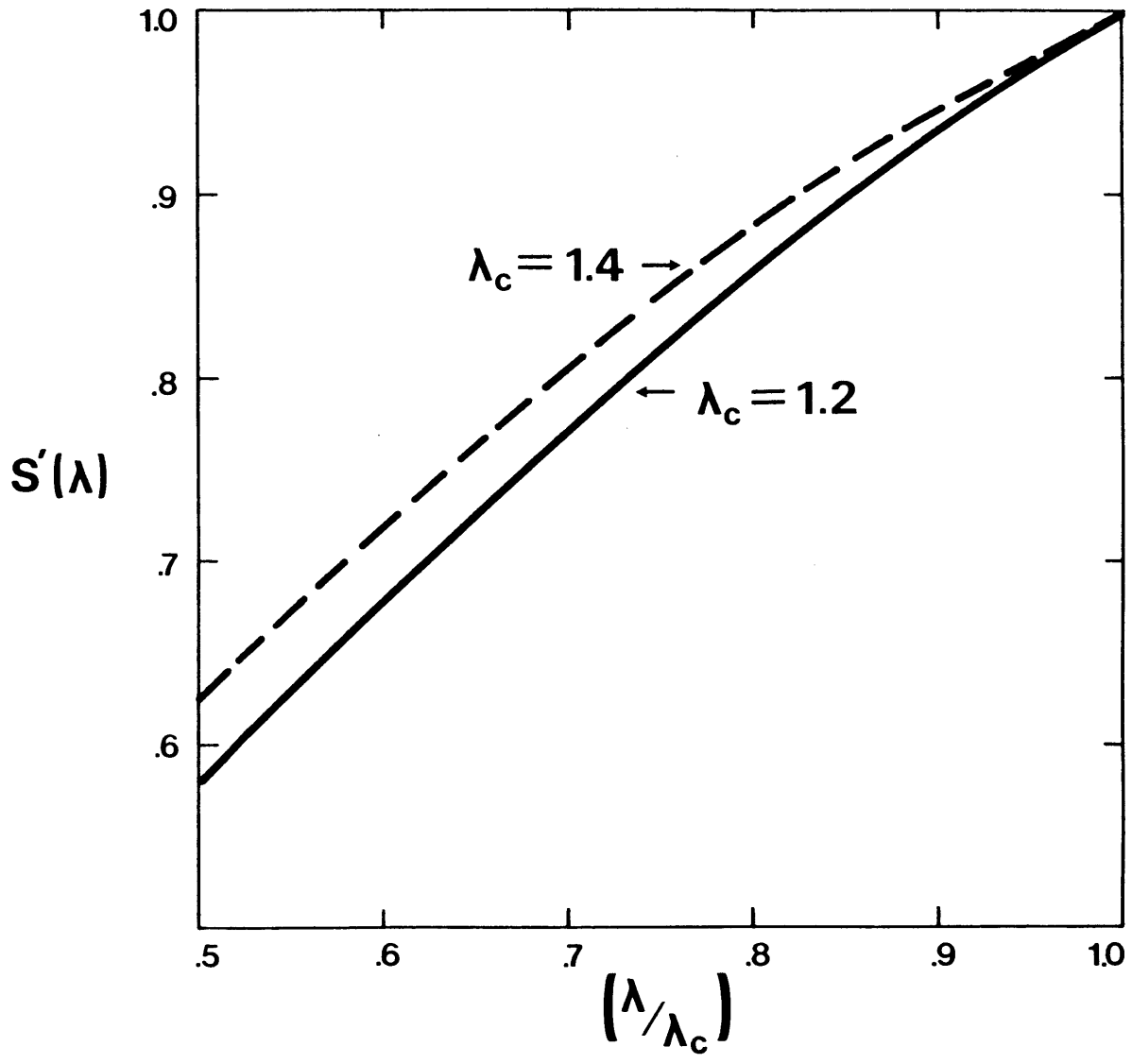

Figure 3.13

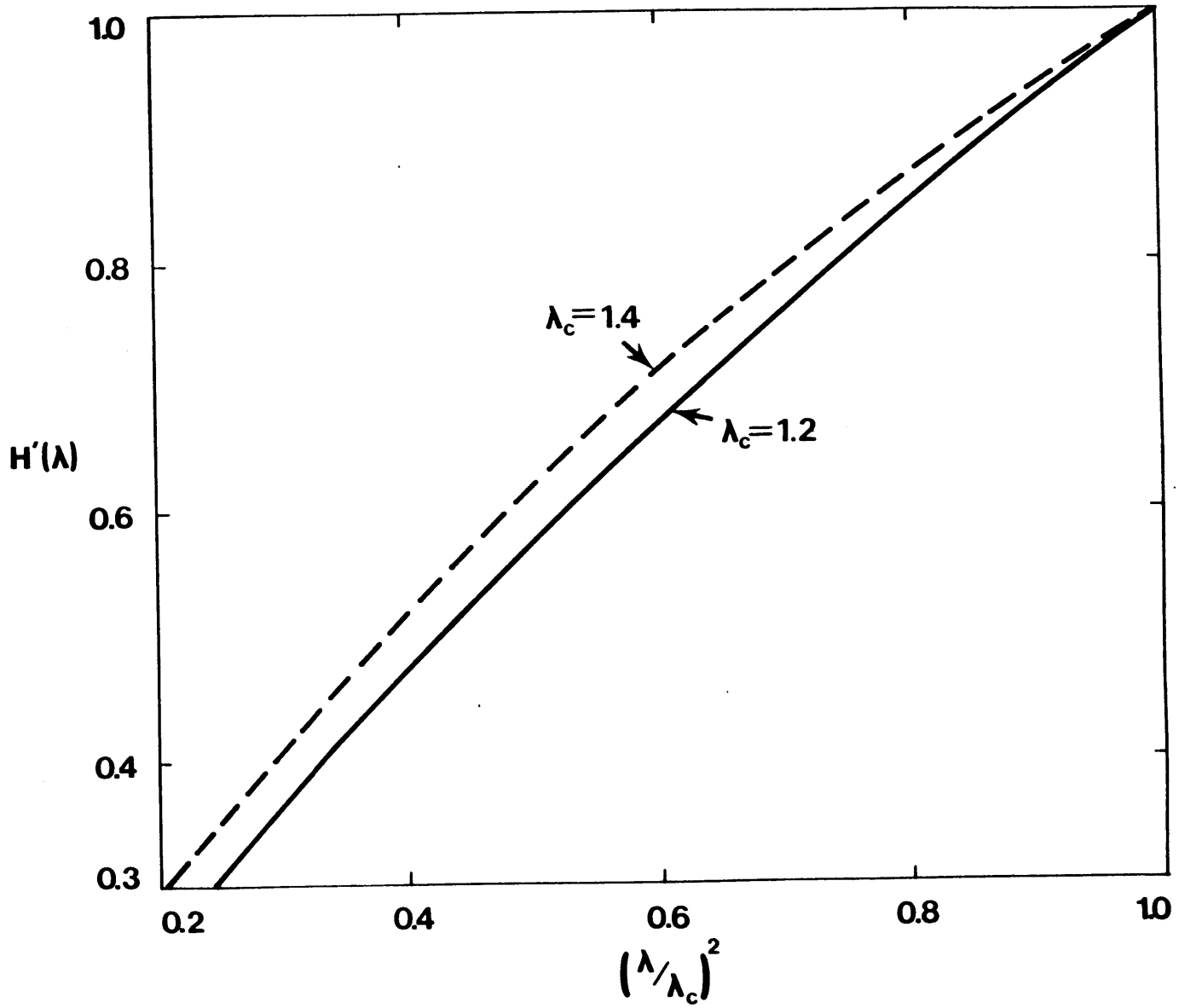

Figure 3.14

"The little rift between the sexes is astonishingly widened by simply teaching one set of catch words to the girls and one to the boys."

- Robert Louis Stevenson,"Virginbus Puerisques."

CHAPTER 4

EFFECTS OF CONVECTION INDUCED BY LATERAL TEMPERATURE VARIATIONS ON PASSIVE RIFTS

4.1 Introduction

Rifting is the pulling apart of the crust and lithosphere. Sleep (1971) showed that conductive cooling of the thinned lithosphere at a continental margin was consistent with the long term subsidence of the Atlantic margin. The possibility that the thinning of the lithosphere is caused by stresses transmitted horizontally, or passively rifted, has been suggested by Salveson (1978) and McKenzie (1978). A thermal model based on passive rifting, called the uniform stretching or the extension model has been suggested by McKenzie (1978) to explain the subsidence of rifts. Analysis of data from intracratonal basins (Sclater et al., 1980) and deep well holes on the Atlantic margin (Royden and Keen, 1980; Keen and Barrett, 1981) has shown that large corrections need to be made to the uniform extension model in many cases where the data on subsidence is complete to the earliest stages of sedimentation. There are also data that indicate that uplift of the flanks of rifts accompanies rifting and that this uplift extends well beyond the area where rifting has thinned the crust (Hellinger

and Sclater,1984). Uplift of the areas adjacent to rifted crust is not predicted by the stretching model. Convection which is induced by the large horizontal temperature gradients in the mantle where the lithosphere has been thinned by rifting may explain some of these features.

The convection calculations described in this chapter are conceptually the simplest of those considered in this thesis, but the execution of this set of numerical experiments is the most complicated. The purpose of this study is to determine if convection beneath rifts can affect the rate of subsidence as a function of position in the rift and if the uplift of the rift flanks can be related to this. The technical difficulties inherent in this study include determination of a reasonable rift temperature structure and setting up a meaningful way to compare the results of these calculations to previous models. The numerical methods used are an extension of the methods used in chapter 2 to a case where the boundary between the convecting region and the conductive lid is not flat. This required a new method to handle curved boundaries. A major difference between this problem and those considered in the chapers 2,3 and 5 is that convective flow will occur regardless of the viscosity parameters assumed, since the flow is driven by the assumed temperature structure of the rift. The rate of flow, and its effect on the cooling of the rift and the uplift of the flanks, does depend on the viscosity parameters and on whether the viscosity is assumed to be Newtonian or stress dependent.

In this chapter data on the subsidence of rifts and the uplift of their flanks will be reviewed. Next, we will discuss the justification for a mechanically simple model of rifting caused by tectonic stresses, outline the simple thermal model, called the extensional or stretching model (McKenzie, 1978), which is based on it. We will review the subsidence data for several areas which indicates limitations to the model. Then we describe numerical calculations on the effect of mantle flow induced by large horizontal temperature gradients in the mantle produced by passive rifting. The initial temperature structure assumed in this work is similar to that used in the stretching model. Finally, we will discuss how the convective flow modifies the thickness and subsidence of the lithosphere as a function of time.

4.2 Models of Rifting

4.2.1 Passive vs. Active Rifting

In our calculations we assume that rifting is passive rifting. Here passive refers to the role of the asthenosphere in the rifting. Passive rifting is driven by stress transmitted by the mechanically strong lithosphere. Active rifting is produced by upwelling of anomalously hot asthenosphere which thins and causes uplift of the lithosphere. Active rifting results in volcanism and doming preceeding rifting while for passive rifting rifts form first and then doming may follow (Segnor and Burke, 1978). Areas which are clearly associated in space and time with stresses manifest in continental convergence such as the Rhinegraben (Illies and

Greiner, 1978) and the Baikal Rift (Zoneshain and Saugtin, 1981; Zorin, 1981) are thought to be passive examples (Turcotte, 1981). The great length of continental margins argues for for a passive origin for at least some of the length of these rifted areas, since it is likely that anomalous upwelling of asthenosphere should be concentrated in individual hotspots.

The two rifting mechanisms are not mutually exclusive. As shown by Neuguebauer and Temme (1981) the uplift of continental lithosphere by active asthenospheric processes can lead to large, gravitational stresses within the lithosphere due to gravity. These stresses then produce rifting in the same way that stresses transmitted from a distance through the lithosphere will do this in passive rifting. Other ways for active mantle processes to result in thinner crust have been proposed. A change in the density of the lower crust due to phase changes there (Falvey, 1974; Haxby et al., 1976) has been suggested. The phase change hypothesis as well as other active models are difficult to quantify and thus they cannot be used to predict subsidence or heat flow of a rift. It is the simplicity and relative ease of applying the passive stretching model which make it attractive. In a sense the model of asthenospheric convection considered here is a case of a quantifiable active process which is induced by passive rifting.

4.2.2 The Uniform Extension Model

A mechanical model of passive rifting was put forward by Salveson (1978). Figure 1 shows his conception of the sequence

of rifting. The thermal consequences of this model have been discussed in terms of a simple thermal model by McKenzie (1978). He considered the instantaneous extension of each vertical column of the lithosphere and crust by equal amounts, β and assumed that asthenosphere upwells passively to maintain isostatic equilibrium. When a vertical column of the lithosphere is stretched by a factor β, then it thins to $1/\beta$ times its original thickness. The subsidence has two components. There is an initial component due to the thinning of the crust and a long-term component due to the cooling of the lithosphere back to an assumed equilibrium thickness. The initial subsidence or uplift depends on the original crustal thickness and the amount of stretching. The modeling of subsidence and heat flow are done with constant temperature boundary conditions at 125 km analogous to the plate model for the oceanic lithosphere (Mckenzie,1967). The initial thermal structure is derived from the simple movement of temperatures, along with material, vertically up in the lithosphere according to the amount of thinning. The geometry of this is shown in Figure 2 for the case of equal thinning of the crust and lithosphere. For the simple model of extension, the thermal gradient is assumed to be linear with 273 °K at the surface and 1573 °K at the base of the lithosphere.

4.3 Geologic Data on Rifts

The subsidence of passive margins estimated using well corings of sediments, as described by Sclater and Christie (1980), has been used to test the stretching model. Using

gravity and seismic data the thickness of the continental crust beneath sediments is estimated at a well site. The ratio of the average crustal thickness on shore to the well site crustal thickness gives the stretching factor for the crust there (β_c). It is then assumed that the mantle was thinned by the same amount. Using this method the subsidence of rifted continental margins and intracratonic basins has been shown to be consistent with the uniform extensional model (Watts and Ryan, 1976; Steckler and Watts, 1978; Sclater and Christie, 1980; Watts and Steckler, 1979; Royden et al., 1980; Royden and Keen, 1980; Keen and Barrett, 1981; Le Pichon and Sibuet, 1981; Sawyer et al., 1982). In the areas where the agreement between the subsidence data and model predictions is good there is little data on the earliest subsidence of the basin.

Subsidence data for the early period of subsidence of a rifted areas (i.e. the first 25 m.y.) has been shown to require some modification to the uniform extension model. Royden and Keen (1980) showed that the simple stretching model would not fit the data for wells on the margin of the Labrador Sea. They had to modify it to allow for greater thinning of the mantle lithosphere than for the crust. Other workers considering intracratonal rifting (Sclater et al.,1980; Hellinger and Sclater,1984) have found this same need to modify the model to include two layers of stretching, with the amount of mantle thinning (β_{sc}) depending on the site.

A related set of data on the uplift of the flanks of rifts does not easily fit into the uniform extensional model. As

noted by Morgan (1983), a broad regional uplift is usually associated with rifting. The shoulders of the Rhinegraben rift have been uplifted 1000 m since the time of rifting (Illies and Greiner, 1978). The Rio Grande rift (Golombek et al., 1983) and the Baikal Rift (Zorin, 1971) also show uplifted flanks. The flanks of the Red Sea and the Gulf of Suez rifts show up to 1 km uplift which post-dates rifting (Steckler, personal communication; Baker et al., 1983). One can argue that all these cases are examples of passive rifting, but the uniform extension model cannot fit this data. The small-scale convection studied here will be shown to have effects which can match this data.

4.4 Formulation of Rifting Calculations

4.4.1 Rift Temperature Structure

To study the effects of convection on the cooling of a rift we must first define the initial temperatures in the rift after passive rifting, but before convection and conduction has altered the temperatures. As in McKenzie (1978) we consider the instantaneous thinning of an assumed pre-rift horizontally uniform temperature structure for the lithosphere and constant temperatures in the asthenosphere. We choose an initial temperature profile resulting from either half-space cooling for a set length of time (here 100 m.y.) or from the results of the similarity solution to the problem of the cooling of the oceanic lithosphere described in Chapter 3. The initial rift temperature structure is derived from the profile by stretching by β = 1 to 5 (Figure 4.3). Both kinds of temperature profiles

used are similarity solutions in terms of the depth variable. That is, the shape of the profiles does not change with the time of cooling, only its vertical extent increases. Therefore, the thinned profiles at any point in the initial rift temperature structure has equivalent temperatures to model oceanic lithosphere which has cooled for an amount of time less than the unthinned profile. Figure 4.3 also shows the equivalent cooling times for several points in the rift.

The subsidence or uplift of a point in the rift is calculated in the same way that the surface deformations due to pressure variations at the base of the lithosphere and temperature variations within the lithosphere defined by equation 2.13 were calculated in Chapter 2. There deformations were used to calculate gravity anomalies. Here the vertical displacement of a point is defined as the difference in the surface deformation at a given time and the deformation due to the initial temperature structure.

Our main interest is in the effect of convection on subsidence and uplift of the surface in the area of a rift. We must compare the vertical subsidence or uplift at each point with an estimate of the surface deformation in the absence of convection driven by the rift temperature structure. This is done in two ways. The simplest way involves using the same initial temperature structure as for the convective calculation, but considering only conductive heat transport. The other way uses the results of Chapter 2 for subsidence of cooling lithosphere in the presence of small-scale convection.

To do this we use the fact that the temperature profile at each point in the rift corresponds to an age of cooling. Each point can be related to a point on a subsidence versus $t^{1/2}$ plot determined for cooling of oceanic lithosphere with the same rheology. The vertical displacement as a function of time can be plotted along with that curve to give an idea of the difference which the rift temperature structure makes.

4.4.2 Numerical Methods

Just as in Chapter 2, we study the effects of finite amplitude convection by numerically solving the Navier-Stokes equations of mass, momentum and energy conservation in two dimensions. The method we use is similar to the method discussed in Chapter 2 and in the Appendix, but involves curved flow boundaries. This is necessary because the thickness of the lithosphere in this problem varies by up to a factor of 5 for the initial temperature and viscosity structure. In the Appendix an approximate method for solving for the flow adjacent to a curved boundary is described.

4.4.3 Viscosity Relation

We consider viscosity to be a function of temperature, pressure and, in some cases, stress. For viscosity that depends only on temperature and pressure, we use equation 2.1 to define the viscosity at a point. In several cases we take the viscosity to depend on deviatoric stress, or strain rate $(\dot{e})$, as well as temperature and pressure. We then define viscosity as:

$$\mu(T,P,\dot{e}) = \frac{\mu(T,P)}{1 + A_e(\mu(T,P)*\dot{e})^{2/3}} \qquad (4.1)$$

where $\mu(T,P)$ is defined by equation 2.1 and the power 2/3 comes from assuming a power-law rheology (Goetze, 1978) with n = 3 and A_e determines the strength of the strain rate dependence. The factor of 1 added to the denominator insures that viscosities do not become infinite where the strain rates approach zero and is analogous to the cutoff in deviatoric stress used in a similar viscosity relation by Fleitout and Yuen (1984).

4.4.4 Models Considered

Several parameters of these models are varied in an effort to understand what affects the cooling of a rift. The viscosity is changed in two ways. First, the average viscosity is changed through the reference viscosity defined in Chapter 2. Second, the viscosity is taken to be Newtonian in some cases and non-Newtonian in others. The temperature and pressure dependence of viscosity are held constant, since variations in these parameters should have about the same effect as changes in the stress dependence and the average viscosity. Christensen (1983) has shown that the effect of including stress dependence in a viscosity relation for steady-state convection cells has the same effect as a decrease in the activation energy (E). The activation energy controls the temperature dependence of viscosity. The width of the initial rift temperature structure (W_r) is also varied between 50 and 100 km. Finally, as noted before, the temperature

profile used to set up the initial temperatures in the rift is either that resulting from 100 m.y. conductive cooling or the same time of cooling for the Stefan problem. Table 4.1 lists the parameters used to defined the numerical calculations done here.

4.5 Results

Several of the model parameters which were varied in this study had a large effect on the geologically relevant results. We consider the effect of variations in the average viscosity, inclusion of stress-dependent viscosity, different initial temperature profiles and different widths of the rift zone.

There is considerable uplift produced by combination of the lateral conduction of heat and the increase in the general advective heat flux in all these calculations. The deformation of the surface for several of the convective cases is illustrated in Figures 4.4 to 4.6. In Figures 4.4 and 4.5 contours of the temperature field are shown which illustrate how the flow changes the temperatures under a rift. Figure 4.6 shows that dynamical effects on the surface deformation are much smaller than the lateral temperature variations. It is important to estimate the amount of uplift which would have occurred without convective heat transfer. The surface deformation with only conduction acting on the initial temperatures of case 104 is shown in Figure 4.7, compared to the results from that convective calculation. The uplift is restricted to a narrower region and is of smaller amplitude than the uplift for the corresponding times for model 104. The

total uplift integrated over area is about 2.5 times greater for this particular convective case.

The surface deformation is compared with that predicted if the effects of rift induced convection are ignored. We compare the elevation or subsidence of points in the rift for case 105 to the subsidence predicted by a one-dimensional cooling model in Figure 4.8. This shows that although the flanks of a rift are elevated, the center of the rift cools more rapidly than predicted by a one-dimensional calculation.

In case 101 much of the uplift relative to the initial surface elevation is not centered over the unthinned flanks of the model rift but is closer to its center. This is due to the large width of the rift and to the two-cell pattern of convection which developed in this case. The effect of the concentrated downwelling due to this pattern is illustrated in Figure 4.6 which shows the components of the surface deformation for a time 25 m.y. into case 101. The part of the deformation which is due to the flow induced stresses at the base of the lithosphere is negative over the downwelling, but, as in all the cases, this component is small compared to the effect of temperature and thickness variations in the lithosphere. The uplift in the cases which did not break into two cells (ie. cases 104 and 105) is centered on the rift flanks. Case 103 was defined with the same parameters as case 101 but the average viscosity was higher by a factor of 4. This resulted in a similar pattern of surface deformation while the amplitude of the deformation was reduced by about 40% compared to case 101.

Inclusion of non-Newtonian rheology increases the uplift produced by convection. Case 102 and case 101 had the same amount of uplift on the rift flanks even though case 102 had a higher reference Newtonian viscosity than case 101 by a factor of 4. Simply increasing the reference viscosity acts to decrease the uplift. This is shown by case 103 which had the same reference viscosity as cases 102 but had no stress dependence included in calculating the viscosity.

The effect of considering a thinner and more linear initial temperature profile for the unrifted lithosphere is considered in cases 104 and 105. The more linear temperature profile is probably more applicable to most rifts. Case 101 only differs from case 105 in the initial temperature structure. Since the lithosphere is thicker in case 101 there is a thinner low viscosity asthenosphere and the initial single convection cell breaks into two early in the calculation. The uplift of the basin flanks is greater for case 101 because there is a thicker region at the base of the lithosphere which can flow down away from the rest of the lithosphere and thus results in a rapid thinning of the lithosphere.

We were forced to consider model rifts which are wider than many rifts on earth, because of the numerical difficulties in dealing with very narrow zones where temperature gradients and physical parameters vary rapidly. Since we do consider two different model widths (50 and 100 km widths of the half-rift), we have learned something about the importance of the width in changing the effect of convection beneath the

rift. One case was done for a narrower model rift. In case 104 the width of the half-rift (W_r) was taken to be 50 km, which is half the value used in the other cases. The viscosity parameters were the same as those used in case 105. The uplift of the flanks was greater than for that case by a factor of 2 and occurred relatively farther from the center of the rift than for the other cases. The two-dimensional conductive calculation for this narrow model rift also showed higher predicted uplift than for the wider cases, but less average uplift than for the convective case 104. Figure 4.7 shows a comparison of the uplift for case 104 with the corresponding conductive case.

To show that the results of these calculations are consistent with uplift data for continental rift zones we consider the uplift of the flanks of the Rhinegraben. Figure 4.9 shows a map view of the Rhinegraben from Illies and Greiner (1978) and the position of a cross-section across the rift which is shown in Figure 4.10(a). In Figure 4.10(b) the relative uplift of the east side of the cross-section is plotted along with the model results for case 104 and the curves are very similar. The width of the model rift in case 104 and the amount of thinning in the center of the model rift may not exactly match these quantities for the Rhinegraben, but this exercise shows that simple convective effects can produce uplifts which are of the same magnitude and have the same spatial distribution as those observed. Conductive transport of heat cannot do this.

4.6 Conclusions

These results show that the effects of convection induced by a passive rift temperature structure can explain data on the uplift of the flanks of rifts. We have shown that the predicted uplift is greater for narrower rifts and for lower average viscosities. The stress dependence of viscosity can also add to the effects of uplift since this tends to reduce the viscosity in the high stress areas at the edge of the rift compared to the areas of lower stress. The small-scale convection beneath a passive rift can also account for the apparent need for two levels of thinning of the lithosphere in conductive models of the subsidence of rifts.

Table 4.1

Case Number	W_r (km)	λ/λ_c	μ_{ref} (x 10^{18} Pa-s)	A_e
101	100	1.0	1.0	0
102	100	1.0	4.0	1.00 x 10^{-3}
103	100	1.0	4.0	0
104	50	1.0	1.0	0
105	100	0.9	1.0	0

Table 4.1 The parameters which define the cases considered in this chapter are shown. The parameter λ/λ_c determines the temperature profile using equation 3.4 which is used to construct the initial rift temperature structure, as discussed in the text. For λ/λ_c=1, the profile is that resulting for conductive cooling of a half space for 100 m.y. with the physical parameters given in Table 2.1. The width of the rift is W_r. The viscosity is defined by μ_{ref}, which is the initial viscosity at 150 km in the model, and the value of A_e defines the non-Newtonian rheology described by equation 4.1. For all cases the activation energy (E) was taken to be 100 kcal/mole and the activation volume (V) was 10^{-5} m^3/mole.

Figure Captions

Figure 4.1. The hypothetical sequence of events in passive rifting as envisaged by Salveson (1978) is shown. Our calculations start with stage 4.

Figure 4.2. This illustrates the thermal model of McKenzie (1978) for one point in a rift. The cross-section shows an area of the lithosphere (L) which initially (t=0) is of equal width and depth (a). The temperature profile is linear with depth to the base of the lithosphere. The crust (c) and lithosphere are instantaneously stretched by a factor (β) and so is thinned by a factor ($1/\beta$). The area where the lithosphere was thinned is replaced by isothermal asthenosphere (A). Thermal subsidence occurs as the temperature profile returns to the original profile as time goes to infinity.

Figure 4.3. The geometry of the initial rift temperature structure for a flow calculation is shown. The width of the rifted region (Wr) is varied in the models considered, but for all of them the lithosphere is thinned by a maximum factor of 5.

Figure 4.4. Contours of constant values of temperature and stream function are shown for the indicated times for case 105 as defined in table 4.1. The temperature contours are for every 50 °K between 273 and 1573 °K and the stream function contours are evenly spaced between zero and the

maximum value in the box. The grid point positions are indicated by tick marks on the left and bottom sides of the box.

Figure 4.5. Temperature contours and the surface deformation are shown for the four times through the calculation of case 104. Temperature contours are the same as in Figure 4.4. The calculation of the surface deformation is described in the text.

Figure 4.6. The two components of the surface deformation along with the combined effect for a time 25 m.y. into the calculation of case 101. These components are defined in text. As for other cases the component due to the convective stresses is small compared to that due to the temperature variations.

Figure 4.7. The elevation for a conductive case with the same initial temperature structure as for case 104 is compared to the results of case 104 at a model time of 20 m.y. in each case. Here elevation is defined in the same way as water loaded surface deformation, but we consider this to be sub-aerial, so the magnitude of deformation is reduced by 30%. The uplift averaged over area is about 40% of that for case 101 and the subsidence of the center of the rift is greater than for the convective case.

Figure 4.8. The average temperature in the top 150 km of the box is shown as a function of time for 5 points in case

105. This quantity can be directly related to subsidence or uplift. The initial temperature profiles correspond to profiles for cooling for the times where they are plotted, as described in the text. The straight solid line shows the average temperatures in the top of the box for the similarity solution used to define case 105. The dashed line is the same plot for a one-dimensional conductive cooling case.

Figure 4.9. This map view of the Rhinegraben area, taken from Illies and Greiner (1978), shows the amounts of uplift of the flanks of this rift. Profile A - A' is plotted in Figure 4.10.

Figure 4.10. Plot (a) shows the estimated uplift along the profile A - A' shown in Figure 4.9. In part (b) we show the elevation of the rift flanks predicted by case 104 at 20 m.y. Also shown as a dashed line is the uplift along the left side of profile A - A' plotted now as relative uplift. The vertical and horizontal scale of (a) and (b) are the same.

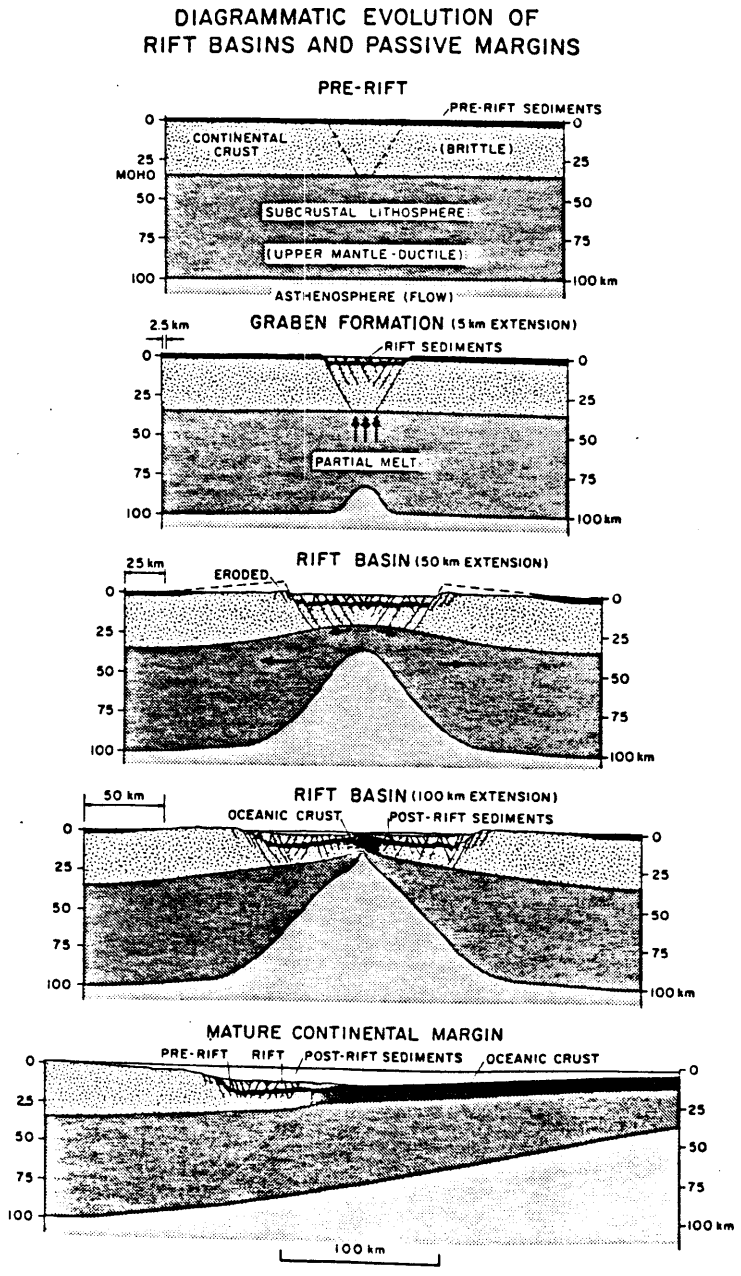
DIAGRAMMATIC EVOLUTION OF
RIFT BASINS AND PASSIVE MARGINS
PRE-RIFT
PRE-RIFT SEDIMENTS
CONTINENTAL CRUST
(BRITTLE)
MOHO
SUBCRUSTAL LITHOSPHERE
(UPPER MANTLE - DUCTILE)
ASTHENOSPHERE (FLOW)
0
25
50
75
100
100 km
2.5 km
GRABEN FORMATION (5 km EXTENSION)
RIFT SEDIMENTS
PARTIAL MELT
25 km
ERODED
RIFT BASIN (50 km EXTENSION)
50 km
RIFT BASIN (100 km EXTENSION)
OCEANIC CRUST
POST-RIFT SEDIMENTS
MATURE CONTINENTAL MARGIN
PRE-RIFT
RIFT
POST-RIFT SEDIMENTS
OCEANIC CRUST
100 km

Figure 4.1

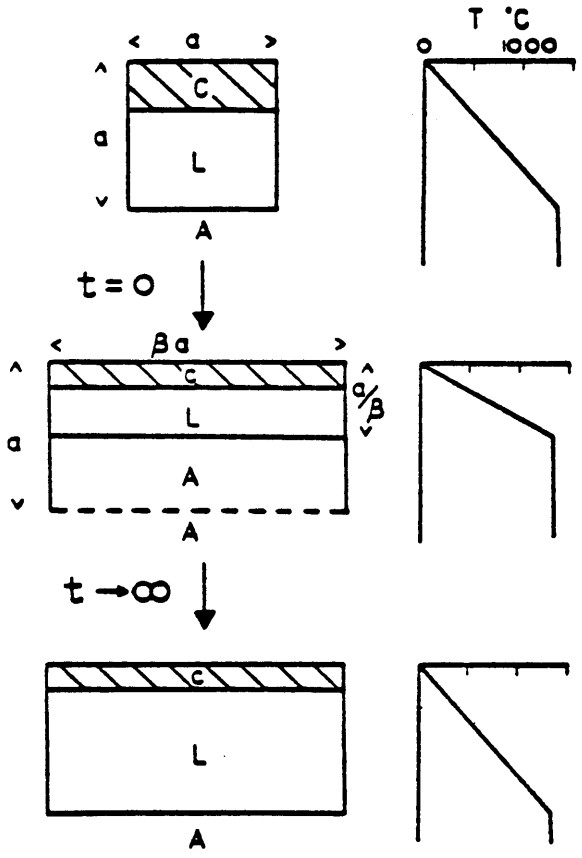

Figure 4.2

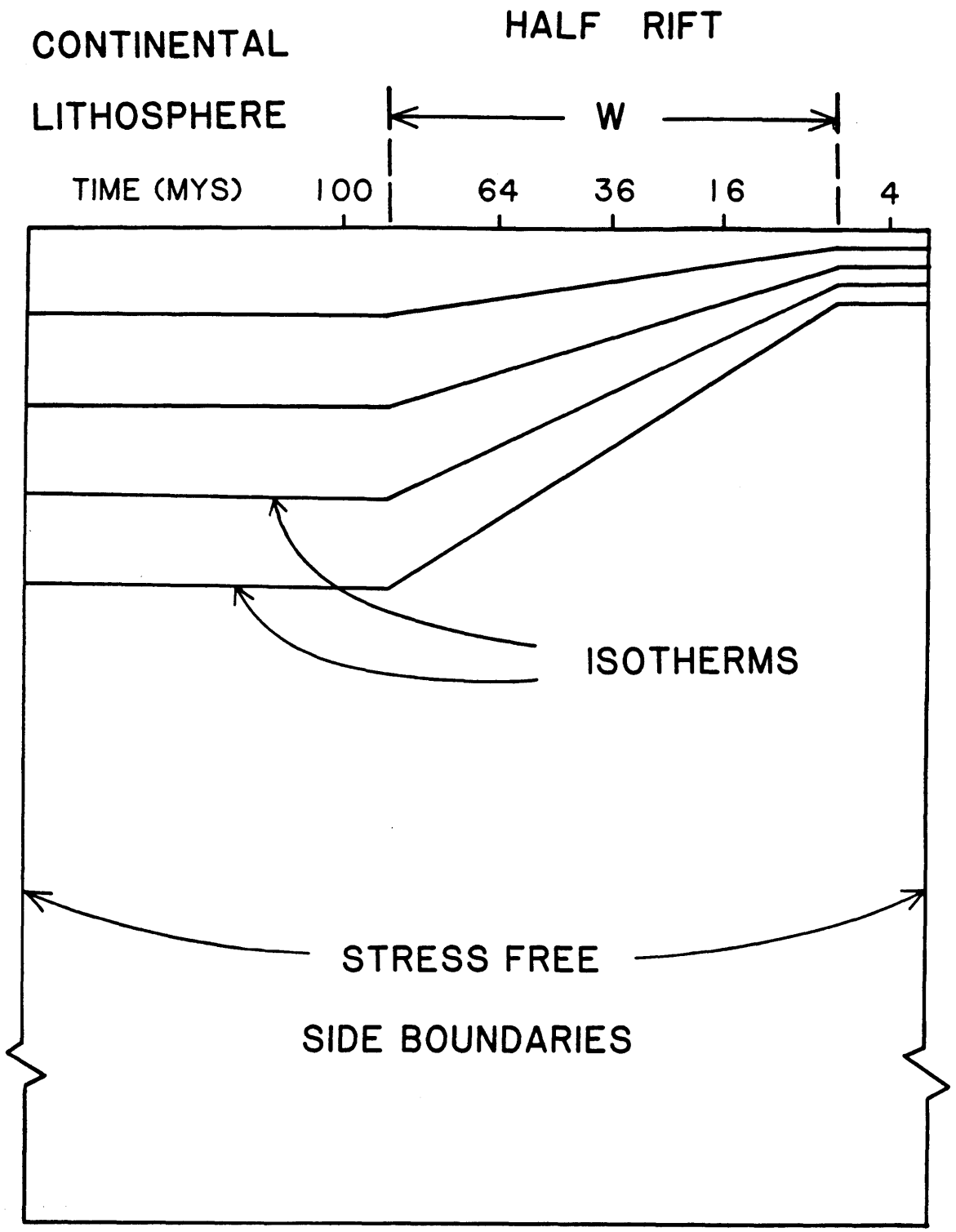
CONTINENTAL
LITHOSPHERE
HALF RIFT
W
TIME (MYS)
100
64
36
16
4
ISOTHERMS
STRESS FREE
SIDE BOUNDARIES

Figure 4.3

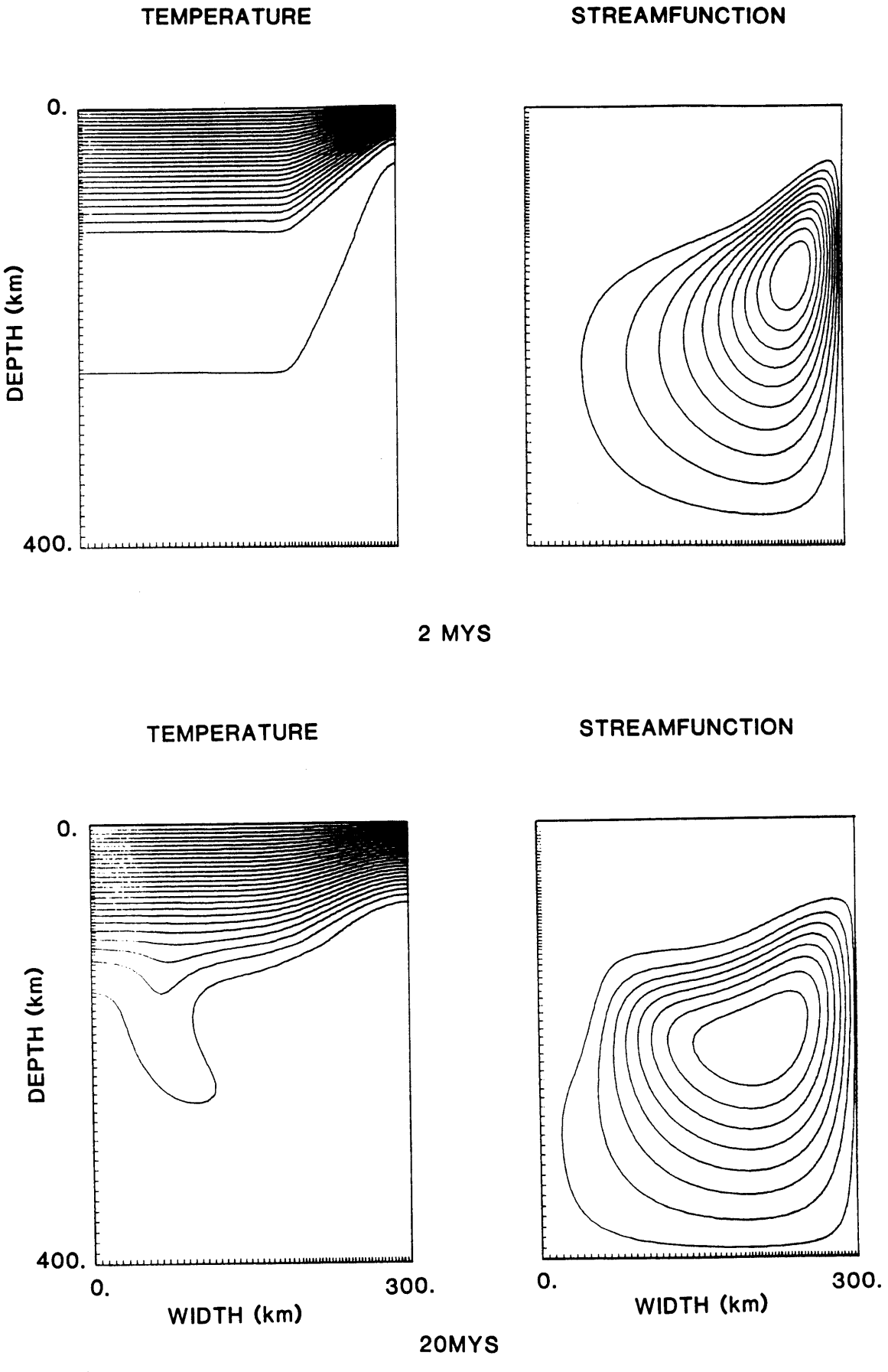
TEMPERATURE
STREAMFUNCTION
0.
DEPTH (km)
400.
2 MYS
TEMPERATURE
STREAMFUNCTION
0.
DEPTH (km)
400.
0.
300.
WIDTH (km)
0.
300.
WIDTH (km)
20MYS

Figure 4.4

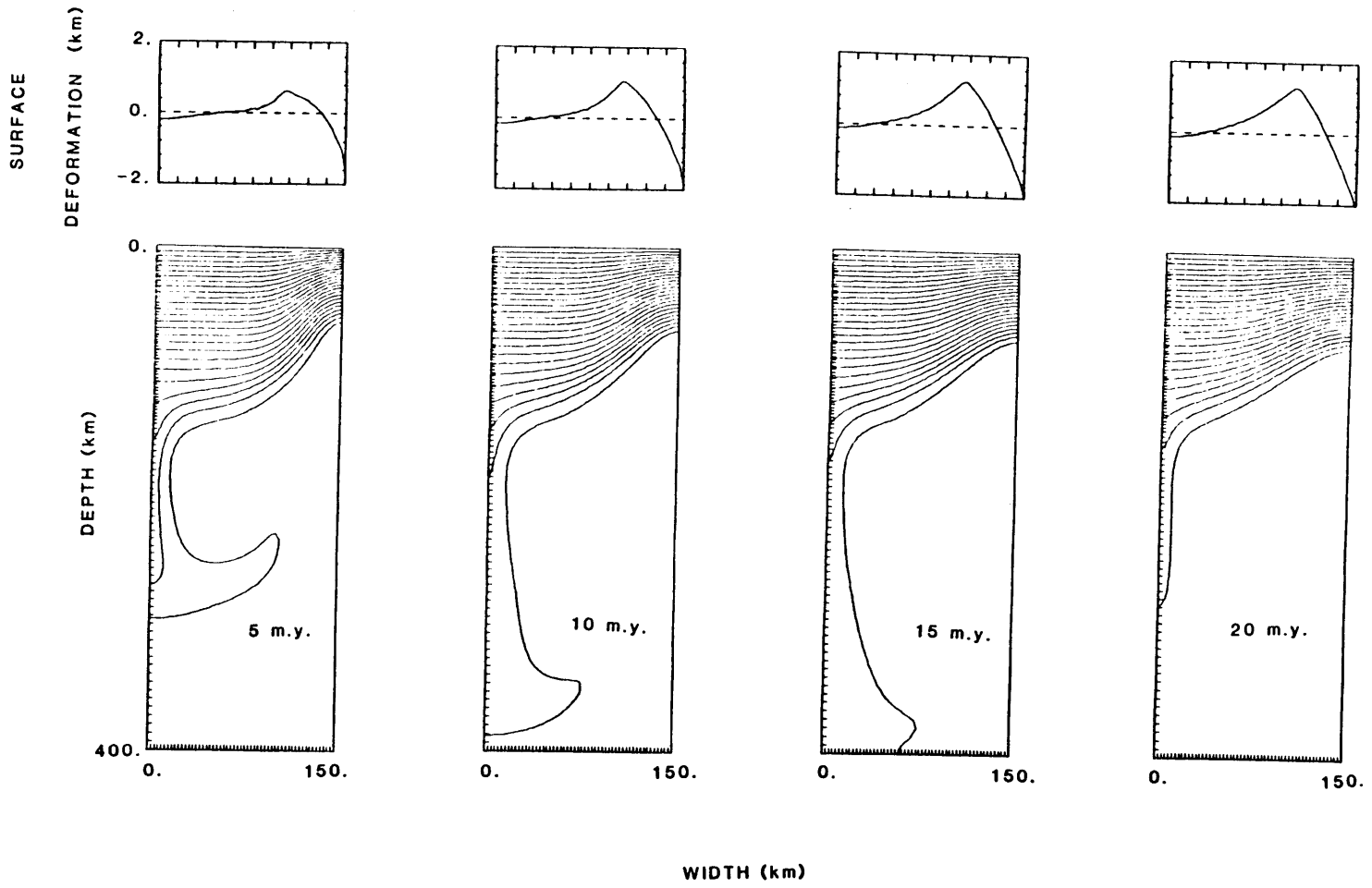
SURFACE DEFORMATION (km)
2.
0.
-2.
DEPTH (km)
0.
400.
5 m.y.
10 m.y.
15 m.y.
20 m.y.
0.
150.
WIDTH (km)

Figure 4.5

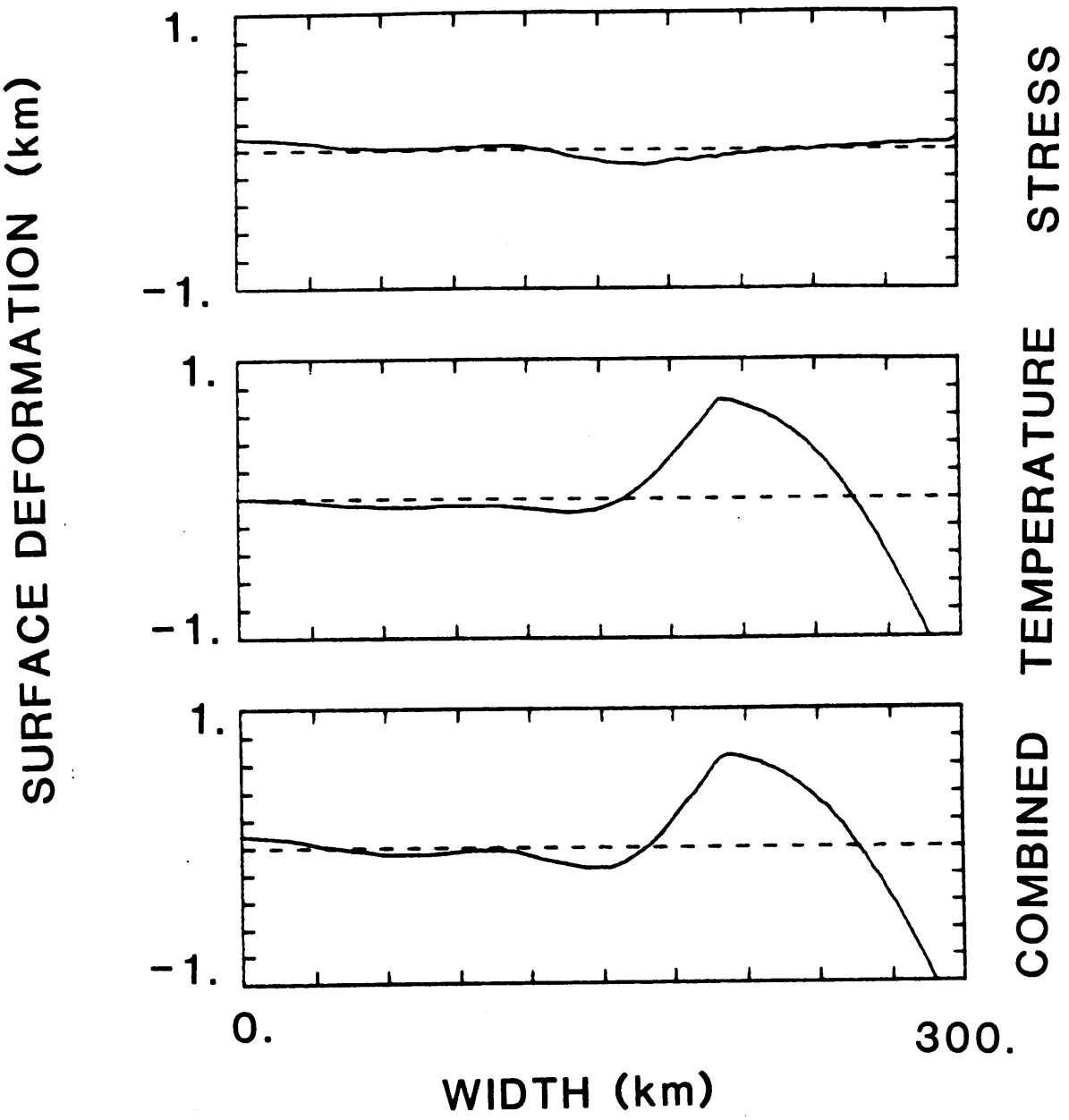
SURFACE DEFORMATION (km)
1.
-1.
STRESS
1.
-1.
TEMPERATURE
1.
-1.
COMBINED
0.
300.
WIDTH (km)

Figure 4.6

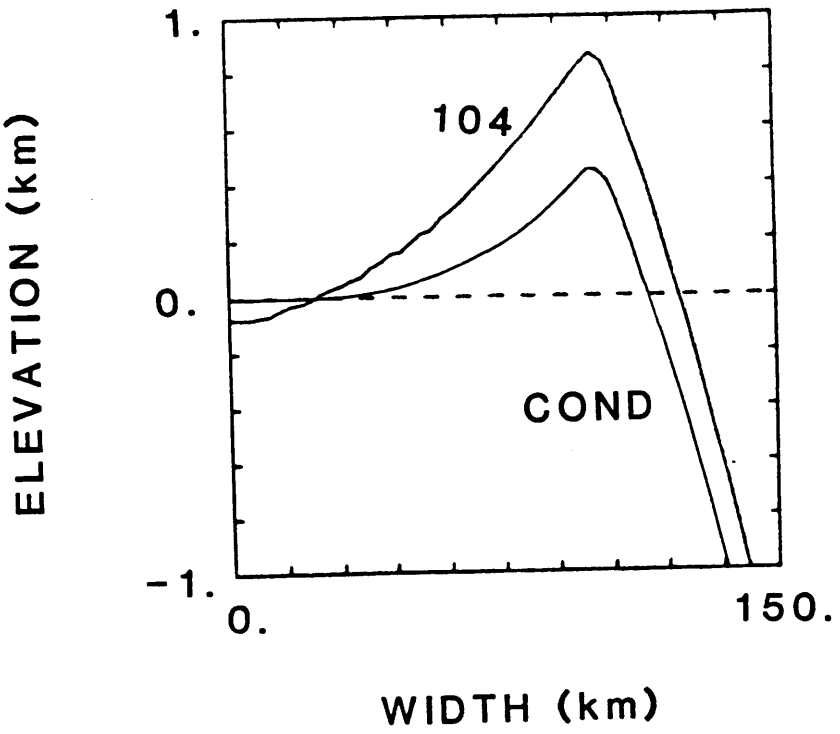

Figure 4.7

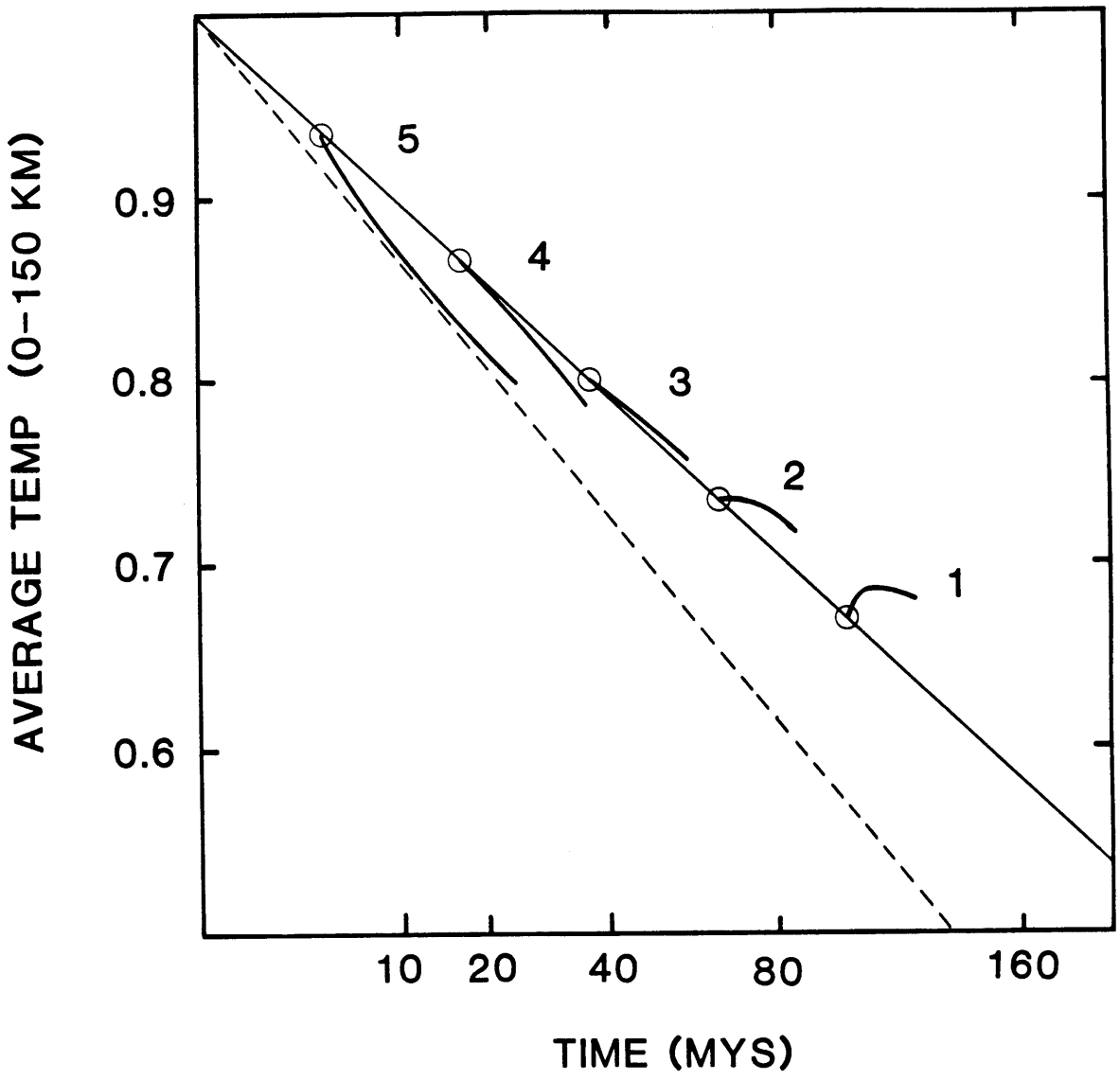

Figure 4.8

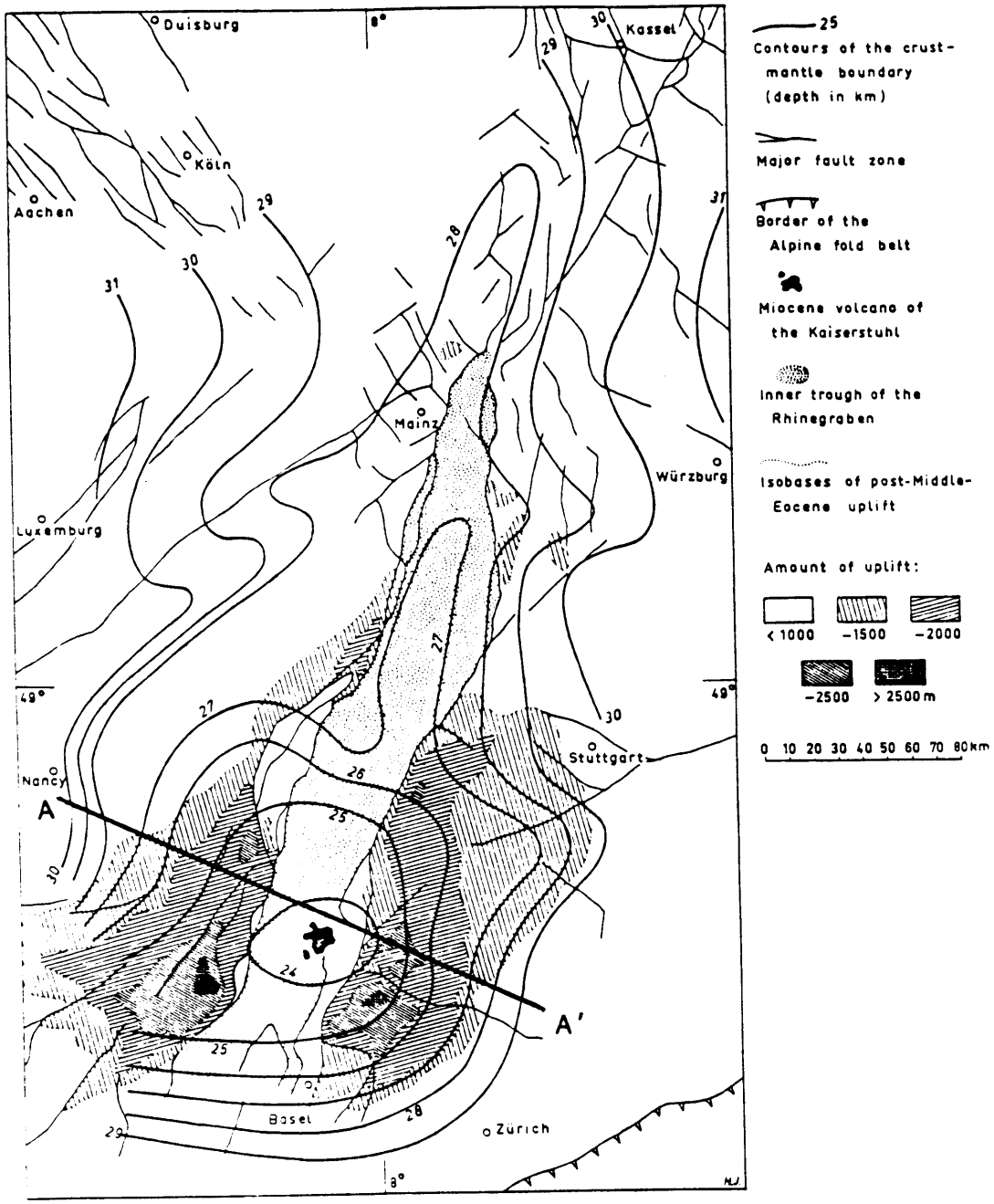
Duisburg
Kassel
Köln
Aachen
Mainz
Würzburg
Luxemburg
Stuttgart
Nancy
Basel
Zürich
A
A'
8°
49°
25
Contours of the crust-mantle boundary (depth in km)
Major fault zone
Border of the Alpine fold belt
Miocene volcano of the Kaiserstuhl
Inner trough of the Rhinegraben
Isobases of post-Middle-Eocene uplift
Amount of uplift:
< 1000
-1500
-2000
-2500
> 2500 m
0 10 20 30 40 50 60 70 80km

Figure 4.9

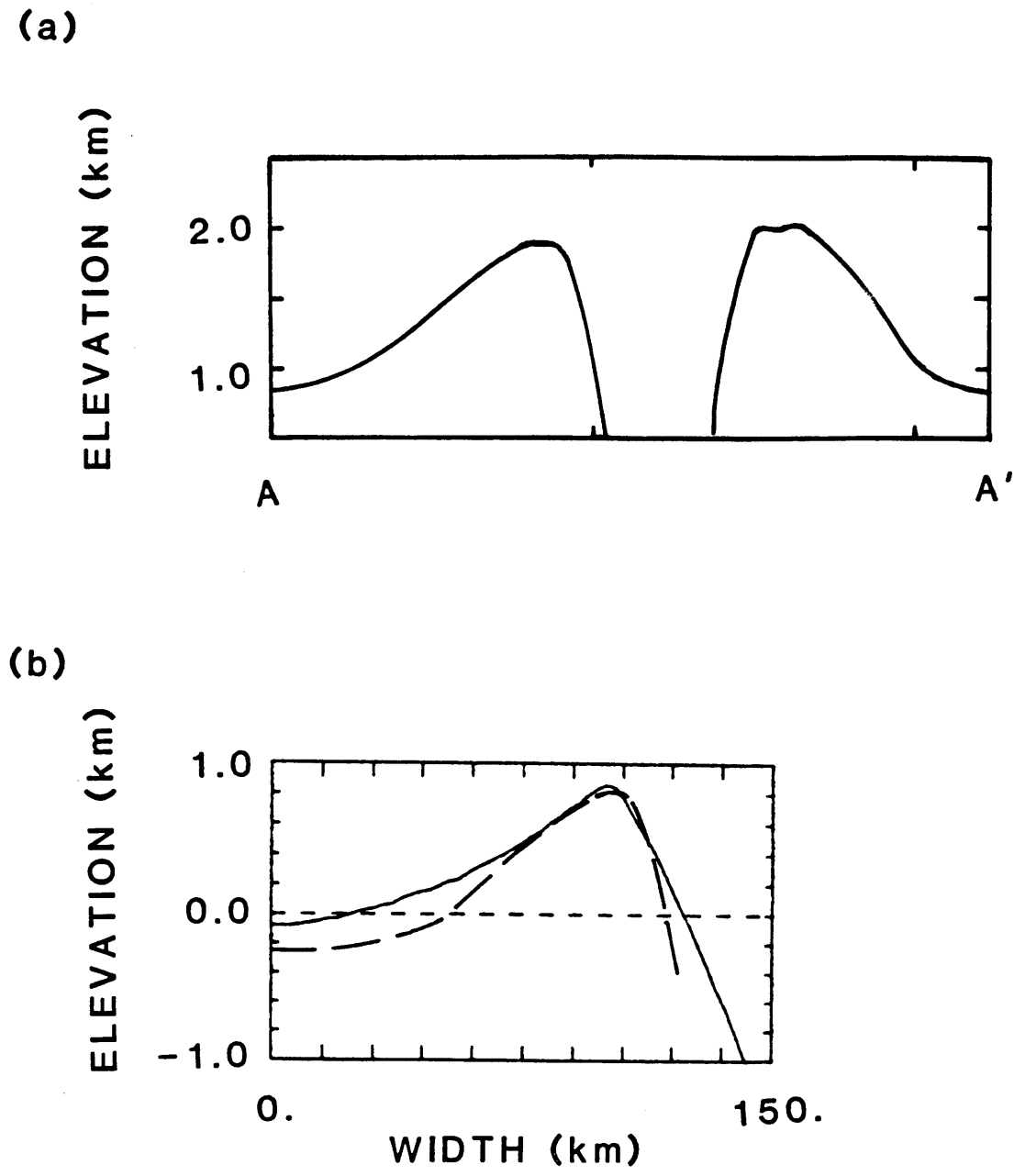

Figure 4.10

"Deep in the human unconscious is a pervasive need for a logical universe that makes sense. But the real universe is always one step beyond logic."

-From "The sayings of Muad'Dib" by Princess Irulan.

CHAPTER 5

MECHANISMS OF DEFORMATION IN CONTINENTAL CONVERGENCE ZONES

5.1 Introduction

The growth of continents occurs primarily by the collisions and suturing of continental fragments. Subduction of the lithosphere under a continent may eventually lead to the convergence of two continents. Unlike the oceanic crust and lithosphere, a continental plate cannot be subducted easily because of the lower density of the continental crust and the resulting bouyancy forces. If the convergence continues after the initial collision of continents, this leads to faulting and mountain ranges (Dewey, 1980; Dewey and Bird, 1970; Bird et al., 1975). A consequence of such a collision is a thickening of the crust, not only in the collision zone, but also under elevated plateaus (such as Tibet and the Iranian Plateau) that may develop behind the mountain ranges.

As in the preceeding three chapters the main focus of this chapter is a study of the interaction of convection in the asthenosphere and the thermal lithosphere. In this chapter

we consider the hypothesis that convective thinning of thermal boundary layers which have been thickened by processes of continental convergence can be rapid enough to explain geologic data on the thermal evolution of such regions. High surface heat fluxes are measured in Tibet, which we take to be the archtypical convergence zone, less than 40 m.y. after the crust there was thickened by a major continental collision. Thickening of the crust acts to reduce the temperature gradients and so the surface heat flux in proportion to the amount of thickening. Simple thermal modelling requires that the temperature gradients in the mantle lithosphere must have been near normal or higher during most of the time since the thickening of the crust in order to supply sufficient heat to the base of the crust to match the heat flow data. If the mantle lithosphere were thickened along with the crust then it would have to be thinned by some prosess in 10-20 m.y. to match the constraints of the simple thermal models. This is the scenario suggested by Houseman et al. (1982) and is the possibility we test using numerical calculations which are similar to those described in earlier chapters. One difference between this and previous chapters is that the results of these numerical experiments indicate that convective effects cannot explain the geologic data under consideration. Therefore, we explain a model for the thickening of the crust in Tibet which explains the geologic data because it does not involve lithospheric thickening.

In this chapter we will first review previous studies on

the convective thinning of the lithosphere due to instability of the thermal boundary layer at the base of the lithosphere. The data on crustal thickness and present thermal state of Tibet are reviewed as are calculations which indicate the amount of mantle heat flux required for crustal melting (from Toksoz et al., 1981). Numerical calculations on the rate of convective thinning of a lithosphere with viscosity which is a strong function of temperature are presented and the results are discused in relation to the data. Finally, a model of crustal thickening in Tibet is presented which does not involve thickening of the mantle lithosphere.

5.2 Previous Work

A schematic of homogeneous lithospheric thickening, which is discussed here, is shown in Figure 5.1. The question of the stability of thickened lithosphere has been treated for the case of a lithosphere made of several constant viscosity layers by Fleitout and Froidevaux (1982). They found that such a thickened lithosphere is unstable and can be convectively removed in a relatively short time. Houseman et al. (1981) looked at the long term evolution of a unstable thickened lithosphere. They modeled the lower lithosphere and asthenosphere as having the same constant value of viscosity. They found that a lithosphere which was in equilibrium with a background mantle heat flux and then thickened to twice it original thickness could be convectively thinned to its original thickness in only a few m.y. We feel that this

conclusion is a result of the very simple treatment of the boundary between the constant viscosity convecting region and the conductive lid above. The position of the boundary between the asthenosphere, where heat is primarily transfered by convection, and the rigid lithosphere, where the heat transfer is all by conduction, is critical to this problem. In the Houseman et al.(1981) treatment this boundary was set at a given depth and does not depend on the temperature there. When the lithosphere was thickened this depth was not changed, although the temperature at that depth decreased by nearly a factor of 2. Figure 5.2 shows the effect of thickening the lithosphere on a temperature and a viscosity profile of the mantle. That the viscosity of the mantle depends strongly on temperature has long been accepted (eg. Stocker and Ashby,1972; Weertman and Weertman, 1975). For lithospheric boundary layers to go unstable at all the viscosity in the region must be lower than the average mantle value of about 10^{21} Pa-s determined from post glacial rebound (Cathles,1975). Considering a temperature dependent viscosity, but neglecting the effect of pressure on viscosity Yuen, Peltier and Schubert (1981). They find that boundary layers with a minimum viscosity of 10^{21} Pa-s should not be unstable even if they are as thick as those considered by Houseman et al. (1981) or in the present study. As noted in Buck (1983) the dependence of viscosity on pressure allows the viscosity at the bottom of the boundary layer to be much lower than the value at greater depth. Thus low viscosities in the thermal boundary layer can

be consistent with the average viscosity of the mantle being much higher.

5.3 Data and Models of the Effects of Crustal Thickening

Among the mountain ranges which have clearly resulted from continental collisions are the Zagros, the Himalayas, the Alps, the Urals and the Southern Appalachians (Bird,1978a). Thrusting and folding in the crust caused thickening of the crust in all these ranges and may have been accompanied by thickening of the lithosphere through internal deformation. The Himalayas are associated with a large region, the Tibetan plateau, where the crustal and lithospheric deformation is apparently of this type. Geological and geophysical data indicate that the crust there is abnormally hot today. Since Tibet is the only mature example of such a plateau it is discussed in detail.

Tibet is an area where the crust has been thickened over 700,000 km^2. The crustal thickness over most of the plateau is about 70 km, nearly twice as great as normal continental crust. This has been determined by surface wave studies (Bird and Toksoz,1977; Feng and Teng,1983) and refraction lines reported by Teng et al.(1981) and Hirn et al. (1984a) in the plateau and by Hirn et al. (1984b) in the northern Himalayas. This is consistent with the average elevation of five kilometers being isostatically compensated (Bird,1978). Figure 5.3 show the topography and crustal thickness for a profile across Tibet. The crust of Tibet was accreted onto

Asia in several sections over about 150 million years as estimated from the ages of syntectonic granites in regions taken to be the suture zones between these sections (Gansser, 1980; Zhou,1981; Allegre et al., 1984). The timing of the crustal uplift and thinning is disputed, but paleobotanical evidence indicates that the uplift post-dates the collision of India and Asia (Xu, 1980). The Indian collision occured about 40 myrs ago (Gansser, 1966; Powell and Conaghan, 1973; Molnar and Tapponnier, 1975). The northern part of the plateau has widespread calc-alkaline volcanics of Cenozoic age, presumably derived from melting of the lower crust (Dewey and Burke,1973). There are also numerous hot springs indicating higher than normal crustal temperatures (Tong and Zhang, 1981). Heat flow measurements in Southern Tibet described in Francheteau et al. (1984) are greater than average values for the continental crust. There are also large spatial variations in the heat flow values which they associate with recent emplacement of magma bodies. Furthermore, the attenuation of certain periods of surface waves may be an indication of partial melting of the lower crust (Bird and Toksoz,1977).

In previous work (Toksoz et al.,1981) the thermal effects of the thickening of the crust have been considered. In that work the mantle heat flux was varied and only the temperatures in the crust were monitored. The same assumption was used in that work and the present one as to the way the crust deformed. The deformation was taken to be by internal strain

rather than by crustal scale underthrusting suggested by Powell and Conaghan (1973). The formulation of numerical calculations of conductive heat transport through crust which is thickening is illustrated in Figure 5.4. The one dimensional heat flow equation (simplified from equation A.1) is solved at sucessive time steps on a Lagrangian finite difference grid. Figure 5.5 shows positions of isotherms in the crust as a function of time after the initiation of crustal thickening for different amounts of shear heating in the crust, crustal radioactive content and mantle heat fluxes. It was found that neither shear heating nor redistribution of radioactive rich layers in the crust could lead to crustal melting without greater than normal heat flux from the mantle. An average of at least 0.8 HFU from the mantle was required.

Three mechanisms to give a thin lithosphere and thus a large mantle heat flux have been proposed. (1) The entire lithosphere could be removed by "delamination" or peeling away from the crust (Bird and Baumgardner,1981); This hypothesis is not advocated because because seismic data for old continental cratons indicates that the lithosphere there is very thick (Leveque, 1981; Grand and Helmberger, 1982). The lithosphere could not be so thick if it were subjected to frequent removal. (2) An extremely large amount of the lithosphere could be convectively removed (McKenzie, 1978; Chen and Molnar, 1981; Houseman et al., 1981). This is critically examined using the numerical experiments which are described in this chapter. (3) The lithosphere could have been thin at

the time of the collision of India (Dewey and Burke,1973; Toksoz and Bird,1976; Toksoz et al.,1981; Buck and Toksoz, 1982). This third possibility is consistent with the observation that only tectonically young areas of lithosphere (which should be hot and thin) were deformed by the collision of India with Asia (Molnar and Tapponnier, 1981).

5.4 Numerical Model Description

The philosophy behind the approach used here is to consider the simplest possible set up for the calculations which retains the basic physics of the problem. In the treatment used in this chapter the boundary between the rigid and flowing regions was not specified, but came out of the calculation. This was a result of the temperature dependence of viscosity. In low temperature regions the viscosity increases to values so high as to preclude significant flow. Heat had to be conducted into these areas to allow them to flow. As cooling or heating of a region occured the boundary moved. It should be emphasized that the most important result presented here does not depend on particular values of the viscosity parameters. It results from a moderate level of dependence of the viscosity of the mantle on temperature. The non-dimensional equations of energy, mass and momentun conservation for the variable viscosity case are given in the appendix. They are solved explicitely on a finite difference grid with time stepping in the energy equation. The areas considered correspond in the study to a 700 x 700 kilometer

region of the mantle when dimensionalized according to the parameters given in table 2.1, but with the length scale set at 700 km. This size allows for three or more convective rolls to develop in all cases. The relation between temperature, pressure and viscosity is a standard one applicable to creep, taken from Weertman and Weertman (1975) and is given in the appendix.

The variations in viscosity define the flow boundary for this problem, as was found in the linear stability analysis of variable viscosity boundary layers by Jaupart(1981), and no arbitrary boundary need be used. The boundary for the flow is the top of the lithosphere, but it is computationally more efficient to place a no slip boundary at the depth in the lithosphere where the viscosity is 10^{22} poise. This is between 2 and 3 orders of magnitude above the minimum viscosity in the flow region. Runs with the boundary placed higher in the lithosphere, where the viscosity was 10^{23}, poise gave the same results, but required at least twice the computer time. The side boundary conditions on the flow were stress free, except in the case of one model with periodic conditions (case 1). The bottom boundary is always taken to be stress free. The boundary conditions on the energy equation are fixed temperature (corresponding to 273 °K) at the top and insulating on the sides and bottom. Case 1 had periodic conditions on the side temperatures.

The initial temperature profile for cases 1-7 was derived from purely conductive half-space cooling of an initially isothermal material, with diffusivity given in table 1, for a

given length of time. This temperature profile was then stretched in depth by a factor of two to simulate lithospheric thickening. Figure 5.2 shows an initial and thickened temperature profile along with the corresponding viscosity profile. Next, a random temperature perturbation (between 0° and 1° K) is given to each grid point. Without perturbations the instabilities would not be initiated in the calculations. The initial flow velocities are zero. In the periodic test a periodic perturbation was given to excite a particular wavelength of flow. This thickening of a conductive temperature profile is not the same procedure used by Houseman et al.(1981), where the temperature structure resulting from a convection calculation was stretched vertically for the initial condition. This procedure of achieving a steady state is costly in terms of computer time for the variable viscosity calculations, where runs take 20-50 times the computer time for the comparable constant viscosity calculations. Thus, only in cases 8 and 9 were the initial conditions gotten by thickening a steady state temperature structure in the region of calculation. After steady state had been reached the top quarter of the box was doubled in thickness while the rest of the box was thinned so the depth extent of the box was not changed.

In the first cases no heat sources were incorperated and only the falloff of the unstable boundary layer was followed. Later internal heat generation which would result in smaller equilibrium lithospheric thicknesses than existed at the start

of the calculation were used. This was done to see how quickly equilibrium thicknesses would be approached. The runs were generally carried out to times that correspond to at least 40 million years, since this is the time since the lithospheric thickening commenced in Tibet.

Resolution of the solutions on the grids used here were guaranteed in two ways. First, the numerical experiments were done on successively refined grids until the same results were achieved on two different grids. Second, the heat flux out of the grid and the internal heat generation were compared to the rate of change of the average temperature of the region to ensure conservation of energy. The grids used were at least 56x56 points with even spacing in the horizontal direction and varible mesh spacing in the vertical. The variable spacing of points allowed the needed resolution in the regions of the largest gradients of viscosity and flow, without an excessive number of points overall. The grid positions are shown in Figure 5.6 as tick marks around the boxes.

5.5 Results

The cases considered here are sumarized in table 5.1. The parameters varied were the bondary conditions, the reference viscosity, the heat sources, the effective activation volume (V^*), defined in chapter 2, the activation energy (E) and the time of the initial conductive cooling (which effectively changes the initial lithospheric thickness). The heat sources are up to 3 times values estimated for the average mantle

(Ringwood,1975), but are meant to include the effect of both internal heat production and heating from below. The activation volume, V^*, was varied within the range of experimentally determined values for olivine as was done for the activation energy E^*. The range of activation volume is 10-20 cm^3/mole (Kohlstedt et al.,1980; Sammis et al.,1981) and for activation energy is 70-125 kcal/mole (Goetze, 1978). The reference viscosity was set so as to give viscosity mimina in the asthenosphere under young lithosphere close to the estimates of the viscosity there (Passey,1981; Richter and McKenzie,1978). Each case required between 3 and 9 hours of c.p.u. on a Vax 11/780 computer.

Case 4 resulted in the greatest convective thinning of the lithosphere for the cases with a conductive initial condition, so it will be discussed in detail and be used as a reference when discussing the other models. Figure 5.6 shows snapshots at 10 million year intervals of the isotherms and streamlines of the flow for this case. The boundary layer can be seen flowing down in a droplet-like fashion. The horizontally averaged temperature profile shows that the thermal lithosphere is not greatly thinned over the 40 my period. Figure 5.4 is a more quantative picture of the variation in the thickness of the lithosphere through the duration of the run. It shows the variation to the depth where the horizontally averaged viscosity equals a constant value (either 10^{20} or 10^{19} Pa-s). The base of the lithosphere could be defined as the place where the viscosity reaches such a value. Figure 5.7

shows that the depth to the 10^{20} Pa-s level has changed neglibly during the calculation. The 10^{19} Pa-s level has changed about 20 percent in this time.

To quantify the vigor of the flow at different times, the average dissipation for the flowing region was calculated. Figure 5.8 shows that the maximum horizontally averaged rate of dissipation (e^2) in case 4 occurs at a depth just below the lithosphere, at about 150 kilometers. It also indicates that there is a depth range over which the flow is much more vigorous than above and below. This is due to the viscosity structure having a minimum in that region. The reason for the low between two highs is that the vertical flow occurs only in narrow zones. The horizontal averaging emphasises the top and bottom of the convection cells where the flow is horizontal. The average dissipation (D) is proportional to the integral of the strain rate squared $(e)^2$ over the area(A):

$$D = \iint \dot{e}^2 \, dA \quad . \tag{5.1}$$

Figure 5.9 shows the average dissipation through time for all cases except number 5 which was not on scale and 8 and 9 where the average dissapation was nearly constant. In all cases the maximum dissipation was associated with the first convective removal of the conductive boundary layer. This maximum took over 20 mys to develop in runs 1-7. In the cases with internal heat sources the high rate of flow is maintained through the rest of the run. But, as shown in Figure 5.7, the bulk of the

convective thinning is associated with this boundary layer removal and not with ablation due to the heat sources and rapid flow rates.

Another measure of the difference between the results is the dissipation weighted viscosity of the flow region. This average viscosity is defined following Parmentier (1978) in equation 3.10. This quantity was calculated for all the cases and it is tabulated along with other output information in table 5.2. The average viscosity was fairly constant over the time of the calculations, but is tabulated a time 20 million years into the runs. This parameter is useful in calculating an average Rayleigh number for the varible viscosity flow region. The average Rayleigh number is defined in equation 3.7. Parmentier (1978) has shown that this parameter bears the same relationship to the heat flux across a region convecting in steady state as does the Rayleigh number in a constant viscosity case. There is ambiguity in the calculation of this parameter since the length scale of the flow is not clearly defined. One way to estimate this scale is to take the depth extent of the region where dissipation is within a factor of ten of the maximum horizontally averaged value. For case 4 it gives a value of 250 kilometers for the length scale and $1.x10^5$ for the Rayleigh number. Unlike the calculations discussed in chapters 2 and 3 there is little time in the calculation when the convective flow and the boundary layer are in equilibrium (i.e. with a boundary layer thickness which scales with the Rayleigh number). During most

of the calculation the very thick boundary layer is falling off and the convective pattern is changing. Once this period is over and transient equilibruim is established it is a simple matter to estimate the rate of thinning of the lithosphere due to the convective supply of heat to the base of the lithosphere, as will be described in the discussion section.

Case 1 shows that the higher the reference viscosity the lower the maximum dissipation rate for the flow. The high rate of dissipation early in the run was due to the periodic initial conditions which forced coherent flow quickly. This is the only case where the 10^{20} Pa-s level moved down through the calculation. This was due to the high effective viscosity and lack of heat sources for the model. Case 2 indicates that the removal of the lower lithosphere can result in a thinner lithosphere even without heat sources. Case 3 shows that the inclusion of small heat sources does not greatly affect the thinning of the lithosphere over 40 mys. In case 5 the doubling of the pressure dependence of viscosity (V^*) raised the effective viscosity and narrowed the depth range of vigorous flow. The boundary layer was still unstable in this case but was not removed over the time of the calculation. Case 6 demonstrates that the thicker the lithosphere the slower the flow in response to boundary layer instablities. The effective viscosity and maximum dissipation were low in this case. Case 7 shows that increasing the temperature dependence of viscosity (E^*) by 20 percent had a small effect

on the maximum dissipation, but that the lower lithosphere was made more resistent to convective thinning.

The two runs which started with thickened steady state profiles (8 and 9) showed that the rate of thinning of the lithosphere is not greatly increased relative to the cases with simpler initial conditions. This is due to two offsetting differences between these cases and the others. The fact that the most rapid change in the lithospheric thickness is due to the removal of the thickened boundary layer and that layer was thicker for the other cases. But, the convective pattern and temperature variations were already established at the beginning of the calculation for cases 8 and 9 there was no period of slow increase of the vigor of the flow. Case 8 had the same viscosity parameters as case 4 and showed a slightly greater decrease in the depth to the 10^{20} Pa-s level (table 5.2)during the calculation while the depth to the 10^{19} Pa-s level changed by about the same amount in the two cases. Case 9 shows that decreasing the temperature dependence of the viscosity could be offset by an increase in reference viscosity.

5.6 Discussion of Numerical Results

In all of the cases considered of the effect of the instability of thickened varible viscosity lithosphere on the rate of thinning of the lithosphere was not sufficient to bring it to equilibrium thickness in 40 mys when the lithosphere was initially (before thickening) about 100 km

thick. This was true over a wide range of experimentally determined parameters controlling the viscosity of the lithosphere and asthenosphere. The difference between these results and those of Houseman et al.(1981) are due to the inclusion of viscosity which depends on temperature and pressure, which we consider to be more consistent with laboratory data on the materials thought to constitute the mantle. The effect of temperature dependent viscosity is to limit the temperature range over which convective heat transfer dominates that by conduction. This has been noted in the calculations of Jaupart (1981), Christenson (1983), Fleitout and Yuen (1984a, 1984b) as well as in the results of the preceeding chapters. The temperature difference across a convecting region depends on the rheology assumed for that region and so may be termed the rheological temperature scale (ΔT_r). This temperature scale also depends on the Rayleigh number of the flow, but as shown in chaper 3 this dependence is generally not as important as the temperature dependence of viscosity. As noted by Christenson (1983) the effect of stress dependent viscosity is to reduce the effective temperature dependence of viscosity by an amount which depends on the Rayleigh number, but for the Rayleigh numbers considered here this effect should not be great. The value of ΔT_r in the calculations described here seldom exceed 100 °K. Thus, the temperature drop across the thickened thermal boundary layers, whose removal accounts for the relatively rapid thinning of the lithosphere, is about this value. The

slower stage of thinning of the lithosphere shown in Figure 5.7, must involve conduction of heat into the conductive lid and ablation of the material which has been heated and softened.

Inclusion of large internal heat sources in the model mantles for cases 3 to 9 maintained a higher level of vigor in the flow than for cases 1 and 2, but still did not result in rapid thinning of the lithosphere through ablation. For the cases which had heat sources the lithosphere would eventually return to an equilibrium thickness, but on a time scale of much greater than 40 m.y. The calculations of chapters 2 and 3 show that the heat flux out of the convecting region depends on its temperature. If the rate of heat generation within the region is less than the heat flux out of it then it cools and the heat flux goes down. Once we estimate the amount of material which can be quickly removed we can calculate the time required to thin the lithosphere due to heat sources in the mantle.

A simple calculation, based on the formulation of Crough and Thompson (1976), can be used to do this. This is illustrated in Figure 5.10 which shows an initial lithospheric thickness (Z_i) with a linear temperature gradient ($T_i(z)$). We calculate the time required to thin the lithosphere to a final thickness (Z_f), which is half the initial thickness, due to a uniform heat flux from below. By considering the heat flux out of the surface to be constant and equal to its initial value (KdT_i/dz) we can calculate the time required to input

sufficient heat to change the temperature profile to the linear gradient ($T_f(z)$) on the figure). The heat flux into the lithosphere from the constant temperature region below is taken to be constant and equal to the equilibrium flux through a lithosphere of thickness Z_f (i.e. KdT_f/dz). The time (t) required to do this is shown on Figure 5.10 as :

$$t = \frac{Z_i^2}{4\kappa} \qquad (5.2)$$

where κ is the thermal diffusivity. Taking κ to be 10^{-6} (m^2/s) and Z_i equal to 200 km, the time given by equation 5.2 is 320 m.y. This corresponds to a lithosphere that was only 100 km before hypothetical thickening of the lithosphere by a factor of two. Inclusion of the radioactive heat sources in the crust will decrease this estimate a small amount. To thin the lithosphere on a time scale appropriate for Tibet requires much higher than normal mantle heat fluxes. In a study of the effect of mantle plumes Spohn and Schubert (1982) find that 300 km thick lithosphere could be locally thinned to half this thickness in 50 mys, but this required 5 times the normal mantle heat flux.

A reasonable value of the pre-collisional thickness of the lithosphere in Tibet comes from using the tectonic age of the lithosphere (age since the last tectonic and thermal disturbance). This has been estimated for the different parts of Tibet by Molnar and Tapponier (1981). This age should

correlate with lithospheric thickness in much the same way that the thickness of the oceanic lithosphere correlates with its age. At the time of the collision of India with Asia Northern Tibet had a tectonic age of about 150 m.y. while southernmost Tibet might be said to have had an age of zero. An average value of lithospheric thickness at the time of the collision is about 100 km. Thus, homogeneous thickening of the lithosphere would produce a 200 km thick lithosphere while thickening the crust to 70 km. Values of heat flux which would be required to thin a 200 km thick lithosphere by one half in 20 m.y., as is required by the thermal models of the crust, would be about 15 times greater than that required to maintain the lithosphere at a thickness of 100 km. Such fluxes are unlikely to exist over the entire region of the Tibetan plateau.

5.7 Speculative Model for Convergence Zone Crustal Thickening

To get around the problem of the present-day high heat flow, without requiring that the lithosphere be unusually thin before the collision, we suggest that the mantle lithosphere was not thickened in the process of horizontal compression after the collision. In this model horizontal shortening of the lithosphere is accomplished by mantle lithospheric subduction in a number of locations through the plateau. At each area of intracontinental subduction, the process of scraping off of the crust should be similar to the process which is now believed to occur under the Himalayas based on the gravity model of Lyon-Caen and Molnar (1983), illustrated in

Figure 5.11. In this model the lithosphere must have some elastic strength to transmit stresses over hundreds of kilometers. The oceanic lithosphere is assumed to transmit stresses over long distances (Richardson et al., 1979). Though the continental lithosphere may be weaker than the oceanic (England, 1983) it should do the same. It has been noted before that a large fraction of the convergence in several areas of continental collision (McKenzie, 1972; Molnar and Tapponier, 1976) seems to be concentrated along large strike slip faults. In this model of deformation the continents behave in an intermediate manner between rigid plates and a continuum with uniform properties as used by Molnar and Tapponier (1976). For a continental convergence zone the weakest places are expected to break first. These might be the former sutures between the fragments such as those which make up Tibet. The localized nature of subduction zones is consistent with relative weakness of those regions. The nature of this weakness is uncertain, but non-linear rheology for the lithosphere can contribute to the continued weakness of an area where strain rates are high (Kopitze, 1979; Jacoby and Schmeling, 1982). Intracontinental mantle lithospheric subduction should lead to the build-up of thicker crust in these areas. The stresses necessary to maintain the local elevation of the thickened crust may exceed a critical value required to initiate lithospheric subduction in an adjacent area. The form of local crustal thickening and viscous flow of the crust in response to its elevation are discussed below. Figure 5.12 shows an idealized possible

sequence of events for the crustal thickening in Tibet, which may apply to other convergence zones. The multiple sites of mantle lithospheric subduction shown there may not have been active at the same time.

Recent field work in Southern Tibet has shown that the crust north of the Yarlung Zangbo suture is not uniformly deformed, but is largely free of folding and faulting (Allegre et al., 1984). Large-scale thrust faulting seems to occur in narrow regions. This argues against the mechanism of fairly homogeneous thickening of the crust and lithosphere in Tibet since the collision of India (see Figure 5.1). Paleobotanical evidence that the entire plateau was uplifted fairly uniformly (Xu, 1981) and that the Himalayas were uplifted later than the plateau are consistent with this model. In this model the reason for the late formation of the Himalayas is that the cold craton of India could only be fractured when sufficient elevation had been built up on the plateau that kilobar stresses were needed to maintain it. Another mechanism for crustal thickening is that of underthrusting of India at the suture with Tibet, with crustal material being scraped off (Powell and Conaghan, 1973), but this would lead to an uplift of Southern Tibet before the rest of the plateau.

A new question is raised by this model which makes us consider temperature-dependent mechanisms of crustal thickening (Buck, 1984). Why is the topographic relief so different for the Himalayas than for Tibet, if we propose a similar process for crustal thickening? If the crustal temperature profiles

were 20-30 percent higher in Tibet, then the lower (ductile) crust could be thicker and lower in viscosity as shown in Figure 5.13. This would allow only a relatively small amount of topographic relief to be maintained. The equation for the average velocity ($\bar{u}$) of material with a constant viscosity (μ)in a horizontal channel (Turcotte and Schubert, 1982) is:

$$\bar{u} = \frac{H_1}{12\ \mu} \cdot \frac{dP}{dx} \qquad 5.3$$

where H_1 is the thickness of the lower crustal channel and dP/dx is the horizontal pressure gradient due to topographic variations We find that 1 km of elevation difference spread over 100 km lateral extent would drive lower crustal flow at 3 cm/year average velocity if the average viscosity of the lower crust were 10^{19} Pa-s and it was 20 km thick. If average lower crustal temperature were 100°C higher given estimates of the rheology of the lower crustal materials (Caristan, 1982; Brace and Kohlstedt, 1980) then flow would be ten times slower. Thus, with convergence "pumping" material into a deforming region at several cm/year, only small amounts of relief could be supported if crustal temperatures are high as we suppose them to be in Tibet. On the other hand, the Himalayas are thought to be formed by breaking of what was part of the stable and cold Indian craton with a much greater tectonic age than Tibet. The much cooler temperatures for a craton (Sclater et al. 1980) would allow the build-up of considerably topographic relief without significant viscous flow of the lower crust.

5.8 Conclusions

We first considered thermal models for the crust which has been thickened in convergence zones and found that mantle heat fluxes of at least 0.8 HFU were needed to account for the partial melting of the thickened crust. There is evidence that the crust in Tibet is partially melted and that this is related to the thickening of the crust which began 40 m.y. ago. Finite amplitude numerical calculations showed that convection in fluids with temperature dependent viscosity would not be sufficient to thin the lithosphere at the same rate that it thickened if it were homogeneously thickened at the same rate as the crust in Tibet. Therefore the mantle heat flux would go down during thickening. If the lithosphere were 100 km thick before being homogeneously thickened then the mantle heat flux would the not return to its initial value for several hundred million years. A simple mechanical model is suggested to get around the difficulty of maintaining a constant moderate mantle heat flux in an area of crustal thickening.

TABLE 5.1

Case	Reference viscosity ($x10^{18}$ Pa-s)	Side boundary condition	Heat sources ($ergs/cm^3$)	$V^*(cm^2/mole)$	E^*(kcal/mole)	Initial cooling time(myrs)
1	2.5	periodic	0.	10.	100.	40.
2	1.0	free	0.	10.	100.	40.
3	1.0	free	$2.14x10^{-7}$	10.	100.	40.
4	1.0	free	$6.42x10^{-7}$	10.	100.	40.
5	1.0	free	$6.42x10^{-7}$	20.	100.	40.
6	1.0	free	$6.42x10^{-7}$	10.	100.	80.
7	1.0	free	$6.42x10^{-7}$	10.	120.	40.
8	1.0	free	$6.42x10^{-7}$	10.	100.	steady state
9	10.0	free	$6.42x10^{-7}$	10.	50.	steady state

Table 5.1. Descriptions of the cases considered for the numerical calculations.

TABLE 5.2

Case	Effective viscosity (Pa-s)	Max. Average Dissipation (dimensionless)	Change in depth(km) of viscosity level (10^{20} Pa-s)	(10^{19} Pa-s)
1	6.5×10^{19}	2.8×10^{6}	-1.9	*
2	3.0×10^{19}	1.8×10^{7}	2.4	*
3	2.8×10^{19}	2.3×10^{7}	3.9	48.4
4	2.5×10^{19}	3.5×10^{7}	7.0	49.1
5	1.4×10^{20}	6.0×10^{1}	4.4	*
6	8.6×10^{19}	5.0×10^{5}	1.3	*
7	2.3×10^{19}	2.2×10^{7}	3.5	36.4
8	2.4×10^{19}	*	* 12.1	45.3
9	3.6×10^{20}	1.0×10^{6}	8.0	*

Table 5.2. Results of numerical experiments described in Table 1. See text for methods of calculating the parameters. The character * indicates the viscosity level was not present for that case.

FIGURE CAPTIONS

Figure 5.1 A scematic illustrating stages of homogeneous lithospheric thickening (a to b) and then thinning of part of the mantle lithosphere by convection (c).

Figure 5.2 The effect of doubling the thickness of the lithosphere on the temperature and viscosity profiles. Solid lines show the original thickness of the bottom of the crust and lithosphere as well as the temperature and viscosity profiles. Dashed lines show the thickness and profiles after thickening. The temperature profile is for conductive cooling for 40 million years of an isothermal crust and mantle using using the diffusivity and temperature scale of table 1. The viscosity profile results from the viscosity parameters used for case 2 in table 2.

Figure 5.3 Vertically exaggerated crustal depth and topographic profile across Tibet approximately Southwest to Northeast going throught Lasa from Luo et al. (1981). The vertical exagggeration of the topographic profile is five tims greater than for the depth profile.

Figure 5.4 A schematic of the formulation of the thermal problem of crustal thickening which is described in Toksoz et al. (1981). The thickness of the crust (H) at a time (t) can be varied by changing the grid spacing (ΔZ). The mantle lithospheric thickness is not changed, which

results in an nearly constant mantle heat flux into the crust with time.

Figure 5.5 Results of crustal thermal calculations in Toksoz, Buck and Hsui, 1981. Dashed lines are isotherms against time since the beginning of crustal thickening. The solid line is the crust mantle boundary position. All cases have the doubling of the crust taking 20 million years except case B which is for twice that time. Case A is for a uniform radioactive distribution in the crust and 1 kilobar shear stress during deformation. Case B differs only in that the shear stress is 2 kb. Case C shows that when the concentration of crustal radioactive sources is twice as large in the upper crust than the lower that temperatures remain lower in the crust. Case D has one third more mantle heat flux than the others.

Figure 5.6 Streamlines, isotherms and horizontally averaged temperature at ten million year intervals for case 4. The boxes represent 700x700 km of mantle. The tick marks around the boxes show the grid point positions. The eight contours for the streamfunction have the following non-dimensional ranges: -4.3 to 11.3 for case A; -58.2 to 59.6 for case B; -33.4 to 25.9 in case C ; and -40.2 to 24.4 for case D. The contour intervals for the temperature are 50^{o} C. The range of the horizontally averaged temperatures is 1300 °K.

Figure 5.7 The depth to the level where the horizontally averaged viscosity equals the indicated value for case 4.

Figure 5.8 The variation of the horizontally averaged dissipation with depth for case 4 at the indicated times into the runs.

Figure 5.9 The average dissapation (D) given by equation 5.1 versus time into the run for the cases indicated. Dissipation for case 5 was too low to be on scale.

Figure 5.10 This is a sketch of the simplified model of lithospheric thinning due to mantle heat flow which is disucced in the text. The initial thickness of te lithosphere is Z_i and the final thickness is Z_f is half of the initial value. The initial and final temperature profiles are considered to be linear. In the intermediate stages (b) the surface heat flux is considered to be constant an equal to its initial value.

Figure 5.11 A schematic is shown of the subduction of the mantle lithosphere with the crust being scrapped off as has been suggested for the Himalaya by Lyon-Caen and Molnar (1983). Within the crust the primary difference between the upper and lower crust is that the upper crust is brittle and the lower crust deforms through ductile flow.

Figure 5.12 This is a scematic of the possible evolution of of Tibet with crustal thickening centered on several sites of mantle lithospheric subduction. The several sites of subduction may not have been contemporaneous. In this model the elevation of the Himalaya are considered to have occured after most of Tibet had been uplifted because of the thicker and colder lithosphere in the area of the Himalaya (the left side of the figure).

Figure 5.13 Profiles of the log of the non-dimensionalized viscosity for a hypothetical lower crust and mantle lithosphere are shown. The parameters for the crust (feldspar) and manlte lithosphere(olivine) are taken from Caristan (1982) and Brace and Kohlstedt (1980) assuming power law rheology with a strain rate of 10^{-13} s^{-1}. The temperature profile is varied by ±100 °K around an approximately equilibrium profile for a temperature of 1500 °K at 100 km depth.

HOMOGENEOUS LITHOSPHERIC THICKENING

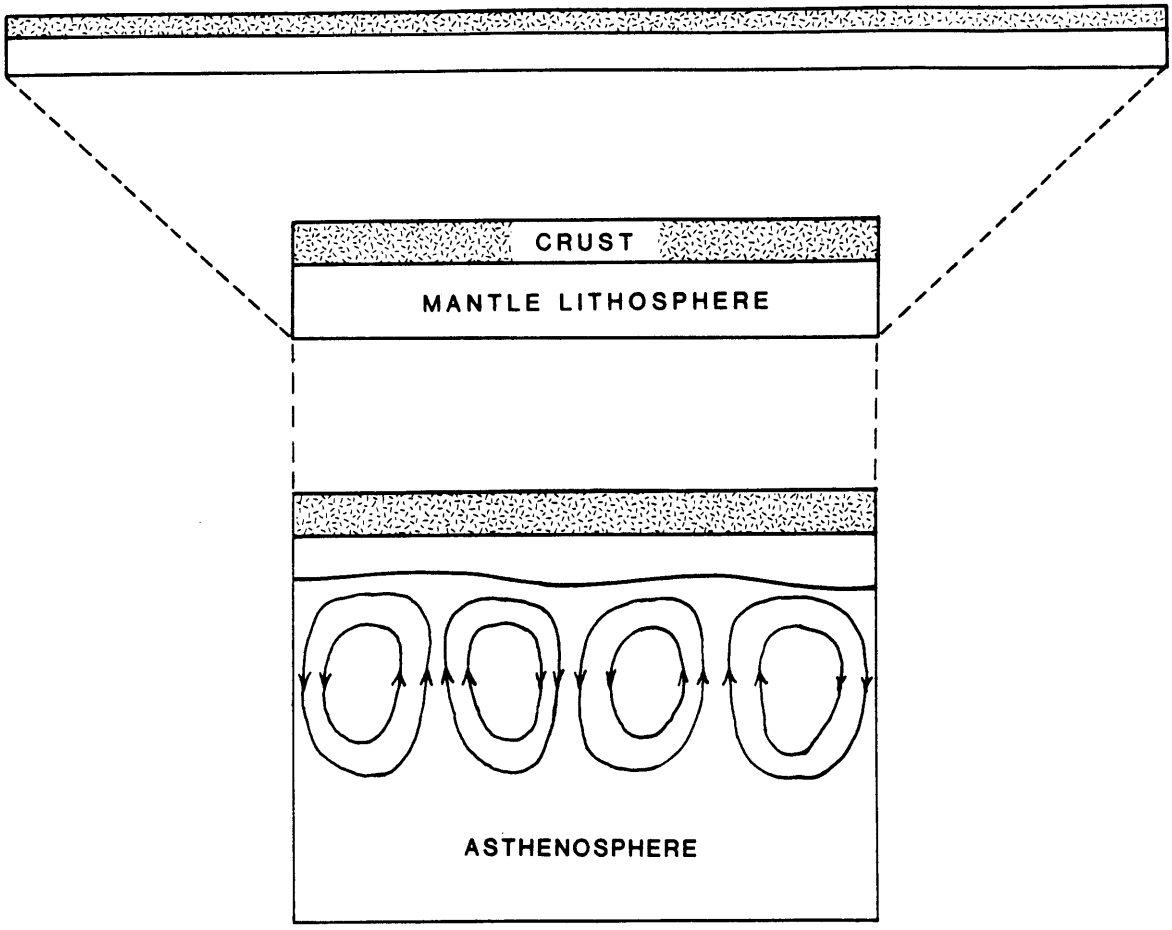

Figure 5.1

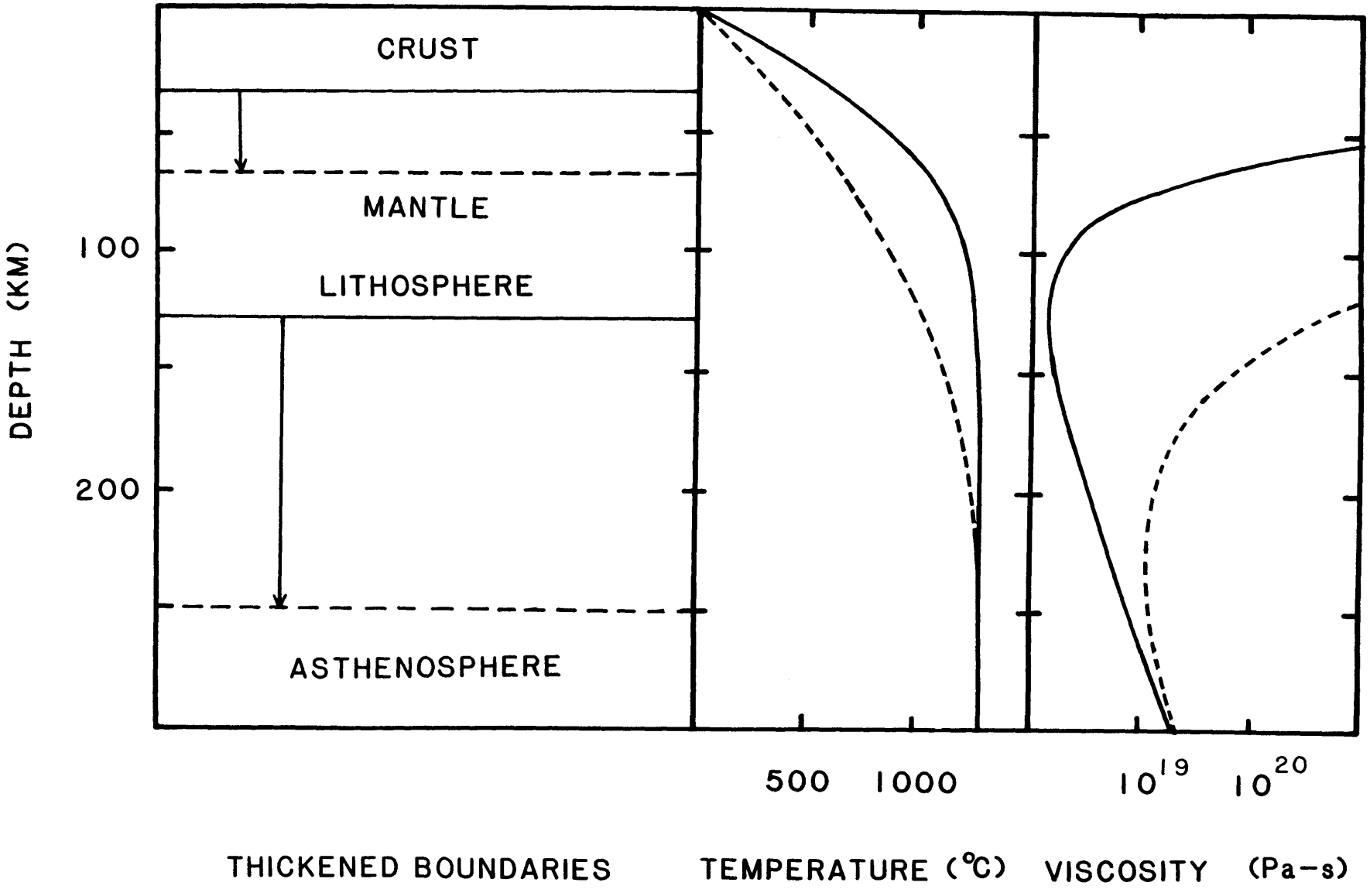
CRUST
MANTLE
LITHOSPHERE
ASTHENOSPHERE
DEPTH (KM)
100
200
500
1000
10^{19}
10^{20}
THICKENED BOUNDARIES
TEMPERATURE (°C)
VISCOSITY (Pa-s)

Figure 5.2

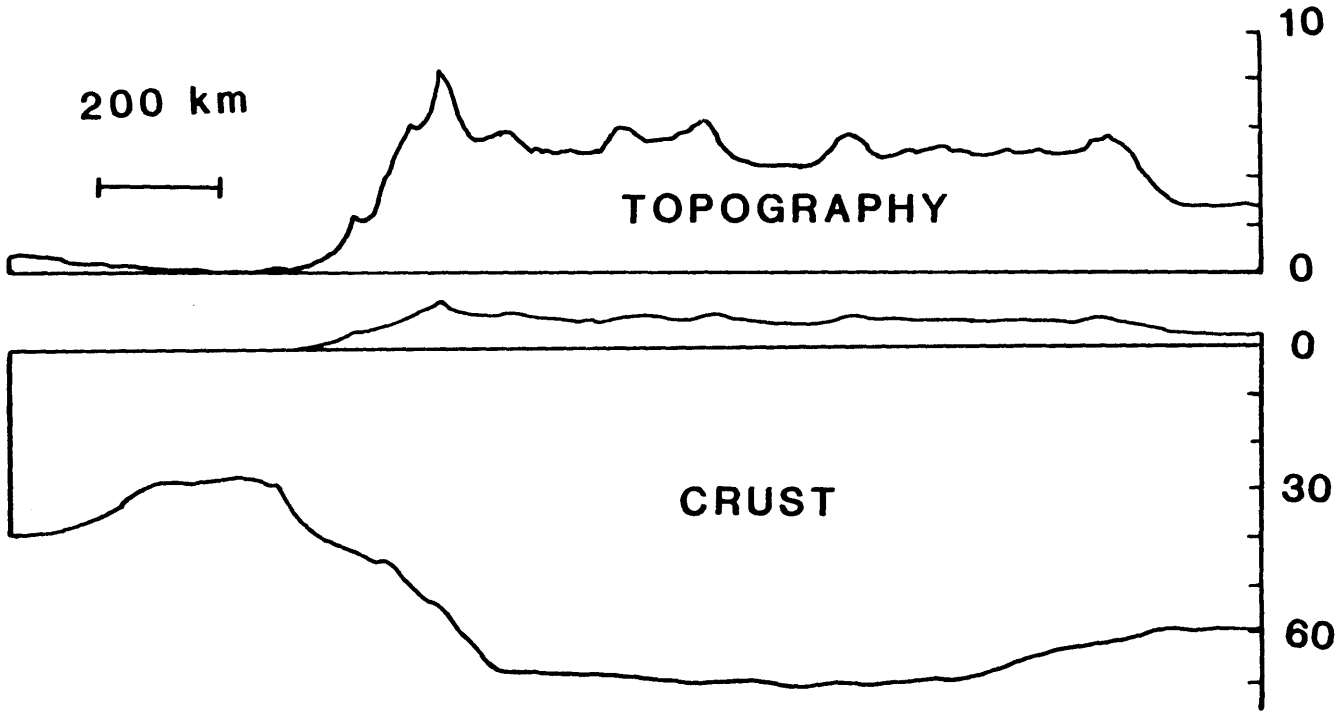

Figure 5.3

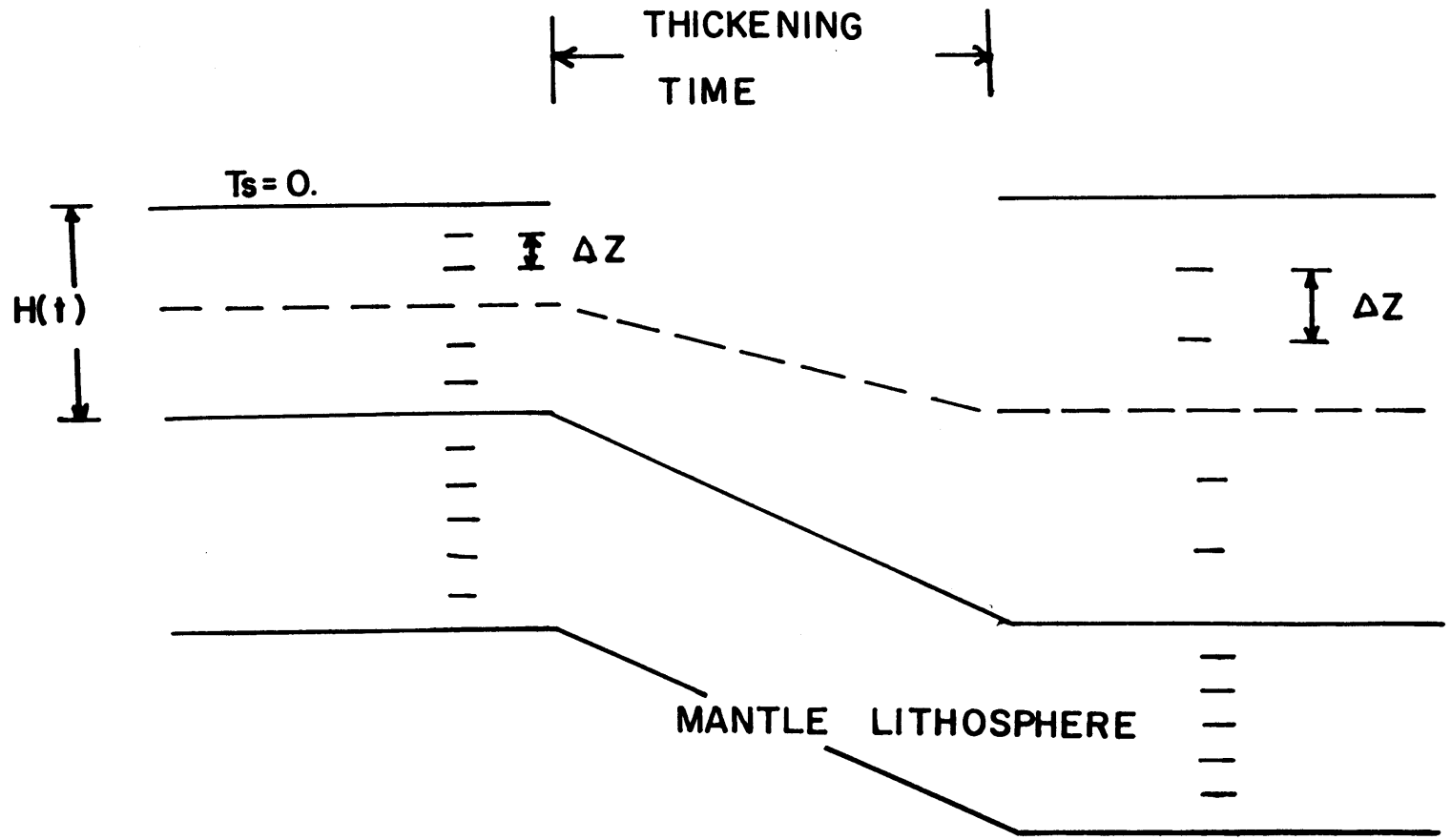

Figure 5.4

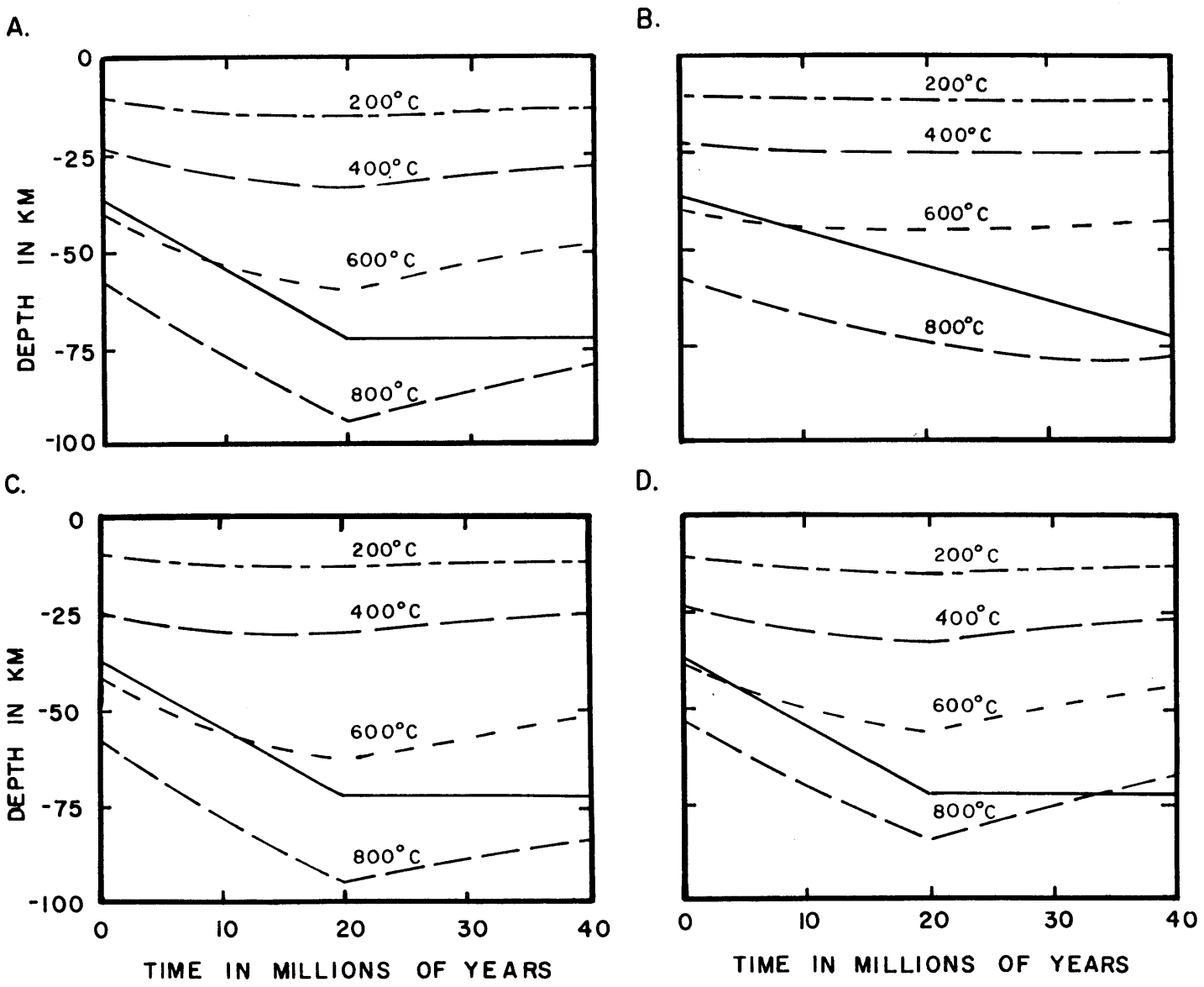
A.
B.
C.
D.
0
-25
-50
-75
-100
DEPTH IN KM
200°C
400°C
600°C
800°C
0
10
20
30
40
TIME IN MILLIONS OF YEARS

Figure 5.5

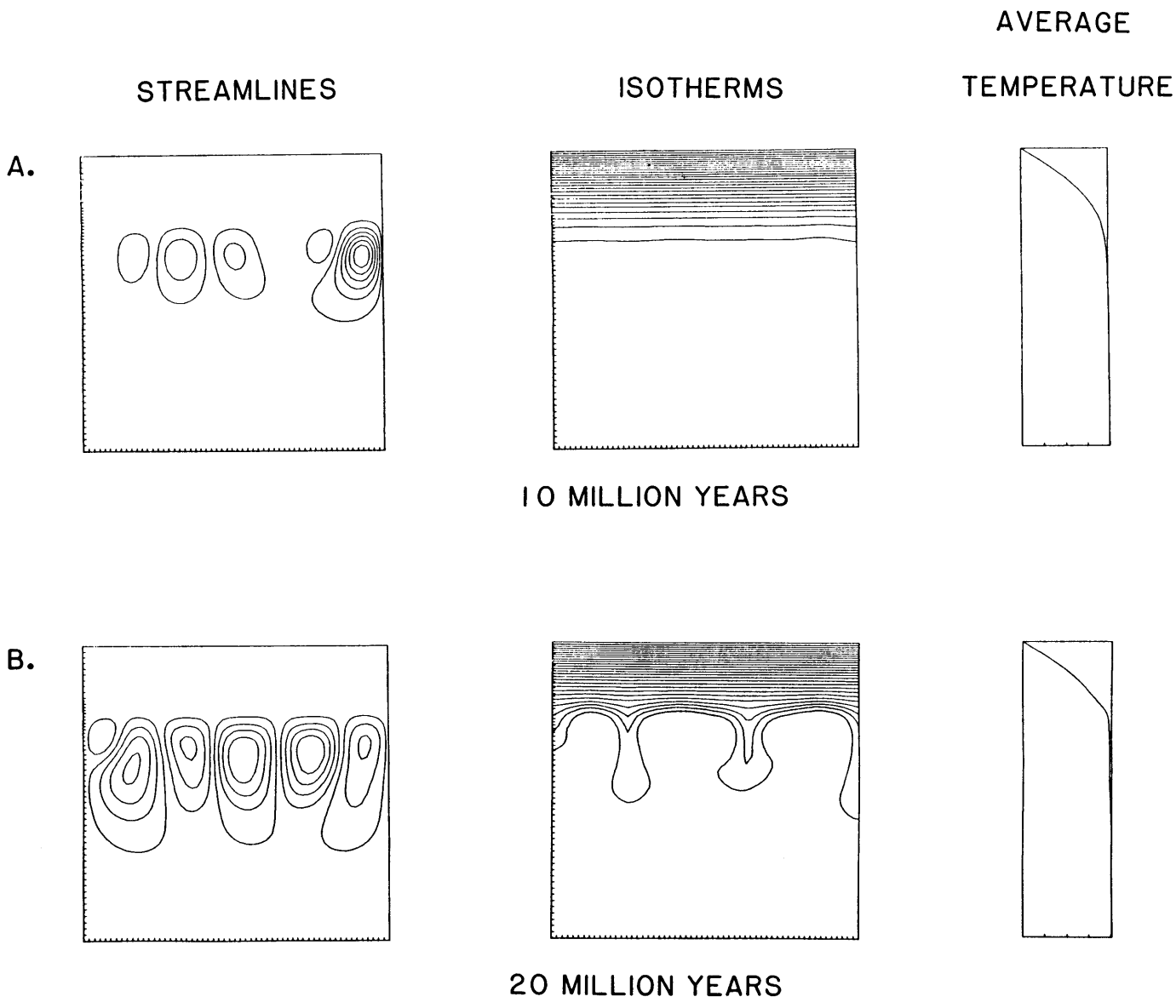
STREAMLINES
ISOTHERMS
AVERAGE
TEMPERATURE
A.
10 MILLION YEARS
B.
20 MILLION YEARS

Figure 5.6

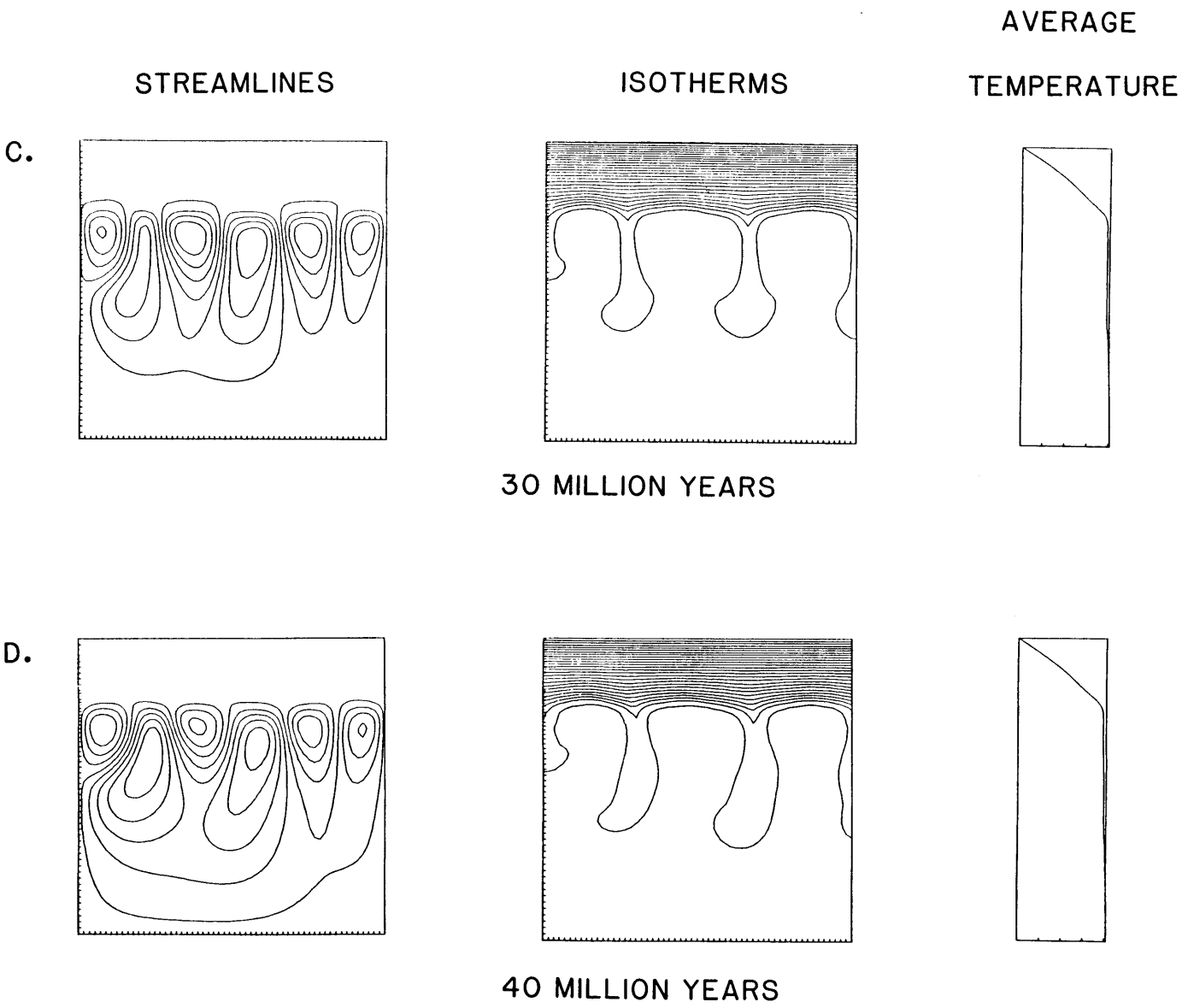

Figure 5.6 cont.

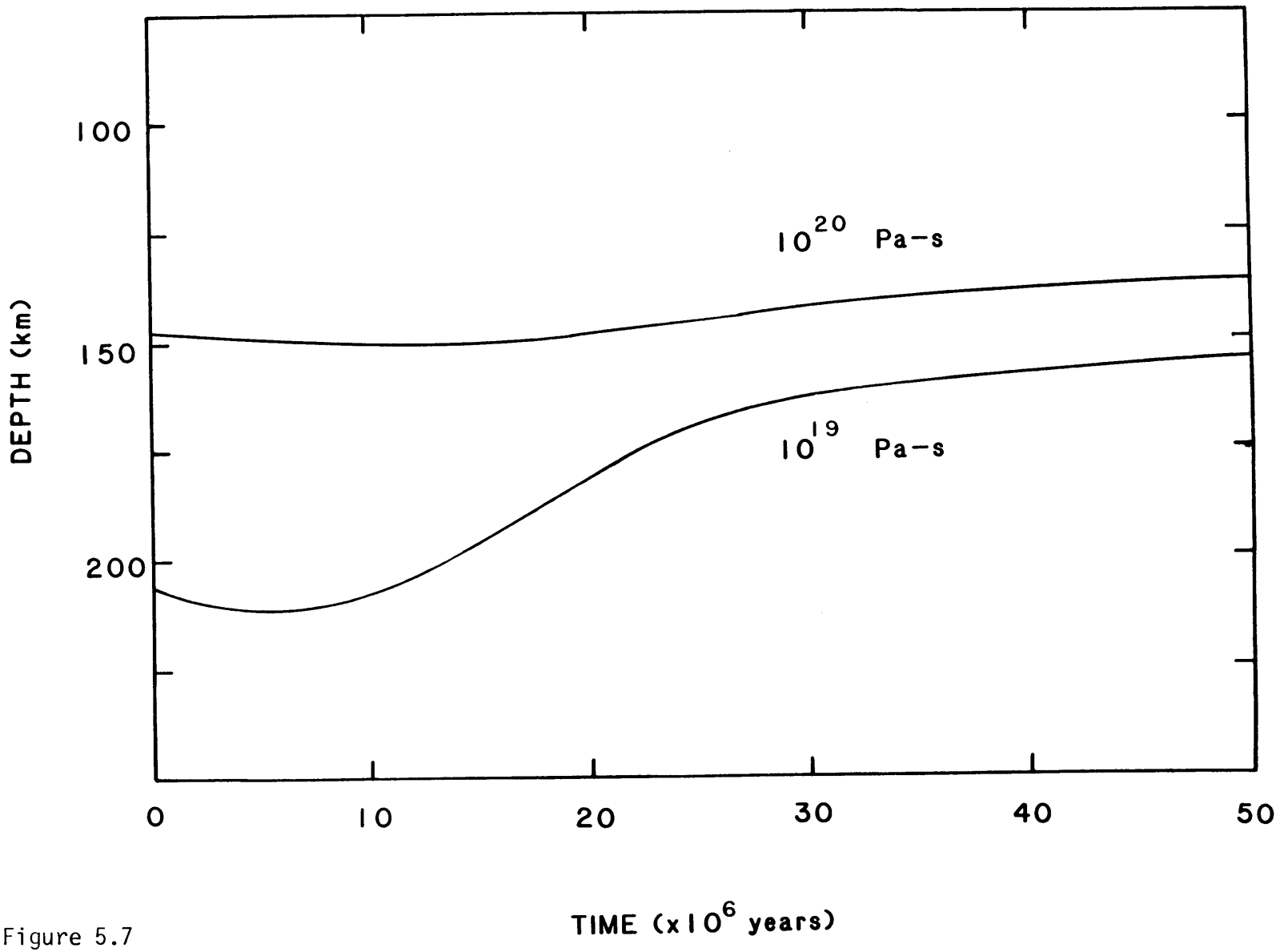
100
150
200
DEPTH (km)
10^{20} Pa-s
10^{19} Pa-s
0
10
20
30
40
50
TIME (x10^6 years)

Figure 5.7

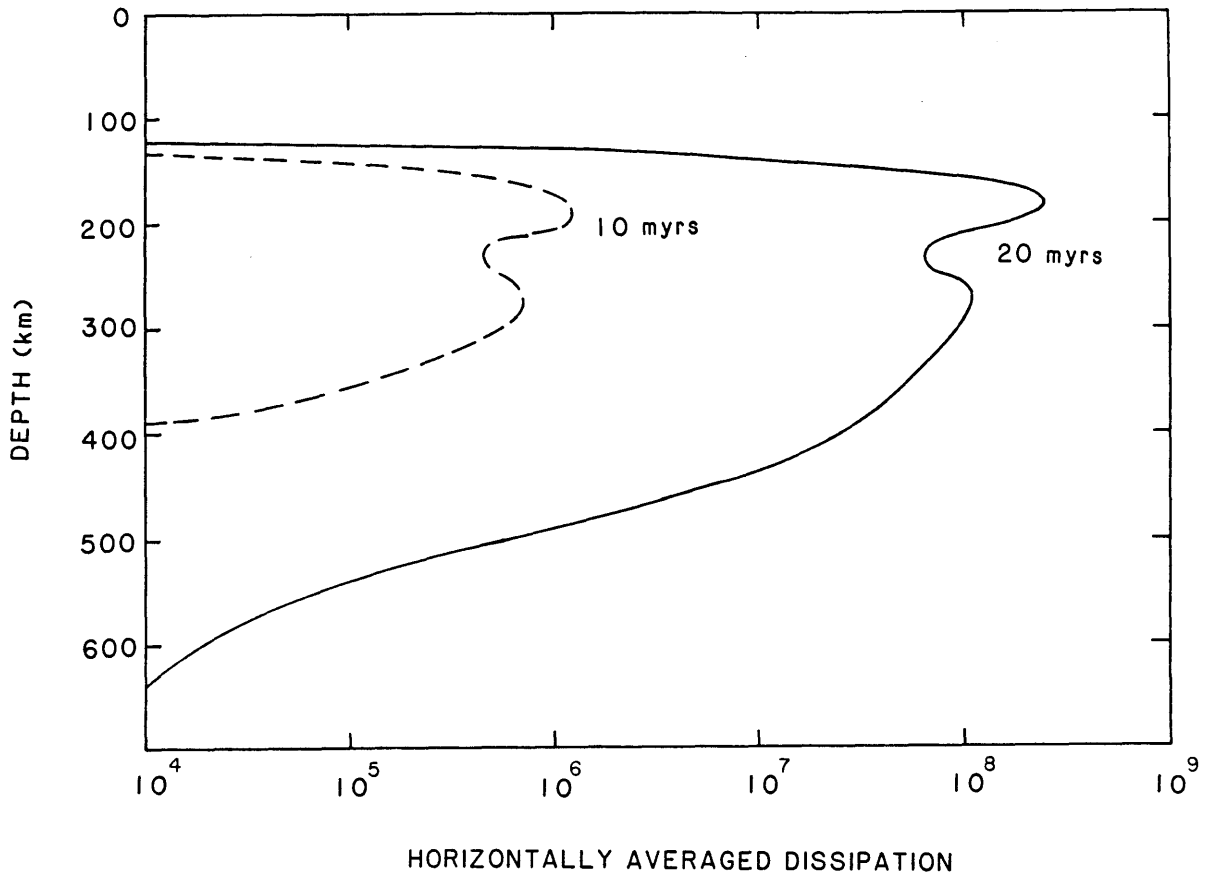
0
100
200
300
400
500
600
DEPTH (km)
10 myrs
20 myrs
10^4
10^5
10^6
10^7
10^8
10^9
HORIZONTALLY AVERAGED DISSIPATION

Figure 5.8

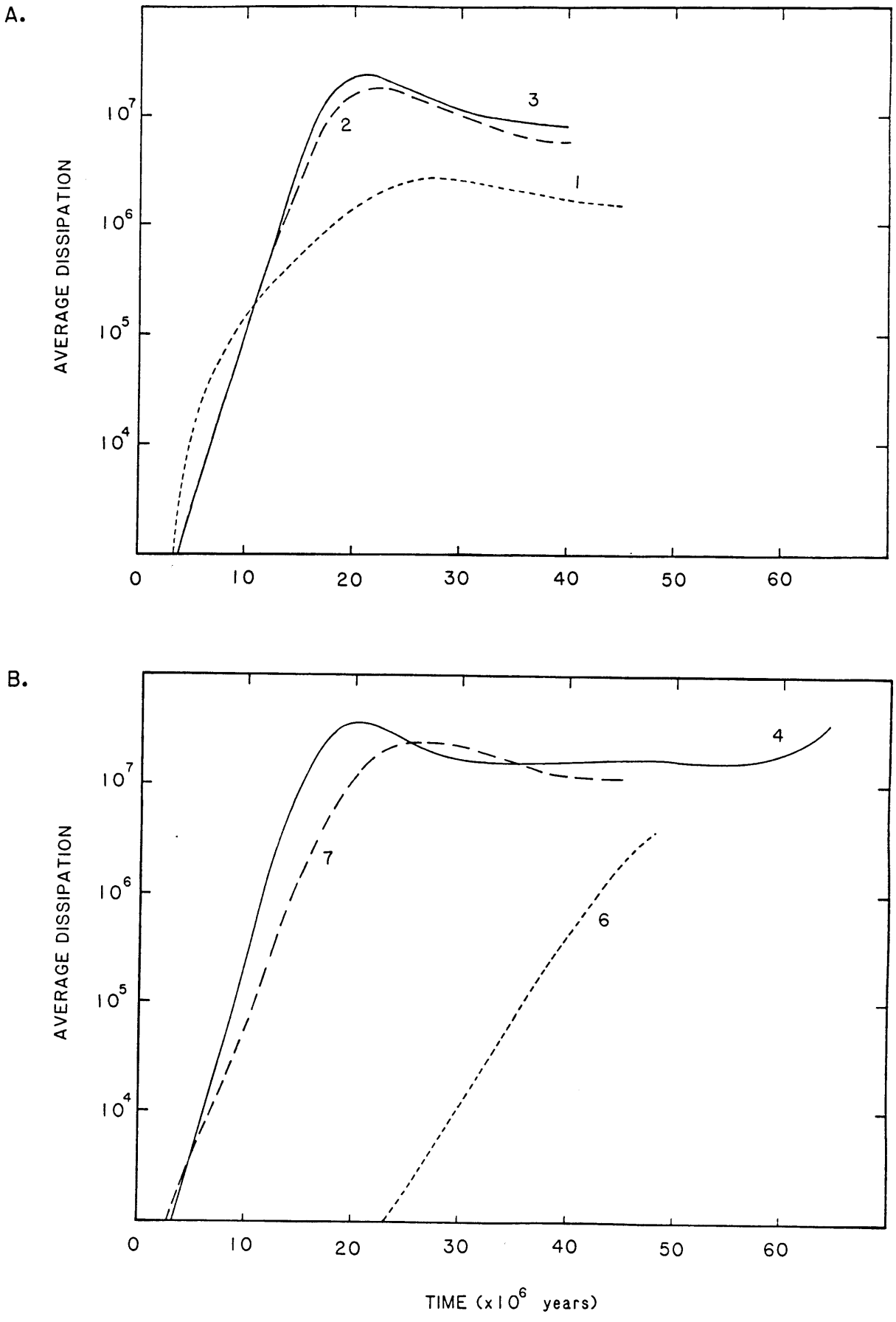
A.
AVERAGE DISSIPATION
10^7
10^6
10^5
10^4
3
2
1
0
10
20
30
40
50
60
B.
AVERAGE DISSIPATION
10^7
10^6
10^5
10^4
4
7
6
0
10
20
30
40
50
60
TIME (x 10^6 years)

Figure 5.9

MANTLE HEAT BUDGET CALCULATION

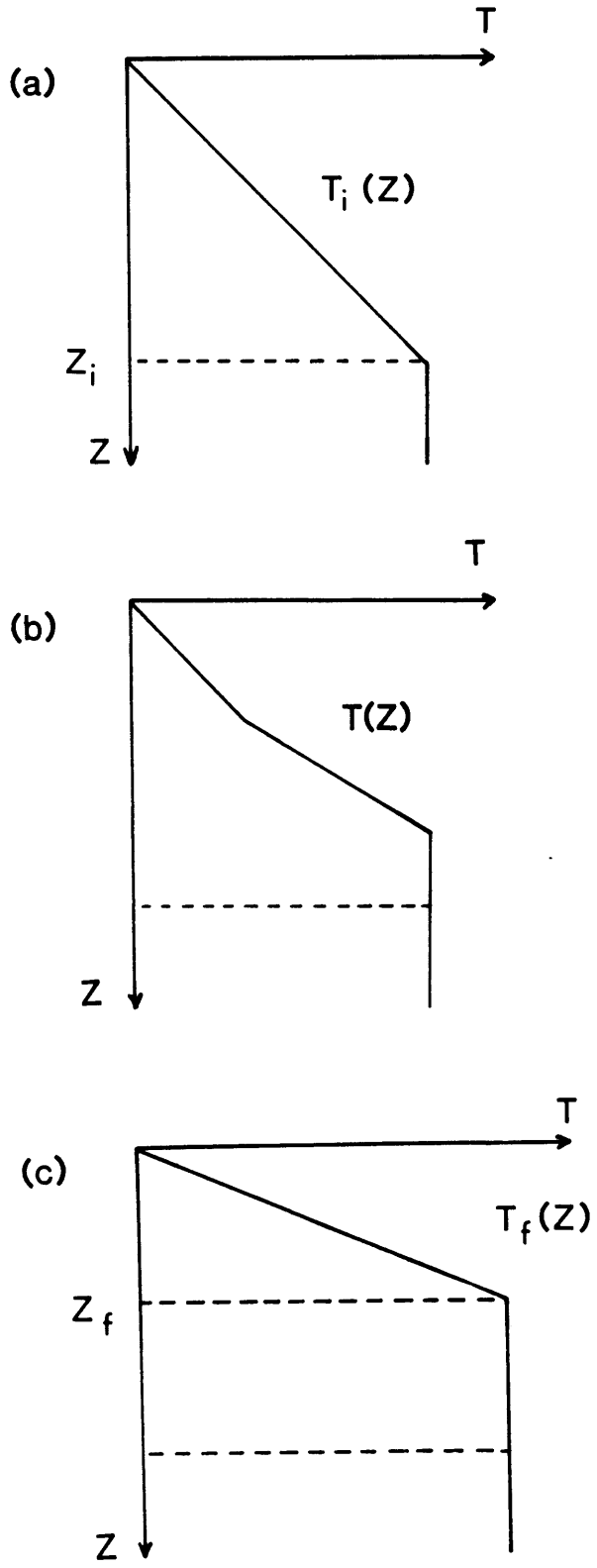

Figure 5.10

SUBDUCTION OF MANTLE LITHOSPHERE

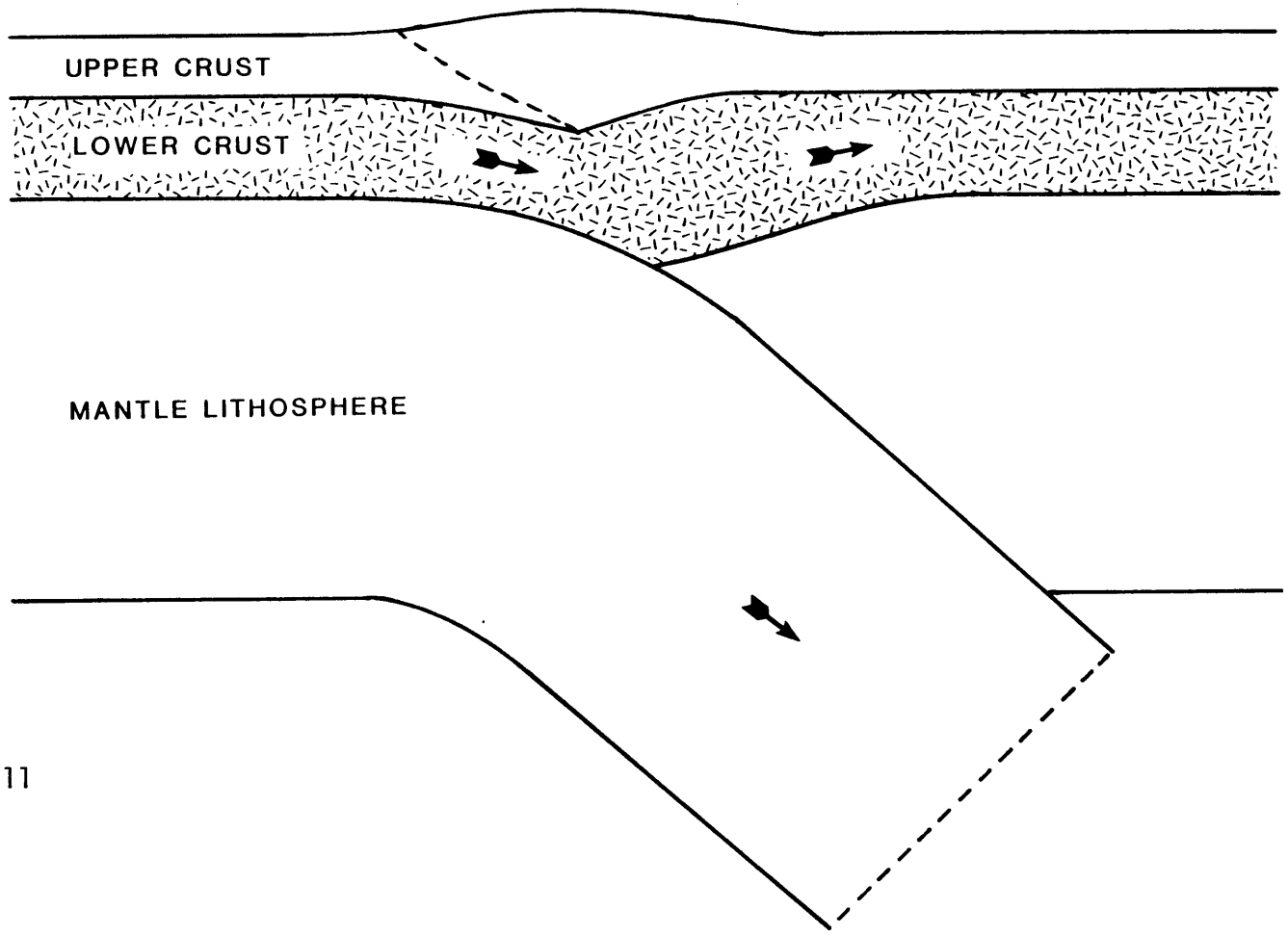

Figure 5.11

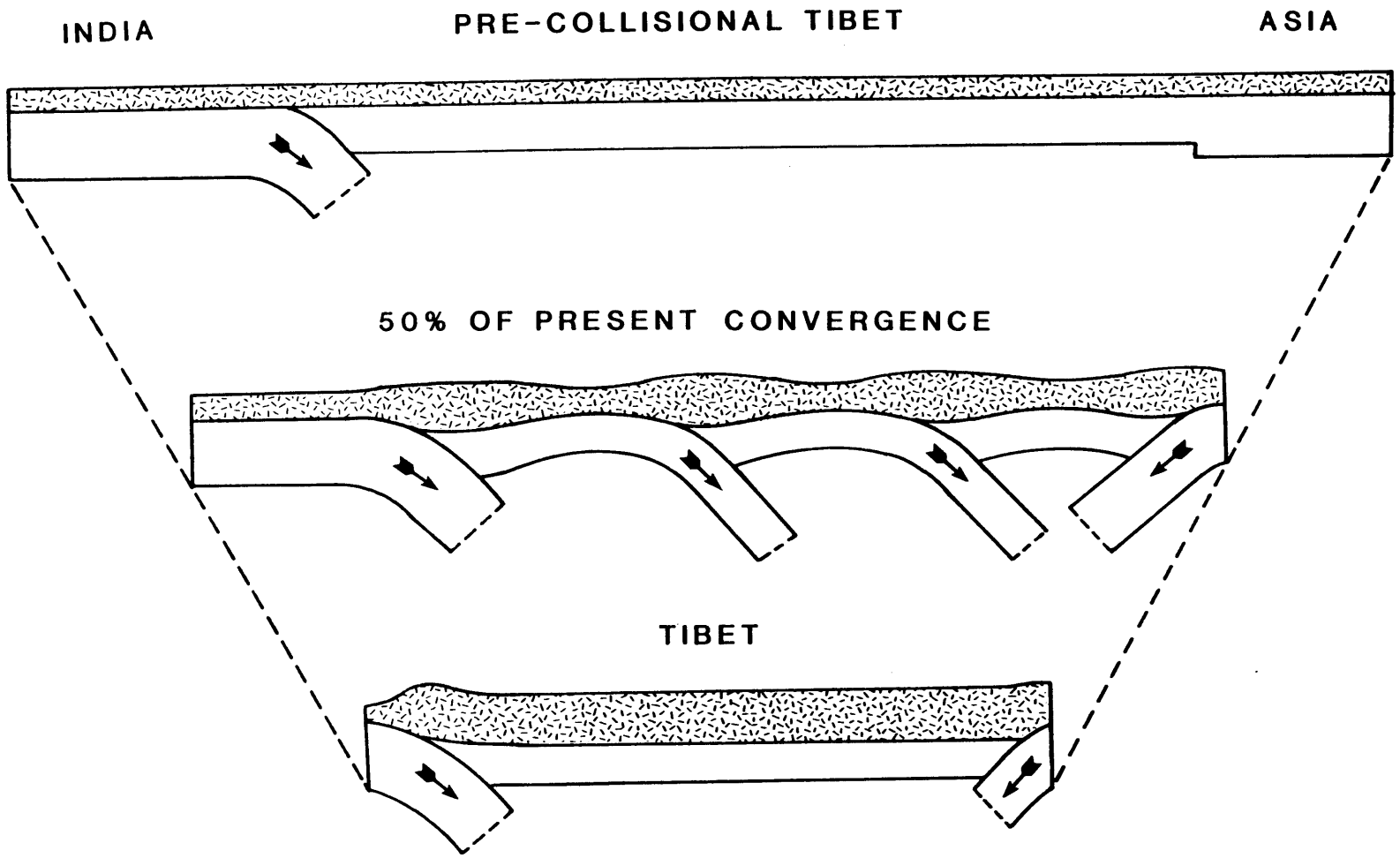
INDIA
PRE-COLLISIONAL TIBET
ASIA
50% OF PRESENT CONVERGENCE
TIBET
500 KM

Figure 5.12

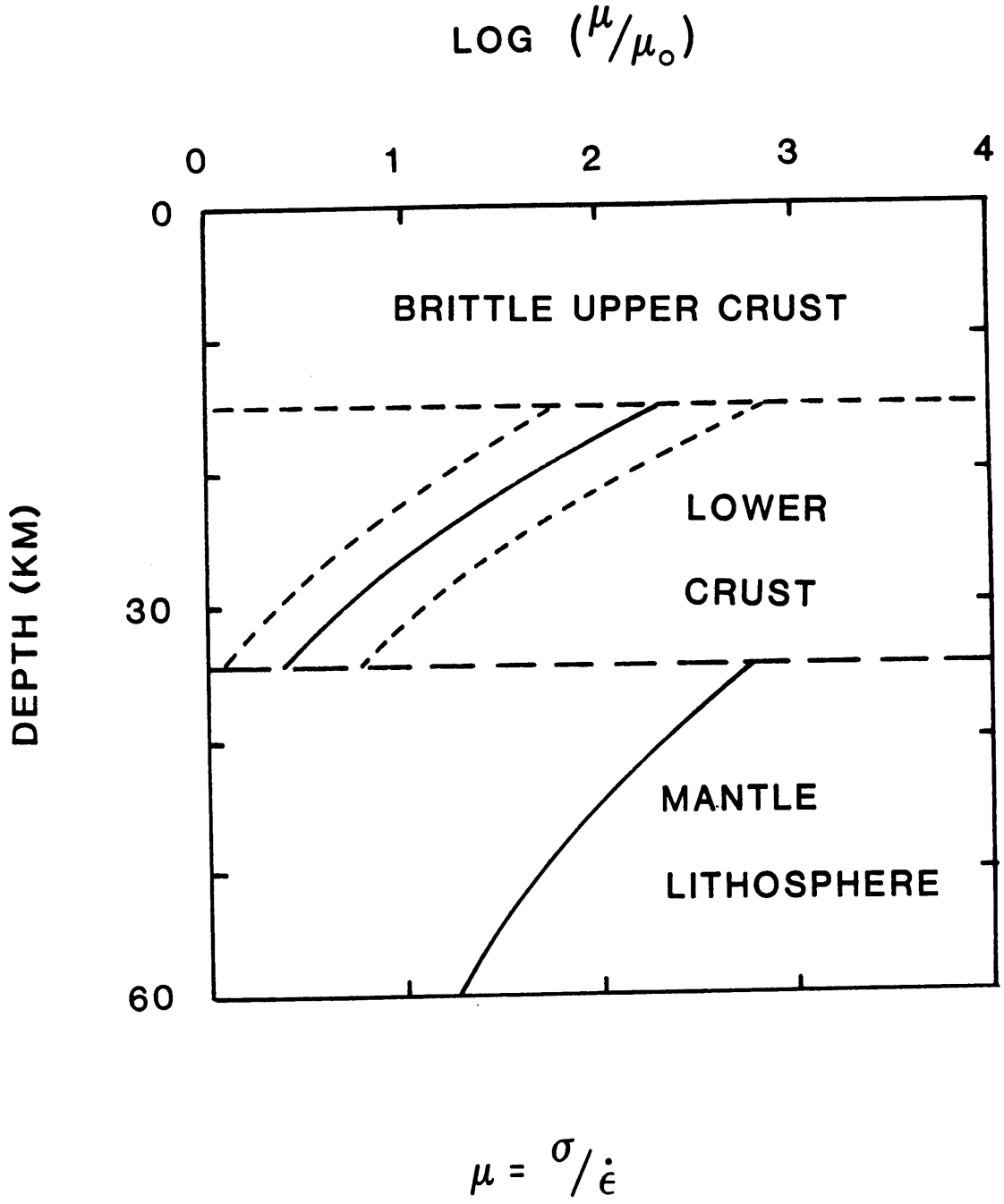
LOG (μ/μ_o)
0
1
2
3
4
0
30
60
DEPTH (KM)
BRITTLE UPPER CRUST
LOWER
CRUST
MANTLE
LITHOSPHERE
$\mu = \sigma/\dot{\epsilon}$

Figure 5.13

"Sometimes I just wish I were happening on a larger scale."

-Wm. Hamilton in a New Yorker cartoon.

CHAPTER 6

CONCLUSIONS

Three geophysical problems in which small-scale convection in a variable viscosity mantle may play an important role have been studied in this work. For two of those problems - the cooling of the oceanic lithosphere and the cooling of passive rifts - we have shown that the effects of small-scale convection can explain data which no other single mechanism can. The third problem concerns the effect of small-scale convection on lithosphere which has been thickened in a hypothetical convergence zone. As expected, when a temperature dependence in the viscosity relation is included we find that small-scale convection cannot lead to the extremely rapid thinning of the lithosphere which has been predicted in models which only consider constant viscosities. We have suggested a mechanism for deformation in convergence zones which does not involve thickening of the mantle lithosphere and so does not violate data from such regions.

Several kinds of data are matched by the results of these calculations. Certain short wavelength gravity anomalies

derived from Seasat altimeter data may be produced by small-scale convection which begins under oceanic lithosphere of only a few m.y. age. The data on the offset of the geoid height across fracture zones is very difficult to explain by any other mechanisn than that of small-scale convection. The variations in the rate of subsidence for the oceanic lithosphere from one area to another may be explained by the large effect that variations in asthenospheric temperature have on the vigor of small-scale convection. Data on the uplift of the flanks of passive rifts and details of the subsidence of rifted continental margins can be matched by the predictions of models which include small-scale convection.

We were successful in deriving parameterizations of the effects of small-scale convection on the cooling of the oceanic lithosphere. These are useful to anyone who would like to estimate the effect of considering different viscosity parameters other than those which were used in the numerical calculations described here. The relationships describe the effect of convection on the rate of cooling, subsidence, geoid height anomalies and heat flow out of the lithosphere. The parameterization is general and should apply even outside of the range of the numerical models which have been carried out.

Future work that might be done as an outgrowth this thesis include all aspects of the work considered here. It may be possible to do simple calculations aimed at estimating the effect of three-dimensional flow on the growth in size of

small-scale convective rolls. This could be useful as more gravity data on the approximately linear short wavelength gravity features over the oceans is collected and analysed. Data on the variation of the rate of subsidence of the ocean floor can be analysed in terms of the parameterized model we have developed. Estimates of the corresponding asthenospheric temperature variations can be compared to seismic estimates of those temperatures. Models of oceanic fracture zones should be considered which include lateral transport of material and heat with an eye toward a more complete explanation of the offset of the geoid height anomalies across such areas. For the problem of lithospheric rifting we need to consider the details of the growing data set on that topic and also try to develop a simple parameterized model of the effects of small-scale convection in that case.

REFERENCES

Aherns, T.J., and G. Schubert, Gabbro-ecologite reaction rate and its geophysical significance, Rev. Geophys. Space Phys., 13, 388-400, 1975.

Allegre, C.J., V. Courtillot, P. Tapponnier, A. Hirn, M. Mattauer, C. Coulon, J.J. Jaeger, J. Achache, U. Scharer, J Marcoux, J.P. Burg, J. Giradeau, R. Armijo, C. Gariepy, C. Gopel, Li Tindong, Xiao Xuchang, Chang Chenfa, Li Guangqin, Lin Baoyu, Teng Jiwen, Wang Naiwen, Chen Guoming, Han Tonglin, Wang Xibin, Den Wanming, Sheng Huaibin, Cao Yougong, Zhou Ji, Qui Hongrong, Bao Peisheng, Wang Songchan, Wang Bixang, Zhou Yaoxiu and Ronghua Xu, Stuucture and evolution of the Himalaya-Tibet orogenic belt, Nature, 307, 17-22, 1984.

Anderson, C.A., and R.J. Bridwell, A finite-element method for studying the transient non-linear creep of geological structures, Int. J. Num. and Analy. Methods in Geomech., 4, 255-276, 1980.

Baker, B.H., P.A. Mohr, and L.A.J. Williams, Geology of the eastern rift system of Africa, Geol. Soc. of Am., Spec. Pap., 1136, 67 pp., 1972.

Batchelor, G.K., An introduction to fluid dynamics, Cambridge University Press, 1967.

Bird, P., Finite element modelling of lithosphere deformation: The Zagros Collision orogeny, Tectonophysics, 50, 307-336, 1978a.

Bird, P., Thermal and mechanical models of continental convergence zones: Zagros and Himalayas, Ph.D. Thesis, Massachusetts Institute of Technology, Cambridge, Massachusetts, 1978b.

Bird, P. and M.N. Toksoz, Strong Attenuation of Surface waves in Tibet, Nature, 266, 161-163, 1977.

Bird, P., M.N. Toksoz and N.H. Sleep, Thermal and mechanical models of continent-cintinent convergence zones, J. Geophys. Res., 80, 4405-4416, 1975.

Bird, P. and J. Baumgardner, Steady propagation of delamination events, J. Geophys. Res., 86, 4891-4903, 1981.

Black, P.R., and L.W. Braile, P_n velocity and the cooling of the continental lithosphere, J. Geophys. Res., 87, 10557-10568, 1982.

Booker, J.R., Thermal convection with strongly temperature dependent viscosity, J. Fluid Mech., 76, 741-754, 1976.

Bott, M.H.P., Mechanisms of basin subsidence: An introductory review, Tectonophysics, 36, 1-4, 1976.

Bott, M.H.P., Crustal doming and the mechanism of continental rifting, Tectonophysics, 73, 1-8, 1981.

Brace, W.F., and D.L. Kohlstedt, Limits on lithospheric stress imposed by laboratory experiments, J. Geophys. Res., 85, 6248-6253, 1980.

Bridwell, R.J., and C.A. Anderson, Thermomechanical models of the Rio Grande Rift, in Mechanisms of Plate Tectonics and Continental Drift, NATO Adv. Study Inst. Academic Press, 1980.

Buchner, F., Rhinegraben: Horizontal stylolites indicating stress regimes of earlier stages of rifting, Tectonophysics, 73, 113-118, 1981.

Buck, W.R., Small scale convection and the evolution of the lithosphere (abstract), EOS, 64, 309, 1983.

Buck, W. R., Temperature dependent mechanisms of crustal thickening, EOS, 65, 231, 1984.

Buck, W.R. and M.N. Toksoz, Boundary layer instabilities and the evolution of the Tibetan lithosphere (abstract), EOS, 63, 1097, 1982.

Burke, K., Development of graben associated with the initial ruptures of the Atlantic Ocean, Tectonophysics, 36, 93-112, 1976.

Burke, K., and A.J. Whiteman, Uplift rifting and teh break-up of Africa, in Implications of Continental Drift to the Earth Sciences, ed. Tarling and Runcorn, Academic Press, pp. 735-757, 1973.

Caldwell, J.G., and D.L. Turcotte, Dependence of the thickness of the elastic oceanic lithosphere on age, J. Geophys. Res., 84, 7572-7576, 1979.

Campbell, D.R. and T.J. Mueller, A numerical and experimental investigation of incompressible ramp-induced seperated flow, UNDAS TN-1068-MI, Dept. of Aerospace Engineering, University of Notre Dame, Notre Dame, Indiana, 1968.

Caristan, Y., The transition from high-temperature creep to fracture in Maryland diabase, J. Geophys. Res., 87, 6781-6790, 1982.

Carslaw, H.S. and J.C. Jaeger, Conduction of heat in solids, London, Oxford University Press, 510 pp., 1959.

Cathles, L.M., III, The viscosity of the earth's mantle, Princeton, N.J., Princeton University Press, 341pp., 1975.

Cazenave, A., Thermal cooling of the oceanic lithosphere: new constraints from geoid height data, submitted to Earth Planet. Sci. Letts., 1984.

Cazenave, A., B. Lago and K. Dominh, Thermal parameters of the oceanic lithosphere estimated from geoid height data, J. Geophys. Res., 88, 1105-1118, 1983.

Chapman, D.S., and H.N. Pollack, Heat flow and incipient rifting in the Central African Plateau, Nature, 256, 28-30, 1975.

Chapin, C.E., Evolution of the Rio Grande Rift--A summary, in Rio Grande Rift: Tectonics and Magmatism, ed. R.E. Ricker, AGU, Washington, D.C., pp. 1-6, 1979.

Chen, W.P., and P. Molnar, Constraints on seismic velocity beneath the Tibetan plateau and their tectonic implications, J. Geophys. Res., 86, 5937-5962, 1981.

Christensen, U., Convection in a variable viscosity fluid: Newtonian vs. power-law rheology, Earth Planet. Sci. Lett., 64, 153-162, 1983.

Crough, S.T., Geoid anomalies across fracture zones and the thickness of the lithosphere, Earth Planet. Sci. Lett., 44, 224-232, 1979.

Crough, S.T., and G.A. Thompson, Numerical and approximate solutions for lithospheric thickening and thinning, Earth Planet. Sci. Lett., 31, 397-402, 1976.

Curlet, N.W.E., Experimental and numerical modelling of natural convection in an enclosure, Ph.D. thesis, Massachusetts Inst. of Technology, 1976.

Detrick, R.S., Jr., An analysis of geoid anomalies across the Mendocino fracture zone: Implications for thermal models of the lithosphere, J. Geophys. Res., 86, 11, 751-762, 1981.

Dewey, J.F., Suture zone complexities: a review. In: M.N.Toksoz, S. Uyeda and J. Francheteau (editors) Oceanic ridges and arcs, Elsevier, Amsterdam, 477-491, 1980.

Dewey, J.F. and J.M. Bird, Mountain belts and the new global tectonics, J. Geophys. Res., 75, 2625-2647, 1970.

Dewey, J.F. and K.C. Burke, Tibetan, Varsican and Precambrian basement reactivation: products of continental collision, J. Geology, 81,683-692, 1973.

England, P.C., Some thermal considerations of the Alpine metamorphism--past, present and future, Tectonophysics, 46, 21-40, 1978.

England, P., Constraints on the extension of continental lithosphere, J. Geophys. Res., 88, 1145-1152, 1983.

England, P., and D. McKenzie, A thin viscous sheet model for continental deformation, Geophys. J. R. Astr. Soc., 70, 295-322, 1982.

Feng, C.-C. and T.-L. Teng, Three dimensional crust and upper mantle structure of the Eurasian continent, J. Geophys. Res., 88, 2261-2272, 1983.

Falvey, D.A., The devolopment of continental margins in plate tectonic theory, Petroleum Exploration Assoc. Journal, 14, 95-106, 1974.

Fleitout, L. and C. Froidevaux, Tectonics and topography for a lithosphere containing density heterogeneities, Tectonics, 1, 21-56, 1982.

Fleitout, L., and C.M. Froidevaux, Tectonic stresses in the lithosphere, Tectonics, 2, 315-324, 1983.

Fleitout, L., and D. Yuen, Secondary convection and the growth of the oceanic lithosphere, Phys. Earth Planet. Inter., in press, 1984a.

Fleitout, L., and D. Yuen, Steady-state, secondary convection beneath lithospheric plates with temperature- and pressure-dependent viscosity, J. Geophys. Res., submitted, 1984b.

Forsyth, D.W., The early structural evolution and anisotropy of the oceanic upper mantle, Geophys. J.R. Astr. Soc., 43, 103-162, 1975.

Francheteau, J., C. Jaupart, Shen Xian Jie, Kang Wen-Hua, Lee De-Lu, Bai Jia-Chi, Wei Huan-Pin and Deng Hsia-Yeu, Heat flow in Southern Tibet 1984.

Freeth, S.J., Deformation of the African plate as a consequence of membrance stress domains generated by post-Jurassic drift, Earth Planet. Sci. Lett., 45, 93-104, 1979.

Fuchs, K., K.P. Bonjer and C. Prodehl, The continental rift system of the Rhinegraben--structure, physical properties, and dynamical processes, Tectonophysics, 73, 79-90, 1981.

Gage, K. and W. Reid, The stability of thermally stratified Poiseille flow, J. Fluid Mech., 33, 21-32, 1968.

Gansser, A., The significance of the Himalayan suture zone, Tectonophysics, 62, 37-52, 1980.

Gansser, A., The Indian Ocean and the Himalayas: A geological interpretation, Eclogne Geol. Helv., 59, 832-848, 1966.

Girdler, R.W., and T.R. Evans, Red Sea heat flow, Geophys. J. R. Astr. Soc., 51, 245-251, 1977.

Girdler, R.W., J.D. Fairhead, E.C. Searle and W.T.C. Sowerbutts, Evolution of rifting in Africa, Nature, 224, 1178, 1969.

Goetze, C., The mechanisms of creep in olivine, Phil. Trans. Roy. Soc. London, Ser. A, 288, 99-119, 1978.

Golombek, M.D., G.E. McGill and L. Brown, Tectonic and geologic evolution of the Española Basin, Rio Grande Rift: Structure, rate of extension and relation to the state of stress in the Western United States, Tectonophysics, 94, 483-507, 1983.

Goranson, R.W. Heat capacity: Heat of fusion, Handbook of physical constants, Geol. Soc. Am. Spec. Paper, 36, 223-242, 1942.

Graham, A., Shear patterns in an unstable layer of air, Philos. Trans. R. Soc. London Ser. A., 232, 285-296, 1933.

Grand, S.P. and D.V. Helmberger, Regional upper mantle shear velocity in North America from the SS phase (abstract), EOS, 63, 379, 1982.

Haxby, W.F., and D.L. Turcotte, On isostatic geoid anomalies, J. Geophys. Res., 83, 5473-5478, 1978.

Haxby, W.F. and J.K. Weissel, Evidence for small-scale convection from SEASAT altimiter data, EOS, 64, 838, 1983.

Haxby, W.F., D.L. Turcotte and J.M. Bird, Thermal and mechanical evolution of the Michigan Basin, Tectonphysics, 36, 57-75, 1976.

Hayes, D.E., Global studies of ocean crustal depth-age relationships, EOS, 64, 760, 1983.

Heestand, R.L. and S.T. Crough, The effect of hotspots on the ocean age-depth relation, J. Geophys. Res., 86, 6107-6114, 1981.

Hellinger, S.J. and J.G. Sclater, Some comments on two-layer extensional models for the evolution of sedimentary basins, J. Geophys. Res., in press, [1984?].

Houseman, G.A. and D.P. McKenzie, Numerical experiments on the onset of convective instability in the Earth's mantle, Geophys. J.R. Astr. Soc., 68, 133-164, 1982.

Hirn, A., J.-C. Lepine, G. Jobert, M. Sapin, G. Wittlinger, Xu Zhong Xin, Gao En Yuan, Wang Xiang Jing, Teng Ji Wen, Xiong Shao Bai, M.R. Pandey and J.M. Tater, Crustal structure of the Himalayan border of Tibet, Nature, 307, 23-25, 1984a.

Hirn, A., A. Nercessian, M. Sapin, G. Jobert, Xu Zhong Xin, Gao En Yuan, Lu De Yuan and Teng Ji Wen, Nature, 307, 25-27, 1984b.

Houseman, G.A., D.P. McKenzie and P. Molnar, Convective instability of a thickened boundary layer and its relevance for the thermal evolution of continental convergence belts, J. Geophys. Res., 86, 6115-6132, 1981.

Houston, M.H., Jr., and J.-Cl. De Bremaecker, Numerical models of convection in the upper mantle, J. Geophys. Res., 80, 742-751, 1975.

Howard, L.N., Convection at high Rayleigh number, in Proc. 11th Cong. Appl. Mech., ed. H. Gortler, pp. 1109-1115, Springer-Verlag, N.Y., 1966.

Illies, J.H., Mechanism of graben formation, Tectonophysics, 73, 249-266, 1981.

Illies, J.H. and G. Greiner, Rhinegraben and the Alpine system, Geol. Soc. Am. Bull., 89, 770-782, 1978.

Ingersoll, A., Convective instabilities in plane Couette flow, Phys. Fluids, 9, 682-689, 1966.

Isacks, B., and P. Molnar, Distribution of stresses in the descending lithosphere from a global survey of focal mechanism solutions of mantle earthquakes, Rev. Geophys. Space Phys., 9, 103-174, 1971.

Jarvis, G.T., and D.P. Mckenzie, Sedimentary basin formation with finite extension rates, Earth Planet. Sci. Lett., 48, 42-52, 1980.

Jarvis, G.T., and W.R. Peltier, Mantle convection as a boundary layer phenomena, Geophys. J. Roy. Astr. Soc., 68, 389-427, 1982.

Jaupart, C., On the mechanisms of heat loss beneath continents and oceans, Ph.D. Thesis, M.I.T., 215 p., 1981.

Jaupart, C., and B. Parsons, Convective instabilities in a variable viscosity fluid cooled from above, Phys. Earth Planet. Inter., submitted, 1983.

Jordan, T.H., The continental tectosphere, Rev. Geophys. Space Phys., 13, 1-12, 1975(a?).

Jordan, T.H., Lateral heterogeneity and mantle dynamics, Nature, 257, 745-750, 1975(b?).

Karner, G.P., and M.S. Steckler, Thermal and mechanical properties of the continental lithosphere and implications for the development of sedimentary basins (abstract), EOS Trans. Amer. Geophys. Un., 64, 322, 1983.

Keen, C.E. and D.L. Barrett, Thinned and subsided continental crust on the rifted margin of Eastern Canada: crustal structure, thermal evolution and subsidence history, Geophys. J.R. Astr. Soc., 65, 443-465, 1981.

Kohlstedt, D.L. H.P.K. Nichols and P. Hornack, The effect of pressure on the rate of dislocation recovery in olivine, J. Geophys. Res., 85, 3125-3130, 1980.

Kopitze, U., Finite element convection models: Comparison of shallow and deep mantle convection and temperature in the mantle, J. Geophys., 46, 97-121, 1979.

Lachenbruch, A.H., and J.H. Sass, Heat flow and energetics of the San Andreas fault zone, J. Geophys. Res., 85, 6185-6222, 1980.

Le Pichon, X., and J.-C. Sibet, Passive margins: A model of formation, J. Geophys. Res., 86, 3708-3720, 1981.

Leveque, J.J., Regional upper mantle s-velocity models from phase velocities of great-circle Rayleigh waves, Geophys. J.R. Astr. Soc., 63, 23-43, 1980.

Logatchev, N.A., and N.A. Florensov, The Baikal system of rift valleys, Tectonophysics, 45, 1-13, 1978.

Long, R.R., Relation between Nusselt number and Rayleigh number in turbulent thermal convection, J. Fluid Mech., 73, 445-451, 1976.

Luo, Huan-yan, Yu-jian Xu, Hui-zhen Song, Jun-xiu Sun, Cai-hua Guo, Ru-ze Zhang and Zhi-juan Gu, Finite element analysis for recent Qinghai-Xizang Plateau uplifting and its relation to seismicities, Proceedings of Symposium on Qinghai-Xizang Plateau, pp. 815-822, [Beijing?], Academic Press, 1981.

Lyon-Caen, H. and P. Molnar, Constraints on the structure of the Himalaya from an analysis of gravity anomalies and a flexural model of the lithosphere, J. Geophys. Res., 88, 8171-8193, 1983.

Mattauer, M., P. Tapponnier and F. Proust, Some analogies between the tectonic histories of Afghanistan and Tibet, Proceedings of Symposium on Tibet Plateau, 315-324, Gordon and Breach, N.Y., 1981.

McKenzie, D.P., Some remarks on heat flow and gravity anomalies, J. Geophys. Res., 72, 6261-6273, 1967.

McKenzie, D.P., Active tectonics of the Mediterranean region, Geophys. J. R. Astron. Soc., 30, 109-186, 1972.

McKenzie, D.P., Surface deformation, gravity anomalies and convection, Geophys. J. Roy. Astr. Soc., 48, 211-238, 1977.

McKenzie, D.P., Some remarks on the development of sedimentary basins, Earth Planet. Sci. Lett., 40, 25-32, 1978.

McKenzie, D.P., Active tectonics of the Alpine Himalayan Belt: The Agean Sea and surrounding regions, Geophys. J. R. Astron. Soc., 55, 217-254, 1978.

McKenzie, D.P., and C. Bowin, The relationship between bathymetry and gravity in the Atlantic Ocean, J. Geophys. Res., 81, 1903-1916, 1976.

McKenzie, D.P., J.M. Roberts and N.O. Weiss, Convection in the earth's mantle: towards a numerical simulation, J. Fluid Mech., 62, 465-538, 1974.

Mitchell, B.J. and G.K. Yu, Surface wave dispersion, regionalized velocity models and anisotropy of the Pacific crust and upper mantle, Geophys. J.R. Astr. Soc., 63, 497-514, 1980.

Molnar, P. and P. Tapponier, Tectonics of Asia: Consequences and implications of a continental collision, Science, 189, 419,425, 1975.

Molnar, P. and P. Tapponnier, A possible dependence of tectonic strength on the age of the crust in Asia, Earth Planet. Sci. Lett., 52, 107-114, 1981.

Molnar, P. W.P. Chen and E. Padovani, Temperatures in overthrust terrains and the origin of tertiary granites in the greater Himalaya, J. Geophys. Res., in press, 1982.

Montagner J.P., and N. Jobert, Variation with age of the deep structure of the Pacific Ocean inferred from very long-period Rayleigh wave dispersion, Geophys. Res. Lett., 10, 273-276, 1983.

Morgan, P., Constraints on rift thermal processes from heat flow and uplift, Tectonophysics, 94, 277-298, 1983.

Morner, N.-A., Asthenospheric conditions in the Fenoscandian shield region (abstract), EOS Trans. Am. Geophys. Un., 62, 809, 1981.

Nakanishi, I. and D.L. Anderson, World-wide distribution of group velocity of mantle Rayleigh waves as determined by spherical harmonic inversion, Bull. Seis. Soc. Am., 72, 1185-1194, 1982.

Nakibolu, S.M. and K. Lambeck, A reevaluation of the isostatic rebound of Lake Bonneville, J. Geophys. Res., 88, 10439-10447, 1983.

Neugebauer, H.J., and P. Temme, Crustal uplift and propagation of failure zones, Tectonophysics, 73, 33-51, 1981.

Oldenburg, D.W., Conductivity structure of oceanic upper mantle beneath the Pacific plate, Geophys. J.R. Astr. Soc., 65, 359-394, 1981.

Oxburgh, E.R., and D.L. Turcotte, Membrane tectonics and the East African rift, Earth Planet. Sci. Lett., 22, 133-140, 1974.

Parker, R.L., and D.W. Oldenburg, Thermal model of ocean ridges, Nature, 242, 137-139, 1973.

Parmentier, E.M., Studies of thermal convection with application to convection in the Earth's mantle, Ph.D. Thesis, Cornell University, 1975.

Parmentier, E.M., A study of thermal convection in non-Newtonian fluids, J. Fluid Mech., 84, 1-11, 1978.

Parmentier, E.M. and J.E. Oliver, A study of shallow global mantle flow due to accretion and subduction of lithospheric plates, Geophys. J.R. Astr. Soc., 57, 1-21, 1979.

Parmentier, E.M. and D.L. Turcotte, Two dimensional mantle flow beneath a rigidly accreting lithosphere, Phys. Earth Planet. Int., 17, 281-289, 1978.

Parsons, B., and S. Daly, The relationship between surface topography, gravity anomalies and temperature structure of convection, J. Geophys. Res., 88, 1129-1144, 1983.

Parsons, B. and D. McKenzie, Mantle convection and the thermal structure of plates, J. Geophys. Res., 83, 4485-4496, 1978.

Parsons, B. and J.G. Sclater, An analysis of the variation of ocean floor bathymetry and heat flow with age, J. Geophys. Res., 82, 803-827, 1977.

Passey, Q.R., Upper mantle viscosity derived from the difference in rebound of the Provo and Bonneville shorelines: Lake Bonneville basin, Utah, J. Geophys. Res., 86, 11701-11708, 1981.

Peltier, W.R. and J.T. Andrews, Glacial isostatic adjustment I, the forward problem, Geophys. J.R. Astr. Soc., 46, 605-646, 1976.

Powell, C.M. and P. Conaghan, Plate tectonics and the Himalayas, Earth Planet. Sci. Lett., 20, 1-12, 1973.

Ramberg, I.B., F.A. Cook and S.B. Smithson, Structure off the Rio Grande Rift in southern New Mexico and West Texas based on gravity interpretation, Geol. Soc. Am. Bull., 89, 107-123, 1978.

Reddy, K.P.R., S.M. Oh, L.D. Major, and A.R. Cooper, Oxygen diffusion in fosterite, J. Geophys. Res., 85, 322-326, 1980.

Richards, M.A. and B.H. Hager, Geoid anomalies in a dynamic earth, J. Geophys. Res., 89, 5987-6002, 1984.

Richardson, R.M. and S.C. Solomon, Tectonic stress in the plates, Rev. Geophys. Space Phys., 17, 981-1091, 1979.

Richter, F.M., Convection and the large scale circulation of the mantle, J. Geophys. Res., 78, 8735-8745, 1973.

Richter, F.M. and D. McKenzie, Simple plate models of mantle convection, J. Geophys., 44, 441-471, 1978.

Richter, F.M. amd B. Parsons, On the interaction of two scales of convection in the mantle, J. Geophys. Res., 80, 2529-2541, 1975.

Ringwood, A.E., The composition and petrology of the Earth's mantle, McGraw-Hill, New york, 618 pp, 1975.

Roache, P.J., Computational Fluid Dynamics, Albequrque, NM, Hermosa Press, 466 pp., 1982.

Roberts, G.O., Fast viscous Bernard convection, Geophys. Astrophys. Fluid Dynamics, 12, 235-272, 1979.

Ross, J.V., H.G. Ave Lallement, and N.L. Carter, Activation volume for creep in the upper mantle, Science, 203, 261-263, 1979.

Royden, L. and C.E. Keen, Rifting process and thermal evolution of the continental margin of eastern Canada determined by subsidence curves, Earth Planet. Sci. Lett., 51, 343-361, 1980.

Royden, L., J.G. Sclater, and R.P. Von Herzen, Continental margin subsidence and heat flow: Important parameters in formation of petroleum hydrocarbons, A.A.P.G. Bull., 64, 173-187, 1980.

Salveson, J.O., Variations in the geology of rift basins-a tectonic model, paper presented at: Rio Grande Rift Symposium, October (Draft preprint courtesy of Chevron Resources Company, P.O. Box 7147, San Francisco, CA 94120), 1978.

Sammis, C.G., J.C. Smith and G. Schubert, A critical assessment of estimation methods for activation volume, J. Geophys. Res., 86, 10707-10718, 1981.

Sandwell, D.T., and G. Schubert, Geoid height-age relations from SEASAT altimeter profiles across the Mendocino fracture zone, J. Geophys. Res., 87, 3949-3958, 1982.

Sawyer, D.S., B.A. Swift, J.G. Sclater and M.N. Toksoz, Extensional model for the subsidence of the Northern U.S. Atlantic continental margin, Geology, 10, 134-140, 1982.

Schatz, J.F. and G. Simmons, Thermal conductivity of earth materials at high temperature, J. Geophys. Res., 77, 6966-6983, 1972.

Schubert, G., and D.L. Turcotte, One-dimensional models of shallow mantle convection, J. Geophys. Res., 77, 945-951, 1972.

Schubert, G. C. Frodeveaux, D.A. Yuen, Oceanic lithosphere and asthenosphere: thermal and mechanical structure. J. Geophys. Res., 81, 3525-3540, 1976.

Schubert, G., D.L. Turcotte, and E.R. Oxburgh, Stability of planetary interiors, Geophys. J. Roy. Astr. Soc., 18, 441-460, 1969.

Schubert, G., P. assen, and R.E. Young, Sobsolidus convective cooling histories of terrestrial planets, Icarus, 38, 192-211, 1979.

Sclater, J.G. and P.A.F. Christie, Continental stretching: an explanation of the post and mid-Cretaceous subsidence of the central North Sea Basin, J. Geophys. Res., 85, 3711-3739, 1980.

Sclater, J.G. and J. Francheteau, The implications of terrestrial heat flow observations on current tectonic and geochemical models of the crust and upper mantle of the Earth, Geophys. J.R. Astr. Soc., 20, 509-542, 1970.

Sclater, J.G., C. Jaupart and D. Galson, The heat flow through oceanic and continental crust and the heat loss of the Earth, Rev. Geophys. Space Phys., 18, 269-311, 1980.

Sclater, J.G., L. Royden, F. Horvath, B.C. Burchfiel, S. Semkien and L. Stegena, The formation of the intra-Carpathian basins as determined from subsidence data, Earth Planet. Sci. Lett., 51, 139-162, 1980.

Sengor, A.M.C. and K. Burke, Relative timing of rifting and volcanism on earth and its tectonic implications, Geophys. Res. Letts. , 5, 419-421, 1978.

Sharpe, H.N. and W.R. Peltier (1978) Parameterized mantle convection and the Earth's thermal history, Geophys. Res Letts., 5, 737-740.

Simmons, G., and H. Wang, Single Crustal Elastic Constants and Calculated Aggregate Properties: A Handbook, 2nd ed., 370 pp., Cambridge, MA, MIT Press, 1971.

Skinner, B.J., Thermal Expansion, Geol. Soc. Am. Mem., 97, 75-96, 1966.

Sleep, N.H., Thermal effects of formation of Atlantic continental margins by continental breakup, Geophys. J. Roy. Astr. Soc., 24, 325-350, 1971.

Sleep, N.H., The double seismic zone in downgoing slabs and the viscosity of the mesosphere, J. Geophys. Res., 84, 4565-4571, 1979.

Spohn, T. and G. Schubert, Convective thinning of the lithosphere: A mechanism for the initiation of continental rifting, J. Geophys. Res., 87, 4669-468, 1982.

Steckler, M.S. and A.B. Watts, Subsidence of the Atlantic-type margin of New York, Earth and Planet Sci. Lett., 41, 1-13, 1978.

Stefan, J., Über die Theorie der Eisbildung, insbesondere über die Eisbildung im Polar meere, Ann. Phys. Chem., 42, 269-286, 1891.

Stocker, R.L. and M.F. Ashby, On the rheology of the upper mantle, Rev. Geophys. Space Phys., 11, 391-426, 1973.

Sweet, R.A., A generalized cyclic reduction algorithm, SIAM J. Numer. Anal., 11, 506-520, 1974.

Tapponier, P., and P. Molnar, Slip line field theory and large scale continental tectonics, Nature, 264, 1976.

Taylor, S.R. and M.N. Toksoz, Crust and upper mantle structure in the Appalachian orogenic belt: Implications for tectonic evolution, Bull. Geol. Soc. Am., 93, 315-329, 1982.

Teng Ji-wen, Xiong Shao-po, Sun Ke-zhong, Yao Hung, Chen Li-fang, Mu Teng, Lai Ming-hui,, Wu Ming-chu, Su De-yuan, Wang shao-zhou, Huang Wen-jian, Ou Ren-sheng, Hao we-cheng, Shao An-min, Gao En-yuan, Wang Meng-lin, Lin Zhong-yang, Qu Ke-xin, Explosion seismic study for velocity distribution and structure of the crust and upper mantle from Damxung to Yadong of Xizang Plateau, in Geological and Ecological Studies of Qinghai-Xizang Plateau, NY, Gordon and Breach, pp. 691-710, 1981.

Toksoz, M.N. and P. Bird, Modelling of temperatures in convergence zones, Tectonophyics, 41, 181-193, 1977.

Toksoz, M.N. and A.T. Hsui, Numerical studies of back-arc convection and the formation of marginal basins. Tectonophysics, 50, 177-196, 1978.

Toksoz, M.N., Buck, W.R. and Hsui, A.T., Crustal evolution and thermal state of Tibet, in Geological and Ecological Studies of Qinghai-Xizang Plateau, NY, Gordon and Breach, pp. 847-858, 1981.

Tong Wei and Zhang Mingtao, Characteristics of geothermal activities in Xizang Plateau and there controlling influence on Plateau's tectonic model, in Geological and Ecological Studies of Qinghai-Xizang Plateau, NY, Gordon and Breach, pp. 841-846, 1981.

Turcotte, D.L., Rifts: Tensional failures of the lithosphere, in: Conference on the process of planetary rifting, L.P.I. topical conference, 5-8, 1981.

Turcotte, D.L., and J.L. Ahern, On the thermal and subsidence history of sedimentary basins, J. Geophys. Res., 82, 3762-3766, 1977.

Turcotte, D.L., and E.R. Oxburgh, Finite amplitude convective cells and continental drift, J. Fluid Mech., 28, 29-42, 1967.

Turcotte, D.L., Torrance, K.E. and Hsui, A.T., Convection in the Earth's mantle, Methods in Computational Physics, 13, 431-454, 1973.

Turcotte, D.L., F. Cook, and R.J. Willeman, Parameterized convection within the moon and terrestrial planets, Proc. Lunar Planet. Sci. Conf., 10th, 2375-2392, 1979.

Turcotte, D.L. and G. Schubert, Geodynamics applications of continuum physics to geological problems, John Wiley and Sons, New York, 450 pp., 1982.

Wang, C.-Y., Y. Shi and W-H. Zhou, On the tectonics of the Himalaya and the Tibet Plateau, J. Geophys. Res., 87, 2949-2957, 1982.

Watts, A.B., and W.B.F. Ryan, Flexure of the lithosphere and continental margin basins, Tectonophysics, 36, 25-44, 1976.

Watts, A.B., and M.S. Steckler, Subsidence and eustasy at the continental margin of eastern North America, in Maurice Ewing Symposium Ser. 3, pp. 218-234, Washington, D.C., AGU, 1979.

Watts, A.B., and M.S. Steckler, Observations of flexure and the state of stress in the oceanic lithosphere, J. Geophys. Res., 85, 6369-6376, 1980.

Weertman, J. and Weertman, J.R., High temperature creep of rock and mantle viscosity, in Ann. Rev. Earth Planet. Sci., 3, 293-315, 1975.

Weins, D.A. and S. Stein, Implications of oceanic intraplate seismicity for plate stresses, driving forces and rheology, Tectonophysics, in press, 1984.

White, W.M., and J.-G. Schilling, The nature and origin of geochemical Variations in mid-Atlantic ridge basalts from the central north Atlantic, Geochim. Cosmochim. Acta., 42, 1501-1516, 1978.

Woodhouse, J.H. and Dziewonski, Mapping the upper mantle: three dimensional modelling of earth structure by inversion of seismic waveforms, J. Geophys. Res., 89, 5953-5986, 1984.

Xu, R., Vegetational changes in the past and the uplift of the Qinghai-Xizang Plateau, in Geological and Ecological Studies of Qinghai-Xizang Plateau, NY, Gordon and Breach, pp. 139-144, 1981.

Yuen, D.A., and L. Fleitout, Stability of the oceanic lithosphere with variable viscosity: An initial-value approach, Phys. Earth Planet. Inter., submitted, 1984.

Yuen, D.A., W.R. Peltier, and G. Schubert, On the existence of a second scale of convection in the upper mantle, Geophys. J. R. Astr. Soc., 65, 171-190, 1981.

Zhou, Y.-s., et al., The migration and evolution of magmatism and metamorphism in Xizang since cretaceous and their relation to the Indian plate motion A possible model for the uplift of Qinghai-Xizang Plateau, Proceedings of the Symposium on Tibet Plateau, 363-378, Gordon and Breach, N.Y., 1981.

Zielinski, G., On the thermal evolution of passive continental margins, thermal depth anomalies, and the Norwegian-Greenland Sea, J. Geophys. Res., 84, 7577-7588, 1979.

Zonenshain, L.P., and L.A. Saugtin, Geodynamics of the Baikal Rift zone and plate tectonics of Asia, Tectonophysics, 75, 1-26, 1981.

Zorin, Y.A., The Baikal Rift: An example of the intrusion of asthenospheric material into the lithosphere as the cause of disruption of lithospheric plates, Tectonophysics, 73, 91-104, 1981.

"There is something to be said for every error, but whatever may be said for it, the most important thing to be said about it is that it is erroneous."

-G.K. Chesterton,"All is grist."

Appendix: Governing Equations and Numerical Methods

A.1 Introduction

This appendix is a discussion of the equations and numerical techniques used for this study. The governing partial differential equations are given. These equations are highly nonlinear, therefore numerical methods must be used to solve them. Various numerical methods are briefly reviwed and the basic form of the finite difference approximations to the governing differential equations are given. Next, a method to deal with curved solid no-slip boundaries, called the "repeated corner" method, is developed. A comparison between the use of Jacobi iteration formulas to solve the difference equations for a range of viscosity profiles and a more recently developed direct technique (Sweet, 1975) is described.

A.2 Governing Partial Differential Equations

For this study we solve the Navier-Stokes equations in two dimensions for mass, momentum and energy conservation (Batchelor, 1967). They are modified for the problem of flow in the earth's mantle by dropping inertial terms and terms that depend on material compressibility (Turcotte et al., 1972). They are written in terms of a stream function (ψ) and a vorticity (ω) as:

$$\frac{\partial \Theta}{\partial t} = u \cdot \frac{\partial \Theta}{\partial x} + w \cdot \frac{\partial \Theta}{\partial z} + \nabla^2 \Theta + H \qquad (A.1)$$

$$\nabla^2(\mu\omega) = Ra \frac{\partial T}{\partial x} + 2 \left[\frac{\partial^2 u}{\partial x^2} \frac{\partial^2 \psi}{\partial z^2} - \frac{\partial^2 \mu}{\partial z^2} \frac{\partial^2 \psi}{\partial x^2} - 2 \left(\frac{\partial^2 \mu}{\partial x \partial z} \frac{\partial^2 \psi}{\partial x \partial z}\right)\right] \qquad (A.2)$$

$$\nabla^2 \psi = \omega : \qquad \nabla^2 \equiv \frac{\partial^2}{\partial x^2} + \frac{\partial^2}{\partial z^2} \qquad (A.3)$$

where the non-dimensional variables are: $\Theta = (T-T_o)/\Delta T$ where T = temperature, T_o = temperature at top of box, ΔT = temperature difference initially across box; t = time ; μ = viscosity ; x is the horizontal coordinate and z the depth u,w = x and z velocities ; $u = \delta\psi/\delta z$, $w = -(\delta\psi/\psi x)$, $H = (h L^2)/\rho cp$, with h in joules/sec, is the heat production rate; L is a length scale, usually the height of the box, and $Ra = ga\Delta TL^3/\mu\kappa$ is the Rayleigh number. Horizontal distance is measured by x and z is depth as shown in figure 1.

A.3 Numerical Methods

A.3.1 Review of Methods

Many kinds of numerical methods have been used to solve equations (1)-(3) to study finite amplitude thermal convection since they cannot be solved analytically. We will briefly describe the different methods which are used and explain why the finite difference scheme we use was chosen. Torrance (1979) has reviewed three major types of numerical methods used to study solid-state convection: finite differences, the finite element method and spectral methods. He notes that finite differences have reasonably well understood accuracy, stability and convergence characteristics. The coding for finite differences is simple and computer storage is modest. For finite elements stability and accuracy are not well

understood, but some comparisons wtih finite difference results have been carred out for complex rheologies (Christensen, 1982). The greatest drawback to the finite element method is the large amount of computer space and time required for calculations with even modest resolution. Finally, spectral methods have not been extended to complex rheologies, such as are considered here. It is the very large computer storage which have caused us to choose finite differences in solving equations A.1 to A.3. Finite element studies have recently been successfully used with complex rheologies (Kopitze, 1982; Christensen, 1982, 1984; Fleitout and Yuen, 1984), but the meshes considered have been considerably coarser than those used here, and large computers were used in their calculations.

A variety of finite difference schemes exist to solve problems in thermal convection. A common features of these schemes is that the governing partial differential equations (1-3) are approximated by finite difference equations. The values of field variables are defined at discrete points in the solution domain (grid points) and the partial derivatives of these variables appearing in the governing equations are approximated by finite difference derivatives, as noted by Parmentier (1975). Roache (1982) discusses the general application of finite difference methods to problems in fluid mechanics. Problems of thermal convection with variable viscosity using finite differences have been carried out by Torrance and Turcotte (1972), Andrews (1972), Houston and DeBraemaker (1974), Parmentier et al. (1976), Toksoz and Hsui (1978). The stream function can be computed either by solving

two second-order equations (2) and (3) as is done by Torrance and Turcotte (1972), Parmentier et al. (1976), and Toksoz and Hsui (1978) on a single fourth-order equation as is done by Andrews (1972) or Houston and DeBraemaker (1974). The energy equation (eqn. A.1) can be solved using an explicit method as is done by Turcotte et al. (1973), Parmentier et al. (1976), Parmentier and Turcotte (1978) and others or by using the alternating direction implicit method as in Houston and DeBraemaker (1972). Other implicit methods (Sweet, 1975) will be evaluated here for the solution for the stream function.

A.3.2 Basic Finite Difference Forms

The basic forms of the finite difference approximations which we will use for solving the Navier-Stokes equations A.1 to A.3 are taken from Turcotte et al. (1973). They are valid only for grids with uniform spacing between grid points. They are included as background to the development of a method to treat irregular boundaries. Also, we will use a general form of the finite difference equations, described by Parmentier (1975), so that irregular mesh spacings may be used. The spacial derivatives in equations A.1 to A.3 are approximated using three point central differences:

$$\left(\frac{\partial \Theta}{\partial x}\right)_{i,j} = (\delta_x \Theta)_{i,j} = \frac{\Theta_{i+1,j} - \Theta_{i-1,j}}{2\Delta x}$$

$$\left(\frac{\partial^2 \Theta}{\partial x^2}\right)_{i,j} = (\delta_x^2 \Theta)_{i,j} = \frac{\Theta_{i+1,j} - 2\Theta_{i,j} + \Theta_{i-1,j}}{\Delta x^2} \qquad \text{(A.4)}$$

$$\left(\frac{\partial^2 \Theta}{\partial x \partial z}\right)_{i,j} = (\delta_x \partial_z \Theta)_{i,j} = \frac{\Theta_{i+1,j+1} - \Theta_{i+1,j-1} - \Theta_{i-1,j+1} + \Theta_{i-1,j-1}}{4\Delta x \Delta z}$$

where the subscripts (i,j) denote the ith grid point in the x-direction and the jth point in the z direction. The expressions are accurate to $O(\Delta x^2)$.

The advective terms of equation A.1 are approximated using the upwind difference form discussed by Torrance (1968):

$$\begin{aligned}\left(u \cdot \frac{\partial \Theta}{\partial x}\right)_{i,j} \cong \left(\delta^x[U_T]\right)_{i,j} = \frac{1}{2\Delta x}\{&\left(U_{T_{i,j}} - |U_{T_{i,j}}|\right)\Theta_{i+1,j} \\ &+ \left(U_{T_{i,j}} + |U_{T_{i,j}}| - U_{T_{i-1,j}} + |U_{T_{i-1,j}}|\right)\Theta_{i,j} \\ &- \left(U_{T_{i-1,j}} + |U_{T_{i-1,j}}|\right)\Theta_{i-1,j}\}\end{aligned} \tag{A.5}$$

where:

$$\begin{aligned}U_{T_{i,j}} &\equiv \frac{1}{2}\left(U_{i+1,j} + U_{i,j}\right) \\ U_{T_{i-1,j}} &\equiv \frac{1}{2}\left(U_{i,j} + U_{i-1,j}\right)\end{aligned} \tag{A.6}$$

This is a conserving form of upwind differencing. This one-sided difference form has the advantage over central differences of numerical stability but it introduces an $O(\Delta t, \Delta x)$ truncation error. All space derivatives are evaluated at a time t^n. The time derivative is given by the forward difference:

$$\left(\frac{\partial \Theta}{\partial t}\right)^n_{i,j} = \frac{\Theta^{n+1}_{i,j} - \Theta^n_{i,j}}{\Delta t} \tag{A.7}$$

We then have an explicit marching difference form for the temperature equation:

$$\frac{\Theta^{n+1}_{i,j} - \Theta^n_{i,j}}{\Delta t} = -\left(\delta_x{}^*[U_T]\right)^n_{i,j} - \left(\delta_z{}^*[W_T]\right)^n_{i,j} + \left(\delta_x{}^2\Theta + \delta_z{}^2\Theta\right)^n_{i,j} + H_{i,j} \tag{A.8}$$

$$H_{i,j} = \frac{H\ L^2}{C_p\ \Delta T\ \kappa}$$

The representation of the vorticity and stream function equations (A.2 and A.3) are

$$\delta_x^2[\eta\omega] + \delta_z^2[\eta\omega])_{i,j} = 2(\delta_x^2\eta\gamma_z\kappa - \delta_z^2\eta\delta_x w + \delta_x\delta_z\eta[\delta_z w-\delta_x u])_{i,j} + Ra(\delta_x\Theta)_{i,j} \quad (A.9)$$

and:

$$\omega_{i,j} = (\delta_x^2\psi)_{i,j} + (\delta_z^2\psi)_{i,j} \quad (A.10)$$

The given finite difference equations conserve heat and vorticity in transport between grid points. A scheme of difference equations which is conserving as well as allowing for non-uniform grid spacing was developed by Parmentier (1975). This was used in the present study to allow fine meshes in the regions of rapidly varying viscosity, temperature and stream function, while not having an inordinate number of grid points overall.

The boundary conditions on the temperature stream function and vorticity must be written in a suitable difference form. The temperature boundary conditions are either constant temperature or constant heat flux. For a zero heat flux boundary condition an extra row of grid points is added outside the boundary with the temperatures set equal to the first internal row of points. Equation 8 is used to advance the temperatures along the boundary.

The stream function is set to be zero along all the boundaries. This ensures that the velocity normal to the boundary is zero.

The vorticity boundary condition is different for a zero

stress than for a no-slip condition. For zero stress the boundary value of the vorticity (ω_b) is set to zero. For fixed boundaries a one-sided difference approximation of the vorticity equation is used. We advance the boundary vorticity using:

$$\omega_{i,o} = -\frac{2\eta\psi_{i,1}}{(\Delta z)^2} \qquad (A.11)$$

The numerical stability of the individual equations can be guaranteed. The stream function and vorticity equations (A.9 and A.10) may be rewritten as Jacobi iteration formulas for ψ_i and $\omega_{i,j}$, respectively. Stability on the interior of the mesh is assured for the equations alone, but at a solid boundary where the viscosity decreases away from the boundary Parmentier (1975) has a linear instability. He combines a one-dimensional stability analysis with experience with two-dimensional calculations to find that the condition on the Jacobi iteration factor (β) which insures stability of the vorticity-stream function equations is:

$$\beta \lesssim \left(\frac{\mu_{2,j}}{\mu_{1,j}}\right)\Bigg|_{\text{minimum}} \qquad (A.12)$$

Here $\mu_{1,j}$ is the viscosity at the jth boundary point and $\mu_{2,j}$ at the one grid space away from the boundary, the minimum subscript refers to the minimum value over the fixed boundary.

The time step used to advance the temperature equation must be restricted to ensure stability as described by Lax and Richtemyer (1956). Their definition of stability is that the numerical solutions will converge to the exact solution of the differential equations as ΔX, ΔZ and ΔG tend to zero. The

required condition on the time step is:

$$\Delta t < \left[\frac{1}{2\Delta x}\left(|U_{T_{i,j}}| + |U_{T_{i-1,j}}|\right) + \frac{1}{2\Delta z}\left(|W_{T_{i,j}}| + |U_{T_{i-1,j}}|\right) + \frac{2}{(\Delta x)^2} + \frac{2}{(\Delta z)^2}\right]^{-1} \qquad (A.13)$$

Again the minimum (Δt) over the grid is used as the time step.

The stability of each of the equations A.8 to A.10 is insured with the foregoing restrictions on the boundary vorticity Jacobi factor and time step, but the stability of the coupled system of equations is not. As a practical way to damp instabilities in the system the Jacobi factor for the vorticity and the stream function equations was set to be the same one used for the boundary vorticity equation (A.11).

A.3.3 Repeated Corner Approach to Curved Boundaries

In dealing with the problem of cooling of fluid with strongly temperature-dependent viscosity, which we do here, it is found to be computationally advantageous to make the fixed flow boundary approximate an isoviscous line. The method described here is applicable to the case when the viscosity decreases away from the boundary and the exact motions in the vicinity do not need to be accurately modelled. This is true because we can choose a viscosity value for the boundary line which is high enough that the flow near the boundary is negligible compared to the flow in regions of lower viscosity. The problems considered here are transient and the position of an isoviscous line changes with time through the course of a

calculation. Therefore, we want a method of approximating the position of the no-slip boundary which uses the grid point positions initially chosen for the problem and can easily be adjusted at each time step.

The method we use to calculate the boundary vorticity on an irregular boundary is illustrated in Figure 1a. The smooth isoviscous line is approximated by the jagged one which goes through the grid points closest to that line. Where the boundary through the grid points is horizontal or vertical on both sides of a boundary grid point the standard expression (equation A.11) is used to update the boundary vorticity. At corners of the boundary a special treatment using discontinuous values of the boundary vorticity is employed, shown in Figure 1b. The use of discontinuous values in specifying the boundary conditions was suggested by Richardson (1910). Its use for evaluation of the boundary vorticity was suggested by Thom and Apelt (1961), Roache and Mueller (1970) and Kacker and Whitlaw (1970). Roache and Mueller (1970) evaluated several methods of dealing with the vorticity at a sharp corner and concluded that allowing dual values at the corner point is the best method. The two values of vorticity at the corner grid point correspond to second derivatives of the stream function in the x and z directions, respectively. The corner vorticities can be thought of as place holders of the value of the vorticity for the two directions defined by the grid lines. There is no reason for these values to be equal at a corner. Calculations,

such as those described in Chapter 2, were done with both the method of "repeated corners" and with the fixed boundary taken to be straight and horizontal give the same results, but the "repeated corner" approach was more efficient. The calculations described in Chapter 4 where the geometry of the temperature structure is more extreme would have been too costly to do without this method.

The sequence used in doing the calculations was as follows:

(1) Set up a system of grid points which gives fine spacing in the areas where quantities vary rapidly.

(2) Give initial temperatures to all grid points.

(3) Check for minimum time step Δt using equation A.13.

(4) Advance the temperatures in time with equation A.8.

(5) Select the flow boundary according to the viscosity, which is calculated from the temperatures using an equation for viscosity which will differ for the case considered. The boundary points will lie below a prescribed viscosity cutoff value. The advancement factor β is determined by applying equation A.12 to the rigid boundary points.

(6) Advance the vorticity ω at the grid points interior to a boundary using equation A.9.

(7) Using equation A.10 the stream function ψ is brought up to date with the new vorticity values by applying it to the interior points and iterating until a satisfactory

level of convergence is achieved. The convergence criterion used here is that the maximum change in ψ from one iteration to the next at a given grid point divided by the maximum value of ψ must be less than 0.0001.

(8) The vorticity on the rigid boundaries is determined from the most recent values of the ψ and ω fields using equation A.11 once if the boundary is flat and twice if it is a corner.

(9) The vorticity field is iterated to convergence by repeating steps (6) through (8) until a convergence criterion, defined the same way as for ψ, of 0.0001 is achieved.

(10) Calculate the velocity field from the stream function values using centered differences and continue to step (3), unless the model time computed by summing the time steps is greater than a value set for the run to end.

A.3.4 Test of Alternative Numerical Method

A comparison was made between the method just outlined and another method of solving the finite difference system of equations (A.8 to A.11). The new scheme uses a recently developed numerical technique to solve the Poisson equation for the vorticity on the interior mesh (equation A.9) and the stream function equation A.10, while everything else is calculated as listed above. The individual Poisson equations are solved simultaneously for the values of the function (ω or ψ) for all grid points using a cyclic reduction algorithm developed by Sweet (1974). The advantage to this method is

that no iteration is required on the individual vorticity or stream function equations to get the field values which satisfy the equations. The problem is that the two equations (A.9 and A.10) are coupled by the terms in the vorticity equation which depend on second derivatives of the viscosity field multiplied by derivatives of the stream function. Thus for cases of constant viscosity or where there are only linear viscosity gradients use of the cyclic reduction algorithm to solve the equations for ω and ψ require just one iteration each and is much faster than the Jacobi iterative technique (see Table A.1). This is not the case for viscosity which changes in a more complicated manner. A series of calculations was done in a square box with an even mesh of 16 x 16 grid points for both methods. The viscosity was taken to be depth dependent only and is given by:

$$\mu(z,x) = e^{-\gamma z} \qquad \text{(A.14)}$$

Where γ is varied from 0 to 20. With a reference viscosity of 1.0 the Rayleigh number was 8.3×10^4. Damping is used for vorticity values in the method using the fast Poisson equation solver. This is done in a similar fashion to damping using hte relaxation method (Roache, 1982). After each iteration the new vorticity value at each point ($\omega_{i,j}^{N+1}$) is given by:

$$\omega_{i,j}^{N+1} = \omega_{i,j}^{N} + z_{rel} * \omega_{i,j}^{pois} \qquad \text{(A.15)}$$

where $\omega_{i,j}^{pois}$ is the vorticity value resulting from solving the

vorticity equation with a matrix method such as cycling reduction and z_{rel} is the damping factor.

The results of the comparison are summarized in Table A.1. For the method using Jacobi iteration or the equations the number of iterations and amount of computer time to achieve convergence of the solution, so that the vorticity and stream function fields are in equilibrium with the given temperature field, initially goes down with increasing value of γ then goes up again. This is due to the two factors which control the rate of iterative convergence of the coupled equations. One is the average viscosity over the region of the calculation and the other is the size of the coupling terms in the vorticity equation. The average viscosity goes down with increasing value of γ, but the size of the second derivative of viscosity with respect to depth increases with increasing γ. For the case of using the matrix methods to solve the vorticity and stream function equations it was found that the damping factor (z_{rel}) had to be reduced for increasing γ to achieve stability of the system. Also the number of iterations required for convergence went up with increasing values of γ. The constant viscosity case ($\gamma = 0$) required only one iteration of the vorticity equation to achieve convergence. Experience with the matrix method applied to these equations for the cases given in Table A.1 and for more general cases of variable viscosity it was found that the damping factor required to achieve stability is given by:

$$zrel = \left. \frac{Ra \cdot \delta_x \theta}{2[\delta_x^2 \eta \cdot \delta^2 \psi - \delta^2 \eta \delta^2 \psi - 2(\delta x \delta z \eta \cdot \delta x \delta z \psi)]} \right|_{min} \qquad (A.16)$$

which is the minimum ratio of the linear term to the coupling term in the vorticity Poisson equation over the grid. For viscosity fields which depend strongly on temperature and pressure, as is the case for the models considered in this study, the value of zrel given by equation (A.16) often becomes very small ($< 10^{-6}$). This was found to slow the convergence to an iterative solution to the system so that it was impractical to use this method. Thus, in all the discussions which follow the Jacobi iteration method is used to solve the vorticity and stream function equations.

TABLE A.1

γ	zrel	itz	cpu	zrel	itz	cpu
0	1.0	58	14.3	1.00	1	2.6
1	1.0	54	14.1	.98	4	3.3
5	1.0	31	9.2	.60	9	4.4
10	1.0	24	7.04	.18	30	9.0
20	1.0	53	11.03	.01	80	24.3

Table A.1. This is a comparison of the program using relaxation on the vorticity and streamfunction equations and a program where those equations are solved using the a direct method (cyclic reduction using the POIS subroutine of Sweet, 1974). For the optimal value of the damping factor (z_{rel}), as determined by trial and error, the number of iterations of the vorticity equation (itz) required for convergence and the total c.p.u. time to do the calculation on a Honeywell Multics systen is shown in seconds. The calculation was for a square box with 16 x 16 evenly spaced grid points with a viscosity which only varied with depth accorinding to the formula $\mu = \exp[-\gamma z]$, where z is the non-dimensional depth in the box. The temperature variation was linear with depth through the box with a cosine variation in the x-direction. The Rayleigh number was 8.3×10^4.

Table A.2

Table of Defined Parameters

μ	-	Dynamic viscosity
E	-	Pre-exponential in viscosity relation
V*	-	Effective activation volume; takes into account the effect of an adiabatic temperature gradient
μ_{ref}	-	Initial viscosity at 150 km depth in the model
R	-	Universal gas constant
T_m	-	Initial temperature inside box
W_b	-	Width of numerical box
D_b	-	Depth of numerical box
$Q_c(z)$	-	Horizontally averaged advective heat flux
w	-	Vertical component of velocity
T_{cm}	-	Average temperature of the convecting region
T_L	-	Average non-dimensional temperature of conductive lid
s	-	Subsidence defined using T_L
Z_L	-	Depth of the base of conductive lid (or lithosphere)
λ	-	Parameter which defines the rate of movement of the base of the lithosphere; depends on convective vigor
Z_c	-	Depth of compensation
H	-	Isostatic geoid anomaly
$T_h(z)$	-	Horizontally average temperature
G_T	-	Gravity anomaly due to two-dimensional density anomalies
ν	-	Kinematic viscostiy (μ/ρ)
P	-	Pressure
σ_{zz}	-	Total normal stress
τ_{zz}	-	Deviatoric normal stress

η - Non-dimensional viscosity

σ_T - Surface normal stress due to lid temperature variations

σ_{ws} - Total surface normal stress

$E(x)$ - Vertical deformation of the surface assuming point-wise isostatic response to the surface normal stress

$E_f(x)$ - Vertical deformation given an elastic plate flexure reducing the effect of the normal stress

D - Flexural rigidity estimated for the oceanic elasitic lithosphere

G_E - Gravity anomnaly due to E_f

G_σ - Component of G_E due to convective stresses

G_L - Component of G_E due to lid temperature variations

Q_s - Average surface heat flux

Z_p - Position of phase boundary in classic Stefan problem

L - Latent heat of fusion

T_p - Temperature of the phase change for the Stefan problem

T_s - Temperature at a depth and time for the solid region in the Stefan problem

T_{sc} - Average temperature in the solid region for the Stefan problem

Q_{cmax} - Maximum horizontally averaged heat flux; equated to the steady state Nusselt number

ℓ - Length scale for the flow weighted by advective heat flux

$\bar{\mu}$ - Dissipation averaged viscosity

Nu - Nusselt number

Ra - Rayleigh number

FIGURE CAPTIONS

Figure A.1a. Schematic shows the way a curved boundary of a isoviscous line is approximated by a boundary with corners for the numerical approximations described in the text.

Figure A.1b. Blow-up of a portion of figure 1a showing one sharp corner and the way in which the boundary vortiity is set at that corner. The two expressions for the boundary vorticity for the vertical and horizontal directions are given.

CURVED BOUNDARY APPROXIMATION

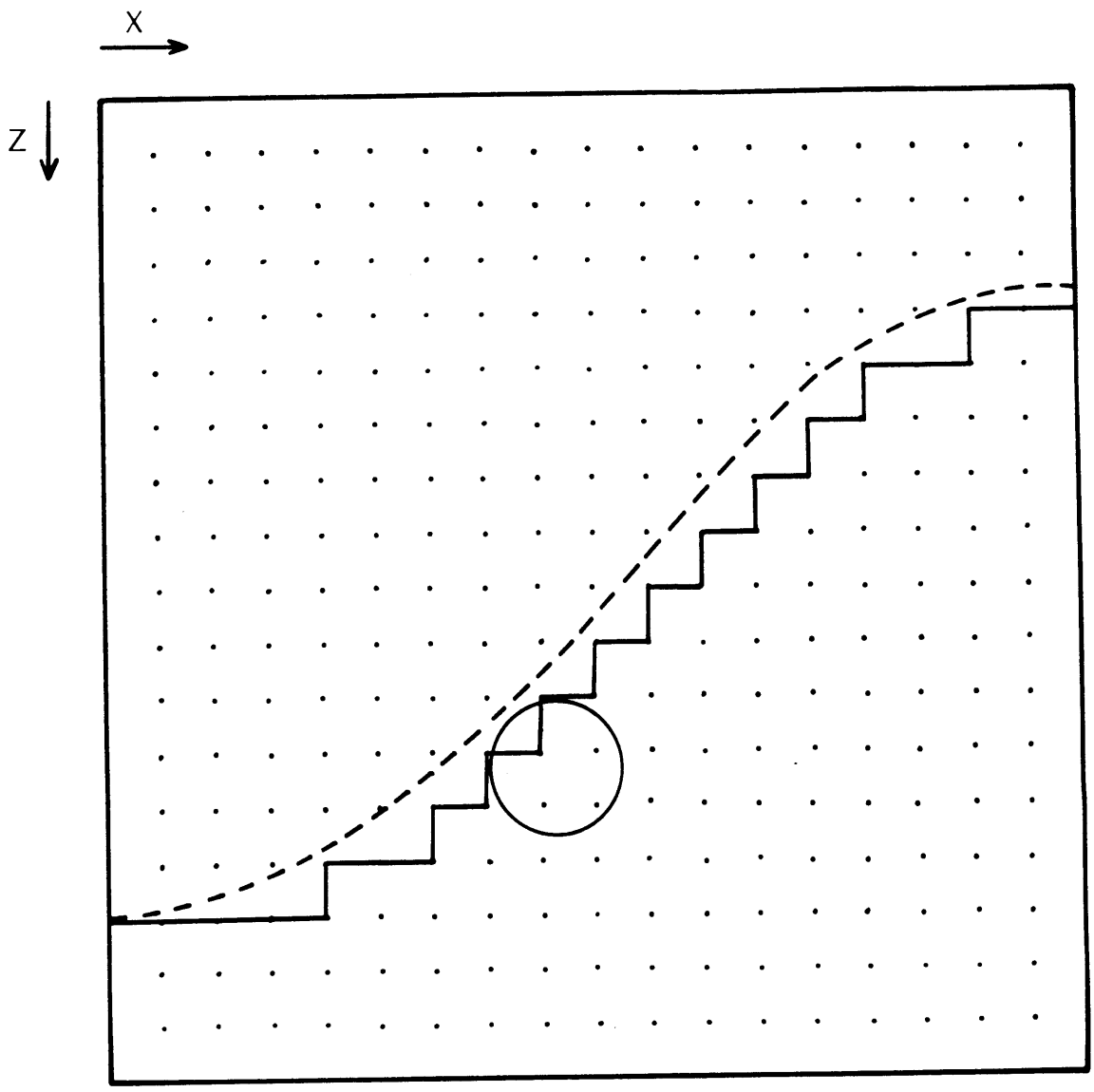

ISOVISCOUS LINE

NUMERICAL BOUNDARY

Figure A.1 (a)

VORTICITY AT CORNERS

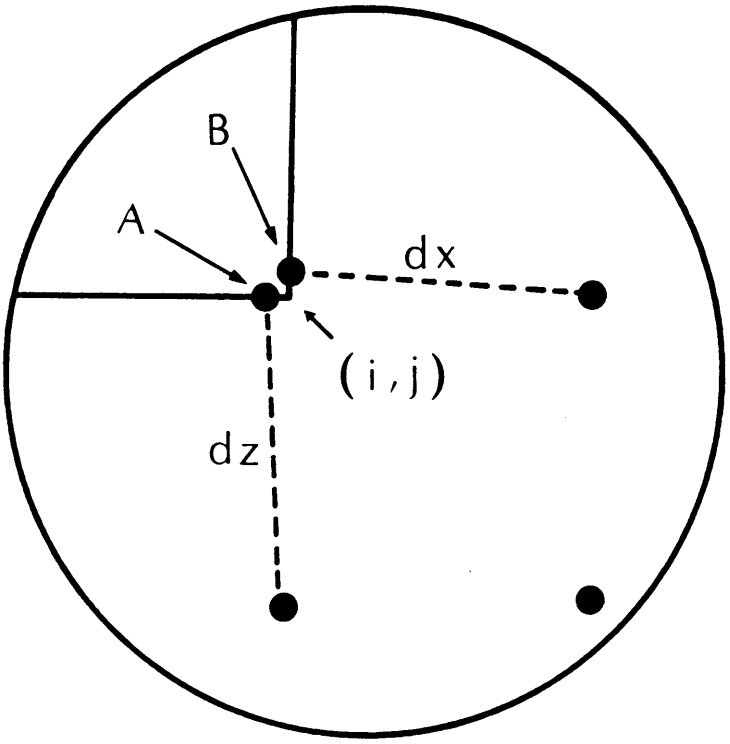

$$\omega_A(i,j) = -2\,\psi(i+1,j)/(dz)^2$$

$$\omega_B(i,j) = -2\,\psi(i,j+1)/(dx)^2$$

Figure A.1 (b)

Biographical Note

When I was three years old I came to Boston and thus began the course that led to this thesis. While my father was doing a couple of weeks of work in an area research lab I explored the parks, museums and shops with my mother. I decided that I would someday leave the quieter life in Virginia and make my way back.

It took about twenty years to go through the public schools of Richmond and York County, Va., then the College of William and Mary. I also took a brief detour to go to Eastboune College - an English public school - for a year. At William and Mary I started off majoring in Physics, but then decided it would be good to go outside once in a while so I majored in Geology as well.

Since returning to the Boston area I have almost never gone outside in connection with my research in Geophysics, but I have frequented the parks, movie theaters, basketball courts and other places which make this city fun. In my research I worked for years trying to figure out the Moon, and finally decided to let it alone for a while and do this thesis.

For the next few years I will be splitting the difference between Virginia and Boston and living in New York while working at the Lamont-Doherty Geological Observatory.